Performance Improvement of Optical High-Speed Short-Range Communication Systems Utilizing Bandwidth Extension and Advanced Digital Signal Processing

vorgelegt von
Dipl.-Ing.
Christoph Kottke

von der Fakultät IV - Elektrotechnik und Informatik
der Technischen Universität Berlin
zur Erlangung des akademischen Grades

Doktor der Ingenieurwissenschaften
- Dr. Ing. -

genehmigte Dissertation

Promotionsausschuss:

Vorsitzender:	Prof. Dr.-Ing. Friedel Gerfers
Gutachter 1:	Prof. Dr.-Ing. Klaus Petermann
Gutachter 2:	Priv.-Doz. Dr. Volker Jungnickel
Gutachter 3:	Prof. Dr.-Ing. Stephan Pachnicke

Tag der wissenschaftlichen Aussprache: 10.05.2019

Berlin 2019

Abstract

High-speed short-range optical links are a key technology for data center applications. Today, they enable the transmission of huge amounts of information in a cost and energy efficient way and are typically based on simple optics and on-off keying modulation. In order to meet the world-wide increasing demand on transmission capacity for these optical links, new approaches are required to improve the currently achievable capacity. In this thesis two strategies are discussed. The first one utilizes a bandwidth extension concept based on analog mixing to increase the signal bandwidth beyond the limits of today's signal generators. The second one investigates the application of linear and nonlinear pre-equalization for vertical cavity surface emitting lasers (VCSEL) based links.

The bandwidth extension concept is experimentally investigated for a high-speed optical link based on intensity modulation (IM) and direct detection (DD). The achieved transmission rates are well beyond 100 Gb/s showing the feasibility of such an approach. The thesis further includes a detailed investigation of the relevant components, the suitability of different modulation formats and the use of digital signal processing (DSP) to compensate for the system impairments such as inter-symbol interference and in-phase and quadrature (I/Q) imbalance. Furthermore, the demonstration of a wideband digital-analog converter based on this concept is shown.

DSP will be one major aspect for future high-speed short-range optical links, enabled by the ever decreasing cost of application-specific integrated circuits (ASIC). Optical links using VCSELs, with their typically non-ideal characteristics, benefit especially from enhanced equalization schemes, which enable an error free transmission at higher symbol rates and the use of higher order modulation formats. Linear and nonlinear pre-equalization are two options to achieve this goal. In this work an optimized linear pre-equalization approach is utilized to demonstrate record high transmission rates for a VCSEL-based IM/DD link. Furthermore, the influence of using a nonlinear pre-equalizer on the system performance is investigated and compared to pure linear pre-equalization.

Acknowledgements

Thanks to my family for their support.
Thanks to Luz for her patience.
Thanks to my colleagues for the useful comments and discussions.

Contents

List of Figures

List of Tables

List of Abbreviations

ADC	Analog to Digital Converter
A/D	Analog-Digital
ASIC	Application-Specific Integrated Circuit
AMUX	Analog Multiplexer
AWG	Arbitrary Waveform Generator
ASE	Amplified Spontaneous Emission
btb	back-to-back
BER	Bit Error Rate
BPF	Band-Pass Filter
CAP	Carrier-less Amplitude Phase modulation
CMOS	Complementary Metal-Oxide-Semiconductor
CW	Continuous Wave
D/A	Digital-Analog
DAC	Digital to Analog Converter
DBI	Digital Bandwidth Interleaving
DCF	Dispersion Compensating Fiber
DD	Direct Detection
DFB	Distributed Feedback
DFE	Decision Feedback Equalizer
DML	Directly Modulated Laser
DMT	Discrete Multitone
DSP	Digital Signal Processing
EA	Electrical Amplifier
EAM	Electro-Absorption Modulated
EDFA	Erbium-Doped Fiber Amplifier
EML	Externally Modulated Laser
ENOB	Effective Number Of Bits
EVM	Error Vector Magnitude
FEC	Forward Error Correction
FDE	Frequency Domain Equalizer
FET	Field Effect Transistor
FFE	Feed-Forward Equalizer
FFT	Fast Fourier Transformation
FI-DAC	Frequency Interleaved DAC
FM	Few Mode
HD	Hard Decision
IC	Integrated Circuit
IF	Intermediate Frequency
IFFT	Inverse Fast Fourier Transformation
IM	Intensity Modulation
IMP	Intermodulation Product
I/Q	In-phase/Quadrature

IP3	Third order Intermodulation Point
LS	Least Square
LO	Local Oscillator
LPF	Low-Pass Filter
MDM	Mode Division Multiplex
MIMO	Multiple-Input-Multiple-Output
MM	Multi-Mode
MMF	Multi-Mode Fiber
MLSE	Maximum Likelihood Sequence Estimation
MMSE	Minimum Mean Square Error
MPN	Mode Partition Noise
MUX	Multiplexer
MZM	Mach-Zehnder Modulator
OAM	Orbital Angular Momentum
OFDM	Orthogonal Frequency Division Multiplex
OOK	On-Off Keying
QAM	Quadrature Amplitude Modulation
PAM	Pulse Amplitude Modulation
PAPR	Peak-to-Average Power Ration
PD	Photodiode
POF	Plastic Optical Fiber
PolMUX	Polarization Multiplex
P1dB	1 dB Compression Point
RF	Radio Frequency
RIN	Relative Intensity Noise
RMS	Root Mean Square
RRC	Root Raised Cosine
Rx	Receiver
SD	Soft Decision
SDM	Space Division Multiplex
SM	Single Mode
SMF	Single-Mode Fiber
SMSR	Side-Mode Suppression Ratio
SNR	Signal-to-Noise Ratio
SSB	Single Side-Band
SSMF	Standard Single-Mode Fiber
SST	Spurious Suppression Table
Tx	Transmitter
VCSEL	Vertical Cavity Surface Emitting Laser
WDM	Wavelength Division Multiplex

List of Symbols

$a_{m,n}$	Coefficients of a polynomial description of mixer nonlinearities with intermodulation order m and LO order n
$a_{0..3}$	Coefficients of a polynomial description of the VCSEL thermal offset current
$\bar{a}$	Differential gain coefficient of a laser
A	Amplitude
$b_{0..2}$	Coefficients of a polynomial description of the VCSEL current-voltage relation
$c_{0..2}$	Coefficients of a polynomial description of the VCSEL current-voltage relation
C_{cl}	Mixer conversion loss
d_{a}	Thickness of the active layer
f_{OUT}	Mixer output frequency
f_{LO}	Mixer LO frequency
$f_{1,\mathrm{IN}}$	1st mixer input frequency
$f_{2,\mathrm{IN}}$	2nd mixer input frequency
f_{c}	Electrical carrier frequency (QAM signal)
f_{sc}	Electrical subcarrier frequency (OFDM signal)
Δf_{Rx}	Receiver bandwidth
F	Noise figure
F_{n}	Noise figure of the amplifier following the photodiode
F	Langevin forces
g	Material gain
G	Gain
G_0	Gain coefficient
h_{I}	Impulse response in the I branch of an I/Q mixer
h_{Q}	Impulse response in the Q branch of an I/Q mixer
$h_{\mathrm{RF},1}$	Impulse response in the 1st RF branch of an I/Q mixer
$h_{\mathrm{RF},2}$	Impulse response in the 2nd RF branch of an I/Q mixer
$h_{\mathrm{LO},1}$	Impulse response in the 1st LO branch of an I/Q mixer
$h_{\mathrm{LO},2}$	Impulse response in the 2nd LO branch of an I/Q mixer
h	Impulse response
h_p	Volterra kernel of order p
H_{IQ}	Frequency response for I/Q imbalance
H_{sys}	System frequency response
H_{ct}	Crosstalk frequency response
H_{laser}	Laser transfer function
$\Im$	Imaginary valued part of signal
I_{PD}	Photocurrent
$Iso_{\mathrm{LO\text{-}RF}}$	Isolation mixer LO to RF port
$Iso_{\mathrm{RF\text{-}LO}}$	Isolation mixer RF to LO port
I_{th}	Threshold current

I_{b}	Bias current
I_{tho}	Constant part of threshold current
I_{off}	Thermal offset current
$IMP_{m,n}$	Relative power of intermodulation product to desired signal with intermodulation order m and LO order n
$IMP_{m,n,\mathrm{ref}}$	Reference relative power of intermodulation product to desired signal form mixer spurious suppression table with intermodulation order m and LO order n
ΔI	Change in current density
I	Current
i	Index
j	Index
j_{IN}	Injected current density
k_B	Boltzmann constant
k	Index
k_{cpl}	Laser coupling factor
l	Index
m	Index
M	Modulation order
n	Index
N_{cr}	carrier density (electron or hole)
$N_{\mathrm{cr},0}$	carrier transparency number (i.e. carrier density at which the gain is zero)
N	Volterra kernel memory length
N_{sc}	Number of subcarrier
p	Index order of Volterra kernel
P_{RF}	Mixer RF port signal power
P_{IF}	Mixer IF port signal power
$P_{\mathrm{IN,LO\ port}}$	LO signal power at mixer LO port
$P_{\mathrm{OUT,\ LO@RF\ port}}$	LO signal power at mixer RF port
$P_{m,n}$	Power of signal with intermodulation order m and LO order n
P_{IN}	Mixer input power
$P_{\mathrm{IN,ref}}$	Reference input power form mixer spurious suppression table
P_{OUT}	Mixer output signal power
P_0	Optical output power VCSEL
q	Elementary charge
$s(t)$	Signal
S_{RIN}	Relative intensity noise
$S(k)$	kth OFDM subcarrier at the transmitter
$\tilde{S}(k)$	kth OFDM subcarrier at the receiver
S_{ph}	Photon density
$S_{\mathrm{ph},0}$	Operating point photon density
ΔS_{ph}	Change in photon density
$\Re$	Real valued part of signal
$\mathrm{rect}(t)$	Rectangular function
R_{L}	Load resistance
R_{PD}	Photodiode responsivity
R_{th}	Thermal impedance

$s_m(t)$	Signal
s_{OUT}	Mixer output signal
s_{IN}	Mixer input signal
$S_{\mathrm{Tx,tr}}$	Transmitted OFDM trainings symbol
$S_{\mathrm{Rx,tr}}$	Received OFDM trainings symbol
t	Time
T	Temperature
T_{texts}	Symbol time
T_0	Ambient temperature
$u(t)$	Complex modulated time domain baseband signal
$u_{\mathrm{I}}(t)$	Real valued part of complex modulated time domain baseband signal
$u_{\mathrm{Q}}(t)$	Imaginary valued part of complex modulated time domain baseband signal
$\tilde{u}(t)$	I/Q imbalance impaired complex modulated time domain baseband signal
V_{OUT}	Mixer output signal amplitude
V_{RF}	Mixer input signal amplitude
V_{IF}	Mixer output signal amplitude at IF frequency
V_{p}	Effective volume occupied by the lasing mode
V	Voltage
$x(t)$	Signal
$x(n)$	Discrete signal
$x_{\mathrm{test}}(n)$	Transmitted test signal
$x_{\mathrm{Pre}}(n)$	Pre-equalized signal
$y(t)$	Signal
$y(n)$	Discrete signal
$x_{\mathrm{test}}(n)$	Received test signal
α	Magnitude
β_{sp}	Spontaneous emission factor
β	Raised cosine filter roll-off factor
ϵ	Gain compression factor
η_{I}	Injection efficiency
η_{sl}	Differential slope efficiency of a VCSEL
γ	the damping coefficient (damping of the relaxation oscillation)
Γ_{r}	Gain enhancement factor (longitudinal)
Γ	Total gain enhancement factor (longitudinal and transverse)
ϕ	Phase
$\tau_{\mathrm{sp,r}}$	Radiative part of the spontaneous recombination lifetime
τ_{sp}	Spontaneous recombination lifetime
τ_{th}	Thermal time constant
Θ	Phase
ω_{RF}	Mixer RF port angular frequency
ω_{IF}	Mixer IF port angular frequency
ω_{LO}	Mixer LO angular frequency
ω_{IN}	Mixer input signal angular frequency
Θ_m	Phase of a signal
ν	Frequency

ν_r	Relaxation resonance frequency
ν_{gr}	Group velocity of the laser mode

Mathematical syntax

$*$	Convolution
^{T}	Matrix transpose
^{H}	Matrix conjugate transpose
*	Complex conjugate
$\mathfrak{F}_{DFT}$	Discrete Fourier Transform

Bold letters between square brackets indicate matrices and vectors.

Chapter 1

Introduction

Today more than 50% of the global population is connected to the Internet, with a steady increase of this number [1]. This development has been enabled by new technologies in the field of processing, storing and transmission of information. They enable the immediate exchange of information, the communication with business partners, friends and family and the participation in digital communities worldwide. Complete new economies have been developed around the Internet, changing the way we live and work. Optical communications networks are the backbone of the communications networks worldwide. They range from long-haul networks between continents, over metro networks connecting cities, down to access networks forming the backbone of mobile radio networks and even connecting the end user. A special part of the optical access networks are short-range links, which are mainly located in data centers. The requirements for these links differ greatly from typical long-haul, metro and normal access links. Short-range optical links demand low-cost systems, low energy consumption and simple optics. This results in serious challenges to address the ever increasing capacity demand in these networks.

1.1 Short-range optical communications

The competitiveness of copper cabling for short-range interconnects relied on its simplicity and availability. But today more and more interconnects are realized with optics, primarily driven by the data rate requirements. Data centers and high-performance computing are two examples for the application of such links, which encompass distances from in-rack connections (<m) up to intra data center connects (a few km). The ongoing demand for fast, reliable, power-efficient and low-cost optical links has driven numerous developments in the field of optical communications. This encompasses especially the improvement of optical modulators, with vertical cavity surface emitting lasers (VCSEL), the most important ones for short-range interconnects. The availability of low-cost lasers resulted in the wide deployment of optical links in various applications and the domination of the market by VCSELs. An important product for short-range links are also active optical cables (AOC), which consist of a fiber cable with integrated optoelectronic transceivers at the end. These cables do not only offer several advantages compared to copper in terms of weight, distance and cost, but they are also much easier to use since only the electrical interfaces have to be standardized. This allows an easy adaptation of the optical properties to the actual requirements. Today AOCs for 400 Gb/s over 100 m MMF are available [2].

Up to now the further growing demand on transmission capacity for short-range links could primarily be satisfied by developing faster VCSELs and detectors. However, a further capacity increase requires new approaches like the use of more advanced modulation formats and the application of digital signal processing (DSP).

This is e.g. already the case for the new 400G Ethernet standard using a 4-level pulse amplitude modulation (PAM) [3]–[5]. Both aspects, the use of advanced modulation formats and the application of DSP, require high-speed digital-to-analog and analog-to-digital converters (DAC/ADC). However, today these devices present bandwidths below those of their optical counterparts, resulting in a bandwidth bottleneck which has to be addressed. There are other approaches to increase the capacity of these short-range links, like the use of parallel optics or the use of optical multiplex techniques. The former is typically limited by the available space for the fibers and the latter due to the high cost of optical solutions.

1.2 Objective of the thesis

The main objective of this thesis is the improvement of the transmission capacity for high-speed short-range communications systems. Two approaches are investigated to achieve this. The first is the investigation of a technique to increase the available signal bandwidth for high-speed short-range communication systems. With this bandwidth extension technique it is possible to go beyond the bandwidth limitations of current DACs and ADCs and exploit the entire capacity of modern optical components, which have typically significantly better characteristics than their electrical counterparts. This thesis demonstrates the feasibility of the bandwidth extension concept using a high-speed short-range transmission system. Further work includes a detailed investigation of the relevant components, the suitability of different modulation formats for the concept and the use of digital signal processing (DSP) to compensate the systems impairments. This approach can also be used in the realization of a new wideband DAC as a further application of this concept. The experimental demonstration is presented in this thesis.

The second approach consists of the investigation of linear and nonlinear pre-equalization concepts for VCSEL-based high-speed short-range communications systems. Today's VCSELs are the most used optical modulators for short-range systems, primarily due to their low cost. However, their non-ideal characteristics are a challenge for advanced modulation formats and require the application of DSP. One option is the use of pre-equalization algorithms to compensate for the linear and nonlinear VCSEL properties and thus improving the transmission capacity for such links. In this thesis a linear pre-equalization approach is presented which enables record-high transmission rates using an IM/DD link in combination with a multi-carrier modulation format. Furthermore, the influence of a nonlinear pre-equalization scheme on the system performance is investigated and its performance compared to a pure linear pre-equalization.

1.3 Outline

The thesis is organized in three parts. The first part, presented in chapter 2, gives an overview about high-speed short-range communication systems. This includes the state-of-the-art, the general link design with the important properties of the relevant components and possible concepts to improve the performance

The second part, presented in chapter 3, investigates the bandwidth extension approach. It starts with the state-of-the-art of these techniques and the system model. Afterwards, a detailed analysis of the most critical component, i.e. the analog mixer is given. In the next sections, the simulation environment supporting the measurements

is described, followed by the experimental verification of the concept. These include the experimental setup, the DSP and the results. Furthermore, the wideband DAC concept is presented and experimentally verified, followed by the conclusion and the outlook for the bandwidth extension approach.

The third part, presented in chapter 4, investigates the use of pre-equalization in a VCSEL-based transmission system. It starts with the state-of-the-art of these systems and a brief introduction to VCSELs and their important characteristics for high-speed short-range optical links. Afterwards, the system model based on a Volterra series and the pre-equalization scheme are presented. The next section describes the high-speed VCSEL experiments focusing on linear pre-equalization. This includes the VCSEL characteristics, the experimental setup, the DSP and the results. The nonlinear pre-equalization approach is investigated in more detail in the following sections. First, the simulation environment with its VCSEL model is presented, followed by the DSP and the simulation results. Furthermore, experiments are performed to verify the simulative findings. Chapter 4 ends with a conclusion and an outlook.

Chapter 2

High-speed short-range optical communication systems

This chapter gives an overview of high-speed short-range communication systems currently investigated in the research community. This includes the state-of-the-art, the general link design focused on the relevant components and the digital signal processing and concepts to further improve the transmission performance.

2.1 State-of-the-art high-speed short-range communication systems

In the last years many scientific publications with the focus on high-speed short-range communications systems were presented, primarily driven by activities related to the standardization of 400G Ethernet [3]–[5]. To give an idea about the state-of-the-art, the most interesting systems are presented in this section.

Today the most common modulation format for commercial short-range solutions is non-return-to-zero (NRZ) on-off keying (OOK), due to its simple transmitter (Tx) and receiver (Rx) realization. However, data rates of 100 Gb/s and beyond are a significant challenge, due to the high bandwidth demand of NRZ OOK. There are only few demonstrations showing the feasibility of the concept. In [6] a silicon-organic hybrid Mach-Zehnder modulator (MZM) enabled open eyes[1] at 100 Gb/s NRZ OOK in a back-to-back (btb) configuration. 116 Gb/s NRZ OOK were shown in [7] utilizing a 100 GHz external modulated laser (EML) based on a traveling-wave electro-absorption modulator (EAM) and equalization at the receiver. Also an EAM was used in [8], showing 100 Gb/s over 500 m of standard single-mode fiber (SSMF). One way to ease the bandwidth requirements of NRZ OOK is to use electrical duo-binary modulation. In [9] a 103 Gb/s transmission was shown, using the system frequency response[2] to generate the electrical 3-level duo-binary signal from the NRZ OOK signal. A real-time duo-binary OOK transmission experiment using sophisticated integrated circuits (IC) for Tx and Rx was also demonstrated in [8]. The generation of the electrical duo-binary signal was realized with a feed forward equalizer (FFE) at the Tx and the subsequent component frequency response.

PAM with 4 or 8 levels are of major interest for 400G Ethernet standardization due to their reduced bandwidth requirements compared to OOK, the relatively simple signal generation and their still acceptable sensitivity requirements. In 2015 transmission experiments at 112 Gb/s over 20 km SSMF utilizing 4-PAM, pre- and post-equalization

[1] Without equalizer

[2] A duo-binary signal can either be generated in the digital domain using a multiple-bit DAC or in the analog domain by transmitting the original OOK signal over an analog low-pass filter with a corresponding cut-off frequency.

and an MZM were shown in [10]. Similar data rates and distances were demonstrated with commercially available transmitter and receiver optical sub-assembly devices in [11]. Higher data rates of up to 180 Gb/s were shown in [12] utilizing more complex equalizer design and a dual-drive MZM. Even higher rates are possible using the newest DAC types for signal generation and an MZM as shown by Lange [13], where 200 Gb/s were achieved. The application of duo-binary schemes for 4-PAM was demonstrated in [12], [14], with a typically better performance compared to standard 4-PAM but more complicated signal generation. Transmission experiments utilizing 8-PAM, which eases further the bandwidth requirements at the cost of higher sensitivity requirements, were shown in [10], [15]. In [10], 112 Gb/s over 20 km SSMF were demonstrated, using post and pre-equalizer structures and up to 150 Gb/s were demonstrated in [15] using a sophisticated power DAC for signal generation.

Other modulation formats of interest are quadrature amplitude modulation (QAM), carrier-less amplitude phase modulation[3] (CAP) and orthogonal frequency division multiplex (OFDM) with its real-valued representation discrete multitone (DMT). CAP transmission experiments were demonstrated in [17], [18] showing 100 Gb/s over up to 10 km of SSMF. In [19] a 160 Gb/s QAM transmission was realized on a single electrical carrier with the help of a dual-drive MZM and enhanced DSP over 2 km of SSMF.

For DMT several transmission experiments at 100 Gb/s were demonstrated [20]–[23]. In [20], [21], a novel complementary metal-oxide-semiconductor (CMOS) DMT IC was utilized to modulate and demodulate the DMT signal, showing 100 Gb/s over 10 km of SSMF with 10G class optical components[4]. Similar results were shown in [21], with a detailed analysis of the impairments for DMT. In [23] an MZM enabled 130 Gb/s at 1550 nm, by utilizing the chirp of the modulator to combat the chromatic dispersion.

There are also several publications which compare the performance of these modulation formats for short-range systems. For example, in [5] duo-binary OOK, PAM, CAP and DMT are discussed for 400G Ethernet and in [24], [25] the performance of PAM, CAP and DMT formats are compared experimentally.

These publications have demonstrated the feasibility of single wavelength solutions for IM/DD-based links at data rates targeting 100 Gb/s and beyond. Different modulation formats are possible to achieve these data rates, each with its benefits and challenges. The performed experiments with advanced modulation formats[5] typically only use a single digital/analog converter for the signal conversion, thus the signal bandwidth is mostly limited by the electrical components while the optical bandwidth limitations are not yet reached. Approaches to extend the available signal bandwidth are therefore presented in the next chapter in Section 3.1. Note that transmission systems based on VCSELs haven't been mentioned here since their state-of-the-art is discussed in detail in chapter 4.

[3] Carrierless amplitude phase modulation (CAP) is a variant of quadrature amplitude modulation (QAM). Instead of modulating the amplitude of two carrier waves, CAP generates a QAM signal by combining two PAM signals filtered through two filters designed so that their impulse responses form a Hilbert pair. If the impulse responses of the two filters are chosen as sine and a cosine, the only mathematical difference between QAM and CAP waveforms is that the phase of the carrier is reset at the beginning of each symbol. The CAP signal is commonly digitally generated and digital-analog converted using a single DAC. [16]

[4] Optical components designed for 10G transmission systems, like 10 Gb/s OOK. Their relative slow frequency roll-off enables signal bandwidths beyond the cut-off frequency.

[5] 4/8-PAM, QAM, CAP, DMT, OFDM

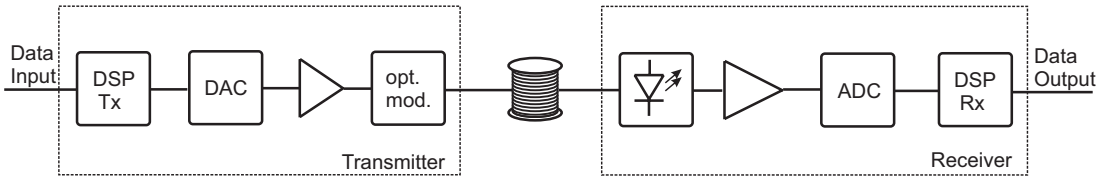

FIGURE 2.1: General high-speed short-range communication link consisting of the transmitter with DSP unit, DAC, driver and optical modulator, the fiber of single-mode or multi-mode type and the receiver consisting of photodiode, transimpedance amplifier, ADC and DSP unit.

2.2 Link design

High-speed short-range links based on IM/DD consist of three main elements in principle as shown in Fig. 2.1. First, the transmitter, which includes the DAC, the driver amplifier and the optical modulator. Second, the channel, which can be either an SMF or a multi-mode fiber (MMF). Third, the receiver, which consists of the photodiode (PD), the electrical amplifier and the ADC. Furthermore, there are DSP units in front of the DAC and after the ADC with their complexity depending on the transmission scenario. In the following sections each element of Fig. 2.1 is discussed, its behavior characterized and its limitations shown.

2.2.1 Optical modulator

There are two different types of optical modulators utilized in IM/DD-based links. The first one is a directly modulated laser (DML) and the second type an EML. Various types of DMLs exists like simple Fabry-Perot lasers or lasers with distributed feedback (DFB) structures, which are typically used in higher speed communications environments. The achievable transmission performance with DMLs strongly depend on its characteristics like the available modulation bandwidth. VCSELs are an important DML type and are typically used for short transmission distances due to their cost effectiveness. Enhanced VCSEL types are even used for longer distances. A more detail introduction to VCSELs can be found in Chapter 4.

Today's DMLs are mainly applied for lower speeds ($\leq$ 25Gbps) and shorter distances (up to 10 km) in telecom and datacom applications, due to constraints such as sensitivity to chromatic dispersion, lower frequency response and relatively low extinction ratio compared to EMLs. These constraints are mainly due to the fact that the direct modulation changes the laser properties. The drift of the lasing wavelength in DMLs is originated in the change of the refractive index in its active area due to changing amounts of injected current. This makes these devices sensitive to the influence of the chromatic dispersion. The frequency response of a DML strongly depends on the relaxation frequency[6], limiting the maximum operating frequency. The extinction ratio[7] is limited by the required above-threshold operation to avoid the turn-on delay [26]. State-of-the-art DFB laser prototypes have shown modulation bandwidths

[6]The oscillation frequency of the output power of a laser in continuous wave operation after a strong change in pump power, like turn on or off. The frequency response of a laser drops significantly beyond its relaxation frequency.

[7]In telecommunications, extinction ratio is the ratio of two optical power levels of a digital signal generated by an optical source.

of up to 30 GHz and more sophisticated designs with additional distributed reflectors, bandwidths up to 50 GHz [27]–[29]. An important parameter for lasers is the relative intensity noise (RIN), which can be one of the main noise sources in IM/DD systems. It originates from the random carrier generation and recombination process in the laser and is a fundamental limit for high-speed systems.

Common externally modulated lasers are electro-absorption modulators (EAMs) and MZM. EAMs rely on the modification of the absorption of a semiconductor material when an external field is applied and MZMs on the change in refractive index and thus the optical phase. The required intensity modulation is achieved by transforming the phase modulation with the help of an interferometric structure. MZMs are typically only used for metro and long-haul transmissions scenarios. Their ability to modulate the phase and the amplitude of the optical field enables together with coherent detection, a significant increase in spectral efficiency compared to simple IM/DD links where only the optical power is modulated. The disadvantages of MZMs are the higher cost and the required size to achieve a sufficient phase shift. However, from a research point of view MZMs are interesting as intensity modulators due to their superior performance in terms of extinction ratio, modulation bandwidth or chirp, compared to other modulator types. So far, MZM research prototypes achieve bandwidths beyond 70 GHz and commercial available modulators present bandwidths up to 40 GHz [30]–[32]. Transmission rates of up to 200 Gb/s using IM/DD links were demonstrated with these devices [12], [13], [33].

EAMs operate under a continuous wave (CW) condition provided by a laser driven by a constant current. Therefore the laser properties of EMLs are not changed when being modulated, as they are for DMLs. This results in higher modulation bandwidths, better wavelength stability and less sensitivity regarding the chromatic dispersion. An EML is mainly used for higher speeds ($\geq$25 Gb/s) and longer distances ($\geq$10 km) in telecom applications. However, they are not as cost effective as DMLs due to their more complicated structure and are commonly only used for applications with more demanding requirements. Today, modulation bandwidths beyond 40 GHz are possible while more sophisticated devices achieving up to 100 GHz [7], [34], [35].

2.2.2 Fiber

There are three different fiber types in the field of optical communication, SMFs, MMFs and plastic optical fibers (POF). For high-speed short-range links typically only SMF and MMF are feasible due to the strong bandwidth limitations of the POF. SMF and MMF differ in their core diameter, which is 9 μm for SMFs and 50 or 62.5 μm for MMFs. The smaller core diameter of the SMF allows only the propagation of the linearly polarized fundamental mode in contrast to MMFs where several hundred modes are possible [36]. This results in a nearly infinite bandwidth for the SMF and makes it together with its very low attenuation the standard transmission medium for distances beyond a few 100 m. The main limitations of SMFs in general are the chromatic dispersion, the nonlinear behavior at higher optical signal powers and the still appreciable attenuation at longer distances. The attenuation of today's SSMF is as low as 0.2 dB/km, which is nearly negligible for high-speed short-range communications systems. Only for long-haul and metro network distances, optical amplification is required to enable a successful transmission. The chromatic dispersion in SMFs refers to the pulse broadening induced by the wavelength dependence of the fiber refractive index. In optical transmission systems it results in inter-symbol-interference (ISI) and can be separated into the the waveguide dispersion and the material dispersion. The

former originates from the wavelength dependent distribution of the optical field between the core and the cladding, which in turn changes the effective refractive index. The material dispersion is caused by the wavelength dependency of the refractive index.

For IM/DD systems transmitting at 1550 nm, this effect can be especially critical due to the detection of the envelope of the optical signal at the photodiode, which results in a fading pattern if the spectral components left and right of the optical carrier experience different delays [37], [38]. However, for most high-speed short-range systems this effect is not a typical issue. First, at transmission distances of a few km only signals with very high bandwidths (e.g. $\geq$40 GHz and 2 km of SSMF) are affected and second, since most short-range links are point-to-point connections, the transmission in the O-band at 1300 nm is desirable to avoid the influence of the chromatic dispersion at all.

Fiber nonlinearities are a fundamental limitation for the transmission capacity since they set an upper limit to the maximum signal power and thus the optical signal-to-noise ratio (SNR). There are several nonlinear effects, e.g. Kerr effect related processes like four wave-mixing or self-phase modulation, or resonant processes like Brillouin scattering which degrade the signal. However, since no optical amplification is required in short-range communications due to the short transmission distances and the low fiber loss, commonly only low signal powers (~0 dBm) are present in the fiber, at which those nonlinear distortions can be neglected.

Today MMFs are the most popular fiber type for transmission distances up to a few 100 m and are typically used in VCSEL-based transmission systems. Their main advantage compared to SMFs is the much easier alignment[8] due to their larger core diameter, since packaging costs are critical for these short-range links. Their disadvantage is the high number of possible propagation modes, which may have different group velocities. This translates into a difference in mode delay and effectively causes mode dispersion [39]. Furthermore, the influence of the chromatic dispersion is also relevant at the typical transmission wavelengths around 850 nm, due to the broad spectrum of multi-mode VCSELs[9]. Both effects limit the usable signal bandwidth and the maximum fiber length. The mode dispersion can be reduced by using a graded index MMF, which minimizes the difference in group velocity between different modes. This is achieved by having the highest refractive index at the fiber axis and a gradually decrease towards the cladding [41]. MMFs are identified by the "optical mode" (OM) designation as OM1, OM2, OM3 and OM4. They are described by the standards ISO/IEC 11801, TIA-492-AAAD and ISO/IEC 60793-2-10 which define their performance requirements, but do not define how the performance is to be achieved [42]. This includes parameters like the attenuation or the bandwidth-distance product with some constraints regarding the geometry and numerical aperture.

2.2.3 Receiver

The optical receiver in IM/DD systems converts the optical power into an electrical current. The most common device is a *pin*-PD followed by an electrical amplifier. The amplifier used for most high-speed systems is a transimpedance amplifier (TIA) which operates as a current-voltage converter and allows a high bandwidth [43]. Today's commercial available high-speed receivers show bandwidths up to 37 GHz for

[8] Coupling between laser/photodiode and fiber

[9] The different modes of a multi-mode VCSELs have slightly different wavelengths due to differences in the effective refractive index for each mode [40].

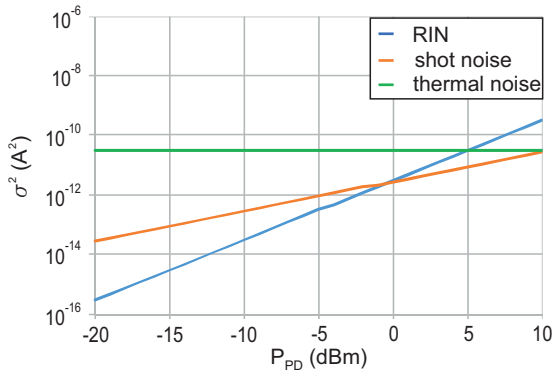

FIGURE 2.2: Contribution of thermal and shot noise as well as the VCSEL RIN for the VCSEL experiments for different optical powers at the photodiode.

SMF applications and up to 22 GHz for MMF applications[10], which is close to their Tx counterpart [44], [45]. An important parameter for IM/DD system is the receiver noise. It can be separated into thermal noise and shot noise. Shot noise originates from the quantum nature of light and current, which results in random time intervals for the photon absorption and the electron-hole generation process even for a constant optical power. This gives rise to random variations in the signal current, which can be described by variance of the shot noise

$$\sigma_{\mathrm{s}}^2 = 2qI_{\mathrm{PD}}\Delta f_{\mathrm{Rx}}\,, \tag{2.1}$$

with q the elementary charge, I_{PD} the photocurrent and Δf_{Rx} the receiver bandwidth [46]. Shot noise increases with the photocurrent and thus with the average optical power.

Thermal noise comes from the fact that at any temperature above the absolute zero, electrons are moving inside the conductor which results in a current noise. The variance of the thermal noise is defined by

$$\sigma_{\mathrm{t}}^2 = \frac{4k_{\mathrm{B}}TF_{\mathrm{n}}\Delta f}{R_{\mathrm{L}}}\,, \tag{2.2}$$

with k_B the Boltzmann constant, T the temperature, F_n the noise figure of the amplifier following the photodiode and R_{L} the load resistance [46]. The thermal noise does not depend on the optical signal power.

To give an idea of the noise sources in an IM/DD system, the amount of noise for the VCSEL transmission system as investigated in Chapter 4 is shown in Fig. 2.2. Additionally to the shot and thermal noise, the laser RIN is added by calculating the noise variance of the RIN after the photodetector with

$$\sigma_{\mathrm{RIN}}^2 = S_{\mathrm{RIN}}I^2\Delta f\,, \tag{2.3}$$

with S_{RIN} the RIN values in 1/Hz[11]. For the calculation of the noise terms in Fig. 2.2 values from data sheets were used: $T = 298$ K, $F_n = 6$ dB, the photodiode responsivity $R_{\mathrm{PD}} = 0.35$ A/W, $R_{\mathrm{L}} = 50\,\Omega$ and S_{RIN}=150 dB/Hz. As it can be observed, the primary

[10]The difference in cut-off frequency originates primary from the size of the photodiodes.
[11]The RIN is typically given in dB/Hz.

TABLE 2.1: Overview of commercial and prototype DACs

	Sample rate (GS/s)	3 dB bandwidth	Resolution	ENOB
Micram DAC4 [51]	100	40	6	4.6 (@48 GHz)
Keysight M8196A [52], [53]	92	32	8	5.3 (@32 GHz)
Anritsu G0374 [54]	64	n/a	2	n/a
SHF 613A [55]	60	36	3	n/a
University Stuttgart [56]	100	13	8	3.2 (@25 GHz)
NTT [57]	90	>40	6	n/a
III-V Labs [58]	84	n/a	3	n/a

noise source is the thermal noise at input power levels below 5 dBm. The Rx power in the VCSEL transmission experiments was typically 0 dBm or less, due to the limits in VCSEL power. Therefore, the transmission performance is dominated by thermal noise. Note that there are additional nonlinear noise sources in the VCSEL experiment, originated by the clipping or the non-ideal VCSEL characteristic. Their exact amount depends primarily on the VCSEL bias and modulation index.

2.2.4 DAC and ADC

High-speed DACs and ADCs are essential for high-speed communication systems due to their ability to use advanced modulation formats (i.e. generate multi-level signals) and to apply DSP. Table 2.1 gives an overview of commercially available DACs and arbitrary waveform generators (AWG) and recent prototype DACs from the research community. Given parameters are the available sample rate, the analog bandwidth, the nominal resolution and the effective number of bits (ENOB). The ENOB is a characteristic of DACs and ADCs which shows the effective resolution at higher frequencies. It is smaller than the nominal bit resolution and comprises all non-ideal properties. Currently, the new DAC4 from Micram has the highest bandwidth of the commercial DACs, however no real-time interface is provided so far. Furthermore, the prototype DACs show a similar performance compared to the newest commercial products, which underlines the importance of research advances in this field. One approach to further increase the sample rate and the bandwidth is the use of several DACs in parallel in combination with interleaving concepts. In Section 3.1 the state-of-the-art for such concepts in IM/DD links will be highlighted.

The main limitations of modern high-speed DACs are the finite bandwidth, the resolution and the nonlinearities. The bandwidth is limited due to the parasitic effects in high-speed circuits and the nominal resolution due to the complexity [47]. Contributions to the nonlinear DAC behavior are for example the dynamics in output impedance, the finite bit resolution of the DAC resulting in quantization noise and amplitude differences between the output signals level of subsequent input codes [48], [49]. Further impairments arise from timing effects like jitter and phase noise and from the fundamental thermal noise of electronic circuits [50]. All these impairments result in a drop in SNR at the output of the DAC, which can be characterized by the ENOB. For IM/DD systems especially relevant are the limited DAC bandwidth and the drop in ENOB at higher frequencies. The former requires additional equalization and amplification of the signal and the latter limits the application of advanced modulation formats.

Today modern oscilloscopes achieve bandwidths of 100 GHz and sample rates of 240 GS/s. This is possible by the so called digital bandwidth interleaving (DBI) approach which utilize several ADC in parallel [59]. The received signal is separated in sub-bands, each consisting of a part of the total signal spectrum. Each sub-band is then down-converted using analog mixing and analog-digital (A/D) converted. Afterwards the signals are combined digitally and equalized to minimize the influence of the mixing process. The utilized ADCs in these oscilloscopes have sample rates of 92 GS/s with bandwidths slightly higher compared to modern DACs [53], [60]. These oscilloscopes enabled several high-speed transmission experiments in last years and their performance is significantly better than their counterpart, i.e. the AWG [61], [62]. A more detailed overview about current ADC and DAC technologies for optical high-speed systems can be found in [60].

2.2.5 Modulation formats

An approach to improve the capacity of high-speed short-range, IM/DD-based links is the use of more spectrally efficient modulation formats. Discussed modulation formats are pulse amplitude modulation (PAM), quadrature amplitude modulation (QAM) and orthogonal frequency division multiplex (OFDM). These formats are used in this thesis for different transmission experiments and are briefly introduced in this section. More information regarding modulation formats can e.g. be found in [63], [64].

2.2.5.1 Pulse amplitude modulation

PAM is in its simplest form the well known OOK, which is used for nearly all commercial short-range communication systems so far, due to its simple realization and robustness to channel impairments. However, PAM formats with 4, 8 or even 16 amplitude levels[12] are increasingly interesting due to their higher spectral efficiency, e.g. in 400G Ethernet applications with symbol rates of 25 or even 50 GBd. A PAM signal $s_m(t)$ consisting of M signal levels (modulation order M), i.e. M-PAM, can be expressed as

$$s_m(t) = A_m \text{rect}(t/T_\text{s}), \quad (0 \leq t \leq T_\text{s}) \tag{2.4}$$

for $m = 1, 2..., M$, with A_m the mth signal amplitude of the M-PAM symbol set, T_s the symbol duration and $\text{rect}(t)$ the rectangular function. The rectangular function is defined as:

$$\text{rect}(t/T) = \begin{cases} = 1, & 0 \leq t \leq T \\ = \frac{1}{2}, & t = 0,\ t = T \\ 0 & \text{otherwise} \end{cases} . \tag{2.5}$$

In Fig. 2.3 an example of a 4-PAM signal is shown in time and frequency domain. The ideally rectangular-shaped PAM signal has a *sinc*-formed spectrum with infinite bandwidth, which has to be matched to the available analog bandwidth. This can be done with a classical analog low-pass filter at the Tx side or a more sophisticated approach using a digital raised-cosine filter, as is done in this thesis. The raised-cosine filter is a filter which fulfills the first Nyquist criterion, i.e. minimizing the intersymbol interference (ISI). It is defined by its roll-off factor β which can be chosen between 0 and 1, depending on the desired filter bandwidth. In Appendix A.1 a mathematical description of the raised cosine filter is given. A further aspect of PAM is related to

[12] Also known as higher-order PAM formats

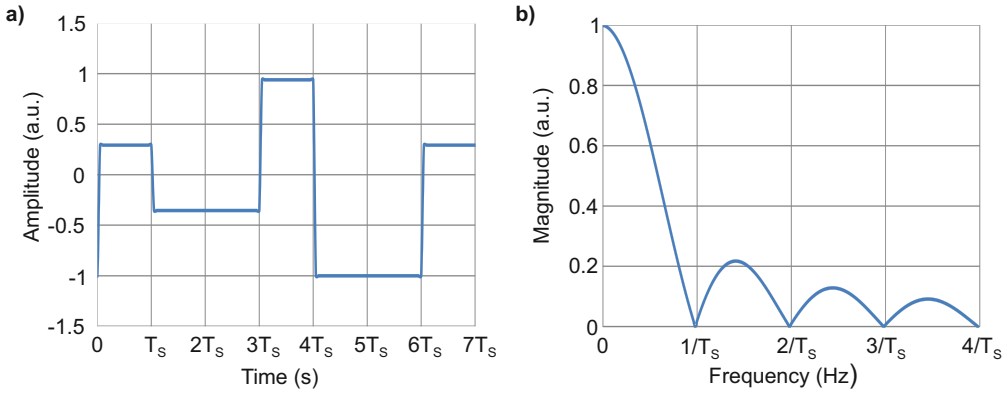

FIGURE 2.3: Example of a 4-PAM signal in (a) time-domain and (b) frequency domain with the PAM symbol duration T_s.

the non-negative constraint of IM/DD-based systems[13] which requires non negative values of A_m for the successful modulation of the optical carrier. Since the information of the PAM signal is coded in the signal amplitude, it is ideally suited for IM/DD based systems by directly modulating the optical power.

One important benefit of PAM is the generally low peak-to-average power ratio (PAPR) of the signal. PAPR is the relation of the squared peak amplitude (i.e. peak power) to the squared root-mean-square (RMS) value of a signal. It can be written as

$$PAPR = \frac{|s_{\text{peak}}|^2}{s_{\text{RMS}}^2}\,, \tag{2.6}$$

with s_{peak} the peak amplitude and s_{RMS} the RMS value of a signal. A low PAPR allows an efficient digital-analog (D/A) and analog-digital (A/D) conversion, due to the limited ENOB of DACs and ADCs and an efficient modulation of the optical carrier in IM/DD systems. In Appendix A.2 the PAPR is discussed and illustrated for the modulation formats used in this thesis. A disadvantage of PAM is the required equalization in bandwidth-limited systems due to the influence of ISI. Especially for higher-order PAM formats, i.e. $M \geq 4$, this results commonly in an increased noise power compared to the total signal power, i.e. noise enhancement.

2.2.5.2 Quadrature amplitude modulation

Quadrature amplitude modulation (QAM) is not commonly used in IM/DD systems since it requires an additional electrical carrier whose amplitude and phase can be modulated by the two QAM baseband signals[14]. An M-QAM signal modulating an electrical carrier with M states for amplitude and phase can be expressed as

$$s_m(t) = A_m \text{rect}(t/T_s)\cos(2\pi f_c t + \Theta_m), \quad (0 \leq t \leq T_s)\,, \tag{2.7}$$

[13]Since no negative optical power exists, an additional bias signal is required to shift the optical modulator driving signal to positive amplitudes only. Otherwise the negative amplitudes of the driving signal would be clipped, resulting in strong nonlinearities. Note that there are modulation formats like asymmetrical clipped OFDM [65] which utilizes this clipping aspect to minimize the energy consumption, e.g. for optical wireless applications.

[14]Note that for coherent systems, optical QAM is a well known modulation format, due to the ability to modulate and detect the optical phase and the amplitude.

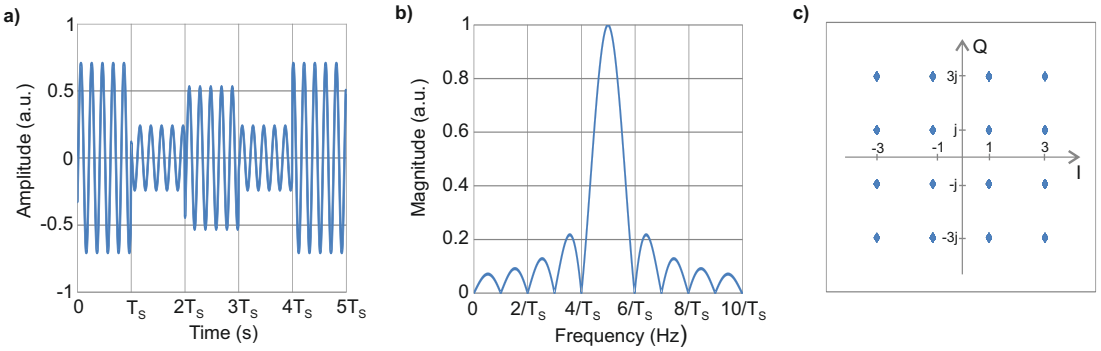

FIGURE 2.4: Example of a 16-QAM signal: (a) time-domain, (b) frequency domain and (c) the associated constellation diagram.

for $m = 1, 2, 3..., M$ with A_m the amplitude and Θ_m the phase of the mth signal in the M-QAM signal set and f_c the electrical carrier frequency. The M-QAM signal $s_m(t)$ can be expressed as a linear combination of two orthogonal[15] functions in the form of

$$s_m(t) = s_{m1}\phi_1(t) + s_{m2}\phi_2(t) \tag{2.8}$$

with

$$\begin{aligned} \phi_1(t) &= \text{rect}(t/T_s)\cos(2\pi f_c t) \;\; 0 \le t \le T_s \\ \phi_2(t) &= -\text{rect}(t/T_s)\sin(2\pi f_c t) \;\; 0 \le t \le T_s \end{aligned} \tag{2.9}$$

and

$$\begin{aligned} s_{m1} &= A_m \cos(\Theta_m) \\ s_{m2} &= A_m \sin(\Theta_m)\ . \end{aligned} \tag{2.10}$$

The two orthogonal functions $\phi_1(t)$ and $\phi_2(t)$ are therefore modulated by the two QAM baseband signals s_{m1} and s_{m2}, also known as in-phase (I) and quadrature (Q) signals. In Fig. 2.4 (a,b) an example for a 16-QAM signal is shown in time and frequency domain with a carrier frequency of $f_c = 5/T_s$. An important aspect of QAM are the available states for s_{m1} and s_{m2}, which can be illustrated in their complex form $(s_{m1} + js_{m2})$ using a constellation diagram. In its complex form the M-QAM signal may then be written as

$$s_m(t) = \Re\Big\{(s_{m1} + js_{m2})e^{j2\pi f_c t}\Big\}\ . \tag{2.11}$$

In Fig. 2.4 (c) the associated diagram of a 16-QAM signal is shown. For vales of $M =$ 4, 16, 64 ,... etc., which represent symbols with 2, 4, 6, ... etc. bits, commonly a rectangular form is chosen. However, for bit values of 3, 5, 7 ... etc. different realization are possible [64]. The QAM constellation diagrams used in this thesis are shown in Appendix A.3. The spectrum of a QAM signal is *sinc*-shaped around the carrier frequency as shown in Fig. 2.4 (b). The rectangular description in time domain results in an infinite bandwidth similar to PAM, which has to be limited using analog[16] or digital filters like raised-cosine based pulse-shaping as is done in this thesis.

In principle there are two different possibilities for the QAM signal generation.

[15] Two functions $f(x)$ and $g(x)$ are orthogonal if $\int_a^b f(x)g(x)dx = 0\ ,\ \ a \le x \le b\ .$

[16] An analog filter to limit the signal spectrum of a QAM modulated electrical carrier could either be applied in the form of low-pass filter for the two baseband signals or in the form of a band-pass filter for the passband signal, i.e. the QAM modulated electrical carrier.

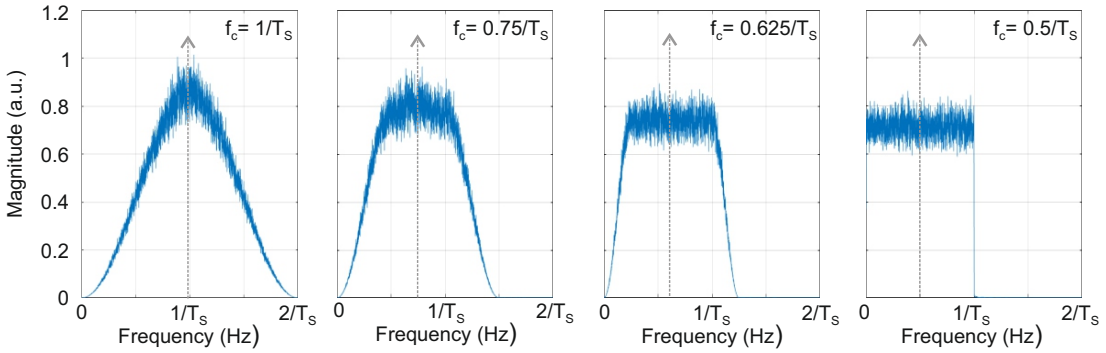

FIGURE 2.5: QAM signal spectra with different amounts of pulse-shaping, i.e. different values for the raised cosine filter roll-off factor β: (a) $\beta = 1$, (b) $\beta = 0.5$, $\beta = 0.25$ and (d) $\beta = 0$. The electrical carrier is located at (a) $1/T_s$, (b) $0.75/T_s$, (c) $0.625/T_s$ and (d) $0.5/T_s$.

The first option consists of the direct generation of the QAM modulated electrical carrier using a single DAC and the second option consists of the generation of the two QAM baseband signals, using two DACs and the analog up-conversion onto the electrical carrier, e.g. with an I/Q mixer. The digital approach mitigates the analog impairments[17] but requires a high-speed DAC and the analog signal generation offers total signal bandwidths beyond the capabilities of today's DAC, but is limited by the analog components.

The simplest form of QAM modulation for IM/DD-based systems uses a single electrical carrier. In this case, the relation of the electrical carrier frequency f_c and the QAM symbol time T_s is $f_c = 1/T_s$. This case is also known as single-cycle subcarrier modulation [66] with the exemplary signal spectrum shown in Fig. 2.5 (a). In this example, the *sinc*-formed spectrum is limited to $\pm f_c$ around the electrical carrier by using a raised cosine pulse-shaping filter with a roll-off factor of $\beta = 1$. A further limitation of the spectrum and thus a smaller electrical carrier frequency, can be realized with lower β factors as shown in Fig. 2.5 (b,c,d). The smallest QAM signal bandwidth is therefore $1/T_s$ and can be achieved with a roll-off factor of $\beta = 0$ and a electrical carrier at $f_c = 1/(2T_s)$ as shown in Fig. 2.5 (d).

M-PAM and M^2-QAM modulated signals of the same data rate[18] have the the same bandwidth requirements, thus the same spectral efficiency. On the other hand QAM has only half the symbol duration compared to PAM, which should ease the digital signal processing and equalization effort. The disadvantage of QAM for IM/DD systems is the complex signal generation and the reduced receiver sensitivity [67] compared to PAM systems, mainly due to the increased bias requirements of the optical modulator.

2.2.5.3 Orthogonal frequency division multiplex

OFDM is a multi-carrier modulation format which utilizes QAM modulation on many orthogonal electrical subcarriers. These subcarriers are separated in frequency by

[17] Especially the impairments of the I/Q mixer are critical, please refer to Section 3.3.3 for details.
[18] Not the same symbol rate.

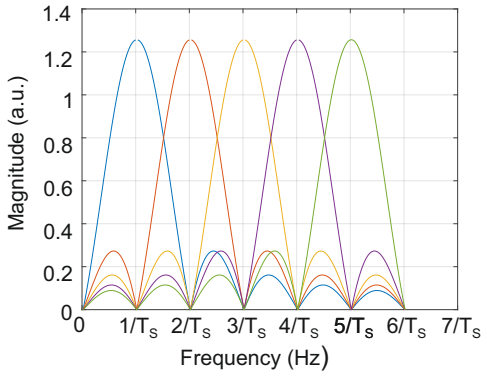

FIGURE 2.6: Exemplary OFDM spectrum for $N_{sc} = 6$.

$\Delta f = 1/T_s$, with T_s the OFDM symbol time. A OFDM symbol consisting of N_{sc} subcarriers can be described by

$$s(t) = \sum_{k=0}^{N_{sc}-1} x_k e^{j2\pi \frac{kt}{T_s}} \ , \ \ 0 \leq t \leq T_s \tag{2.12}$$

where x_k are the complex data symbols from the QAM constellation diagram for each subcarrier k. The subcarrier at $k = 0$ represents the DC component and is not modulated. The orthogonality of the OFDM subcarriers is achieved by setting the individual subcarrier frequencies to $f_{sc} = k/T_s$, which is also illustrated in Fig. 2.6 by an exemplary spectrum for $N_{sc} = 6$. As can be observed, the amplitude of each subcarrier is zero at the maximum amplitude of its neighboring subcarriers, thus no crosstalk occurs assuming the right sampling rate.

Since the OFDM signal from Equation 2.12 is a complex signal, it has to be translated into a real-valued form to be able to be transmitted over an IM/DD-based link. Similar to QAM, this can be realized by multiplying the complex baseband signal with an electrical carrier using an I/Q mixer, which results in a band-pass signal around the electrical carrier. The second options is the application of a Hermitian symmetry operation[19] , which results in a real valued baseband signal, commonly known as discrete multitone (DMT). Note that in this thesis, OFDM denominates a passband signal and DMT a baseband signal.

The number of used OFDM subcarriers depends on the application and ranges from a few 10 to 1000 [69], [70]. Due to the high number of subcarriers, the bandwidth of each is small compared to the total signal bandwidth and thus the symbol time is much longer than the typical channel impulse response. This flat behavior of the transmission channel regarding each subcarrier eases the equalization effort at the receiver, since no noise enhancement exists. Furthermore, the ISI between adjacent symbols can be avoided by the introduction of a cyclic prefix at the end of each symbol. The exact length depends on the transmission channel. Since each subcarrier can be modulated separately, it is possible to adapt the modulation order and the power to the variable SNR in the channel. This is called bit and power loading and is commonly realized with algorithms like Levin-Campello or Krongold [71], [72].

[19]The frequency domain OFDM signal consisting of N_{sc} subcarriers is extended by adding the conjugate symmetric coefficients before the inverse discrete Fourier transformation (DFT) with length N_{sc} [68]

A disadvantage of OFDM for IM/DD links is the high PAPR. An OFDM signal consists of the sum of N_{sc} complex tones, with the number of subcarriers N_{sc}. This results in a worst-case PAPR of $10\log(N_{sc})$ dB. The high PAPR significantly limits the amount of optical signal power in the sidebands relative to the optical carrier, which ultimately decreases the receiver sensitivity. For practical realizations, digital clipping is commonly applied to ease this effect or special coding schemes are used to generate OFDM signals with lower PAPR [63], [73], [74]. In Appendix A.2 the influence of different clipping amplitudes for the OFDM transmission is discussed. A further disadvantage of OFDM is the mandatory DSP to (de)modulate the signal, e.g. the fast Fourier transformation (FFT) and its inverse the IFFT. For real-time high-seed applications this requires very fast application-specific integrated circuits (ASIC), which are not yet widely developed. However, first commercial realizations were shown by Socionext with their 100G OFDM chip [75], and it is expected that OFDM will become increasingly popular in particular for high-speed short-range links.

2.2.6 Digital signal processing

With the increase in transmission rates for high-speed short-range systems the influence of channel impairments also increases. To combat these impairments equalizers are required like feed-forward equalizer (FFE), decision feedback equalizer (DFE) or the more complex maximum likelihood sequences estimation (MLSE). FFEs employs a finite impulse response filter (FIR) with a series of tap weights programmed, adjusted to the impulse response. This is the simplest implementation and can also be designed entirely in the analogue domain.

DFEs have a more complex structure, which consists of a forward filter, a detector and a feedback filter. The basic idea of a DFE is cancellation of ISI, with the help of the known previously transmitted symbols. This is done by subtracting past symbol values with an appropriate weighting using the feedback filter. MLSE is based on a Viterbi decoder in combination with channel estimation to calculate the most probable transmitted symbols. This requires the knowledge of the exact signal state to estimate the probability, thus high-speed ADCs are required. Compared to the other equalizers, MLSE offers the best performance but has also the highest complexity [76]. In other fields, like mobile communication, there has been a trend to use MLSE for narrow band applications (2G GSM) to simplify equalization. For 3G UMTS linear filters are used, while 4G LTE is based on OFDM.

Nonlinear signal impairments cannot be compensated by linear equalizers (see above) and require additional nonlinear filter structures. These can be very simple like in the case of compensating the static nonlinear characteristic of an MZM by its inverse or more complex if e.g. dynamic nonlinearities have to be compensated. One example is the Volterra based nonlinear pre-equalizer utilized in this thesis.

There are many state-of-the-art transmission experiments for high-speed short-range links utilizing different equalizer structures to improve the performance [77]–[80]. Most of these experiments are performed offline and only minor attention is paid to the implementation effort. This left the open question whether more complex equalizer structures are feasible for real world applications. However, with the increased use of DSP in communications systems, such developments can be expected.

Error free transmission is mandatory for communications systems and commonly refers to bit error rates (BER) below 10^{-9}. High-speed systems cannot achieve these BERs due to the intrinsic channel impairments, even if complex equalizers are used. Error control methods like the most widely used forward error correction (FEC) offer a possibility to prevent this by applying redundancy to the bit stream. The receivers can

then use this redundancy to check the consistency of the delivered message and recover the corrupted data if necessary. FEC schemes can be divided into hard-decision (HD) and soft-decision (SD) approaches which differ in the number of bits required for decoding one symbol. HD-FEC uses a single quantization level for decoding, while SD-FEC uses several levels to indicate the reliability of the decision. That results commonly in a gain of 1-2 dB compared to the less complex HD-FEC schemes. Each FEC scheme has a upper pre-FEC BER limit at which the correction starts to fail significantly with more sophisticated schemes having higher BER limits [81], [82]. However, this comes at the cost of higher complexity and overhead. Error free transmission is mandatory for communications systems and commonly refers to bit error rates (BER) below 10^{-9}. High-speed systems cannot achieve these BERs due to the intrinsic channel impairments, even if complex equalizers are used. Error control methods like the most widely used forward error correction (FEC) offer a possibility to prevent this by applying redundancy to the bit stream. The receivers can then use this redundancy to check the consistency of the delivered message and recover the corrupted data if necessary. FEC schemes can be divided into hard-decision (HD) and soft-decision (SD) approaches which differ in the number of bits required for decoding one symbol. HD-FEC uses a single quantization level for decoding, while SD-FEC uses several levels to indicate the reliability of the decision. That results commonly in a gain of 1-2 dB compared to the less complex HD-FEC schemes. Each FEC scheme has an upper pre-FEC BER limit at which the correction starts to fail significantly with more sophisticated schemes having higher BER limits [81], [82]. However, this comes at the cost of higher complexity and overhead.

The most considered FEC scheme for IM/DD systems is the 7% overhead HD-FEC based on Bose-Chaudhuri-Hocquenghem codes with a BER limit of $3.8 \cdot 10^{-3}$ [83], [84]. There are also a few experiments which propose a 20% overhead SD-FEC scheme [85]. This scheme has a BER limit of $2.7 \cdot 10^{-2}$ and is typically only used in coherent systems [86]. Note that FEC schemes are also mandatory for the recent 400G Ethernet standards [4], [87].

2.3 Concepts to improve transmission capacity of high-speed short-range systems

Degrees of freedom to improve the transmission capacities of optical transmission systems[20] are in principle: bits per symbol (modulation order), symbols per time (signal bandwidth), coherent transmission, polarization multiplex (PolMux), wavelength division multiplex (WDM), mode division multiplex (MDM) and space-division multiplex (SDM)[21]. These are supplemented by DSP including advanced equalizer structures and multiple-input multiple-output (MIMO) signal processing. There are also other, more exotic concepts like using the orbital angular momentum (OAM) over special fibers [88]. Each of these has unique features and offers the potential for high-speed communication far beyond 100 Gb/s. However, most of these approaches require costly optics so far, which is not very feasible for low-cost short-range applications, leaving principally only modulation order, bandwidth and DSP.

The modulation order of such systems is primarily limited by the thermal noise as exemplary shown in Section 2.2.3. Other factors like DAC/ADC bit resolution and

[20] in a single fiber

[21] Relates to the transmission of independent signals in the cores of a of a multi-core fiber.

laser RIN (for systems using DMLs) also contribute to SNR degradations, thus limiting the maximum suitable modulation order. Further limitations are bandwidth limitations and nonlinear behavior of the used components in terms of ISI and nonlinear distortions, respectively. Options to increase the usable modulation order of a system are limited and consist typically of the application of equalizer structures and the use of improved components.

The available signal bandwidth is limited by the contributed roll-off of the used components, mainly DAC, ADC, optical modulator[22] and receiver and the dispersion of the transmission medium. There are several options to increase the available data rate. A first option is to choose a more suitable modulation format like OFDM, which can be ideally adapted to the system frequency response with the help of bit and power loading. This results in enhanced spectral efficiency and achievable signal bandwidths far beyond the cut-off frequency of the transmission system as will be shown in Chapter 4. Another option is a bandwidth extension approach to increase the available signal bandwidth. It is based on parallelization of multiple DACs and ADCs, which are one of the main limiting components for high-speed short-range systems as shown in Sections 2.2.4 and 2.2.1. This approach is investigated in Chapter 3. A third option is the application of DSP to pre-compensate for the system frequency response and the nonlinearities, which is discussed in Chapter 4.

All these approaches to improve the capacity of short-range systems require the use of advanced DSP. Advanced DSP allows higher transmission rates even with simple IM/DD systems and similar to fixed and mobile networks it will become cheap in few years from now on. There is a huge potential in signal processing approaches, which can be implemented in silicon for the access domain economically, due to large numbers of units compared to metro and core networks. If most of the cost can be shifted to signal processing, instead of optics, performance can be increased while costs remain competitive. The shift to DSP is boosted by the availability of high-speed DACs and ADCs as shown in Section 2.2.4.

The application of equalization schemes also overcomes the increased sensitivity of higher order modulation formats to nonlinearities. In contrast to long-haul systems, where nonlinear fiber effects are the main limiting factor, short-range systems suffer more from the nonlinearity of the used components, like the optical modulator. Here, with adequate DSP algorithms, it is possible to pre-distort the waveform so that the nonlinear characteristic of the optical modulator is compensated. In Chapter 4 this is addressed for a VCSEL-based system. Also FEC schemes belong to DSP, easing the SNR requirements for an error free transmission. One aspect which is outside the scope of this thesis, but should be more regarded in the future is the use of retransmissions. These have latency issues in metro and core networks but are widely used in fixed and mobile access systems over short distances.

[22] The optical bandwidth is commonly higher than the electrical one.

Chapter 3

Bandwidth extension techniques for high-speed short-range optical links

In the previous chapter it has been highlighted that bandwidth limitations are an important restriction for high-speed short-range transmission systems. These restrictions are primarily due to the properties of the electrical components getting critical, if data rates beyond 100 Gb/s are targeted, like for 400G Ethernet applications [3]–[5]. Especially advanced modulation formats with their higher spectral efficiency are affected by these bandwidth limitations, due to their increased sensitivity against impairments and their need for higher resolution DACs and ADCs.

One way to solve this issue is the application of optical multiplex techniques like WDM and PolMUX or the use of complex modulations. WDM and PolMUX allow the transmission of multiple individual signal bands at different wavelengths and both polarizations in a single fiber. Complex modulations techniques increase the spectral efficiency by utilizing both the amplitude and the phase of the optical carrier. Each approach eases the electrical bandwidth demand compared to simple IM/DD schemes for a fixed data rate. A further benefit is their scalability to meet the requirements of real-world applications. For example, state-of-the-art realizations of WDM for VCSEL based links, utilize four wavelengths around 800 nm, while metro networks utilize dense-WDM, with many optical carriers in a 50 or 100 GHz grid. However, optical solutions tend to be relatively bulky, more expensive and require integration. This makes them less suitable for short-range applications, which are commonly low-cost point-to-point links.

On the other hand, electrical solutions offer an alternative, since they can be more easily integrated and support simple optics. These solutions, namely bandwidth extension techniques, utilize different approaches to generate signals with bandwidths beyond the capability of today's signal generators[1]. In the following sections a bandwidth extension technique based on analog mixing is investigated and combined with an IM/DD-based optical link. Verification of this concept is done experimentally and supported by modeling the link in a simulation environment. It is demonstrated that signal bandwidths and transmission rates beyond state-of-the-art are feasible, which impairments and limitations exist and how they can be addressed.

The chapter is structured as follows. The state-of-the-art of bandwidth extension techniques is presented first giving an idea which concepts are currently discussed and experimentally validated for high-speed short-range links. Afterwards, the new concept investigated in this thesis is presented, as well as a system model developed to allow the influence of the relevant components to be discussed. The latter is done by developing a component model and using simulation and experiment. Furthermore, transmission experiments are described, highlighting relevant challenges of the

[1] The same approach used for the A/D conversion

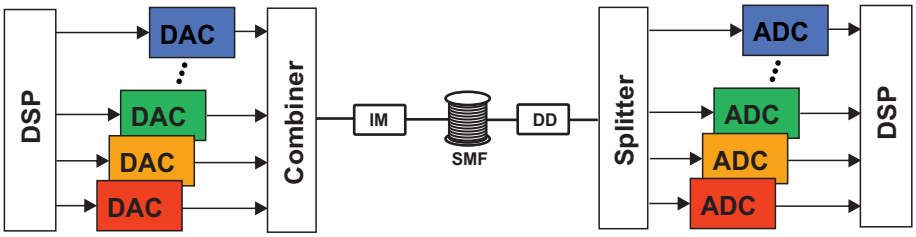

FIGURE 3.1: Bandwidth extension concept using several DACs in parallel and combining their analog signals to a wideband signal with a bandwidth beyond the capabilities of a single DAC. At the Rx side the wideband signal is split and converted using several ADC in parallel.

concept when applied in the real-world. Finally an extension of the concept is investigated, which enables the generation of spectral continuous signals, i.e. a wideband DAC realization.

3.1 State-of-the-art bandwidth extension techniques

Electrical bandwidth extension techniques address the issue of the optical components offering modulation bandwidths beyond that of their electrical counterparts. The general idea, shown in Fig. 3.1, is to use several high-speed DACs in parallel and combine (multiplex) their analog signals in a specific way, with a total signal bandwidth beyond the possibilities of a single DAC. At the receiver side the same approach can be taken, using several ADCs in parallel. Please note that typical ADC bandwidths restrictions are not that critical compared to DAC, as shown in [60]. Different approaches were demonstrated in recent years, enabling bandwidths of 40 GHz and data rates significantly beyond 100 Gb/s. This section discusses these techniques for the signal generation and gives an overview of the achieved high-speed transmissions for short-range applications.

The most straight forward approach to overcome the bandwidth limitations of high-speed DACs is the use of several lower speed 1-bit DACs, 2:1 multiplexing and passive combining. For example, in [78], [89] an integrated 3-bit DAC enabled a 4-PAM signal transmission over 500 m single mode fiber at 1550 nm at a symbol rate of 100 GBd. The same DAC was also applied in [15] but with 8-PAM instead, resulting in 56 GBd transmission over 2 km of SSMF at 1550 nm. In [35] a 107 GBd 4-PAM signal was generated with the help of four 2-bit DACs and two 2:1 multiplexers (MUX) and transmitted over 10 km of SSMF at 1300 nm. An integrated electro-absorption modulator in combination with a distributed feedback laser with 3 dB bandwidth of 59 GHz have been used. Drawbacks of these low-bit DAC combinations are the limited abilities to apply DSP at the Tx, the additional synchronization effort of the DACs and the difficulties to generate more advanced modulation formats like DMT and PAM[2].

A more advanced concept is the application of an analog[3] MUX (AMUX) to combine the output signals of multiple high-speed, high bit resolution sub-DACs. Fig. 3.2 shows the concept for an arbitrary number of sub-DACs. The AMUX hereby switches between the signals of the sub-DACs, resulting in a signal with an aggregated bandwidth of all sub-DACs. Recently, several publications using a high-speed AMUX were

[2]E.g. Nyquist-shaped PAM

[3]The term analog is used to distinguish between the common 2:1 MUX, which combines two digital signals and a MUX which is capable of combining analog signals.

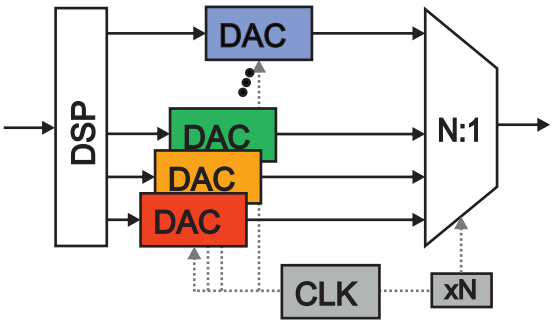

FIGURE 3.2: Wideband signal generation based on dedicated N:1 high-speed AMUX: several lower speed DACs generate pre-defined baseband signals, which are combined using a high-speed analog MUX, operating at N times the sample rate of each DAC.

presented. For example, in [90] such an AMUX showed a 3 dB bandwidth >67 GHz and promising 56 GBd 4-PAM eye diagrams without any pre-processing. First optical transmissions using this concept were shown in [91], [92]. Here, 80 GBd Nyquist-shaped 4-PAM signal was generated and transmitted over several kms of SSMF below the 7% HD-FEC BER limit. Later, the same AMUX was used with DMT modulation achieving up to 300 Gb/s at a higher FEC limit [85], [93]. An interesting aspect of AMUXs is the scalability. In theory, only the bandwidth limitation of the AMUX determines the total signal bandwidth, which enables the use of several lower-speed sub-DACs and thus overcomes the limitations of high-end DACs. However, with a higher number of sub-DACs the effort for a precise synchronization of all components significantly increases. Also impairments like jitter are critical for such systems, if high bandwidths are targeted. Furthermore, the real world parameters of these high-speed AMUXs are challenging, e.g. bandwidth limitations, crosstalk[4], attenuation and non-linear behavior. However, it can be expected to mitigate these issues with the help of DSP.

The third concept to generate wideband signals is the use of frequency up-conversion by means of electrical mixing. In contrast to the previous concept, where a

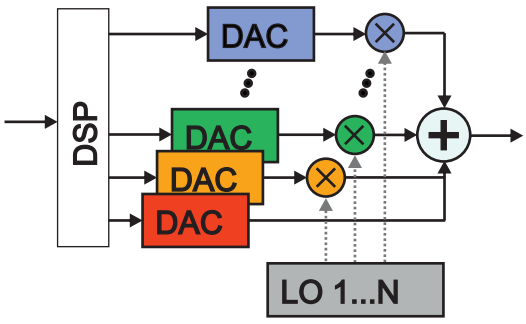

FIGURE 3.3: Electrical up-conversion approach for wideband signal generation: baseband signals are up-converted onto different local oscillator frequencies by electrical mixing and passively combined.

[4]Own experiment with a prototype AMUX have shown a significant crosstalk of the turned off input port to the output.

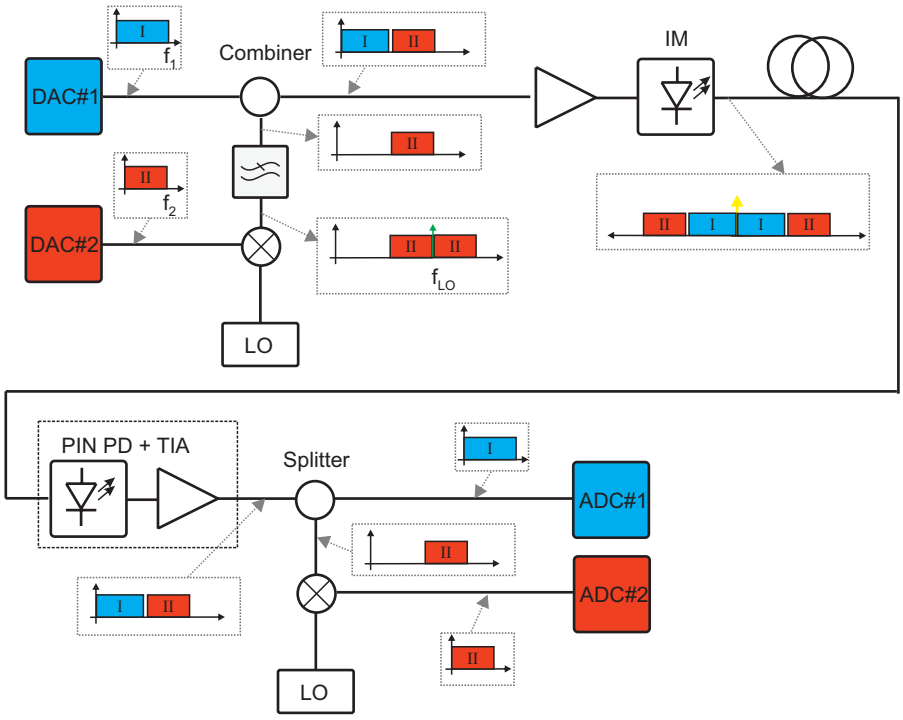

FIGURE 3.4: System concept of bandwidth extension approach using analog mixing for optical IM/DD systems. Two electrical sub-bands are generated and transmitted.

dedicated high-speed AMUX is required, off-the-shelf components, i.e. mixers and filters, can be used. In Fig. 3.3 the principle is shown for the Tx side. Several parallel DACs generate sub-signals, which are up-converted to the desired frequency bands and passively combined afterwards. The resulting signal either consists of independent sub-bands or represents a spectrally continuous waveform. Both schemes were investigated in the last years and showed promising results [33], [62], [94]–[102]. In the following sections this specific approach is investigated.

3.2 System model for bandwidth extension approach

Starting from the general system model of high-speed short-range links shown in chapter 2, a modified version utilizing the bandwidth extension technique based on analog mixing is presented in Fig. 3.4. Two sub-bands (red & blue) are used for the transmission, each independently modulated with a single or multi-carrier scheme. The first sub-signal (blue), generated by DAC #1, ranges from DC up to the frequency f_1 and goes directly into the combiner[5]. The second sub-signal ranges from DC to f_2 and goes to the mixer, driven with a local oscillator (LO) located at f_{LO}. After up-conversion a low-pass filter (LPF) is used to suppress the upper redundant side-band and the LO[6]. Afterwards, the second sub-signal is combined with the first sub-signal.

[5]Typically, there is also a low-pass filter (LPF) after the DAC to suppress the DAC alias, especially if the signal bandwidth is close to half of the DAC sampling rate. The LPF can also be realized with an bandwidth limited amplifier as done in the experiments.

[6]Depending on the steepness of the applied filter, a band gap is required to suppress the LO and the redundant side-band sufficiently. There is also the possibility to use a high-pass filter to suppress the lower side-band, if the LO frequency is appreciatively adapted.

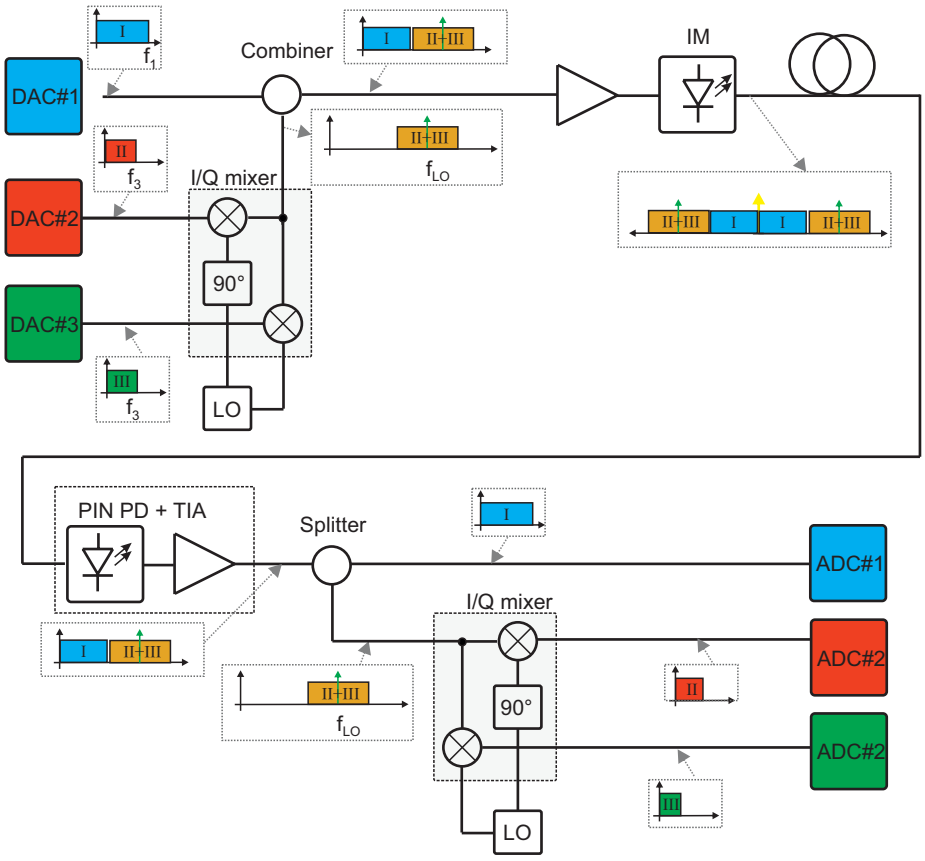

FIGURE 3.5: System concept of bandwidth extension approach using analog I/Q mixing for optical IM/DD systems.

The combiner can be realized with a flat frequency behavior[7] or with a frequency selective behavior[8]. The signal after the combiner consists of both sub-signals, each in its own frequency range without overlap or even with a small gap between the signals. From the combiner the signal goes to the driving amplifier and the optical intensity modulator, which is one of the types discussed in Section 2.2.1. After the optical transmission over the fiber, the signal is optical-electrical converted using a direct detection receiver[9]. In the next step the signal is split into both sub-signals, again with a resistive or a filter approach. The first sub-signal (blue) is then directly A/D converted. The second sub-signal (red) is mixed with the LO and then A/D converted[10].

In the approach shown above, additional filters are necessary to suppress one of the redundant side-bands after the Tx side mixing. This can be mitigated if electrical I/Q mixers are used instead of normal mixers, as shown in Fig. 3.5. In contrast to the first approach an additional DAC (DAC #3) is required, since the in-phase and quadrature of a complex valued signal are needed to drive the electrical I/Q mixer when using OFDM or single-carrier QAM. Furthermore, the bandwidth requirements of DAC #2+3 are halved, if the same signal bandwidth for the upper sub-band is targeted like

[7]Resistive approach, e.g. a 6 dB coupler.
[8]e.g. a diplexer
[9]Typically a *pin*-PD + TIA.
[10]There are also LPF in front of the ADCs, to minimize the noise outside the required signal bandwidth.

in the first approach. After the up-conversion no further filtering of the upper sub-signal is required and it can be combined with the lower sub-band[11]. At the receiver side the same procedure is repeated and all three sub-signals are A/D converted.

In theory, both concepts can be scaled up to N sub-signals, only limited by the maximum bandwidth of the optical modulator and detector. In practice there are several limits for such systems, primary originating from the real world behavior of the mixers, the combiners and splitters. Furthermore, there are issues due to the required clock distribution network and by the required component space.

The investigation of the bandwidth extension concept shown in this thesis is based on the second approach. The I/Q mixer based solution simplifies the filtering of undesired signal parts and reduces the bandwidth requirements of the DACs and ADCs. The investigation is primarily done with experiments, which are supported by a simulation environment. The simulations allow a more detailed characterization of certain systems aspects[12] as well as the test and verification of the appropriate DSP. Each component used for the up-conversion concept causes impairments, which have to be considered if high transmission rates are targeted. Compared to the standard IM/DD system described in Section 2.2, additional distortions arise from the mixers, the combiner and splitter, due to their bandwidth limitations, nonlinearities, I/Q imbalance and insertion loss.

In the next section the core element of the up-conversion concept, i.e. the electrical mixer, is introduced, its impairments are analyzed, a component model is developed and implemented into the system simulation model.

3.3 Mixer

A mixer is a three port device that uses a nonlinear element to achieve frequency conversion. They allow the conversion of signals between a high radio frequency (RF) and a lower intermediate frequency (IF) or baseband. In wireless communications systems, the RF is the transmission frequency being much larger than the signal bandwidth. The RF signal is converted to an IF to allow improved selectivity[13] and an easier implementation of low noise and high gain amplification. Today's mixers are used in a wide field of applications, like radio, mobile and satellite communication or even radar but they have not been designed for the bandwidth interleaving concept investigated. The mixer performance has a major impact on the system sensitivity and signal integrity, especially for communication systems like GSM, UMTS or LTE [103]. At microwave frequencies, they are typically realized with either Schottky diodes, Gallium Arsenide field-effect transistors (GaAs-FET) or CMOS, depending on the actual application [104], [105]. There are also different mixer topologies, like unbalanced (also known as single-ended), single-, double- and triple-balanced types, which differ in the port isolation and suppression of unwanted harmonics. The next sections describe the basic mixer operation, give an overview about the different types and discuss the mixer characteristics. Note that only diode based mixers are discussed.

[11] Compared to the first approach it is not possible to remove the LO, since it is located at the center of the up-converted sub-band. Due to the feedthrough of the LO in real-world mixers, a part of the signal power is therefore wasted, which in turn decreases the SNR.

[12] For example I/Q imbalance, nonlinear mixer behavior and chromatic dispersion

[13] e.g. filtering

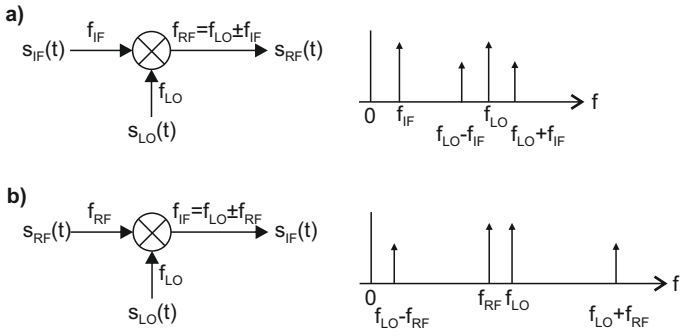

FIGURE 3.6: Mixer operation principle for (a) up-conversion and (b) down-conversion.

3.3.1 Mixer operation

The functional diagram of a mixer for up-conversion operation is shown in Fig. 3.6 (a). A lower frequency baseband or intermediate frequency signal (IF) at the frequency f_{IF} is multiplied with a relative high frequency signal (LO) at the frequency f_{LO}. The LO signal and the IF signal can be represented by

$$\begin{aligned} s_{\mathrm{LO}}(t) &= \cos(2\pi f_{\mathrm{LO}} t) \\ s_{\mathrm{IF}}(t) &= \cos(2\pi f_{\mathrm{IF}} t)\ . \end{aligned} \tag{3.1}$$

The output of the idealized mixer is given by the product of the LO and IF signals:

$$\begin{aligned} s_{\mathrm{RF}}(t) &= s_{\mathrm{LO}}(t) s_{\mathrm{IF}}(t) = \cos(2\pi f_{\mathrm{LO}} t)\cos(2\pi f_{\mathrm{IF}} t) \\ &= \frac{1}{2}\Big[\cos\big(2\pi(f_{\mathrm{LO}} - f_{\mathrm{IF}})t\big) + \cos\big(2\pi(f_{\mathrm{LO}} + f_{\mathrm{IF}})t\big)\Big]\ . \end{aligned} \tag{3.2}$$

As can be observed, two RF frequency components at $f_{\mathrm{RF}} = f_{\mathrm{LO}} \pm f_{\mathrm{IF}}$ are generated at the upper and the lower sideband of the LO. Since both are redundant and commonly only one is desired for the transmission, an additional filtering of the RF signal is required to suppress one sideband. In Fig. 3.6 (b) the ideal mixer operation for down-conversion and the signal's spectra are illustrated. The estimation of the IF output signal is similar for up-conversion operation and can be written as

$$\begin{aligned} s_{\mathrm{IF}}(t) &= s_{\mathrm{LO}}(t) s_{\mathrm{RF}}(t) = A\cos(2\pi f_{\mathrm{LO}} t)\cos(2\pi f_{\mathrm{RF}} t) \\ &= \frac{1}{2}\Big[\cos(2\pi(f_{\mathrm{LO}} - f_{\mathrm{RF}})t) + \cos(2\pi(f_{\mathrm{LO}} + f_{\mathrm{RF}})t)\Big]\ . \end{aligned} \tag{3.3}$$

Note that in realistic mixers many more frequency components are generated due to the more complicated nonlinear behavior of the diode. These products are usually undesirable and removed by filtering.

3.3.2 Mixer types

Single-ended mixers or unbalanced mixers are the simplest mixer realization and consist of a single diode as illustrated in Fig. 3.7 (a). The LO and RF input signals s_{LO} and s_{RF} (down-conversion operation) are superimposed[14] to drive the diode. The diode may be biased with a DC signal, which is decoupled from the other ports with the

[14] For example with a diplexer or a resistive coupler

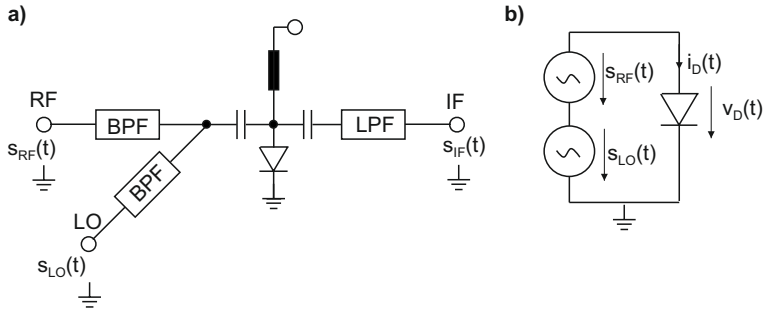

FIGURE 3.7: (a) Circuit for mixer realization using a single diode (single-ended or unbalanced mixer) and (b) equivalent idealized circuit.

help of DC blocks and a RF choke (indicated by the capacitors and the inductor). The low-pass and band-pass filters (LPF, BPF) at the input and output ports perform as isolators[15] between the ports. The equivalent idealized circuit for the single-ended diode mixer is shown in Fig. 3.7 (b). It consists of the LO and RF input signal voltage sources and the diode with its current $i_D(t)$ and voltage $v_D(t)$. Lets assume cosine waves for the RF and LO input signals:

$$\begin{aligned} s_{RF}(t) &= V_{RF}\cos(\omega_{RF}t) \\ s_{LO}(t) &= V_{LO}\cos(\omega_{LO}t)\ , \end{aligned} \tag{3.4}$$

with V_{RF} and V_{LO} the signal voltages of the RF and LO signal. The resulting current at the diode can be calculated with a small-signal approximation using a Taylor series. Please refer to Appendix A.4 for details. The diode current may be written as

$$i_D(t) = I_0 + G_D\Big[s_{RF}(t) + s_{LO}(t)\Big] + \frac{G'_D}{2}\Big[s_{RF}(t) + s_{LO}(t)\Big]^2 + \dots\ , \tag{3.5}$$

with G_D the small-signal conductance of the diode at the bias voltage and G'_D its first derivative. The first term in Equation 3.5 is the DC bias current, which is blocked at the output due to the DC block. The second term consists of the RF and LO input signals, which are also blocked due to the LPF at the output. Extending the third term leads to:

$$\begin{aligned} i_D =& \frac{G'_D}{2}\Big[V_{RF}\cos(\omega_{RF}t) + V_{LO}\cos(\omega_{LO}t)\Big]^2 \\ =& \frac{G'_D}{4}\Big[V_{RF}^2(1+\cos(2\omega_{RF}t)) + V_{LO}^2(1+\cos(2\omega_{LO}t)) \\ &+ 2V_{RF}V_{LO}\cos((\omega_{RF}-\omega_{LO})t) + 2V_{RF}V_{LO}\cos((\omega_{RF}+\omega_{LO})t)\Big]\ . \end{aligned} \tag{3.6}$$

The resulting signal consists of several frequency components, only one of which produces the desired IF product. After removing the unwanted products, e.g. by filtering,

[15] Isolation of mixers refers to the ratio of applied power at one port of the mixer with the power output derived from another port of it. Both the input power and output power will have same frequency. As isolation is ratio of two powers, it is commonly given in dB.

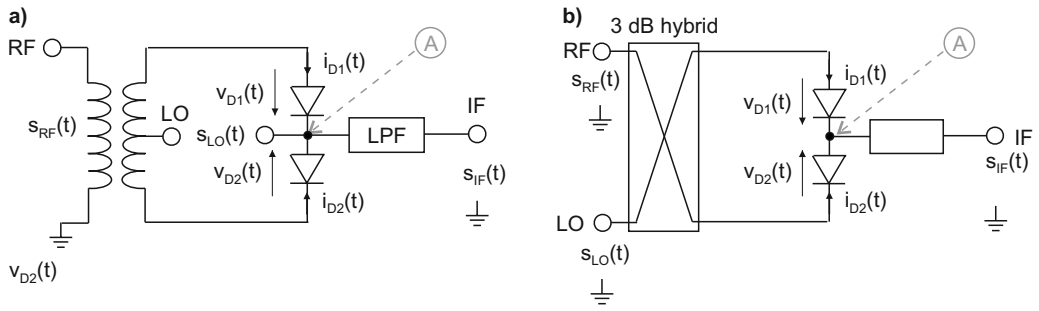

FIGURE 3.8: Single-balanced mixer with (a) a transformer or (b) a 3 dB hybrid coupler.

the IF signal output current i_{IF} is

$$i_{\mathrm{IF}} = \frac{G'_{\mathrm{D}}}{2} V_{\mathrm{RF}} V_{\mathrm{LO}} \cos(\omega_{\mathrm{IF}} t) \ , \tag{3.7}$$

with the desired IF frequency $\omega_{\mathrm{IF}} = \omega_{\mathrm{RF}} - \omega_{\mathrm{LO}}$. Higher order terms for the small-signal approximation (using the Taylor series) at the diode operation point in Equation 3.5 will result in more frequency components at the output f_{OUT} in the form of

$$f_{\mathrm{OUT}} = \pm n f_{\mathrm{LO}} \pm m f_{\mathrm{IN}} \ . \tag{3.8}$$

The integers m and n represent the signal order (intermodulation order) and LO order (modulation order), respectively. The input signal frequency f_{IN} can either be an RF or an IF signal depending on mixer operation[16]. Single-ended mixers generally have a poor performance, especially regarding the suppression of unwanted harmonics and the isolation between the ports and are rarely used today [106], [107].

Single-balanced mixers combine two single-ended types and offer an improved LO to RF isolation, RF input matching and the suppression of even order intermodulation products (either even LO or RF products). In Fig. 3.8 two examples are shown, one with a transformer[17] and one with a 3 dB hybrid coupler for the required signal transition of the inputs signals. The hybrid coupler can either be a 90° hybrid or a 180° hybrid coupler. Both realizations differ in the achievable RF-LO isolation and the impedance match at the RF port [105]. Their scattering parameters can be found in Appendix A.5. Like for the single-ended mixer, the diode currents of the single-balanced mixer can be calculated using the small-signal approximation. Since both diode currents $i_{\mathrm{D1}}(t)$ and $i_{\mathrm{D2}}(t)$ are added in point A in Fig. 3.8, even order intermodulation products cancel each other[18]. Note that either even harmonics of the LO or the RF are canceled out, depending on the actual input ports of both signals. The isolation between the RF and the LO port results from the transmission characteristic of the couplers but depends on the impedance matching of the diodes, which can be difficult to maintain over a reasonable frequency range.

Double and triple-balanced mixers are a combination of two single-balanced mixers and two double balanced mixers. A double-balanced mixer can be realized with

[16] up- or down-conversion operation

[17] The center tapped transformer performs a balanced to unbalanced (balun) transition of the input signal.

[18] This can be shown by calculating the diode currents using the Taylor series approach form Equations A.7 and 3.5 with higher potencies.

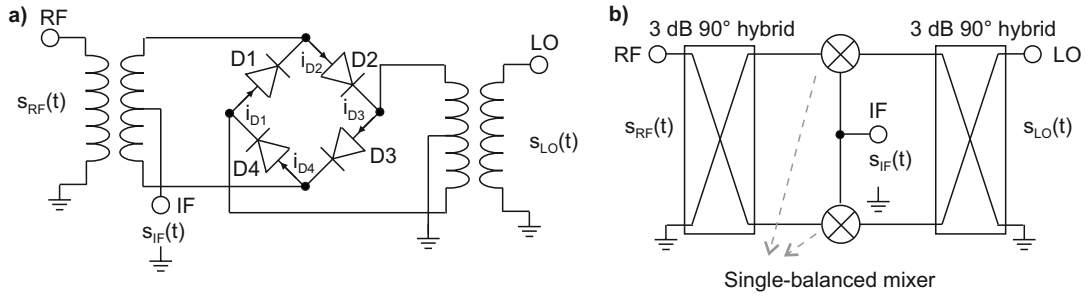

FIGURE 3.9: Double-balanced mixer with (a) transformers or (b) hybrid couplers.

transformers or hybrids as shown in Fig. 3.9. These types enable the isolation of all ports, an improved suppression of spurious products and an increased linearity. The disadvantages are the required higher LO power and the complexity. The mixers used in this thesis are double balanced types.

A further improvement of the mixer properties can be achieved with a triple-balanced type. It consists of two double-balanced mixers driven in push-pull configuration. The advantages of the triple-balanced mixer over the double-balanced mixer are a wider bandwidth, overlapping RF, IF and LO bands, higher spurious suppression and very good port-to-port isolation. The down-side is the circuit complexity [107].

I/Q mixers consist basically of two balanced mixers, which are driven with two different input signals[19] and either the LO or a $\pi/2$ shifted version of the LO. The functional diagram of an I/Q mixer for up-conversion operation is shown in Fig. 3.10 (a). With the LO signal $s_{\mathrm{LO}}(t) = \cos(\omega_{\mathrm{LO}} t)$ the RF output signal can be written as

$$s_{\mathrm{RF}}(t) = \cos(\omega_{\mathrm{LO}} t) s_{\mathrm{IF1}}(t) - \sin(\omega_{\mathrm{LO}} t) s_{\mathrm{IF2}}(t) \; . \tag{3.9}$$

Depending on the waveform of the IF input signals, different I/Q mixer operations are possible, e.g. an I/Q modulator or a single sideband (SSB) mixer as shown in Fig. 3.10 (b,c). For the operation as an I/Q modulator it is required that the IF input signals consists of the in-phase and quadrature symbol information. The amplitude and phase of the LO is then modulated by the two IF signals in the form of

$$s_{\mathrm{RF}}(t) = A(t) \cos(\omega_{\mathrm{LO}} t + \Theta(t)) \; , \tag{3.10}$$

with the amplitude $A(t)$ and phase $\Theta(t)$ defined as

$$\begin{aligned} A(t) &= \sqrt{s_{\mathrm{IF1}}(t)^2 + s_{\mathrm{IF2}}(t)^2} \\ \Theta(t) &= \mathrm{atan} \frac{s_{\mathrm{IF2}}(t)}{s_{\mathrm{IF1}}(t)} \; . \end{aligned} \tag{3.11}$$

The operation of the I/Q mixer as an SSB mixer requires a 90° shift between both IF input signals. SSB means that the RF signal is only present at the lower or upper sideband of the LO. This can be shown with Equation 3.9 and the IF input signals

[19] Either IF or RF signals depending on the mixer operation

defined as

$$\begin{aligned} s_{\mathrm{IF1}}(t) &= \cos(\omega_{\mathrm{IF}} t) \\ s_{\mathrm{IF2}}(t) &= -\sin(\omega_{\mathrm{IF}} t)\ . \end{aligned} \tag{3.12}$$

The RF output signal is now

$$\begin{aligned} s_{\mathrm{RF}}(t) =& \cos(\omega_{\mathrm{LO}} t) A \cos(\omega_{\mathrm{IF}} t) + \sin(\omega_{\mathrm{LO}} t) A \sin(\omega_{\mathrm{IF}} t) \\ =& \frac{1}{2}\Big[\cos\big((\omega_{\mathrm{LO}} - \omega_{\mathrm{IF}})t\big) + \cos\big((\omega_{\mathrm{LO}} + \omega_{\mathrm{IF}})t\big) \\ &+ \cos\big((\omega_{\mathrm{LO}} - \omega_{\mathrm{IF}})t\big) - \cos\big((\omega_{\mathrm{LO}} + \omega_{\mathrm{IF}})t\big)\Big] \\ =& \cos\big((\omega_{\mathrm{LO}} - \omega_{\mathrm{IF}})t\big) \end{aligned} \tag{3.13}$$

and as can be observed, the upper sideband signal is canceled out. The down-conversion operation of an I/Q mixer can be e.g. an I/Q demodulator or a image reject mixer. An image reject mixer cancels the image RF signal which would otherwise be down-converted to the same IF frequency as the wanted RF signal. The I/Q mixer used for the bandwidth extension concept in this thesis operates as I/Q (de)modulator.

3.3.3 Non-ideal mixer properties

Mixers have non-ideal properties, which can cause distortions in the signal. In this section the most important ones are described and their influence on the bandwidth extension technique is discussed. Additionally, the characteristics of the used I/Q mixer are presented to support this discussion (Marki Microwave MLIQ-1845 [108]). The relevant properties are the conversion loss, bandwidth limitations, port isolation, nonlinearities and I/Q imbalance.

3.3.3.1 Mixer conversion loss

Mixer design requires impedance matching at three ports, complicated by the fact that several frequencies and their harmonics are involved. Ideally, each mixer port would be matched for its frequency range and undesired frequency components would be absorbed with resistive loads or blocked with reactive terminations. However, these

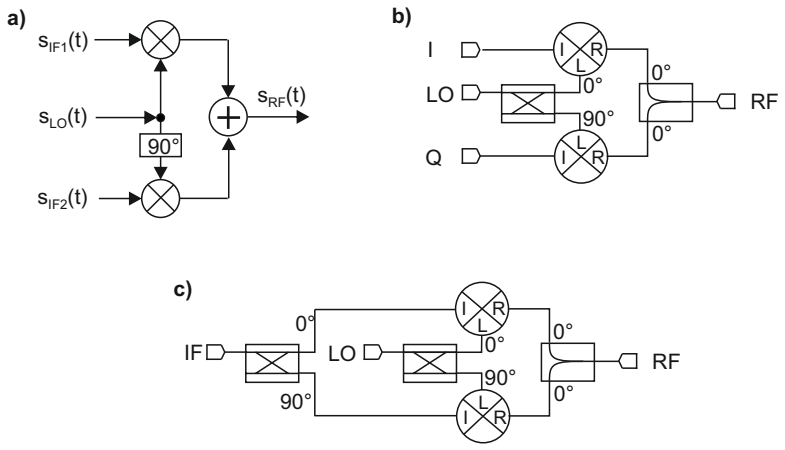

FIGURE 3.10: (a) Functional diagram of an I/Q mixer for up-conversion, (b) I/Q modulation using a I/Q mixer and (c) single sideband mixer.

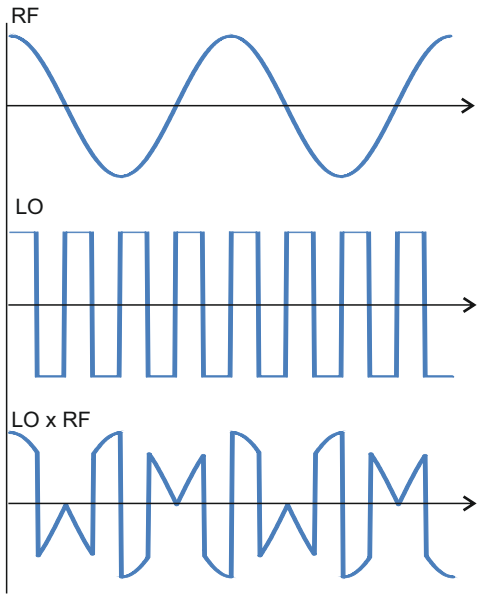

FIGURE 3.11: Schematic ideal switching operation of the mixer. The RF input signal phase changes its phase every time the LO changes polarity, as seen by the IF output port. The resulting signal (LOxRF) corresponds in its form to the multiplication of the rectangular LO switching function and the sinusoidal RF input signal.

elements increase the mixer losses and can be very frequency dependent. In addition, there are inherent losses due to the frequency conversion process, e.g. the generation of harmonics. Mixer conversion loss for up-conversion operation is defined as the ratio of the available IF input power P_{IF} at the frequency f_{IF} to the RF output power P_{RF} at the frequency $f_{\mathrm{LO}} - f_{\mathrm{IF}}$ or $f_{\mathrm{LO}} + f_{\mathrm{IF}}$, expressed in dB

$$C_{\mathrm{cl}}\big|_{\mathrm{dB}} = 10\,\mathrm{lg}\left(\frac{P_{\mathrm{RF}}}{P_{\mathrm{IF}}}\right) . \tag{3.14}$$

Conversion loss accounts for resistive losses in a mixer as well as loss in the frequency conversion process.

A theoretical estimation for the mixer loss[20] can be done by assuming its diodes as ideal switches. This approximation can be made since the LO signal is generally significant stronger compared to the RF input signal. If the common double-balanced mixer type from Fig. 3.9 (a) is considered, the following occurs: during positive LO cycles, diodes D3 and D4 are turned on while D1 and D2 are off and the opposite is the case during negative LO cycles. This causes the RF voltage as seen by the IF port to change its phase by 180° every time the LO signal changes polarity as shown in Fig. 3.11. This can be represented mathematically by multiplying the sinusoidal RF input signal $s_{\mathrm{RF}}(t) = V_{\mathrm{RF}} \sin(\omega_{\mathrm{RF}} t)$ with a switching function $s_{\mathrm{T}}(t)$, i.e. the LO signal $s_{\mathrm{LO}}(t)$. The Fourier series for the square-wave switching function is

$$s_{\mathrm{T}}(t) = \frac{4}{\pi} \sum_{n=1,3,5\ldots} \frac{1}{n} \sin(n\omega_{\mathrm{LO}} t) . \tag{3.15}$$

[20] Assuming impedance matching at all ports

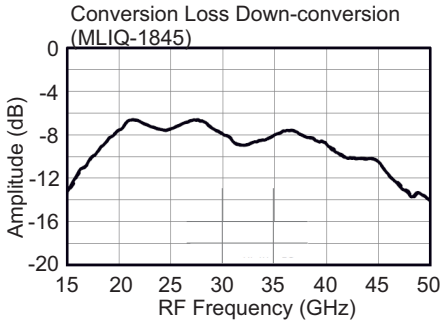

FIGURE 3.12: Data sheet characteristic of the conversion loss for the used I/Q mixer for down-conversion over the RF frequency. In the experiments, RF signal between 18 and 42 GHz have been used.

The IF output signal is therefore

$$\begin{aligned} s_{\mathrm{IF}}(t) =& s_{\mathrm{RF}}(t)\, s_{\mathrm{T}}(t) \\ =& V_{\mathrm{RF}} \sin(\omega_{\mathrm{RF}})\, \frac{4}{\pi} \sum_{n=1,3,5\ldots} \frac{1}{n} \sin(n\omega_{\mathrm{LO}} t) \\ =& V_{\mathrm{RF}} \frac{4}{\pi} \left\{ \frac{1}{2} \Big[\sin\big((\omega_{\mathrm{LO}} - \omega_{\mathrm{RF}})t\big) - \sin\big((\omega_{\mathrm{LO}} + \omega_{\mathrm{RF}})t\big) \Big] \right. \\ & \left. + \frac{1}{6} \Big[\sin\big((3\omega_{\mathrm{LO}} - \omega_{\mathrm{RF}})t\big) - \sin\big((3\omega_{\mathrm{LO}} + \omega_{\mathrm{RF}})t\big) \Big] + \ldots \right\} . \end{aligned} \tag{3.16}$$

The desired IF output signals has the form $s_{\mathrm{IF}}(t) = V_{\mathrm{IF}} \sin(\omega_{\mathrm{IF}} t)$ with $\omega_{\mathrm{IF}} = \omega_{\mathrm{LO}} - \omega_{\mathrm{RF}}$. After inserting into Equation 3.16 and removing all undesired frequency components, the RF to IF signal amplitude relation is

$$\frac{V_{\mathrm{IF}}}{V_{\mathrm{RF}}} = \frac{2}{\pi} , \tag{3.17}$$

and thus the conversion loss yields

$$C_{\mathrm{cl}} = 20 \lg \frac{2}{\pi} \approx -3.9\ dB . \tag{3.18}$$

Real-world mixers have conversion losses <-4.5 dB which originate from transmission line losses, balun mismatches, diode series resistances and mixer imbalances [104], [106]. For mixers with wider bandwidths there are additional losses due to the difficulty in maintaining circuit balance over the entire bandwidth. The mixer conversion loss is strongly related to the mixer noise figure, since they can be seen as passive devices[21]. Their noise figure is therefore principally reciprocal to the conversion loss. However, the noise figure tends to be higher since additional effects exists, like the conversion of the diode shot-noise or impairments from the LO phase noise [106], [109]. An example for the conversion loss of the used I/Q mixer is shown in Fig. 3.12, copied from its data sheet. The loss is between -7 and -10 dB in the relevant frequency band[22] with higher values at the outer frequencies. In the experiments this high loss required additional amplification for the up and down-converted sub-band, with the

[21] Mixer based on diodes

[22] The I/Q mixer is used for signal bandwidths between 18 and 42 GHz.

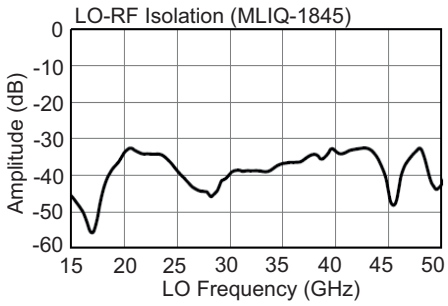

FIGURE 3.13: Data sheet characteristic of the used I/Q mixer LO-RF isolation over the LO frequency.

associated SNR degradation due to the amplifier noise.

3.3.3.2 Mixer port isolation

Isolation is the relation in power between the input signal and the leaked power into the other ports at the same frequency. It is obtained by the mixer balance, e.g. with the use of 3 dB hybrids or transformers as shown in Section 3.3.2 and can be described similarly like the conversion loss. In the case of the LO signal at the RF port (for up-conversion operation), the LO-RF isolation in dB is

$$Iso_{\mathrm{LO,RF}}\big|_{\mathrm{dB}} = 10\lg\left(\frac{P_{\mathrm{IN,LO\ port}}}{P_{\mathrm{OUT,\ LO@RF\ port}}}\right) , \tag{3.19}$$

with $P_{\mathrm{IN,LO\ port}}$ the input LO power at the LO port and $P_{\mathrm{OUT,\ LO@RF\ port}}$ the LO power at the RF port, e.g. for the double-balanced mixer type from Fig. 3.9 (a). The isolation is also approximately reciprocal between two ports, i.e. $Iso_{\mathrm{LO\text{-}RF}} \approx Iso_{\mathrm{RF\text{-}LO}}$ [104]. The IF-RF isolation[23] is likewise

$$Iso_{\mathrm{IF,RF}}\big|_{\mathrm{dB}} = 10\lg\left(\frac{P_{\mathrm{IN,IF\ port}}}{P_{\mathrm{OUT,\ IF@RF\ port}}}\right) , \tag{3.20}$$

with $P_{\mathrm{IN,IF\ port}}$ the input IF power at the IF port and $P_{\mathrm{OUT,\ IF@RF\ port}}$ the IF power at the RF port. The calculation of the isolation for down-conversion operation (RF-IF and LO-IF) is likewise. Poor LO-RF isolation can cause distortions in the RF output signal for up-conversion operation, especially if IF frequencies close to DC are used, since no amount of filtering can separate the arbitrarily close RF signal and LO leakage. For down-conversion similar issues exists, like the contamination of the RF line by either interfering with the RF amplifier or by leaking into other parallel mixing channels causing cross-channel interference [104]. Good LO-IF isolation is important if the LO and the IF frequency are close to each other. The limited filter possibilities can result in saturated IF amplifiers due to the significantly higher LO power levels. The third isolation is between the RF and the IF port of a mixer. Due to the much lower power of both IF and RF signals compared to the LO, it is not that critical. However, good RF-IF isolation of a mixer commonly originates from good overall balancing and thus results in a small conversion loss [104].

The used I/Q mixer in the experiments has a LO-RF isolation between 33 and 45 dB in the operation range (18-42 GHz) as shown by its data sheet characteristic in

[23] For up-conversion operation

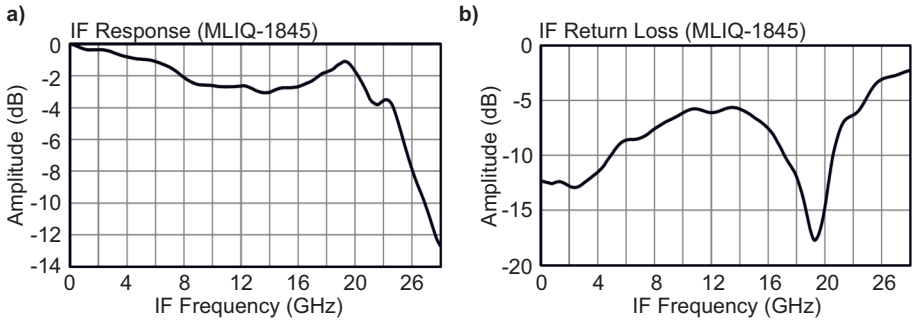

FIGURE 3.14: Data sheet IF frequency response and return loss of the used I/Q mixer.

Fig. 3.13. This LO-RF isolation results[24] in a relatively prominent LO in the RF signal due to the high LO power and the high conversion loss of the I/Q mixer. This in turn impairs the RF signal in terms of total signal power, since it is shared between the sidebands and the undesired LO. The IF-LO and IF-RF isolation and vice versa are not problematic for the experiments due to the frequency gap between the signals, which allows a relatively easy filtering of unwanted signal parts[25].

3.3.3.3 Mixer bandwidth limitations

The three ports of a normal RF mixer have ideally linear transfer characteristics, which define the operation bandwidths of the device. The IF port has typically a low-pass characteristic and the RF and LO ports a passband characteristic. These show ideally a flat amplitude response and a linear phase in the operation band. The return loss of each port, which is especially important at higher frequencies, varies with the frequency too. Devices which target very high port bandwidths, as utilized in this thesis, have commonly a poor characteristic regarding these parameters. This can be attributed to realization issues, like parasitic effects, for these wideband devices.

In Fig. 3.14 (a+b) the data sheet characteristic of the used I/Q mixer is shown, with the frequency response of one IF port at the left and the return loss of the IF port[26] at the right side [108]. The frequency response has already a small drop of 3 dB well inside the operation band and the return loss goes up to -5 dB, also already far below the upper operation band limit. Components with a poor return loss can cause reflections in the system, which in turn overlap with the original signal and cause SNR degradations. Drops in the frequency response increase the equalization effort and require additional amplification of the signal, to compensate for the attenuation.

3.3.3.4 Mixer nonlinearities

Commonly there are two metrics to describe the nonlinearity of a mixer. The first one is the 1 dB compression point (P1dB) and the second the two tone, third order interception point (IP3). For a normal RF mixer in down-conversion operation, the former is the RF input signal power $P_{\mathrm{IN,1dB}}$ at which the IF output signal[27] power P_{OUT} deviates by 1 dB from the linear relation of input to output signal power, offset

[24] observed in the experiments
[25] The IF signals had bandwidths up to 15 GHz and the LO was located at 30 GHz.
[26] It can be assumed that both IF ports of the I/Q mixer have the same frequency characteristic.
[27] At the desired frequency

by the conversion loss C_{cl}. The output signal power P_{OUT} at the P1dB is therefore

$$P_{OUT}\big|_{dBm} = P_{IN,1dB}\big|_{dBm} + C_{cl}\big|_{dB} - 1\,, \tag{3.21}$$

with P_{OUT} and $P_{IN,1dB}$ in dBm and C_{cl} in dB. In Fig. 3.15 this relation is also illustrated. The power saturation typically happens when the input signal power is close to the LO power level. At this point the input signal starts to turn on the diodes by itself and the mixer behaves unpredictably. Among other effects, this causes increased levels of intermodulation distortion and higher conversion loss. Normal operation of a mixer is therefore significantly below the P1dB to avoid this behavior. Note that for applications with high signal power requirements, the P1dB can be increased by using diodes which require higher LO powers.

The nonlinearities of a mixer operating below the P1dB originate primarily from the non-ideal characteristics of the mixer diodes [110] as shown in Equation 3.5 and Appendix A.4. Multiple of the input signal frequencies are possible as expressed in Equation 3.8. Theses (unwanted) intermodulation products (IMP) can partly be suppressed by the mixer architecture[28] and are commonly not an issue. More interesting is the condition when several input signals are present, like in most broadband communication systems. Then Equation 3.8 changes to

$$f_{OUT} = \pm n f_{LO} \pm m_1 f_{1,IN} \pm m_2 f_{2,IN} \ldots\ . \tag{3.22}$$

The critical IMPs are the two tone, third order products, i.e. $m_1 + m_2 = 3$. For example, in a down-conversion operation of a normal RF mixer, with the two RF input signals at f_{RF1} and f_{RF2}, the IF output signals at e.g. $f_{LO} + 2f_{RF1} - f_{RF2}$ and $f_{LO} + 2f_{RF2} - f_{1RF1}$ are both located in the IF band like the desired mixing products (e.g. $f_{LO} - f_{1RF1}$ and $f_{LO} - f_{RF2}$) and can cause distortions.

A metric to describe this behavior is the two tone, third order intermodulation point (IP3). It is defined as the extrapolated input power of the mixer (at each tone) that would cause the output power level of the undesired and the desired products to become equal[29].

In Fig. 3.15 this is illustrated for mixer down-conversion operation. The x-axis is the logarithmic RF input signal power and the y-axis the logarithmic IF output signal power of all intermodulation products. From the power series (Taylor series) description of the diode current (Appendix A.4) it is clear that the different IF output intermodulation products scale differently with an increase in RF input power. For example, an increase of the RF input signal by 1 dB results in an increase of 1 dB for the desired signal, by 2 dB for the 2nd order intermodulation products and by 3 dB for the the third order products as illustrated by the pointed lines in Fig. 3.15. Therefore, the power of the critical two tone third order products would in theory meet the desired signal power at a certain RF input power level, which is the IP3. In practice the mixer is already saturated at this point.

The IP3 points of modern mixers are typically clearly beyond the P1dB and can be determined by the linear extrapolating from the desired signal power and the IMPs power levels. The graphic also shows the P1dB compression point as a deviation of the actual output power (solid blue line) from its ideal linear behavior (1st order product dotted line). The mixer conversion loss is illustrated by the crossing of the output power with the y-axis.

[28] For example, single-balanced types offer the suppression of even order inter-modulation products.

[29] Note that the IP3 can also be defined for the mixer output power.

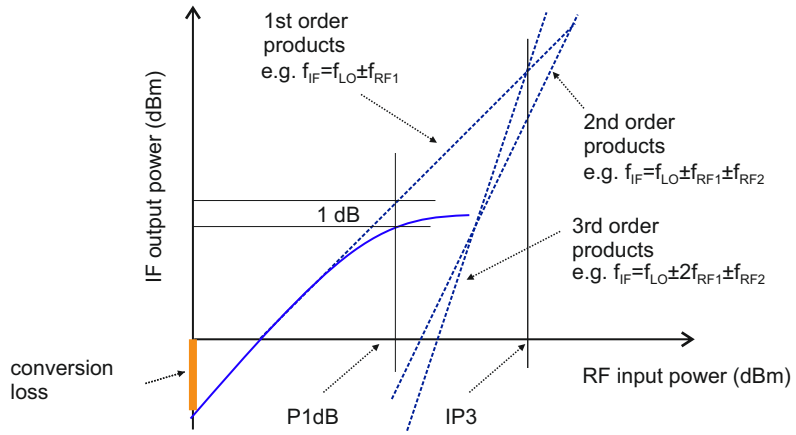

FIGURE 3.15: The 1 dB compression point (P1dB) and the two tone, third order intermodulation point (IP3) of a mixer.

The mixer nonlinearities and the resulting signal distortions limiting the maximum mixer input power for the bandwidth extension approach. A relatively high input power and thus a higher output power are especially desirable at the Tx side, to lessen the necessary amplification of the RF signal, which drives the optical modulator[30]. Generally, there is an optimum for the mixer input power at which the nonlinearities are already present but are not dominating the SNR[31].

The P1dB and the IP3 of the used mixers are at 8 and 15 dBm, respectively. For the experiments, I/Q mixer input powers of -4 to 0 dBm are used, which is well below these points. In Section 3.5.3.6 the influence of the I/Q mixer input power is experimentally shown.

3.3.3.5 Mixer I/Q imbalance

I/Q imbalance is a known problem in wireless applications, e.g. in analog front-ends. Several compensation techniques have been investigated to overcome this issue, e.g. hardware solutions, like high quality requirements for the I/Q mixers and filters or digital compensation schemes. The digital approach did not only compensate the imbalance, but it also eased the requirements for the analog front-ends and helps reducing cost and complexity [94]. The bandwidth of the signals in wireless applications is much smaller (typically below 50 MHz) compared to optical solutions and commonly I/Q imbalance is constant over the frequency band. Therefore, most of the proposed digital compensation schemes do not target frequency selective I/Q imbalance [111], [112]. As the data rates targeted in the bandwidth extension approach are much higher and thus are the signal bandwidths, frequency selective I/Q imbalance has to be taken into account. There are solutions like the use of an adaptive filter to compensate for the imbalance between LPFs in the receiver [113] or an offline calibration-based compensation as shown for coherent transmission [114]. Furthermore, the frequency selective behavior of the I/Q imbalance is not such an issue if subcarrier-based modulation formats like OFDM are used. In this case each individual subcarrier experiences a constant imbalance, and can be separately compensated as shown in [115].

[30] The technical requirements for the amplification of the IF signals are more relaxed compared to the RF amplification.

[31] The exact value of the optimal input power strongly depends on the other components of the transmission system and has to be evaluated by simulations and measurements.

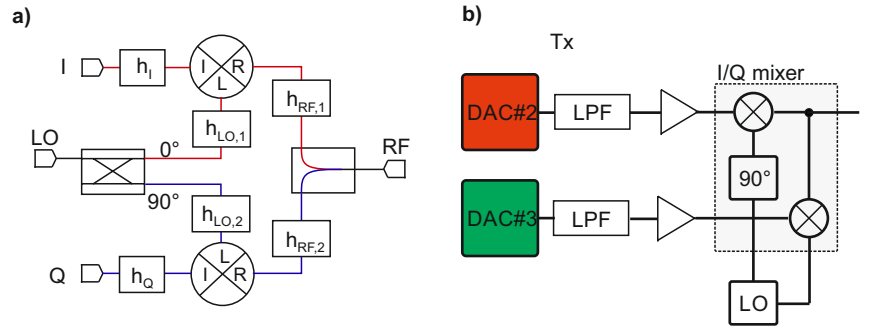

FIGURE 3.16: I/Q mixer with path transfer characteristics in the I (red) and the Q (blue) branch. (b) Part of the experimental Tx setup of the transmission system relevant for I/Q imbalance.

I/Q imbalance in the investigated bandwidth extension approach originates from different path transfer characteristics in the I and Q branch of the I/Q mixers. In Fig. 3.5 (a) this is illustrated with the I branch indicated by the red and the Q branch by the blue color . This imbalances can either be constant, like a delay or an attenuation or can be frequency-selective, e.g. differences in I and Q branch transfer characteristic. The path transfer characteristics of the I and Q branch can be separated into different parts as shown in Fig. 3.16 (a). For an ideal I/Q mixer operating as I/Q modulator these are h_I and h_Q for the IF paths, $h_{\mathrm{LO},1}$ and $h_{\mathrm{LO},2}$ for the LO paths and $h_{\mathrm{RF},1}$ and $h_{\mathrm{RF},2}$ for the RF paths. I/Q imbalance occurs, when any of these transfer functions h differs compared to their counter part. Note that the 90° hybrid for the LO signal and the coupler at the RF output port are assumed ideal. By comparing this I/Q mixer schematic with the relevant part of the experimental Tx setup[32] of the transmission system shown in Fig. 3.16 (b), it is possible to simplify the I/Q imbalance discussion. First, the used I/Q mixers are designed for LO frequencies between 20 and 40 GHz [108]. In the experiments an LO of 30 GHz is used, which is in the middle of the operation range. Thus, it can be assumed that the hybrid coupler at the LO port works properly[33] and $h_{\mathrm{LO},1} = h_{\mathrm{LO},1}$. Furthermore, the LO hybrid coupler is inside the I/Q mixer module and no influence from the outside is possible. The same is valid for the RF path transfer characteristics and $h_{\mathrm{RF},1} = h_{\mathrm{RF},2}$ can be assumed. However, in the IF branches several different elements exist in the transmission system. These are both DACs, the LPFs and the amplifiers. Additionally, there are slight differences in the used cables and connectors due to the discrete realization of the setup. It can be expected that each of these elements behaves slightly different compared to its counterpart in the other branch and therefore $h_\mathrm{I} \neq h_\mathrm{Q}$. For the following discussion only the difference in the transfer characteristic in the IF branches are considered.

A complex time domain baseband signal $s(t) = \Re\{s(t)\} + j\Im\{s(t)\}$ (e.g. OFDM or QAM), which modulates an electrical carrier using an I/Q mixer, is impaired by the different transfer characteristic of the I and Q branch. The impaired baseband signal $\tilde{s}(t)$ can be described as

$$\begin{aligned}\tilde{s}(t) &= h_\mathrm{I}(t) * \Re\{s(t)\} + j \cdot h_\mathrm{Q}(t) * \Im\{s(t)\} \\ &= \frac{h_\mathrm{I}(t) + h_\mathrm{Q}(t)}{2} * s(t) + \frac{h_\mathrm{I}(t) - h_\mathrm{Q}(t)}{2} * s^*(t)\ ,\end{aligned} \tag{3.23}$$

[32] Same setup for Rx side without the amplifiers. Full schematic is shown in Fig. 3.23.
[33] The experiments verified this.

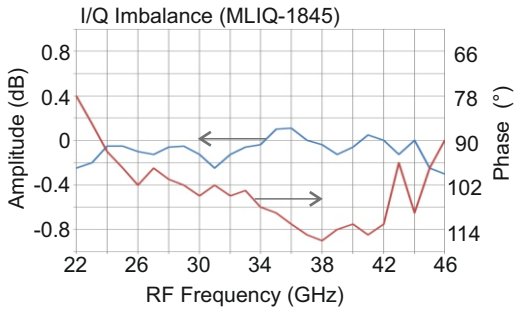

FIGURE 3.17: I/Q imbalance shown as amplitude and phase deviation of the in-phase to the quadrature signals over their RF frequency range taken from the data sheet.

where h_I and h_Q denote the impulse response in the I and Q branch respectively, $\Re\{u(t)\}$ and $\Im\{u(t)\}$ denote the real and imaginary part of the unimpaired complex modulated baseband signal respectively, $*$ is the convolution and $s^*(t)$ the complex conjugate of $s(t)$. After transforming into the frequency domain this is

$$\tilde{S}(k) = \frac{H_\mathrm{I}(k) + H_\mathrm{Q}(k)}{2} S(k) + \frac{H_\mathrm{I}(k) - H_\mathrm{Q}(k)}{2} S^*(-k) \; . \tag{3.24}$$

The indices k and $-k$ describe frequencies left and right from the electrical carrier[34] and are often referred to as mirror frequencies, since they have the same distance from the DC carrier. It can be observed from Equation 3.24 that differences between H_I and H_Q result in crosstalk of the complex conjugate signal component at $-k$ to that at k and vice versa. For equal transfer characteristics of the I and the Q branch, i.e. $H_\mathrm{I}(k) = H_\mathrm{Q}(k)$, the second term in Equation 3.24 is reduced to 0 and no crosstalk occurs. Similar calculations can be done for differences in $h_\mathrm{RF,1}$ and $h_\mathrm{RF,2}$ and between $h_\mathrm{LO,1}$ and $h_\mathrm{LO,2}$. However, with h_I and h_Q the I/Q imbalance can be sufficiently described and implemented in the simulation environment as it will be shown in Section 3.4.1.5. Equation 3.24 can be simplified to

$$\tilde{S}(k) = H_\mathrm{sys}(k) S(k) + H_\mathrm{ct}(k) S^*(-k) \; , \tag{3.25}$$

with

$$\begin{aligned} H_\mathrm{sys}(k) &= \frac{H_\mathrm{I}(k) + H_\mathrm{Q}(k)}{2} \\ H_\mathrm{ct}(k) &= \frac{H_\mathrm{I}(k) - H_\mathrm{Q}(k)}{2} \; . \end{aligned} \tag{3.26}$$

The function $H_\mathrm{sys}(k)$ represents a normal transfer characteristic and the function $H_\mathrm{ct}(k)$ a crosstalk inducing transfer characteristic. The estimation of $H_\mathrm{ct}(k)$ can be done with the help of the I/Q mixer data sheet. In Fig. 3.17 the amplitude and phase deviation of the I and Q signals over the RF frequency is shown for the used I/Q mixer. The amplitude deviation is relatively constant and small but there are strong phase deviations, especially close to the limits of the I/Q mixer operation range[35]. Due to the high signal bandwidths present in the experimental investigation of the bandwidth extension approach, the I/Q imbalance has to be compensated to avoid signal distortions. In

[34] i.e. the LO if up-converted by the mixer

[35] The RF signal was located between 18 and 42 GHz in the experiments

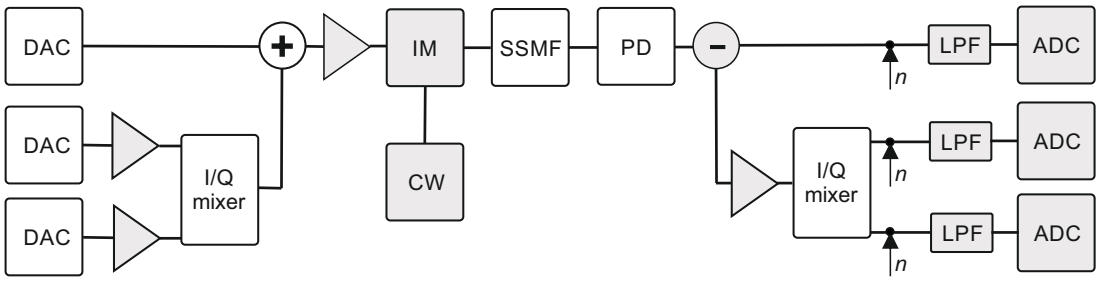

FIGURE 3.18: Simulation setup for the bandwidth extension approach. IM: optical intensity modulator, CW: laser source, PD: photodiode.

this work a frequency selective compensation is used, which is based on a 2x2 MIMO scheme. The details are presented in Section 3.5.2.3.

3.4 Simulation environment for bandwidth extension approach

For the investigation of the bandwidth extension concept, a simplified simulation environment is used, aided by experimental work. The purpose of the simulation is to test the DSP and investigate certain system aspects, e.g. the influence of the chromatic dispersion and the I/Q imbalance. The simulation setup is shown in Fig. 3.18. White blocks are components with a detailed model, covering the relevant component properties. These are DAC, Tx and Rx I/Q mixer, fiber, photodetector and electrical combiner. Grey components are assumed ideal, i.e ADC, optical modulator, electrical amplifiers, LPFs and the electrical splitter. In the following sections the different component models and their realization are presented and main aspects highlighted.

3.4.1 I/Q mixer model

The I/Q mixer model includes the mixer properties discussed in the previous sections. In Fig. 3.19 a block diagram for the up-conversion operation (I/Q modulator at the Tx side) is shown. At first the I/Q imbalance is applied, followed by a normal mixer for each of the I and Q branches. The mixer consists of the input and output filter characteristic[36], the port isolation, the conversion loss and the nonlinearities. The mixing with the LO and the combination of the RF signals are assumed ideal. Note that the same I/Q mixer model is used for the down-conversion operation, with some adaptations in the order of the blocks.

The exact parameters for the mixer properties are taken from the manufacturer data sheet of the used I/Q mixer (MLIQ-1845 I/Q, Marki Microwave [108]). In the next sections this is discussed and a detailed description of the different blocks of the I/Q mixer given.

3.4.1.1 Model of mixer nonlinearities

The (I/Q) mixer nonlinearities are commonly described by the manufactures with the help of a spurious suppression table (SST) as shown in Table 3.1. This table shows the power relation of the intermodulation products (IMP) to the desired signal (in dBc) for

[36] For up-conversion: low-pass at the input and bandpass at the output

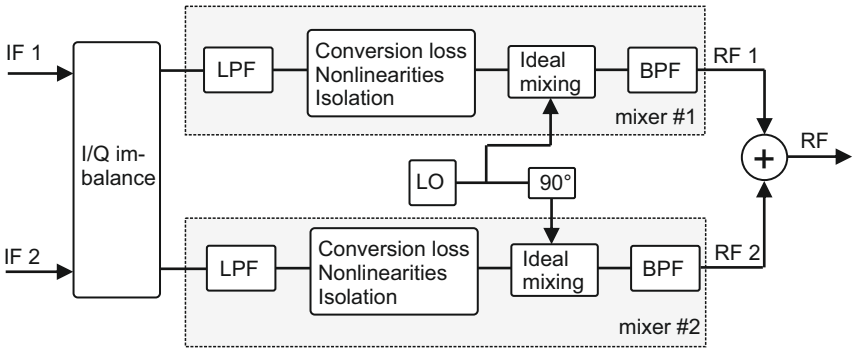

FIGURE 3.19: I/Q mixer simulation model for up-conversion operation (I/Q modulator) consisting of I/Q imbalance in the IF branch, the input and output filter characteristic, the port isolation, the conversion loss and the nonlinearities.

up-conversion operation of the used I/Q mixer[37]. The values in a single row represent different intermodulation orders m and the columns different LO orders n. For example, the relation of the desired signal component at $f_{n=1,m=1}$ to the 3rd harmonic at $f_{n=1,m=3}$ at the RF output of the mixer for a IF signal input power of -10 dBm is 63 dBc. The power relation of the IMPs differs for different LO orders (nLO), as indicated by the different values in each column[38]. Note there are also different SSTs for up and down-conversion.

The power relations of the IMPs are determined by measurements using a single-tone input with a fixed power (-10 dBm in Table 3.1). The mixer is swept across its full output band by tuning the LO[39] and the mean of the intermodulation product power is calculated[40].

This power relation from the SST is denoted as $IMP_{m,n}$ in dBc and can be described by

$$IMP_{m,n}\Big|_{\mathrm{dBc}} = P_{\mathrm{OUT},1,1}\Big|_{\mathrm{dBm}} - P_{\mathrm{OUT},m,n}\Big|_{\mathrm{dBm}}\,, \tag{3.27}$$

with $P_{\mathrm{OUT},1,1}$ the output power of the desired signal component at $m = 1, n = 1$ and $P_{\mathrm{OUT},m,n}$ the output power of the IMPs at m, n, both in dBm. Due to the fact that the slope of the different IMPs is known for the operation of the mixer, it is possible to calculate their power relation for any input signal power with:

$$IMP_{m,n}\Big|_{\mathrm{dBc}} = (m-1)(P_{\mathrm{IN,ref}} - P_{\mathrm{IN}})\Big|_{\mathrm{dBm}} + IMP_{m,n,\mathrm{ref}}\Big|_{\mathrm{dBc}}\,, \tag{3.28}$$

where P_{IN} is the new input power in dBm, $P_{\mathrm{IN,ref}}$ the reference input power from the SST in dBm, $IMP_{m,n,\mathrm{ref}}$ the reference IMP from the SST in dBc and $IMP_{m,n}$ the new power relation in dBc. For example, the $IMP_{2,2}$ is 59 dB below the desired signal $IMP_{1,1}$ for the given SST. Changing the input power to -20 dBm results in an $IMP_{2,2}$ of 69 dB below the desired signal. The absolute power of each IMP at the mixer output

[37] Exemplary values from the I/Q mixer data sheet.

[38] The intermodulation products of higher LO orders are e.g. relevant for harmonic mixers. However they are not relevant for the discussed system concept, since they can be suppressed easily by filters

[39] In case of up-conversion the full RF output band of the mixer

[40] To remove the frequency dependence

can then be written as

$$P_{m,n}\Big|_{\mathrm{dBm}} = P_{\mathrm{IN}}\Big|_{\mathrm{dBm}} - C_{\mathrm{cl}}\Big|_{\mathrm{dB}} - IMP_{m,n}\Big|_{\mathrm{dBc}} , \tag{3.29}$$

with the I/Q mixer conversion loss C_{cl} in dB.

The nonlinear transfer characteristic of a mixer can be described by using a static polynomial approach (power series). This is done by separating the calculation of nonlinear signal terms and the mixing process as illustrated in Fig. 3.19. For a mixer in up-conversion operation the resulting spurious products of the IF input signal (single tone signal) modulating a polynomial can be described by

$$s_{\mathrm{OUT},n} = \sum_{m=0}^{\infty} a_{m,n} s_{\mathrm{IN}}^{m} = a_{0,n} + a_{1,n} s_{\mathrm{IN}} + a_{2,n} s_{\mathrm{IN}}^{2} + a_{3,n} s_{\mathrm{IN}}^{3} + a_{4,n} s_{\mathrm{IN}}^{4} + a_{5,n} s_{\mathrm{IN}}^{5} + \dots . \tag{3.30}$$

The coefficients $a_{m,n}$ denote the scaling of the different spurious products and have to be determined. As already mentioned above, separate equations for each LO order n are necessary, due to different IMPs relations for each LO harmonic in the SST. The given SST is also limited to $m = 5$, which is sufficient for the nonlinear mixer model[41]. Furthermore, LO orders with $n > 1$ are not relevant for the simulation model, since signal components at $n \cdot \omega_{\mathrm{LO}}$ can be easily filtered out[42].

Defining the single tone input signal as $s_{\mathrm{IN}} = A\cos(\omega_{\mathrm{IN}} t)$, the equation above is:

$$\begin{aligned} s_{\mathrm{OUT},n} = {} & a_{0,n} + a_{1,n} A\cos(\omega_{\mathrm{IN}} t) + a_{2,n}(A\cos(\omega_{\mathrm{IN}} t))^2 + a_{3,n}(A\cos(\omega_{\mathrm{IN}} t))^3 \\ & + a_{4,n}(A\cos(\omega_{\mathrm{IN}} t))^4 + a_{5,n}(A\cos(\omega_{\mathrm{IN}} t))^5 , \end{aligned} \tag{3.31}$$

with $n = 0, 1$. Each of the power terms $(A\cos(\omega_{\mathrm{IN}}))^{m=1..5}$ contains several spurious products ($\omega_{\mathrm{IN}}, 2\cdot\omega_{\mathrm{IN}}, ...5\cdot\omega_{\mathrm{IN}}$), including the desired signal. After the addition of all products with the same frequency component $m \cdot \omega_{IN}$ and the calculation of the signal power, the results can be compared to the IMP powers $P_{m,n}$, which in turn can be calculated from Equation 3.29. For example, the equation for the frequency components at $n = 1$ and $m = 1$ is:

$$P_{1,1} = \int_0^{T_{\mathrm{sig}}} \left(A a_{1,1}\cos(\omega_{\mathrm{IN}} t) + \frac{3}{4} A^3 a_{3,1}\cos(\omega_{\mathrm{IN}} t) + \frac{10}{16} A^5 a_{5,1}\cos(\omega_{\mathrm{IN}} t) \right) dt , \tag{3.32}$$

TABLE 3.1: Spurious suppression table of the used I/Q mixer

Data sheet IMPs of the used I/Q mixer for up-conversion operation. Rows denote the intermodulation order m and columns the LO order n. The input power is -10 dBm and all values are given in dBc.

	$n=0$ (0xLO)	$n=1$ (1xLO)	$n=2$ (2xLO)	$n=3$ (3xLO)	$n=4$ (4xLO)	$n=5$ (5xLO)
$m=1$ (1xIF)	16	Ref.	22	9	N/A	N/A
$m=2$ (2xIF)	56	60	59	60	58	N/A
$m=3$ (3xIF)	77	63	71	63	71	58
$m=4$ (4xIF)	103	98	106	105	98	97
$m=5$ (5xIF)	118	108	119	116	111	96

[41] The difference in power between the IMPs at $m > 2$ is >50 dB, which is far above the typical SNR in the experiment and thus can be neglected.

[42] LO frequencies are located at around 30 GHz in the experiment

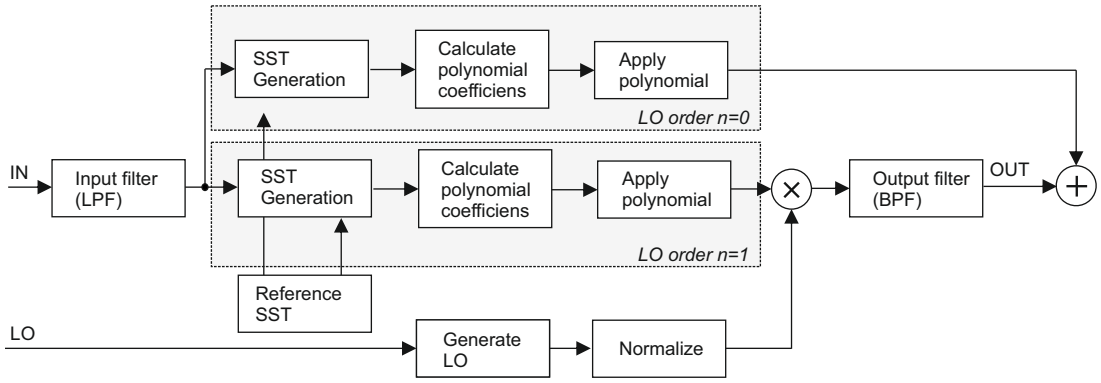

FIGURE 3.20: Mixer up-conversion operation simulation model for LO orders $n = 0, 1$

with T_{sig} the period time of the signal. In total there are $m + 1$ equations (m frequencies and DC) for each n, which form an equation system. Solving this system for the coefficients $a_{0..5}$ results in the complete description of the polynomial and therefore the static nonlinearities of the mixer. Note that for each mixer input power a new polynomial has to be calculated. In Appendix A.6 the details of this calculation can be found.

With the calculated nonlinear characteristic of the mixer it is possible to use any signal for the modulation of the polynomial, i.e. as mixer input. Since the coefficients depend only on the total input signal power and not its spectral form.

In Fig. 3.20 a more detailed block diagram of a single mixer in up-conversion operation is shown as implemented in the simulation. The model consists of three different paths after the initial input low-pass filter of the IF signal. The first path with its polynomial describes the behavior of the LO order $n = 0$ (upper path in Fig. 3.20) and is responsible for nonlinearities and IF-RF isolation. Note that no output filter is applied for this path. The second path with its polynomial describes the behavior for the LO order $n = 1$ (middle path in Fig. 3.20) and is responsible for nonlinearities, conversion loss, LO-RF isolation, mixing with the LO signal and the band-pass output filter. Afterwards, the signal of both paths are combined. Note that both polynomials are calculated from the SST as described above. The third path consists of the LO and is ideal, except for a normalization to suppress its influence on the signal output power.

3.4.1.2 Model of mixer conversion loss

As mentioned in Section 3.3.3.1, the conversion loss C_{cl} of the used I/Q mixer is frequency dependent and varies between 8 and 15 dB over the RF frequency[43] as could be observed from Fig. 3.12. However, for the mixer model a constant conversion loss is used, taken from the data sheet by calculating the mean value of the given characteristic (refer to Fig. 3.12. This approach allows to handle the mixer filter characteristics separately from the conversion loss with the help of separate input and output filters. The conversion loss is implemented using the polynomial description for LO order $n = 1$, which includes the conversion loss as shown in Equation 3.29.

[43] RF signals between 18 and 42 GHz have been used in the experiments.

3.4.1.3 Model of mixer bandwidth limits

The linear frequency behavior of the mixer is modeled with a LPF for the IF and a BPF for the RF ports[44]. For the simulations Butterworth filters[45] are used with their 3 dB frequencies and order approximated from the I/Q mixer data sheet. Note that the filters do not change the power of the signal in the simulation. Furthermore, the output filter is only applied to the signal with LO order $n = 1$, since otherwise all IF-RF isolation products would be suppressed.

3.4.1.4 Model of mixer isolation

The IF-RF and RF-IF isolation is determined from the first column of the SST table, with the LO order $n = 0$. Using Equation 3.31 the polynomial coefficients can be calculated and thus the IMPs with $n = 0$ and $m = 1..5$. Afterwards, they are added to the signal with LO order $n = 1$. The LO-IF/RF isolation is also implemented with the polynomial realization. The DC component $a_{0,n=1}$ in Equation 3.31 results in a LO signal component after the mixing. However, the required IMPs with $n = 1$ and $m = 0$ are not available in the given SSTs and have to be approximated from the LO-RF/IF isolation characteristics of the I/Q mixer data sheet. For example, in Fig. 3.13 the I/Q mixer LO-RF isolation is shown. At 30 GHz LO frequency, which is used for most of the experiments, around -40 dB can be observed. Together with the known LO power from the experiments (~18 dBm) the LO power at the RF port can be calculated and thus the coefficient $a_{0,n=1}$. In Appendix A.6 the details of this calculation can be found.

3.4.1.5 Model of mixer I/Q imbalance

The I/Q mixer model consists of two mixer models, one for the I and one for the Q branch as shown in Fig. 3.19. They are driven by either the LO or the $\pi/2$ shifted LO and have the same properties. In case of up-conversion, the signals of each branch are added after mixing and in case of down-conversion, split previously to the mixing. In Equation 3.24 it was shown that the difference in the IF paths transfer characteristics is responsible for the I/Q imbalance. Therefore, the I/Q imbalance can be implemented by applying a filter ($h_{\mathrm{IQ}}(t)$) to the baseband in-phase signal (or quadrature) as shown in Fig. 3.21 (a). As shown in Section 3.3.3.5, the complex baseband signal at the input of the I/Q imbalance block $s(t) = \Re\{s(t)\} + j\Im\{s(t)\}$ is then impaired by the I/Q imbalance in the form of

$$\begin{aligned} \tilde{s}(t) &= h_{\mathrm{IQ}}(t) * \Re\{s(t)\} + j \cdot * \Im\{s(t)\} \\ &= \frac{h_{\mathrm{IQ}}(t)+1}{2} * s(t) + \frac{h_{\mathrm{IQ}}(t)-1}{2} * s^*(t) \,, \end{aligned} \tag{3.33}$$

with $*$ the convolution and $s^*(t)$ the complex conjugate of $s(t)$. The same equation is in frequency domain

$$\tilde{S}(k) = \frac{H_{\mathrm{IQ}}(k)+1}{2} S(k) + \frac{H_{\mathrm{IQ}}(k)-1}{2} S^*(-k) \,, \tag{3.34}$$

with k to frequency components relative to DC of the complex baseband signal. For $H_{\mathrm{IQ}} = 1$ no I/Q imbalance occurs and the second term is zero. The coefficients

[44] For up-conversion operation

[45] Butterworth filter have a frequency response as flat as possible in the passband, which comes at the cost of a slower roll-off in the stopband compared to other filter types. However, other filter types could be used too.

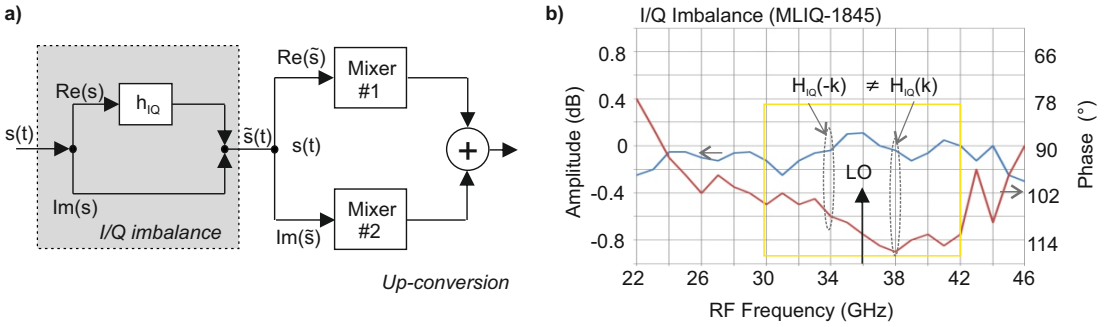

FIGURE 3.21: (a) Principe of I/Q imbalance implementation by using a filter in the in-phase branch of the I/Q mixer. (b) imbalance characteristic from the data sheet and related filter coefficients.

of $H_{\mathrm{IQ}}(k)$ can be estimated from the given I/Q imbalance characteristic, shown in Fig. 3.17, in the form of

$$H_{\mathrm{IQ}}(k) = \alpha(k)e^{j\phi(k)} \,, \tag{3.35}$$

with the amplitude $\alpha(k)$ and phase $\phi(k)$ imbalance at the frequency k. Note that the actual amplitude and phase imbalance at k is also related to the LO frequency, since the I/Q imbalance curves of the data sheet are given over the RF frequency. This aspect is illustrated in Fig. 3.21 (b), showing the I/Q imbalance characteristic of the used I/Q mixer[46]. The coefficients at k and $-k$, left and right of the LO, have different values, i.e. $H_{\mathrm{IQ}}(k) \neq H_{\mathrm{IQ}}(-k)$. Therefore, the filter coefficients are complex in their time representation h_{IQ}. For example, a LO located at 36 GHz results in different amplitude and phase imbalances for the up-converted signal components at $\pm k = 2$GHz of the complex modulated baseband signal as illustrated in Fig. 3.21 (b). If the LO is shifted to another frequency the values change accordingly. The actual implementation of the I/Q imbalance is realized as shown in Equation 3.34. The input signal $s(t)$ is transformed into the frequency domain using the Discrete Fourier Transform (DFT), its conjugate complex calculated and both are multiplied element wise with the filter $H_{\mathrm{IQ}}(k)$. Afterwards, the imbalanced signal is transformed back into the time domain using the inverse DFT (IDFT) and further processed in the mixer model.

3.4.2 DAC, combiner and splitter model

The most important DAC parameters are the nominal bit resolution, the bandwidth and the nonlinearities as shown in Chapter 2. Each of these parameters is included in the DAC[47] model as shown in Fig. 3.22. At first the nominal resolution (8 bit) is implemented by limiting the number of amplitude steps for the signal. Then a polynomial approach is chosen to generate the nonlinearities. The nonlinear transfer characteristic of a DAC can be described by using a static polynomial approach like for the mixer nonlinearities. The spurious products of a DAC, which D/A converts a single tone signal in the form of $s_1 = A\cos(\omega_1 t)$, can be written as

$$s_{\mathrm{spur},m} = a_{0,m} + a_{1,m}A\cos(\omega_1 t) + a_{2,m}(A\cos(\omega_1 t))^2 + a_{3,m}(A\cos(\omega_1 t))^3 ... \tag{3.36}$$

[46] Already introduced in Section 3.3.3.5

[47] The DACs in the experiments are CMOS based with a maximum sample rate of 92 GS/s, ~21 GHz analog 3 dB bandwidth and 8 bit nominal resolution. Similar types are used in the Keysight arbitrary waveform generator [52].

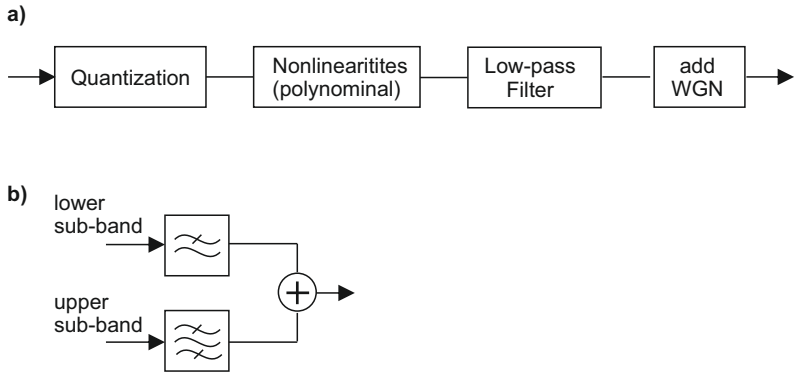

FIGURE 3.22: (a) Implementation of the DAC model with quantization (nominal bit resolution), static nonlinearities (polynomial), frequency response (low-pass filter) and white Gaussian noise (WGN). (b) Implementation of the combiner with a LPF for the lower sub-band and a BPF for the upper sub-band. After filtering both signals are ideally added.

The coefficients a_m denote the scaling of the different spurious products and have to be determined. Each of the power terms $(A\cos(\omega_1))^{m=1\cdots}$ contains several spurious products, including the desired signal at ω_1. After the addition of all products with the same frequency component $m \cdot \omega_1$ and the calculation of the signal power, the results can be compared to the measured spurious products of the DAC and the coefficients a_m can be calculated. In contrast to the mixer only one polynomial is calculated, since the output power is assumed constant[48]. In the next step a LPF (Butterworth type of 2nd order and 21 GHz 3 dB bandwidth) is used to emulate the DAC frequency response. The filter coefficients are chosen according to measurements of the DAC frequency response. At the end white Gaussian noise is added to match the simulative to the measured DAC output SNR characteristics[49]. Note that the implemented nonlinear DAC behavior is static and only the filter is relevant for its frequency characteristic. This is done to reduce the simulation model complexity. However, a nonlinear dynamic approach could be realized as well, e.g. with a Volterra series approach.

The combiner (diplexer) consists of two filters, a low-pass filter for the lower sub-band and a band-pass filter for the upper sub-band. Both are realized with a Butterworth structure. The exact parameters are chosen according to the diplexer data sheet[50]. The splitter at the Rx side is assumed ideal.

3.4.3 Optical part of simulation and noise loading

The optical part of the simulation setup is realized in the VPItransmission Maker environment. It consists of the optical modulator, the fiber and the photodetector. The optical modulator is an ideal[51] amplitude modulator with infinite modulation bandwidth and a modulation index of 0.9. The fiber is SSMF and the photodetector a single PIN-photodiode. Before the photodiode an ideal optical amplifier[52] is used to control

[48] It is preferable to always use the full resolution of the DAC, which results in a relative constant output power.

[49] This is required since the DAC output SNRs were to good compared to measurements

[50] Fig. 3.35 shows an example.

[51] Without any chirp or other impairments

[52] In VPItransmission maker this relates to a block which simply sets the optical power, without any noise added. The only noise source for the optical transmission is the photodiode.

the received signal power. Default values for the photodiode noise are used with the actual values shown in Appendix A.7. The laser wavelength and the optical power after the optical modulator and in front of the photodiode are chosen according to the experiment (1550 nm and 0 dBm fiber launch power). Note that the optical part in the simulation chain has only minor impact onto the total transmission performance. Only in case of fiber lengths beyond a few km, impairments due to the chromatic dispersion occur.

Since only the DAC, the I/Q mixers and the photodiode contribute to the noise in the simulation, an additional noise source is required to meet the SNR values of the experiments and enable sufficient high BERs in the simulation. This is realized by the addition of a white Gaussian noise signal to each sub-band at the receiver indicated by the italic *n* and the black arrow in Fig. 3.18.

3.5 Transmission experiments for bandwidth extension approach

The bandwidth extension approach based on analog mixing is investigated experimentally by means of several transmission experiments. In these experiments various system aspects are studied, like I/Q mixer behavior, modulation formats, influence of the chromatic dispersion, DSP and possible hardware realizations. This section is divided in three parts. The first part covers the experimental setup used in the investigation. The second part consists of the DSP and the third presents the various results.

3.5.1 Experimental setup for bandwidth extension approach

The experimental setup for the bandwidth extension approach is shown in Fig. 3.23. Three high-speed CMOS DACs (80 GS/s, ~19 GHz 3 dB bandwidth, 8 bit resolution) are used to generate the two independent sub-signals: the baseband signal (signal #1) at 0-20 GHz and an up-converted signal (signal #2) at 20-42 GHz. Signal #2 is formed with the help of an electrical I/Q mixer, driven by two baseband signals and an LO at 30 GHz. Tunable electrical amplifiers (EA) and passive attenuators are used to adjust the signal power of all three baseband signals after the DACs. This is required to compensate for the different attenuation in both paths. The amplifiers (SHF 100 BP) also provide the required low-pass filtering of the DAC output signals due to their transfer characteristic (25 GHz 3 dB bandwidth). There are also adjustable phase shifters in front of the I and Q port of the I/Q mixer to compensate the delay in both paths. Afterwards, signals #1 and #2 are combined using a diplexer and further amplified to achieve the required driving amplitude of the optical modulator. The optical modulator is a MZM (Oclaro 40AM, 33 GHz 3 dB bandwidth) driven at the quadrature point[53], to operate as an intensity modulator[54] . The laser is of DFB type (Agilent HP81663A) emitting at 1550.5 nm. Prior to the optical modulator a manual polarization controller is used set the right polarization for the MZM. After optical modulation, the signal is transmitted over various lengths of SSMF. The optical power after the MZM is typically between 0 and 3 dBm. The optical-electrical conversion is

[53]The quadrature operation point of a MZM is defined by a bias current which results in half the maximum output power.

[54]Due to the lack of an DML with the required electrical bandwidth (>40 GHz), which would be more realistic for these transmission systems, an MZM is used.

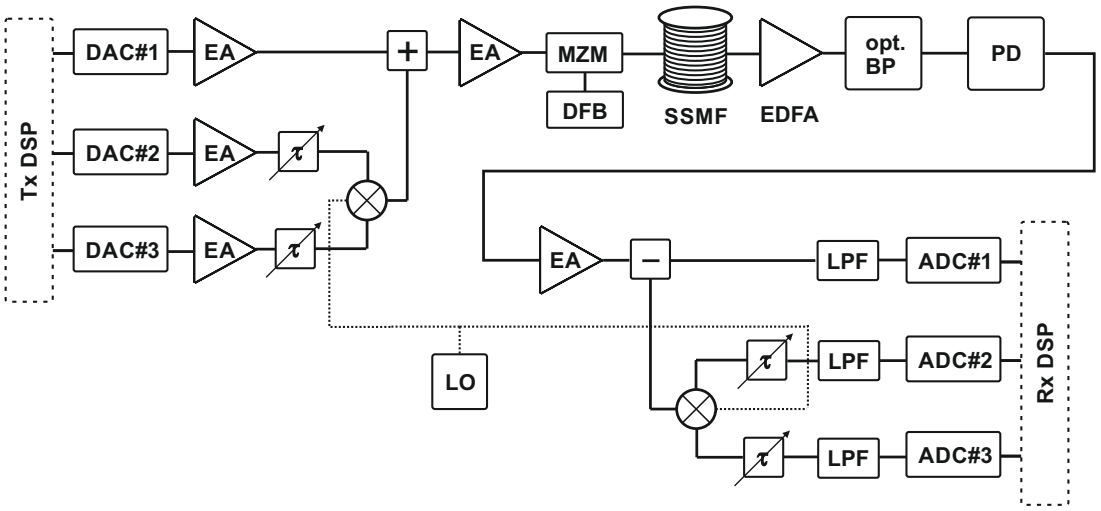

FIGURE 3.23: Experimental setup for the investigation of the bandwidth extension approach based on analog mixing.

realized with a wideband photodetector[55] with 50 GHz bandwidth, since only photoreceivers (i.e. *pin*-PD + TIA) with insufficient bandwidths were available. In order to provide the necessary optical power (10 dBm) for the photodetector, an Erbium-doped fiber amplifier (EDFA) is used and an additional optical band-pass filter (BPF) with 1 nm bandwidth to minimize the EDFA noise. Afterwards, the electrical signal is amplified again to meet the required input power of the I/Q mixer and passively split[56]. One signal is low-pass filtered and recorded by a digital storage oscilloscope (DSO), whereas the second signal is down-converted by an I/Q mixer, filtered and recorded likewise. The ADCs had a sampling rate of 80 GS/s and 30 GHz bandwidth.

The driving amplitude and bias of the MZM are set to minimize the measured BERs in all experiments. Note that changes of 20% for the driving amplitude and the bias did typically not change the BER significantly. The same process is used to optimize the input signal level of the Tx and Rx side I/Q mixer and the LO. This is done in an electrical btb scenario with the results presented in Section 3.5.3.6.

3.5.2 DSP for bandwidth extension approach experiments

For the experiments single-carrier modulation formats like PAM and QAM and multi-carrier modulation formats like DMT and OFDM are used, with each format requiring its own DSP. In this section an overview of the used DSP is given. Furthermore, the I/Q imbalance compensation approach is discussed.

3.5.2.1 DSP for multi-carrier modulation formats: DMT and OFDM

DMT is the real-valued baseband representation of OFDM and is used for the signal modulation in the lower sub-band. It is generated from OFDM by applying conjugate symmetry (often referred to as Hermitian symmetry) before the IFFT. OFDM is

[55] A photodetector commonly denotes a device for optical-electrical conversion, consisting only of photodiodes without any further amplification. In contrast, a photoreceiver commonly denotes a device with photodiodes in combination with electrical amplifiers, e.g. transimpedance amplifiers. In the following sections this distinction is used.

[56] Using a 6 dB power splitter

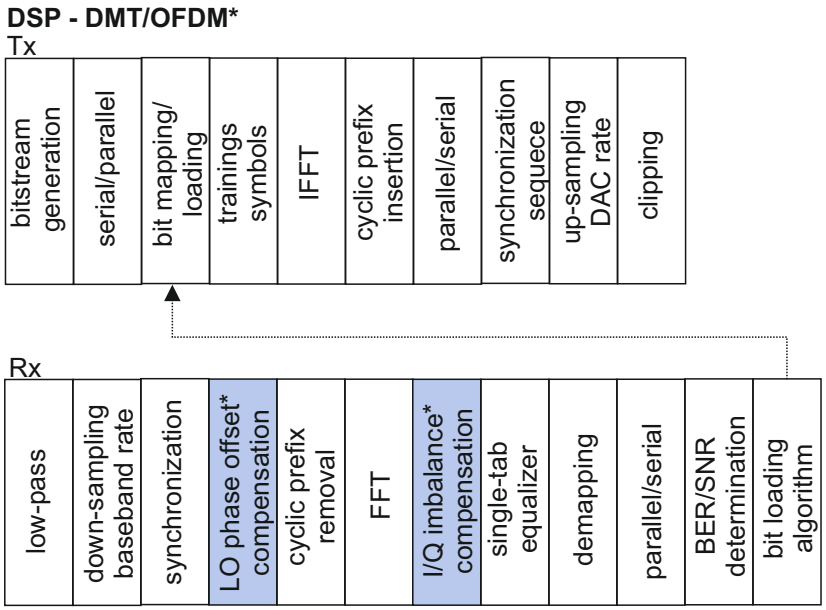

FIGURE 3.24: DSP for DMT and OFDM. The highlighted blocks are only for OFDM. The arrow between the Tx and the Rx block illustrates the application of the optimized subcarrier bit-loading for the transmission of the next signal block.

used for the signal modulation in the upper sub-band, by driving the I/Q mixer with the in-phase and quadrature part of the time domain OFDM signal. Additionally, an I/Q imbalance compensation scheme is used for the OFDM transmission, which is described in Section 3.5.2.3.

In Fig. 3.24 the DSP for DMT and OFDM is presented. The highlighted blocks mark the DSP that is only relevant for OFDM. The transmitter side includes the bit-stream generation, serial-to-parallel conversion, bit mapping, addition of training symbols for the linear channel estimation and the I/Q imbalance compensation, IFFT, cyclic prefix insertion[57] and parallel-to-serial conversion followed by up-sampling to the DAC sampling rate. Afterwards, samples for synchronization are added. Finally, the signal is digitally clipped to limit the PAPR and enable a constant signal power independent of the actual PAPR of the OFDM signal[58] after the DAC. The clipping ratio is set to achieve a PAPR of 10 dB[59]. The optimal bit loading for each DMT and OFDM subcarrier is determined by SNR measurements, using a training sequence consisting of 4-QAM modulated subcarriers. With the known SNR values of each subcarrier, calculated from the EVM values, and a given target BER, a bit loading optimum for each transmission case is determined. This is done by generating a lookup-table, using the analytical relation between the SNR, the BER and the modulation order of a white Gaussian noise limited system [64], [116]. A power loading is not applied in

[57]The length of the cyclic prefix is set to 16 sample. Various experiments with higher lengths showed no benefit.

[58]The peak-to-peak amplitude of the DAC is 500 mV and therefore the peak output power 0.0013 W considering a 50 Ω system. For an OFDM signal with a PAPR of 10 dB this results in an average output power of only -9 dBm.

[59]Simulations have shown that at these clipping levels only minor impairments for the used modulation orders exists as shown in Appendix A.8

the experiment[60]. Note there are more sophisticated approaches like Levin-Campello or Krongold to determine the optimal bit and power loading [71], [72]. Both were also tested but showed no further gain compared to the simple and fast lookup-table implementation.

For the DMT transmissions in the lower sub-band up to 256[61] subcarriers are available with a subcarrier spacing of $20 \cdot 10^9$ Hz$/256 = 7.8125 \cdot 10^6$ Hz if not otherwise stated[62]. For the OFDM transmissions the same subcarrier spacing is used but up to 512 subcarriers are available[63]. However, only a part of the DMT and OFDM subcarriers is generally modulated due to the bandwidth limitations of the lower and upper sub-band. This partial modulation provides also an amount of oversampling[64] which simplifies the DSP.

The receiver side DSP includes low-pass filtering, down-sampling, synchronization[65] and in case of OFDM the correction of the LO phase difference between the Tx and the Rx. This is realized with a simple 2x2 MIMO scheme in the time domain, utilizing the in-phase and quadrature phase of the incoming OFDM signal and the known synchronization sequence. Afterwards, the cyclic prefix is removed, the FFT applied and in case of OFDM the I/Q imbalance compensated. Finally, a single-tap linear equalizer is applied on each subcarrier, followed by demapping, parallel-to-serial conversion, BER and EVM estimation and the bit loading algorithm. The BER is estimated by error counting, if the number of errors at a subcarrier is sufficiently high. In case of only very few or no errors at a subcarrier, the BER is calculated from the relation of EVM (SNR), BER and modulation order. The exact determination is shown in Appendix A.8.

Note that the transmissions of the DMT and OFDM signals are realized block-wise with at least 300 symbols at each subcarrier[66]. The transmission of a single block is then repeated several times to have enough errors for a reliable BER estimation[67]. Furthermore, the first few transmissions of a block are only used to calculate the optimal bit loading, which commonly required a few iterations. This is indicated by the pointed arrow in Fig. 3.24.

[60] Simulations with a linear transfer system using DMT have shown a gain in BER, if an additional power loading is applied (Krongold and Levin-Campello algorithm). However, with the introduction of nonlinear elements like clipping or nonlinear components, this gain becomes significantly smaller or even a loss. In experiments no gain could be observed at all, if using the same algorithms.

[61] Several experiments with higher and lower numbers of subcarriers, at the same total bandwidth, have been performed during the investigation. Significant lower values than 256 for the lower sub-band resulted in a reduced performance due to the no more flat frequency response for each subcarrier and the resulting equalization errors. Higher values showed no further improvement.

[62] For the DMT transmissions in Section 3.5.3.3 up to 256 subcarrier are used with a subcarrier spacing of $25 \cdot 10^9$ Hz$/256 = 9.765625 \cdot 10^6$ Hz due to the different diplexer cross-over frequency.

[63] For the OFDM transmissions in Section 3.5.3.3 up to 512 subcarrier are used with a subcarrier spacing of $50 \cdot 10^9$ Hz$/512 = 9.765625 \cdot 10^6$ Hz due to the different diplexer cross-over frequency.

[64] For example, a DMT signal with a target bandwidth of 17.5 GHz has 223 of 255 subcarrier modulated

[65] cross-correlation with a known sequence

[66] For example, with a DMT signal bandwidth of 20 GHz, a FFT/IFFT size of 512 (i.e. 256 subcarrier), a cyclic prefix of 16 samples, 300 symbols for each subcarrier and a DAC sampling rate of 80 GS/s, each DMT block consists of 316800 samples plus sequences for channel estimation, synchronization and so on.

[67] at least 20 at each subcarrier

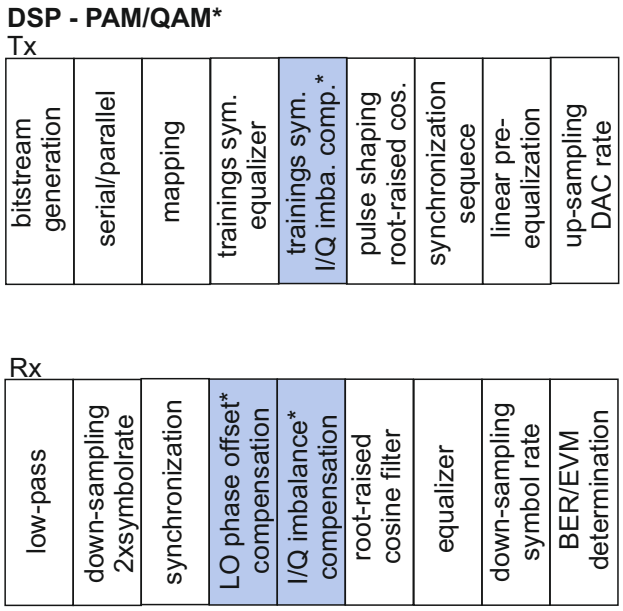

FIGURE 3.25: DSP for PAM and QAM. The highlighted blocks are only for QAM.

3.5.2.2 DSP for single-carrier modulation formats: PAM and QAM

For comparison with DMT and OFDM, PAM and single-carrier QAM are used to modulate the two separate sub-bands in the experiment. PAM is used for the lower sub-band as a baseband signal[68] and QAM for the upper sub-band. The up-converted QAM signal is generated by driving the I/Q mixer with the in-phase and quadrature parts of the complex QAM baseband signal. Like for OFDM, an I/Q imbalance compensation scheme is used for the QAM signal at the receiver. The required pulse shaping, using a raised-cosine filter characteristic (see Section 2.2.5.1), is accomplished by applying two root-raised-cosine filters at the Tx and the Rx. The Tx side filter provides a limitation of the PAM or QAM signal bandwidth and the Rx side filter an additional suppression of noise terms beyond the signal bandwidth. Furthermore, an additional linear pre-equalization of the DAC frequency response is applied at the Tx to ease the equalization effort at the Rx, which in turn improves the overall transmission performance for PAM and QAM.

In Fig. 3.25 the DSP for PAM and QAM is presented. The highlighted blocks mark the DSP which is only relevant for QAM. The transmitter side includes the bit-stream generation, serial-to-parallel conversion, mapping and the addition of training symbols for the linear channel estimation (refer to Appendix A.9) followed by training symbols for the I/Q imbalance compensation. Afterwards, the pulse shaping is applied, using a root-raised cosine (RRC) scheme with a roll-off factor of 0.1 (refer to Appendix A.1 for further details). Then the synchronization sequence is added, the DAC frequency response compensated, the signal up-sampled to the DAC sampling rate and a clipping applied, if the PAPR[69] is above 10 dB.

[68] In theory it is possible to modulate the whole band (0-45 GHz) with only PAM or DMT. However, the performance of the used DACs beyond 30 GHz is very disappointing, especially due to their roll-off.

[69] In contrast to DMT and OFDM, the PAPR of PAM and QAM is commonly below 10 dB even with the relatively strong pulse shaping (low roll-off factor).

The receiver side DSP includes low-pass filtering, down-sampling to twice the symbol rate, synchronization[70] and in case of QAM the correction of the LO phase difference between the Tx and the Rx, followed by the I/Q imbalance compensation. Afterwards, the Rx side RRC filter is applied and the signal equalized using a linear T/2 symbol-spaced minimum mean square error (MMSE) approach (refer to Appendix A.9). Finally the signal is down-sampled to the symbol rate and the BER and EVM are estimated.

Note that the DSP is performed separately for each sub-band (DMT/OFDM and PAM/QAM), since both are completely independent from each other.

3.5.2.3 I/Q imbalance compensation

The I/Q imbalance of the used I/Q mixers impairs the signal and must be compensated to improve the transmission performance. The first compensation is directly realized in hardware by using manual phase shifters and variable amplifiers in the IF branch of the I/Q mixers at the Tx and Rx side. The phase shifters and the amplifier gains are adjusted in an electrical btb OFDM transmission scenario, by minimizing the measured BER without any I/Q compensation in the DSP. This first adjustment (nearly) compensate the constant signal delay and average signal amplitude difference at the Tx side I and Q branches of the I/Q mixer and the constant signal delay at the Rx side I and Q branches of the I/Q mixer. The Rx side average signal amplitude difference is compensated by the DSP.

However, as shown in Section 3.3.3.5, the I/Q imbalance is frequency dependent and cannot be compensated fully by adjusting the delay and the overall gain in the I and Q branches. Therefore a digital compensation scheme is applied at the Rx side DSP. In the following the compensation for an OFDM signal is explained in detail and the difference for QAM is briefly discussed.

In Section 3.3.3.5 it was shown that each frequency component suffers from the crosstalk of the complex conjugate mirror frequency component, if I/Q imbalance is present. The impaired signal can be expressed as shown in Equations 3.25 and 3.26 by

$$\tilde{S}(k) = H_{\text{sys}}(k)S(k) + H_{\text{ct}}(k)S^*(-k)\ , \tag{3.37}$$

with

$$\begin{aligned} H_{\text{sys}}(k) &= \frac{H_{\text{I}}(k) + H_{\text{Q}}(k)}{2} \\ H_{\text{ct}}(k) &= \frac{H_{\text{I}}(k) - H_{\text{Q}}(k)}{2}\ . \end{aligned} \tag{3.38}$$

The function $H_{\text{sys}}(k)$ represent the normal system transfer characteristics and the function $H_{\text{ct}}(k)$ the crosstalk inducing transfer characteristic at the frequency k.

In case of OFDM each frequency component k represents a subcarrier. Therefore, Equation 3.25 can also be interpreted as subcarrier crosstalk induced by the I/Q imbalance, with $\tilde{S}(k)$ the received impaired subcarrier, $S(k)$ the unimpaired transmitted subcarrier, $S^*(-k)$ the transmitted complex conjugate subcarrier at the mirror frequency $-k$. The indices $-k, k$ denote subcarriers left and right from DC. The same equation can be found for the mirror subcarrier at $-k$ with

$$\tilde{S}(-k) = S(-k)H_{sys}(-k) + S^*(k)H_{ct}(-k)\ . \tag{3.39}$$

[70] cross correlation

Adapting Equation 3.39 for the complex conjugate of the mirror subcarrier and combining with Equation 3.37 leads to an equation system:

$$\begin{bmatrix} \tilde{S}(k) \\ \tilde{S}^*(-k) \end{bmatrix} = \begin{bmatrix} H_{sys}(k) & H_{ct}(k) \\ H^*_{ct}(-k) & H^*_{sys}(-k) \end{bmatrix} \begin{bmatrix} S(k) \\ S^*(-k) \end{bmatrix} , \tag{3.40}$$

or in matrix notation:

$$[\tilde{\boldsymbol{S}}] = [\boldsymbol{H}][\boldsymbol{S}] . \tag{3.41}$$

The coefficients of $[\boldsymbol{H}]$ can be estimated for each subcarrier by using training symbols[71] and a least square approach [117], with

$$[\boldsymbol{H}] = [\boldsymbol{S}_{\mathrm{Rx,t}}][\boldsymbol{S}^+_{\mathrm{Tx,t}}] = [\boldsymbol{S}_{\mathrm{Rx,t}}]\Big([\boldsymbol{S}_{\mathrm{Tx,t}}]^H[\boldsymbol{S}_{\mathrm{Tx,t}}]\Big)^{-1}[\boldsymbol{S}_{\mathrm{Tx}}]^H , \tag{3.42}$$

with the transmitted trainings symbols $S_{\mathrm{Tx,tr}}$ and the received trainings symbols $S_{\mathrm{Rx,tr}}$ given as

$$\begin{aligned} [\boldsymbol{S}_{\mathrm{Rx,t}}] &= \begin{bmatrix} S_{\mathrm{Rx,tr}}(k,1) & S_{\mathrm{Rx,tr}}(k,2) & \dots & S_{\mathrm{Rx,tr}}(k,l) \\ S^*_{\mathrm{Rx,tr}}(-k,1) & S^*_{\mathrm{Rx,tr}}(-k,2) & \dots & S^*_{\mathrm{Rx,tr}}(-k,l) \end{bmatrix}_{2,l} \\ [\boldsymbol{S}_{\mathrm{Tx,t}}] &= \begin{bmatrix} S_{\mathrm{Tx,tr}}(k,1) & S_{\mathrm{Tx,tr}}(k,2) & \dots & S_{\mathrm{Tx,tr}}(k,l) \\ S^*_{\mathrm{Tx,tr}}(-k,1) & S^*_{\mathrm{Tx,tr}}(-k,2) & \dots & S^*_{\mathrm{Tx,tr}}(-k,l) \end{bmatrix}_{2,l} . \end{aligned} \tag{3.43}$$

Here $^+$ denotes the pseudo-inverse operation[72], ^{H} the conjugate transpose, $^{-1}$ the matrix inverse and l the number of training symbols.

Finally the received signal can be corrected subcarrier-wise using the estimated coefficients of $[\boldsymbol{H}]$ by

$$[\boldsymbol{S}] = [\boldsymbol{H}^+][\tilde{\boldsymbol{S}}] . \tag{3.44}$$

In Section 3.5.3.7 the impact of the I/Q imbalance and the compensation are demonstrated. Note that in the experiments the Tx and the Rx I/Q mixer cause impairments due to their I/Q imbalance. However, the discussed compensation scheme assumes only a single I/Q imbalance source, which may result in slight errors for the compensation[73].

Since the compensation is realized in the frequency domain, it can easily be applied on the individual subcarriers of an OFDM signal. For the single-carrier QAM signal in the upper sub-band a similar approach is possible, using an overlap-save frequency domain equalizer (FDE) [118], [119]. In Fig. 3.26 the principle is shown. First, the QAM time domain signal consisting of n samples is separated into n/m blocks, each of length $m + 2k$, with k the overlap interval. Each block is then transformed into the frequency domain using the FFT and its I/Q imbalance is compensated using Equation 3.44. The exact parameter of $[\boldsymbol{H}]$ are estimated with the help of an OFDM like trainings sequence. Then each block is transformed back into the time domain using the IFFT. Finally samples at the beginning and at the end of each block are cropped to take the cyclic nature of the FFT/IFFT and the ISI into account. Afterwards, the blocks are combined. The optimal size of m and k depends on the I/Q imbalance properties. In the simulations and experiments it is determined by varying both parameters in respect to the BER.

[71] The training symbols consists of 100 random 4-QAM modulated OFDM symbols at each subcarrier and the estimation of $\boldsymbol{H}$ is done for every data block for practical reasons.

[72] The calculation of the pseudo-inverse is done with the Matlab *pinv* function, which provide significantly better results if the matrix is ill conditioned.

[73] A simulative investigation of this aspect showed only a minimal impact on the compensation.

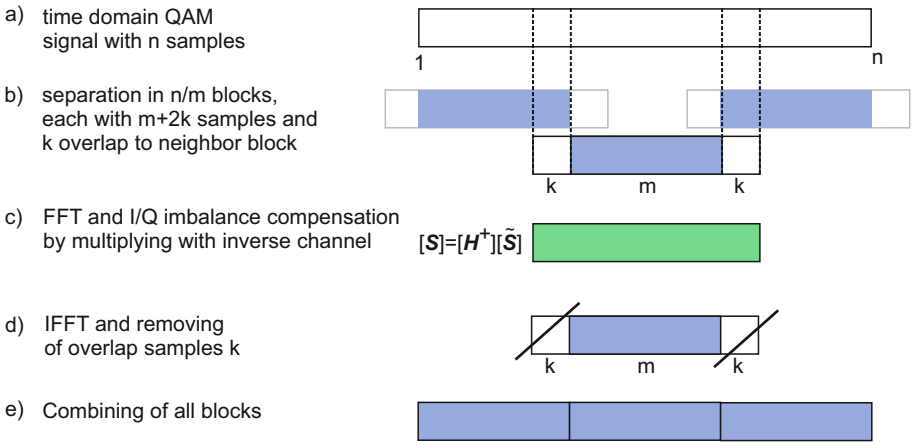

FIGURE 3.26: I/Q imbalance compensation of single carrier QAM in the upper sub-band.

3.5.3 Experimental results for bandwidth extension approach

The system aspects investigated for the bandwidth extension approach are the general transmission performance and distance, the modulation formats, the influence of the combiner and receiver, the I/Q mixer nonlinearity and I/Q imbalance and the degradation of the SNR. The results have been published in [33], [95]–[98].

3.5.3.1 Transmission performance

For the evaluation of the general transmission performance two sub-bands have been transmitted, with DMT in the lower sub-band (baseband) and OFDM in the upper sub-band (passband). The experimental setup shown in Fig. 3.23 is used for the transmissions. In Fig. 3.27 (a) the achieved (gross) data rates and the applied bit loading are shown for the optical btb case (i.e. 10 m SSMF). The lower x-axis shows the actual frequency allocation of both signals and the LO (green dotted arrow at 30 GHz). The upper x-axis shows the corresponding subcarrier number[74] . A total gross data rate of 182.6 Gb/s is achieved, with 84.7 Gb/s for the DMT in the baseband and 97.9 Gb/s for the OFDM in the passband. For DMT with a bandwidth of 17.5 GHz, 223/256 subcarriers are modulated. The QAM bit loading of the subcarriers varies between 2 and 7 bit with the higher values at the lower frequencies. The drop in bit loading can primary be attributed to the DAC and the diplexer frequency behavior.

OFDM has a total signal bandwidth of 24 GHz, located between 18.5 and 42.5 GHz, with 310/512 subcarriers modulated. The QAM bit loading of each subcarrier varies between 2 and 6 bit with the higher values close to the LO at 30 GHz. The drop in bit loading to both sides of the LO can be attributed to the frequency behavior of the upper sub-band, which is dominated by DACs, the diplexer, the I/Q modulators and the optical modulator. Interestingly, the highest bit loading is not directly around the LO at 30 GHz, but instead more towards the lower frequency side. This can be attributed to the frequency behavior of the optical modulator. Note that the in-phase and quadrature OFDM signals, i.e. the Tx side I/Q modulator driving signals, have both a bandwidth of 12.5 GHz. There is also a modulation gap at 18 GHz between the

[74]Note that the subcarrier spacing for DMT and OFDM is equal. Both signals are also completely independent, thus the shown continuous subcarriers numbers are only a visual support.

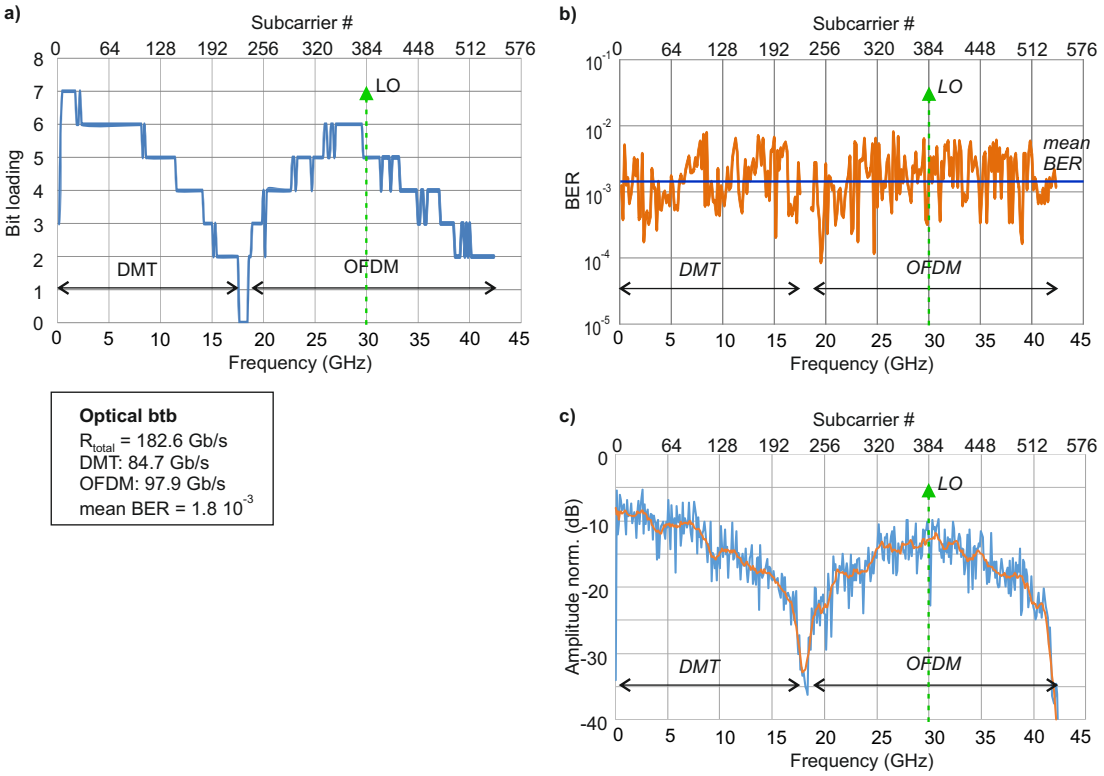

FIGURE 3.27: (a) Bit loading for DMT in the lower sub-band and OFDM in the upper sub-band for optical btb, (b) BER of each subcarrier, (c) combined spectrum of DMT and OFDM after A/D conversion.

DMT and the OFDM signal. At these frequencies no modulation is possible due to the diplexer characteristics[75].

In Fig. 3.27 (b) the measured BER of each subcarrier is shown, with values between $1 \cdot 10^{-4}$ and $1 \cdot 10^{-2}$. The mean BER is $1.8 \cdot 10^{-3}$, which is well below the 7% HD-FEC limit.

In Fig. 3.27 (c) the signal spectrum after A/D conversion is shown. The spectrum is subsequently generated by digitally combining the Rx DMT signal with the Rx OFDM signal[76]. Both sub-bands experience a relatively strong attenuation due to the system frequency response. For DMT up to 15 dB can be observed and for OFDM up to 10 dB. The orange curve in Fig. 3.27 (c) shows a windowed average value of the spectrum, which represents the total system frequency response, apart from frequencies close to 18 GHz.

3.5.3.2 Transmission distance

The maximum transmission distance using the bandwidth extension approach is limited by the influence of the chromatic dispersion due to the transmission at 1550 nm. Increasing the total signal bandwidth by using the bandwidth extension approach consequently leads to a stronger impact of the chromatic dispersion and hence, shorter

[75] The cross-over frequency of the used diplexer is ~18 GHz

[76] The Rx in-phase and quadrature OFDM signals are A/D converted and then ideally up-converted. This is also the reason why no LO can be observed

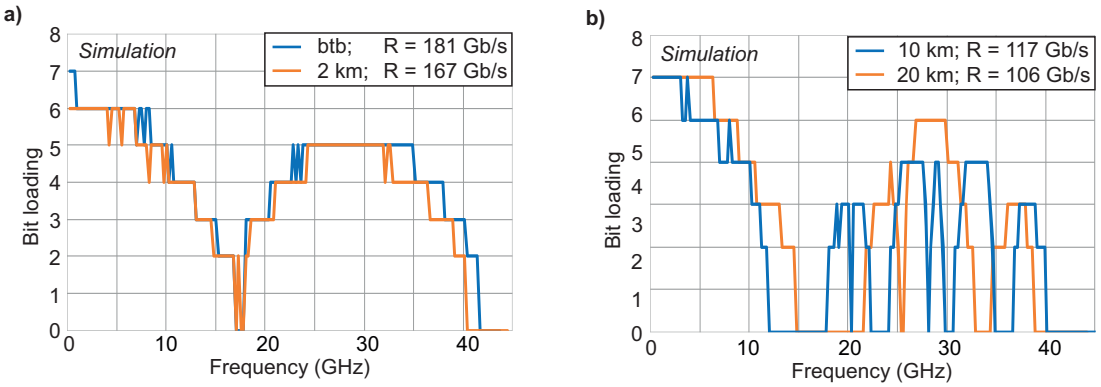

FIGURE 3.28: Simulative transmission performance of DMT and OFDM for different distances at 1550 nm over SSMF.

distances can be bridged with IM/DD. The difference in group-velocity at this wavelength over the whole optical signal spectrum results in the typical power fading effect after direct detection [37], [38]. In case of DMT and OFDM several subcarriers are impaired, depending on the actual transmission distance. As a result, their modulation orders have to be decreased or they have to be turned off.

The influence of the transmission distance is simulatively and experimentally investigated. The used simulation environment has been shown in Fig. 3.4 (Section 3.4). At first the simulation results are discussed. In Fig. 3.28 (a,b) the transmission performance of DMT and OFDM, i.e. the available bit loading and achievable data rates, for different transmission distances are shown for a mean target BER below the 7% HD-FEC limit. The blue curve in Fig. 3.28 (a) represents the optical btb case. It corresponds well to the experimental btb transmission case from the previous section. At 2 km distance (orange curve in Fig. 3.28 (a)) subcarriers at higher frequencies start to get impaired and their modulation order has to be decreased, with no modulation possible at all beyond 40 GHz. Hence, the available data rate at the HD-FEC limit drops from 181 to 167 Gb/s. At 10 km, shown by the blue curve in Fig. 3.28 (b), a stronger degradation can be observed. At 20 km (orange curve in Fig. 3.28 (b)) this degradation is further increased, resulting in a data rate of only 106 Gb/s. However, there are always unaffected subcarriers due to the periodic behavior of the fading pattern as can be observed in Fig. 3.28 (b). This enables a transmission even at longer distances at a reduced data rate. Note that for single-carrier modulation formats like PAM and single-carrier QAM no transmission would be possible at these signal bandwidths and distances.

In the experiments two schemes are tested to minimize the influence of the chromatic dispersion. First, the use of an optical filter directly after the optical modulator to suppress one side band and second, the use of a dispersion compensating fiber (DCF). The single sideband (SSB) filter suppresses one optical sideband of the signal, thus avoiding the power fading effect at the detector. The used SSB filter (Santec OFT-950) has a variable filter bandwidth and center frequency which enabled the exact adaptation to the signal spectrum. However, there are two issues. First, the suppression of one sideband removes half of the relevant signal power (without considering the optical carrier) which in turn decreases the electrical SNR after detection. This is especially critical for short-range IM/DD systems due to the limited fiber launch power and the lack of optical amplifiers. The second issue is the finite slope of the filter, which in turn results in a trade-off for the optimal filter center frequency. Assuming the upper

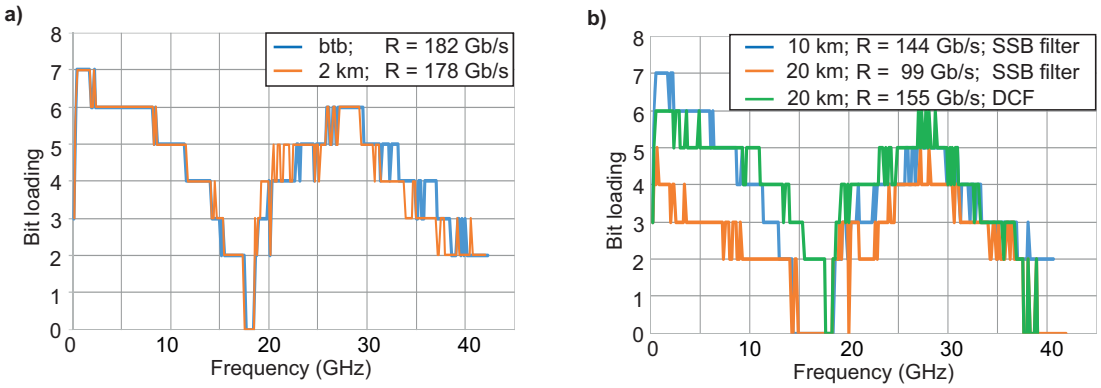

FIGURE 3.29: Experimental transmission performance of DMT and OFDM for different distances at 1550 nm over SSMF.

(higher frequency) optical sideband is suppressed, then a filter center frequency set too low would result in the unwanted suppression of the optical carrier and part of the lower sideband as well. If the filter center frequency is set too high, not enough of the upper sideband would be suppressed and dispersion degrades the signal. During the experiments the filter is adjusted with respect to minimize the BER for 10 and 20 km of SSMF separately.

In Fig. 3.29 (a) the experimental performance for DMT and OFDM for 0 and 2 km is shown (target BER below 7% HD-FEC limit). Similarly to the simulations, only a slight drop in data rate can be observed for 2 km of SSMF, with decreased modulation orders at high frequency subcarriers. For 10 and 20 km of SSMF the transmission experiment is adapted by an additional SSB filter after the optical modulator. To compensate for the additional loss in optical power due to the SSB filter and the longer transmission distance, the EDFA amplification is also adjusted. The blue and orange curves in Fig. 3.29 (b) show the results for 10 and 20 km, respectively. For 10 km an overall drop in the bit loading can be observed, resulting in a data rate of 144 Gb/s. Especially at frequencies close to 18 GHz, where already only low modulation orders are feasible, no modulation is possible any more. This can be attributed to the overall decrease in SNR due to the additional optical amplification. For 20 km this effect increases, resulting in a further drop in data rate. However, there is also a relative strong drop in bit loading at frequencies below 12 GHz compared to the 10 km case. This is possibly caused by a misalignment of the SSB filter.

For comparison, the performance with an additional DCF (4 km) is shown by the green curve in Fig. 3.29 (b). The DCF has a dispersion coefficient of $-100\text{ps}/(\text{km}\cdot\text{nm})$ which slightly over-compensates the 20 km of SSMF dispersion ($-18\text{ps}/(\text{km}\cdot\text{nm})$). As expected the bit loading is closer to the btb scenario, with a slight overall drop due to the SNR degradation caused by the required additional optical amplification and the non optimal dispersion compensation. The achieved total data rate is 155 Gb/s.

At distances beyond a few km, the proposed wideband signals (40 GHz) suffer significantly due to the chromatic dispersion, if transmitted at 1500 nm. The use of optical SSB filters improves the performance but also degrades the overall SNR. A more feasible approach for short range systems is the transmission at the O-band (1300 nm) where the chromatic dispersion effect is reduced, for example as shown in [35] for a signal with 56 GHz bandwidth.

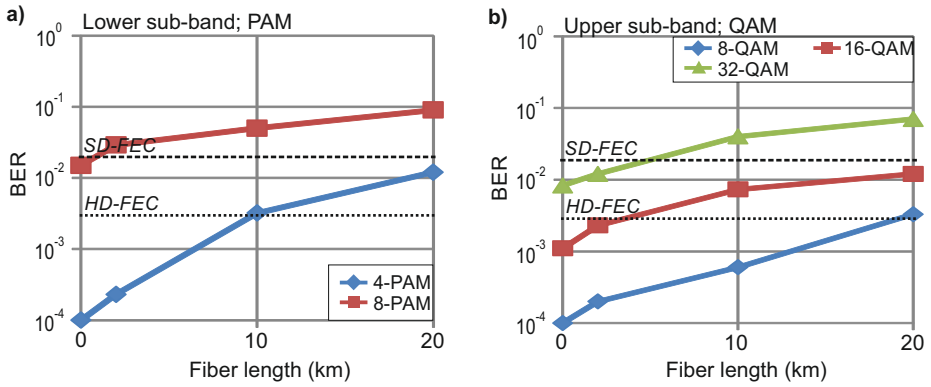

FIGURE 3.30: Scenario #1: (a) measured BERs for PAM in the lower sub-band (0-21 GHz) and (b) QAM in the upper sub-band (21-39 GHz) for different SSMF lengths. (The 7% HD and 20% SD-FEC BER limits are marked.)

3.5.3.3 Modulation formats

In this section the performance of single- and multi-carrier modulation formats is investigated for the bandwidth extension approach. In detail these are DMT and PAM for the lower sub-band and OFDM and QAM for the upper sub-band. In the following the transmission of PAM and QAM is noted as scenario #1 and DMT and OFDM as scenario #2. For PAM a fixed symbol rate of 40 GBd with modulation orders of 2, 4 and 8 and for QAM a symbol rate of 16 GBd with modulation orders of 8, 16 and 32 are chosen. The roll-off factor of the Tx-side RRC filter is 0.1, resulting in a bandwidth of ~21 GHz for the PAM signal in the lower sub-band and ~18 GHz for the QAM signal in the upper sub-band[77]. For DMT and OFDM exatly the same bandwidth assignments are used by adjusting the number of modulated subcarriers. The experimental setup from Fig. 3.23 is used, but with another diplexer for the signal combining at the Tx. Its cross-over frequency is 21 GHz compared to 18 GHz as used for the experiments in Section 3.5.3.2 and 3.5.3.1. For this experiment, the performance at the HD-FEC BER limit ($3.8 \cdot 10^{-3}$) and at the higher SD-FEC BER limit ($2.7 \cdot 10^{-2}$) is marked. For transmission lengths of 10 and 20 km an optical SSB filter after the optical modulator is used like in the previous experiment.

At first the performance of scenario #1 with the single-carrier formats is evaluated. Fig. 3.30 shows the measured BERs for 40 GBd of 4 and 8-PAM in the lower sub-band and 16 GBd of 8, 16 and 32-QAM in the upper sub-band for different lengths of optical fiber. The following can be observed for the lower sub-band at 0-21 GHz: 4-PAM is possible for btb, 2 and 10 km with HD-FEC; 8-PAM is only possible for btb with SD-FEC. For the upper band at 21-39 GHz the observations are: 8-QAM is possible at all fiber lengths with HD-FEC; 16-QAM at btb and 2 km with HD-FEC; and 32-QAM allows only btb transmission using SD-FEC. The total transmission rates for scenario #1 below the HD-FEC limit are thereby 144, 144, 128 and 88 Gb/s for btb, 2, 10 and 20 km of SSMF, respectively. Below the SD-FEC limit they are 200, 160, 144 and 144 Gb/s for btb, 2, 10 and 20 km of SSMF, respectively.

For the scenario #2 (DMT and OFDM), the BERs for different data rates[78] and transmission distances are shown in Fig. 3.31. The measured values are then interpolated,

[77] between 21 and 39 GHz with the LO at 30 GHz

[78] An optimal bit loading was used for eac target BER.

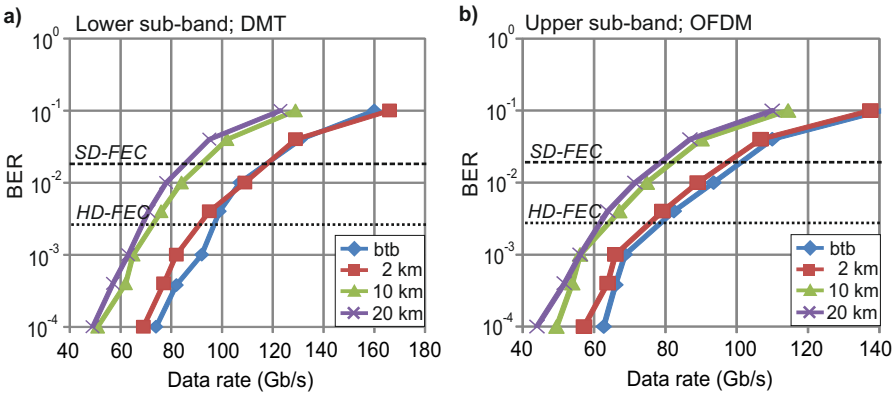

FIGURE 3.31: Scenario #2: (a) Relation of data rate and BERs for DMT in the lower sub-band (0-21 GHz) and (b) OFDM in the upper sub-band (21-39 GHz) for different SSMF lengths. (The 7% HD and 20% SD-FEC BER limits are marked.)

resulting in the shown curves. Now the transmission rates at the HD and SD-FEC limit can be estimated. For the HD-FEC case 179, 171, 141 and 134 Gb/s and for the SD-FEC case 224, 219, 175 and 167 Gb/s for btb, 2, 10 and 20 km of SSMF are possible, respectively. The further drop in performance for 10 and 20 km compared to btb and 2 km can be attributed to the SSB filter issues as explained in Section 3.5.3.2. The slight difference in data rate compared to the results shown in Section 3.5.3.2 and 3.5.3.1 can be explained by the different frequency allocation of both sub-bands.

In order to compare scenario #1 and scenario #2, the BERs of the DMT and OFDM transmission at the data rates of the PAM and QAM transmission are determined. For example, the 40 GBd 4-PAM transmission with data rate of 80 Gb/s at 2 km of SSMF has a BER of $2 \cdot 10^{-4}$ (Fig. 3.30 (a), blue curve). The related DMT transmission at 80 Gb/s and 2 km has a BER of $8 \cdot 10^{-4}$, which can be extracted from the interpolated red curve shown in Fig. 3.31 (a). For the lower sub-band this is done for 40 GBd 4-PAM and 8-PAM (80 and 120 Gb/s), with the results shown in Fig. 3.32. As it can be observed, the PAM transmission performs slightly better compared to DMT, both for 80 Gb/s and for 120 Gb/s data rate.

For the upper sub-band with 16 GBd 16 and 32-QAM (64 and 80 Gb/s) the results

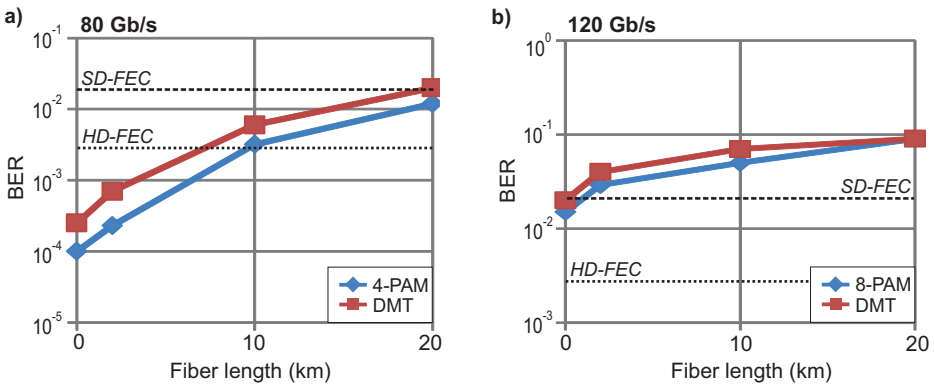

FIGURE 3.32: Measured BERs for PAM and DMT at 80 and 120 Gb/s for the lower sub-band at different fiber lengths.

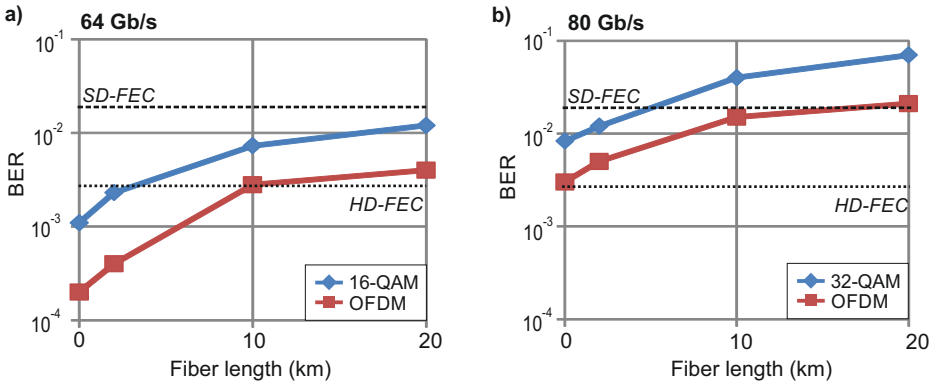

FIGURE 3.33: Measured BERs for QAM and OFDM at 64 and 80 Gb/s for the upper sub-band at different fiber lengths.

are shown in Fig. 3.33. In contrast to the lower sub-band case, the multi-carrier format performs better compared to the single-carrier format. This is possibly caused by two reasons: first, the system frequency response suits much better to the OFDM signal due to the easy adaptation in terms of subcarrier bit loading. For QAM the drop in the frequency response results in a high equalization effort at the Rx, thus in a noise enhancement [25]. Second, the characteristics of the electrical I/Q mixer at the Tx and the Rx causes further degradations like the frequency dependent I/Q imbalance or the limited port isolation. It seems that both penalties can be addressed much better with OFDM, which results in fewer penalties compared to QAM. On the other hand, DMT and OFDM have a worse PAPR than PAM and single-carrier QAM, which leads to a drop in sensitivity in IM/DD systems. However, the sharp filter roll-off chosen for PAM and QAM to maximize the bandwidth utilization and the digital clipping applied for DMT and OFDM result in similar PAPRs, as is shown in Appendix A.2.

3.5.3.4 Combiner type

There are two possibilities for the combiner and splitter realization in the experimental setup, a filter approach with a frequency dependent behavior and a resistive approach with a frequency independent behavior. The task of the Tx-side combiner is merging the lower and upper sub-band signals, whereas the Rx-side splitter divides the whole signal into two sub-bands. The requirements for the devices are a broadband behavior to avoid unnecessary losses, a low insertion loss and a high port isolation. The latter is especially important since the other components in each sub-band are adapted to a fixed frequency range and present an impedance mismatch outside their operation range.

The resistive approach offers the easiest implementation, a very small size and a very broadband behavior compared to other types [120]. Unfortunately it also has the highest insertion loss and an inherently poor port isolation. The inherently poor isolation of the resistive combiner can result in severe signal distortions. This can be understood if the signal flow at the Tx side combiner is considered as illustrated in Fig. 3.34 (a). Here the green arrows indicate the desired signal flow and the blue and red pointed arrows the undesired signal flow of the lower and upper sub-band, respectively. For the lower sub-band the following occurs: first, the signal is equally distributed to port #2 and 3 of the combiner, where port #3 is the desired one. Second, at port #2 the signal faces the RF port of the I/Q mixer, which is is naturally not

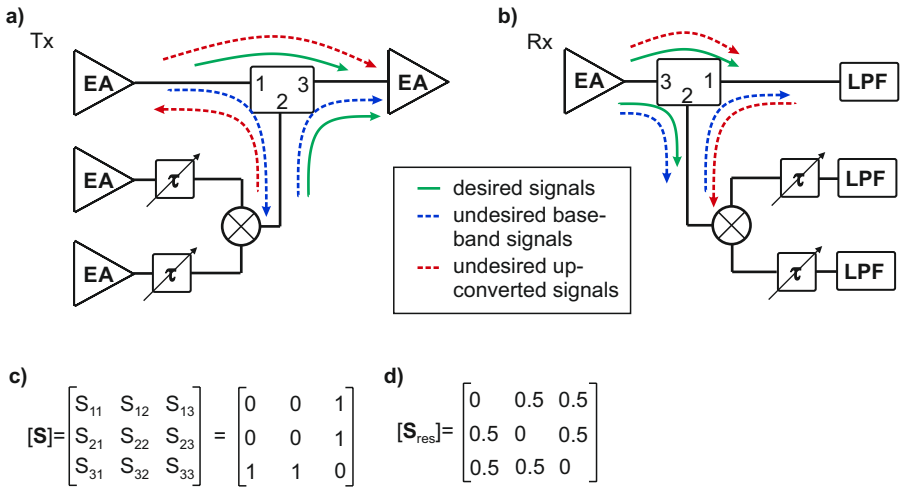

FIGURE 3.34: (a) Combiner at the Tx side with desired signal flow (green arrow), and undesired signal components. The blue pointed arrow indicates the undesired baseband signal flow and the red dotted arrow undesired up-converted signal flow. (b) Splitter at the Rx side with desired signal flow, and undesired signal flow. (c) Ideal scattering parameter of a signal combiner. (d) S-parameter of the resistive coupler (6 dB) used in the experiments.

matched to the frequency range of the baseband signal, thus the signal is partly reflected. Third, after going to the combiner again, equal parts of the delayed baseband signal are present at port #1 and #3. At port #3 the delayed signal overlaps with the desired signal and depending on the return loss at the mixer RF port and the actual insertion loss of the combiner, distortions can occur[79]. To combat this effect, additional attenuators can be placed in front of the combiner, since the reflected signal is attenuated twice compared to the desired signal. However, this also requires additional amplification to meet the driving voltage requirements of the optical modulator. At the Rx side, a similar effect can be observed for the splitter as shown in Fig. 3.34 (b), with the LPF and the I/Q mixer causing reflections of the undesired signals.

This behavior can be also be described using the scattering parameters of the device. The ideal characteristic of a combiner/splitter is illustrated in Fig. 3.34 (c) with no conversion loss between ports 1/2 and 3 and perfect isolation between ports 1 and 2. For the resistive device these values change as illustrated in Fig. 3.34 (d), due to its inherent loss. Note that other values are possible depending on the exact realization.

The second option for the combiner/splitter are frequency selective devices like diplexers, since the two sub-bands signals allocate different frequencies in the bandwidth extension approach. These devices consist principally of two filters as shown in Fig. 3.35 (a) and are commonly applied in radio transmitters and receivers [121]. The only downside of these devices for the discussed bandwidth extension approach is the trade-off between the isolation of the lower and upper sub-band ports (port 1 and 2 in Fig. 3.35 (a)) and the attenuation at the crossover frequency. A high isolation requires a sufficient frequency gap between both ports, since the filter slope is finite. On the other hand, a low attenuation at the crossover frequency requires a small or even no

[79]There is also the undesired signal part at port #1 which is directed back to the amplifier in the lower sub-band branch. This is not desirable since amplifiers are sensitive for reflections. However, no reflections should occur here, since the amplifier output return loss is very small in the operation band.

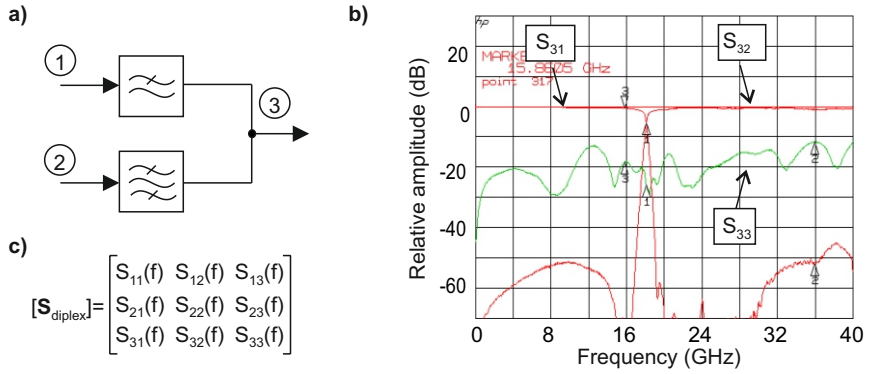

FIGURE 3.35: (a) Diplexer principle with low-pass filter at port 1, band-pass filter at port 2 and ideal combining at port 3.(b) S-parameter of the used device with crossover frequency at 18 GHz. The curves are the insertion losses of port 1/2 to port 3 (S_{31}, S_{32}) and the return loss of port 3 (S_{33}). (c) Frequency dependent S-parameter matrix of a diplexer.

frequency gap[80]. In Fig. 3.35 (b) the transfer characteristics of one of the used diplexers is shown. The device has a crossover frequency of 18 GHz and an attenuation of 6 dB at this point. The transfer characteristic between ports 1 and 3, which can be expressed with the S-parameter S_{31}[81] shows nearly no attenuation up to the cross-over frequency, a drop of ~30 dB/GHz at the cross-over frequency and an attenuation of 50 dB beyond the cross-over frequency. The behavior of the transfer characteristic between ports 2 and 3 (S_{32}) is similar with nearly no attenuation beyond the cross-over frequency. The green curve represents the return loss of the combining port (3) and shows acceptable values with a slight increase up to higher frequencies. The isolation between ports 1 and 2 is not provided by the data sheet. However, it can be expected that there is a peak around the crossover frequency (i.e. poor isolation) due to the inherent limitations of the device.

To test the influence of the combiner, two different transmission experiments were performed. The results are presented in Fig. 3.36. In the first experiment, a diplexer is used for the Tx signal combining[82] and in the second experiment a resistive combiner. To combat reflections in the resistive approach, 6 dB additional attenuation are placed in front of both Tx combiner ports. The additional attenuation is compensated by adapting the electrical amplifier gain at the Tx side. In Fig. 3.36 the achieved bit loading and data rate at the HD-FEC BER limit is shown for different lengths of SSMF. Starting with the btb case (Fig. 3.36 (a)), the performance of the diplexer-based combiner is slightly better compared to the resistive approach. However, at the diplexer crossover frequency at 18 GHz the bit loading of both schemes differs significantly. This behavior is caused by the drop in frequency response of the diplexer around its crossover frequency, which decreases the SNR at neighboring subcarriers. Since the resistive combiner has a flat response over the whole frequency range, a significantly better bit-loading is possible at this point. At 2 km this behavior is generally maintained as it can be observed in Fig. 3.36 (a). For 10 km (Fig. 3.36 (c)) both schemes offer the same performance in terms of achievable data rate and at 20 km (Fig. 3.36 (d))

[80]There are further issues related the to impedance matching of the combining/splitting port, if there is no frequency gap.

[81]The scattering parameters of diplexers are reciprocal.

[82]The device from the experiments (Sections 3.5.3.1 and 3.5.3.2)

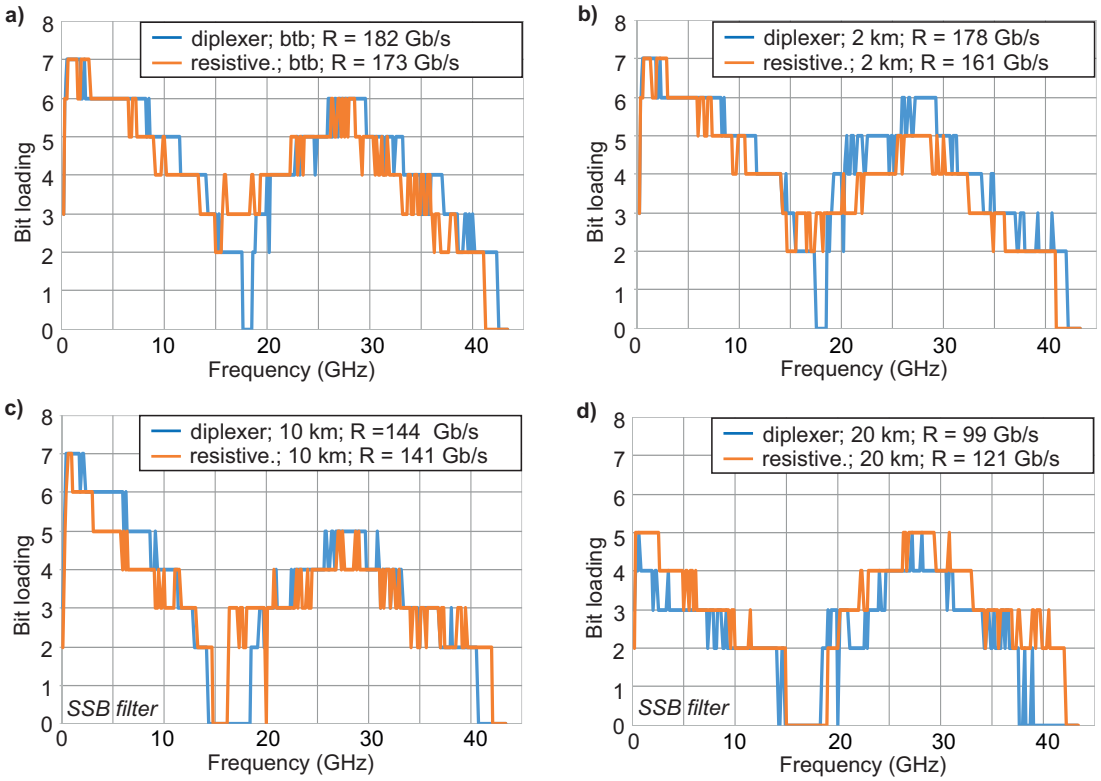

FIGURE 3.36: DMT and OFDM bit loading for resistive and diplexer combiner approach for different transmission distances: (a) btb, (b) 2 km, (c) 10 km and (d) 20 km.

a better behavior of the resistive scheme can be observed[83]. However, as already mentioned in Section 3.5.3.2, the 20 km diplexer based transmission shows an unexpectedly poor performance, which makes a comparison difficult[84]. In conclusion, the resistive combiner approach performs quite good, especially if the additional electrical amplification is considered. The worse behavior of the diplexer at its cross-over frequency and at frequencies beyond 40 GHz[85] degrade its generally superior characteristics in terms of insertion loss and reflections. However, the used diplexers are not specially designed for the bandwidth extension approach and it can be assumed that a better adapted device performs at least as well as the resistive combiner.

3.5.3.5 Receiver type

Most of the system experiments are performed with a wideband photodetector (3 dB bandwidth 50 GHz) in combination with an EDFA to provide the necessary optical power and an optical filter (1 nm) to minimize the EDFA noise. The available photoreceiver, (Finisar, XPRV2021A) has a smaller 3 dB bandwidth (37 GHz) and would additionally limit the performance. A comparison of the transmission performance for both types is given in Fig. 3.37, illustrated by the achievable bit loading and data rate for the 2 km SSMF transmission.

[83] Like in the experiments above, an optical SSB filter is used after the MZM for 10 and 20 km experiments.

[84] The reason is most likely an error in the measurements setup.

[85] Observed in the experiments

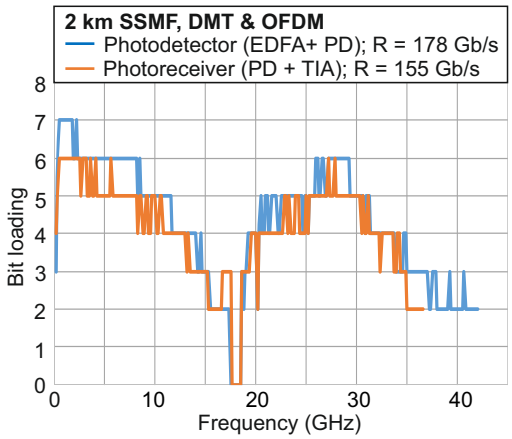

FIGURE 3.37: DMT and OFDM bit loading for two receiver types and 2 km of SSMF: a wideband photodetector (i.e. EDFA+BPF+PD) and a photoreceiver (i.e. *pin*-PD + TIA).

The photodetector approach performs slightly better at lower frequencies due to the typically lower noise of optical amplification vs. electrical amplification. At higher frequencies a clear gain in performance can be observed, which is caused by the higher photodetector bandwidth. Note that the optical power at the photoreceiver is 0.5 dBm for the experiment, which is below the receiver saturation power of 3 dBm. The optical power at the photodetector is set to 10 dBm, which corresponds to the manufacture reference.

In section 2.2.3 it was shown that the thermal noise of the receiver (*pin*-PD + TIA) is the primary noise source in the investigated VCSEL transmission experiment in Chapter 4.5, besides the shot noise and the RIN. The same statement is valid for this system experiment with the photoreceiver, with less influence of the RIN due to the external CW laser. In case of the photodetector the signal noise is dominated by the amplified spontaneous emission (ASE) of the EDFA and the photodiode shot noise. As can be observed, the achievable bitloading at frequencies below the photoreceiver cut-off frequency of 37 GHz is very similar for both cases. Only at higher frequencies a clear drop is visible. Hence, it can be assumed that a photoreceiver with adequate bandwidth will perform similar to the photodetector[86]. Of cause in practical systems a photoreceiver with higher bandwidths would be desired because of lower costs and the integration into small form-factor devices.

3.5.3.6 I/Q mixer nonlinearity

The mixer nonlinearities limit the upper input power into the I/Q mixer at the Tx and the Rx side. Higher input powers can be desirable to ease the signal amplification effort and to limit the relative power of the LO compared to the signal at the output port of the mixer. The first aspect, i.e. the easier amplification effort, is related to the typically simpler amplification of baseband signals compared to the up-converted signal. The second aspect, i.e. the relative power of the LO vs. the signal, is related to the LO-RF/IF isolation and the maximum total signal power after the mixer.

To determine the optimal I/Q mixer input power for the bandwidth extension approach, an electrical btb transmission of the upper sub-band has been realized with

[86]Optical amplification is expensive and bulky compared to electrical amplification and thus avoided for short-range systems. However, it offers a superior performance in terms of noise.

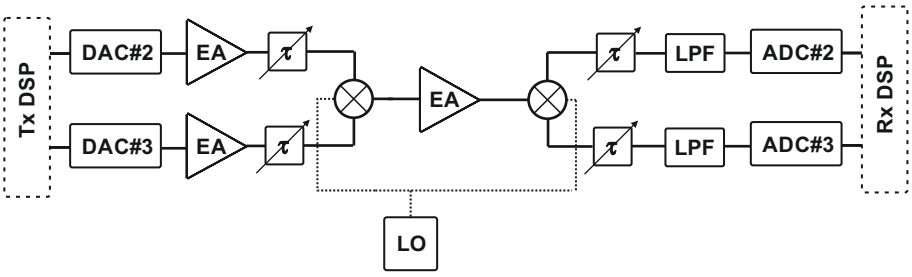

FIGURE 3.38: Experimental setup for I/Q mixer nonlinearity investigation.

its experimental setup shown in Fig. 3.38. It is the same setup as in the previous experiments without the optical part and without the baseband path. The signal is an OFDM signal with a bandwidth of 20 GHz (20-40 GHz signal allocation) and the LO at 30 GHz. The input power of the Tx side I/Q mixer is swept by controlling the Tx side amplifiers (after the DACs). The input power of the Rx side I/Q mixer is set constant with a power level clear below the nonlinear behavior. Additionally to the experiment, a simulation has been performed using the same setup. The simulation uses the DAC model and the I/Q mixer model the from Section 3.4, but only for the Tx side. The down-conversion is assumed ideal. Furthermore, a noise loading is applied after the Tx I/Q mixer to address the inevitable noise floor of experiments.

The results are illustrated in Fig. 3.39 (a) for the experiment (blue curve) and also for the simulation (orange curve). In the experiment and in the simulation the BER improves up to a mixer input power[87] of ~-3 dBm and degrades afterwards. At lower input power levels the transmission performance is limited by the constant noise loading in case of the simulation and by the noisy components after the Tx I/Q mixer, i.e. amplifier, Rx I/Q mixer and ADC, in case of the experiment. At signal input power levels beyond ~-3 dBm the degrading influence of the mixer nonlinearities is visible.

The P1dB of the I/Q mixer is 8 dBm[88] and it can be expected that at input powers

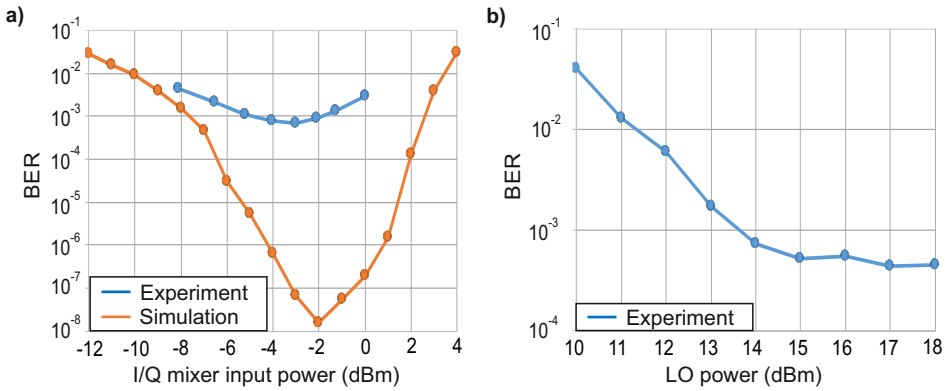

FIGURE 3.39: (a) Experimental and simulative OFDM performance at a fixed bit loading for different Tx I/Q mixer input power levels. (b) Experimental OFDM performance at a fixed bit loading for different Tx I/Q mixer LO power levels.

[87] Input power at the I or Q branch of the I/Q mixer.
[88] input power

close to this value signal degradations due to the nonlinearities occur. However, nonlinear distortion can already be observed at significantly lower input powers (-3 dBm vs. 8 dBm). This can be explained by the following consideration: The determination of the P1dB is done with a single sine waveform, which has a PAPR of 3 dB. The PAPR of the OFDM is 10 dB in all experiments and simulations[89]. This results in a significant difference in the peak power between the sine signal and the OFDM signal, if both have the same average input power. Since the signal peak values are relevant for the nonlinear distortions, OFDM behaves much worse at already low average input powers. Experiments with QAM have shown a similar effect. However the impact of the I/Q mixer nonlinearities is significantly lower when using the same input power compared to OFDM. This is due to QAM's typically lower PAPR. Note that the optimal signal input power for QAM at the higher sub-band differs compared to the OFDM case and was experimentally evaluated too.

The influence of the LO power on the BER is shown in Fig. 3.39 (b). For the experiment[90] only the LO power of the Tx side I/Q mixer is swept, with the Rx side I/Q mixer LO power set constant to 18 dBm. Up to a power of 15 dBm an improvement can be observed, with an error floor at higher power levels. This behavior is expected since higher LO powers result in a more and more ideal switching behavior of the mixer diodes, thus limiting the nonlinear behavior of the mixer.

For the bandwidth extension approach it is required to limit the I/Q mixer nonlinearities to avoid signal impairments. This can be done by choosing the I/Q mixers input powers accordingly, with respect to the target BER (FEC-limit) and other noise sources. For example, the measurements above have shown no further improvement in BER at input powers beyond -3 dBm. Therefore, a good choice of I/Q mixer input powers for this setup is between -6 and -3 dBm. Note that these values are only valid for OFDM. It can be expected that other modulation formats[91] and other signal bandwidth allocations result in different values.

3.5.3.7 I/Q imbalance

The used I/Q mixer has a frequency dependent I/Q imbalance, which results in a cross talk of mirror frequencies around the LO and thus to SNR degradations (refer to Section 3.3.3.5 for details). The exact degradation can be estimated by determining the subcarrier SNR values for OFDM in the upper sub-band. This is illustrated in Fig. 3.40 (a,b) for the optical btb transmission[92] presented in Section 3.5.3.1. The blue curve in Fig. 3.40 (a) represents the SNR values of the OFDM signal with the proposed I/Q imbalance correction and the orange curve the values without it. There is a clear difference in SNR, especially at frequencies far away from the LO (30 GHz) and the average SNR drops from 16.2 to 12.9 dB. In Fig. 3.40 (b) the change in measured BER is shown[93] with a drop of the mean BER from $1.8 \cdot 10^{-3}$ to $2.3 \cdot 10^{-2}$. This behavior corresponds well to the given amplitude and phase mismatch values from the data sheet, which increase at frequencies closer to the mixer operation limit (refer to Fig. 3.17 (b) in Section 3.3.3.5). With the drop in SNR also the achievable data rate at the 7% HD-FEC BER limit decreases by 15% (182 Gb/s vs 159 Gb/s).

[89] PAPR is set with the help of a Tx-side digital clipping

[90] No simulation is performed for this aspect since the simulation model of the I/Q mixer has no elements to model the switching behavior of the diodes.

[91] with different PAPR

[92] OFDM signal between 18 and 42 GHz with 97.9 Gb/s at the 7% HD-FEC limit.

[93] For the BER estimation the same subcarrier QAM modulation order is used for both cases.

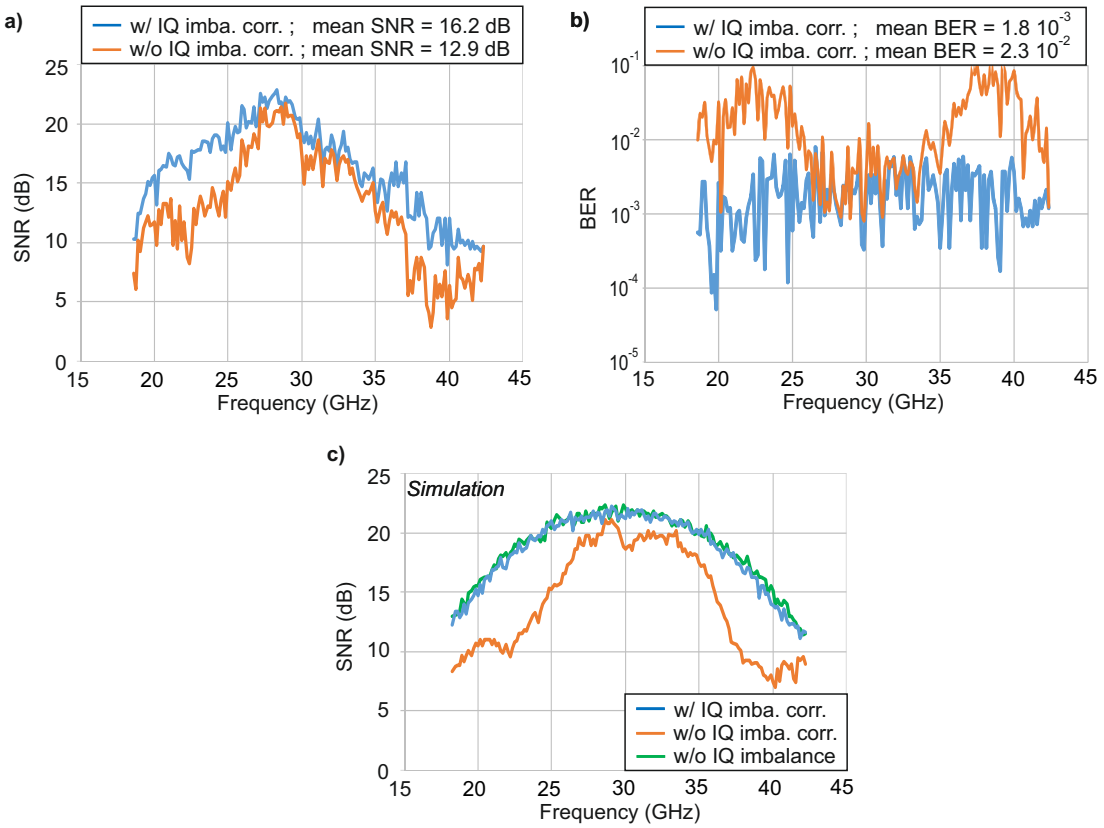

FIGURE 3.40: (a) Experimental OFDM performance at a fixed bit loading with (blue curve) and without (orange curve) I/Q imbalance correction. (b) Related BERs for both cases. (c) Simulative OFDM performance at a fixed bit loading with (blue curve) and without (orange curve) I/Q imbalance correction and additionally without any mixer I/Q imbalance.

In Fig. 3.40 (c) the same aspect is shown for the simulation, using the I/Q imbalance implementation from Section 3.4.1.5 and the setup from Fig. 3.18. Note that an additional white Gaussian noise is added after the Rx side I/Q mixer to enable BERs close to the experiments. Like in the experiment, the blue and the orange curve represent the case with I/Q imbalance correction and the case without, respectively. Additionally, the SNR without any I/Q imbalance is shown by the green curve. As can be observed, there is a similar behavior like in the experiment with increased SNR degradations close to the outer frequencies. The case without I/Q imbalance distortions shows a minimal better SNR compared to the case with correction, which can be explained by slight errors in the cross talk estimation.

In case of single-carrier QAM in the upper sub-band[94], a similar behavior can be observed when applying the I/Q imbalance compensation. The experimental results in terms of measured BERs are shown in Table 3.2 for the 16 GBd 8-, 16- and 32-QAM transmission presented in Section 3.5.3.3. Additionally, BERs for the simulation with the same symbol rates are shown below. When comparing the experimental results

[94]QAM: 21-39 GHz

TABLE 3.2: Performance of single-carrier QAM with I/Q imbalance present

BERs for 16 GBd 8, 16 and 32-QAM in the upper sub-band with and without I/Q imbalance correction (experiment) and without I/Q imbalance (simulation).

Experiment	with I/Q correction	without I/Q correction	
8-QAM	$1.5 \cdot 10^{-4}$	$5.2 \cdot 10^{-4}$	
16-QAM	$2.1 \cdot 10^{-3}$	$6.5 \cdot 10^{-3}$	
32-QAM	$1.9 \cdot 10^{-2}$	$3.7 \cdot 10^{-2}$	
Simulation	with I/Q correction	without I/Q correction	no I/Q imbalance
8-QAM	$1.1 \cdot 10^{-4}$	$3.1 \cdot 10^{-4}$	$9 \cdot 10^{-5}$
16-QAM	$2.4 \cdot 10^{-3}$	$5.3 \cdot 10^{-3}$	$1.3 \cdot 10^{-3}$
32-QAM	$1.8 \cdot 10^{-2}$	$2.8 \cdot 10^{-2}$	$1.5 \cdot 10^{-2}$

with and without I/Q imbalance compensation an improvement in BER can be observed, independent of the symbol rate. As expected, the same is valid for the simulation.

Interestingly, the BER improvement for OFDM is better compared to QAM. This can be attributed to the difference in frequency allocation for both experiments. The OFDM signal is allocated between 18 and 42 GHz and the QAM signal between 21-39 GHz. Since I/Q imbalance is more present at the outer limits of the I/Q mixer operation band (refer to Fig. 3.17 (b) in Section 3.3.3.5), a stronger impact of the I/Q imbalance compensation for OFDM can be expected.

3.5.3.8 SNR considerations

Finally the SNR in the transmission system, shown in Fig. 3.23, is discussed. This is done by comparing the OFDM subcarrier SNRs for different scenarios. In the first scenario, the SNR is directly measured after the DACs[95], with only the DAC characteristics impairing the signal. The second scenario is an electrical btb transmission[96], with additionally the diplexer and the I/Q mixers impairing the signal. The third scenario is the optical btb transmission, with the optical part of the setup additionally impairing the signal. In Fig. 3.41 the results are shown.

At first the SNR degradation of the lower sub-band (0-18 GHz) is discussed. SNR values between 28 dB close to DC and 15 dB close to 18 GHz can be observed directly at the output of the DACs. At this point only degradations from the DAC occur. For the electrical btb case, a small drop (~2 dB) can be observed at frequencies of up to 10 GHz due to the additional electrical amplifiers and a stronger drop (~5 dB) at frequencies close to 18 GHz due to the diplexer. For optical btb, a further drop (~2 dB) in SNR can be observed for the lower sub-band due to the optical transmission.

The SNR degradations in the upper sub-band (18-42 GHz) show a different behavior compared to the lower sub-band. The differences between the DAC output and the electrical btb SNR are significantly stronger, with 3 dB close to the LO and up to 10 dB at the highest frequencies[97]. At frequencies below the LO, the drop is mainly

[95] It can be assumed that the behavior of each of the three DACs is similar.

[96] Fig. 3.23 without optics

[97] For comparison, shift the blue DAC SNR output curve to the left and right side of the LO frequency, with its highest values close to the LO.

caused by the mixer and the diplexer and at frequencies above additionally due to the overall bandwidth limitations of the electrical transmission system. For the optical case, a further drop in SNR can be observed for the upper sub-band. At frequencies close to 20 GHz, this is caused by ripples in the MZM transfer characteristics and at the highest frequencies due to the MZM bandwidth limitations. Overall an average drop of 5 dB is measured for the lower sub-band and a drop of 10 dB for the upper sub-band compared to the SNR directly at the DAC output.

3.5.4 Conclusion on the experiments for bandwidth extension approach

The proposed bandwidth extension based on analog mixing enables the generation and transmission of signals with accumulated bandwidths beyond the capabilities of today's DACs. In the experiments and simulations a signal with up to 42 GHz bandwidth was generated and transmitted over 2 km of SSMF using a simple IM/DD-based optical link. At higher distances the wideband signal degrades notably due to the influence of the chromatic dispersion at 1550 nm. This degradation can partly be avoided by utilizing an optical SSB transmission or even completely using a DCF. The modulation of the sub-bands can be realized with either single or multi-carrier modulation formats, i.e. DMT, OFDM, PAM and single-carrier QAM or a combination of both. It was shown that the multi-carrier formats offer a better performance for the upper sub-band due to their easier adaptation to the system response, which is significantly impaired the combiner/splitter and the I/Q mixers. In the lower sub-band PAM has shown a slightly better performance compared to DMT, due to its smaller PAPR.

The combiner and splitter are important components for the bandwidth extension approach and their realization affects the transmission performance. Experiments with two different combiner types were performed, pure resistive coupler and a frequency selective diplexer. The former offers a better frequency response but suffers from a relatively high insertion loss and poor isolation. The diplexer has a low insertion loss for both sub-bands, but signal degradations close to the cross-over frequency were observed in the experiments. In general, both options are viable, but slightly higher transmission rates are possible with the diplexer approach. The use of a standard *pin*-PD + TIA receiver showed a slightly worse behavior compared to a photodetector type, mainly due to its limited bandwidth. It can be assumed that a *pin*-PD

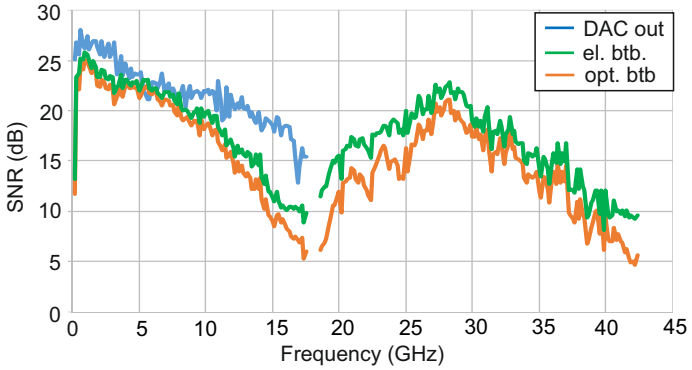

FIGURE 3.41: DMT and OFDM subcarrier SNR: directly after the DAC (blue curve), for electrical btb (green curve) and for optical btb (orange curve).

+ TIA with a sufficient bandwidth will be adequate for such IM/DD-based systems, hence optical amplification can be avoided.

The nonlinear characteristic of the I/Q mixer causes signal distortions for OFDM, already at average input powers of -3 dBm due to the high signal PAPR. The mixer I/Q imbalance has a strong impact on the signal performance, especially at the outer limits of the RF operation range. I/Q imbalance can be minimized with a digital compensation scheme, based on a frequency domain 2x2 MIMO approach. The SNR degradation due to the diplexer, the I/Q mixer and the additional required electrical amplification are the main limitations of the proposed system and has to be considered for implementation outside the laboratory.

3.6 Scalability of bandwidth extension approach

The bandwidth extension approach based on analog mixing offers the possibility of scaling, i.e. increasing the number of sub-bands. Two options for the scaling of the bandwidth extension concept are possible. The first option increases the maximum available signal bandwidth[98] by adding further sub-bands with the same bandwidth than the sub-bands of the original system. The second option increases the number of sub-bands without changing the total signal bandwidth. Both options are illustrated in Fig. 3.42 for the Tx side of a transmission system. In Fig. 3.42 (a) the system investigated in this thesis is shown, consisting of two sub-bands each with ~20 GHz bandwidth (f_1). Adding further sub-bands with the same bandwidth results in the system shown in Fig. 3.42 (b). The total signal bandwidth increases consequently from $2f_1$ to Nf_1. The advantage of such an option is the increased signal bandwidth which should result in a higher data rate compared to the original system. However, as could be observed in the previous investigations, component impairments limit the achievable SNR, especially the DAC, the I/Q mixer and the diplexer.

These impairments can be partly reduced, if smaller signal bandwidth are targeted for each sub-band as is illustrated in Fig. 3.42 (c). This allows the application of more mature DACs with lower sampling rates, which have commonly a better ENOB[99]. Smaller sub-signal bandwidths would also allow the use of I/Q mixers with improved properties, since the design and adaptation for smaller frequencies commonly results in overall better characteristics[100]. This is also true for other components in the system like the amplifiers. Additionally, the effort in DSP is reduced, e.g. a smaller number of equalizer taps. The drawback of the second option is the increased effort for the combiner and splitter, which requires additional steps or a cascaded network to combine and split the higher number of sub-bands. Furthermore, more effort for the integration of all components is required.

The optimal number of sub-bands depends on the total signal bandwidth, the available DACs and ADCs, the combiner and splitter realization and the available I/Q mixers. It can be beneficial to use several lower-speed DACs and ADCs, if they have better ENOBs compared to a single DAC and ADC, which is driven far beyond its cut-off frequency. This is supported by using mature I/Q mixers[101] and amplifiers. The combiners and splitters can be specifically designed to meet the specifications of such systems, which should reduce their impairments. Further important considerations are the power consumption of the components and the integration. Both have to

[98] Assuming an optical system with the required bandwidth is available

[99] vice versa for ADCs

[100] Note that the used I/Q mixers are principally not designed for large IF signal bandwidths.

[101] which are e.g. designed and tested for RF applications with similar bandwidth requirements

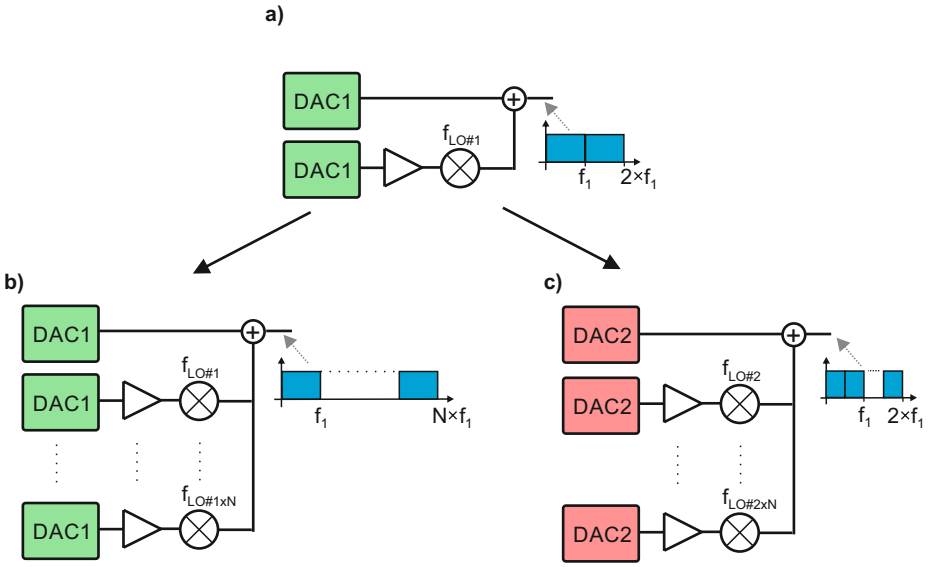

FIGURE 3.42: Scaling options for bandwidth extension approach for the Tx side. a) Original system with two sub-bands; b) System with higher total bandwidth; c) System with original bandwidth but multiple sub-bands.

be incorporated into the design of such systems, but require the specific knowledge of the used components.

3.7 Wideband DAC realization using bandwidth extension

The bandwidth extension approach based on normal mixers (shown in Fig. 3.4 in Section 3.2) offers also the possibility to generate a spectral continuous waveform over the whole frequency range. In this case, the bandwidth extension approach emulates a wideband DAC, named frequency interleaved DAC (FI-DAC) in the following. In this section the FI-DAC concept is briefly investigated. This includes an introduction in the FI-DAC concept, the experimental and simulative setup, the required DSP and the results.

The presented results are published in [100] and [102]. The investigations were done in cooperation with the main author of [100] and [102]. A detailed descriptions of the own contribution can be found in Appendix B.

3.7.1 Digital-to-analog converters using frequency interleaving

The FI-DAC concept utilizes multiple DACs in parallel to perform the D/A conversion, whereby each converter handles a fraction of the digital input signal spectrum. In Fig. 3.43, a conceptual block diagram of the FI-DAC is shown. In the DSP unit on the left side, the input signal (Fig. 3.43 (a)) is split into several sub-signals in the frequency domain as shown in Fig. 3.43 (b), whereby each sub-signal covers a different spectral fraction of the combined spectrum. The sub-signals are then digitally down-converted[102] to baseband in the DSP unit with their spectral allocation shown in

[102]This is realized by multiplying each signal part with an different LO. The LO frequencies are the same as for the analog up-conversion later in the setup.

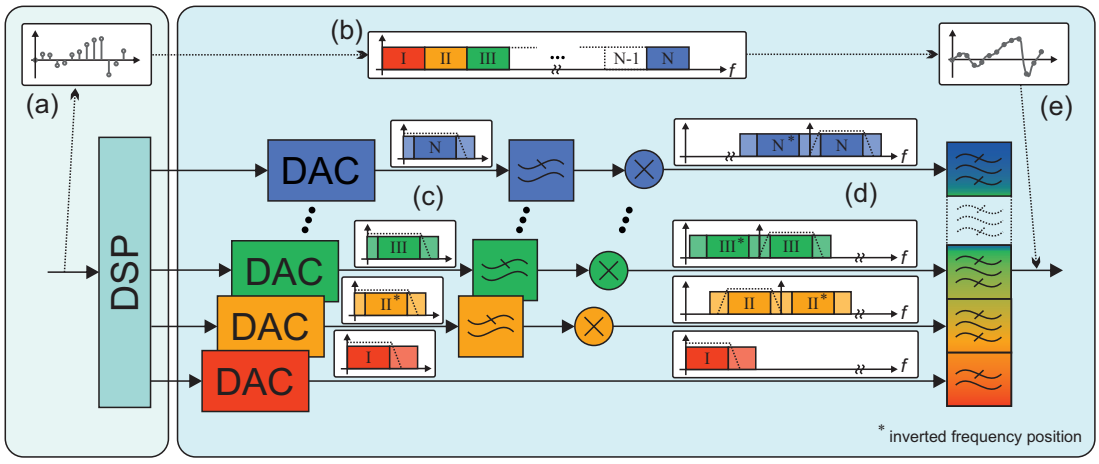

FIGURE 3.43: Conceptual FI-DAC block diagram: the digital input signal (a) is split into several sub-signals in the frequency domain (b). These sub-signals are each D/A converted in baseband (c) and then up-converted back to their native frequency locations (d). Finally, they are combined to form the analog representation (e) of the digital input signal (a).

Fig. 3.43 (c). Depending on the chosen split and LO frequencies, the sub-signals do not cover the whole bandwidth of each DAC. Hence, band gaps are present for both the lower and higher frequencies, which are denoted with lighter colors. These band gaps are necessary to remove undesired spectral components, like the DAC alias spectra, higher harmonics or the LO. Furthermore, a digital pre-equalization of the electrical system frequency response is applied in the DSP. The necessary channel information is previously determined with the help of training signals.

After D/A conversion the output signals are low-pass filtered in order to suppress DAC alias. Then, the sub-signals are up-converted to their native frequency locations by normal RF mixers[103] as shown Fig. 3.43 (d). Note that the first signal is not up-converted. After up-conversion at each mixer two redundant side-bands exist, thus one has to be removed by filtering. If the lower side-band is used, the signal has to be generated in the inverted frequency position denoted by the superscript * in Fig. 3.43. The up-converted signals and the baseband signal are then combined by a frequency multiplexer, which is typically a diplexer or multi-plexer. The resulting analog waveform, shown in Fig. 3.43 (e), corresponds now to the digital input signal from Fig. 3.43 (a).

The combined signal has both a higher sample rate and a higher bandwidth than it could have been generated with a single DAC. The resulting frequency characteristic can be digitally defined with the pre-equalization algorithms in the DSP unit. The sub-signals are stitched together without any gap and form a continuous waveform without spectral gaps. Note that a small overlap of the sub-signals is also possible as will be discussed in Section 3.7.4.3.

An important requirement of this scheme is the phase stability between the sub-signals. A straight forward way to achieve this is to use the same DAC type for each

[103]The concept requires the suppression of the LO in the resulting waveform. This cannot be realized with an I/Q mixer if both sideband are used. With normal mixers, the LO and one redundant() sideband can be suppressed with a filter.

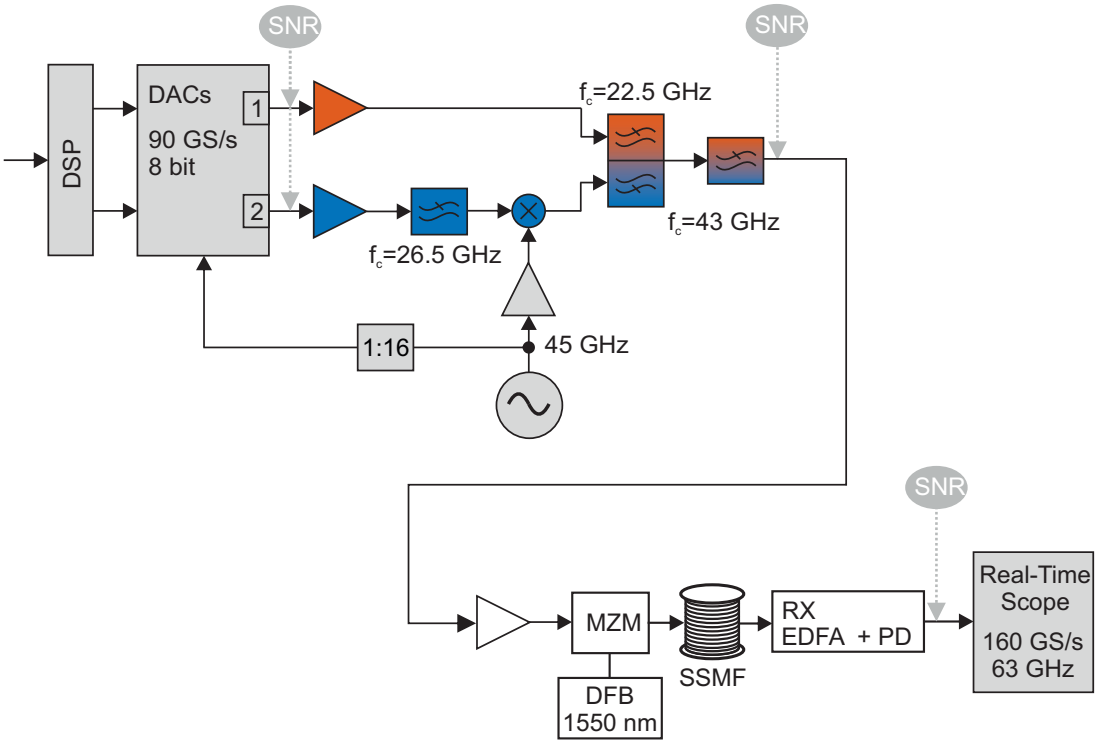

FIGURE 3.44: Experimental setup consisting of an electrical FI-DAC and an optical IM/DD transmission link. Furthermore, SNR measurement points are shown.

sub-signal, i.e. equal sampling rate and memory size, an integer relation of the different LO frequencies and a single clock source for the DACs and LOs. The single clock has to be split and adapted by means of frequency multipliers or dividers.

3.7.2 Experimental and simulative setup

In order to investigate the FI-DAC concept an experiment has been set up, which is shown in Fig. 3.44. Two sub-signals have been generated to form a wideband 80 GBd PAM signal. For the D/A conversion, two high-speed CMOS DACs with 19 GHz analog bandwidth are operated at a sample rate of 90 GS/s. The output signals are amplified (SHF 100BP) in order to adjust the signal amplitudes and also to filter the signal[104]. The RF mixer (Marki Microwave MML1-1850) is driven by a 45 GHz local oscillator, provided by a 45 GHz frequency generator and a driver amplifier. The clock signal for the DACs is obtained with a clock divider, in order to achieve phase stability between the sub-signals. The sub-signals are combined using a custom-designed diplexer with a crossover frequency of 22.5 GHz in order to form the combined output signal having 180 GS/s[105] and 40 GHz bandwidth. The transmission characteristic of the diplexer also acts as a LPF for the lower signal band and as a high-pass filter for the up-converted signal band. The diplexer has a roll-off of 25 dB/GHz and an isolation >53 dB in the stop band. The following LPF suppresses both the fed-through LO signal and the redundant upper side-band.

[104]The amplifier 3 dB bandwidth is 30 GHz.
[105]This is the available theoretical sampling rate with this approach.

After the driver amplifier (SHF 804EA), the combined signal is electrical-optical converted using an MZM, driven at the quadrature point to act as an intensity modulator. A DFB laser provides the optical carrier at 1550 nm. After transmission over 2 km of SSMF the signal is optical-electrical converted. The conversion is realized with a wideband photodetector with 50 GHz bandwidth, similar to the previous experiments. In order to provide the required optical power, an EDFA and an optical BPF (1 nm) are used. The signal is acquired with the high-speed real-time sampling scope (Keysight DSAZ634A), operating at 160 GS/s with 63 GHz bandwidth.

In order to study some effects of the system in detail an additional electrical btb simulation is set up, similar like in the previous experiments. The DACs are modeled as described in Section 3.4.2, which includes the nominal resolution, bandwidth limitation and a static nonlinearity. The mixer parameter are taken from the data sheet (Marki Microwave MML1-1850) and are utilized in the mixer model from Section 3.4.1. The diplexer to combine both sub-bands is modeled as a low-pass and a high-pass Butterworth filter[106]. Afterwards, an additional LPF[107] is used to suppress the LO and the redundant sideband. Finally noise loading is applied to enable useful BER values. The amount is chosen with respect to SNR measurements from the experiment.

3.7.3 DSP FI-DAC

The FI-DAC DSP block diagram at the Tx side is shown in Fig. 3.45 with the individual steps illustrated in the frequency domain. The 80 GBd 4-PAM digital input signal, shown in Fig. 3.45 (a), with 218 and 215 symbols in the simulation and the experiment, respectively, is fed through a FFT and the resulting spectral representation is shown in Fig. 3.45 (b). The signal is then pulse-shaped, using an RRC filter (roll-off = 0.03) as shown Fig. 3.45 (c). Afterwards, it is split into two frequency bands as shown in Fig. 3.45 (d) and Fig. 3.45 (e). The splitting can be performed both with a spectral overlap as shown in Fig. 3.45 (g), e.g. in a raised-cosine manner, or without overlap by means of ideal rectangular frequency domain filters[108] as displayed in Fig. 3.45 (h). The higher frequency signal is then down-converted into baseband with an ideal digital RF mixer, as shown in Fig. 3.45 (f). In both the experiment and the simulation, the lower side-band of the up-converted signal is used, which requires the generation of the baseband sub-signal in reversed frequency position, which is denoted by * in Fig. 3.45. Afterwards, the first sub-signal is located between DC to 22.5 GHz and the second sub-signal between 5 GHz to 22.5 GHz. For both sub-signals two times oversampling is used in order to suppress DAC alias with analog LPFs. The band gap of the second sub-signal from 0 to 5 GHz, is required to enable the sufficient suppression of the LO and the redundant sideband after up-conversion.

Then, both signals are jointly pre-equalized in order to mitigate the linear effects of the analog components. The pre-equalizer coefficients are obtained with the help of training signals and LS channel estimation. After clipping of both sub-signals, they are converted back into time domain by an IFFT and fed to the DACs. More information on the Tx DSP can be found in [122]. At the receiver, the DSP includes synchronization, clock phase recovery, channel estimation, a half-symbol spaced MMSE post-equalizer[109] and BER estimation via error counting.

[106] The filter order is 2 and the 3 dB bandwidth is 22.5 GHz. Values are taken from the data sheet

[107] Butterworth type, order 2, bandwidth 43 GHz

[108] The rectangular filtering in frequency domain results in a significant roll-off in time domain which may degrade the signal

[109] The number of taps is optimized with respect to the BER

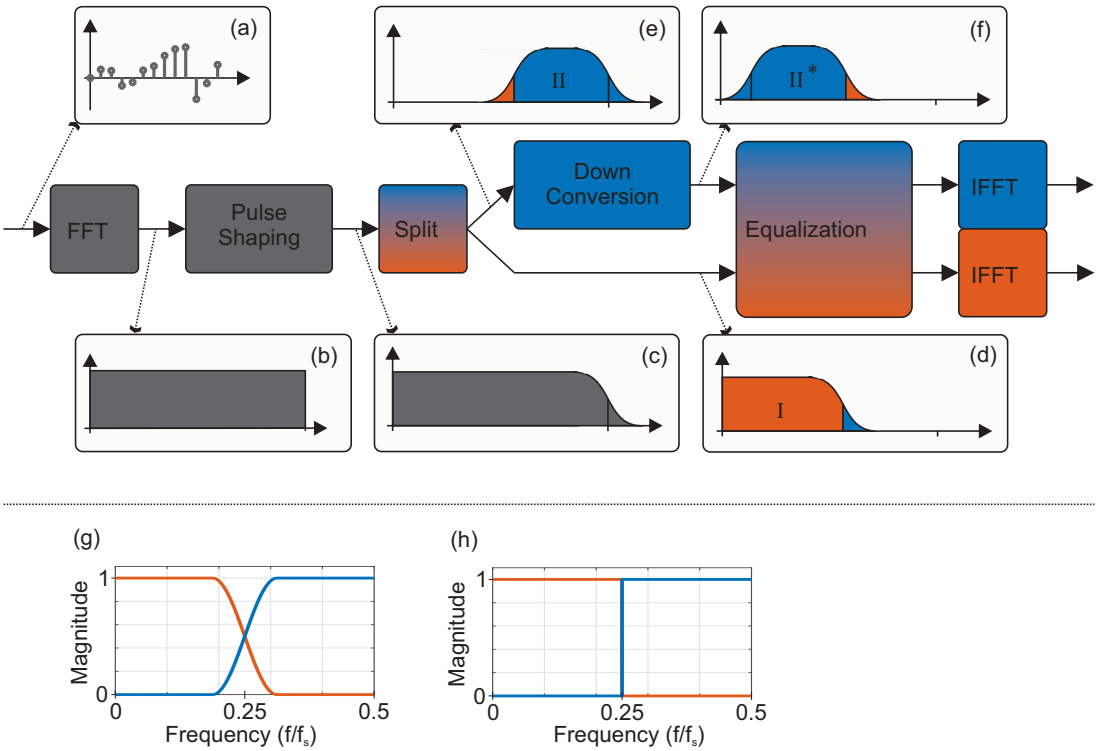

FIGURE 3.45: DSP block diagram: The time domain signal (a) is fed through an FFT and the corresponding frequency domain representation (b) is pulse-shaped (c). Then, the signal is split in the frequency domain with a digital diplexer (e,d). The second sub-signal is further down-converted into baseband with a digital mixer (ideal multiplication with a LO) (f). Both sub-signals are pre-equalized and fed through IFFTs, which are then fed to the DACs. Amplitudes of the sub-signals with spectral overlap (g) and without (h).

3.7.4 Results FI-DAC concept

In the experiment and in the simulation for the FI-DAC concept, various system aspect are investigated like the transmission performance, the influence of impairments and the general characteristics. In detail these are the power and phase mismatches between the frequency bands, the statistical characteristics of the sub-signals, spectral overlap to minimize the PAPR and the SNR degradation.

3.7.4.1 Transmission performance FI-DAC concept

In Fig. 3.46 (a), both the amplitude and phase of the uncompensated frequency response for the FI-DAC system from each DAC output to the combined output are shown. In the experiment, there is a drop of 20 dB in the frequency response for the first sub-signal and a 10 dB drop for the second sub-signal down to the crossover frequency of 22.5 GHz. The simulation shows a smaller drop of only 8 dB at the crossover frequency for the first sub-signal. This results from the fact, that for the simulation only the frequency response of the DAC and of the diplexer are considered and the frequency response of the amplifiers and the coaxial cables are neglected. Furthermore, the frequency responses are defined by means of Butterworth filters, whereby the 3 dB frequency and the order are approximated with information from the data

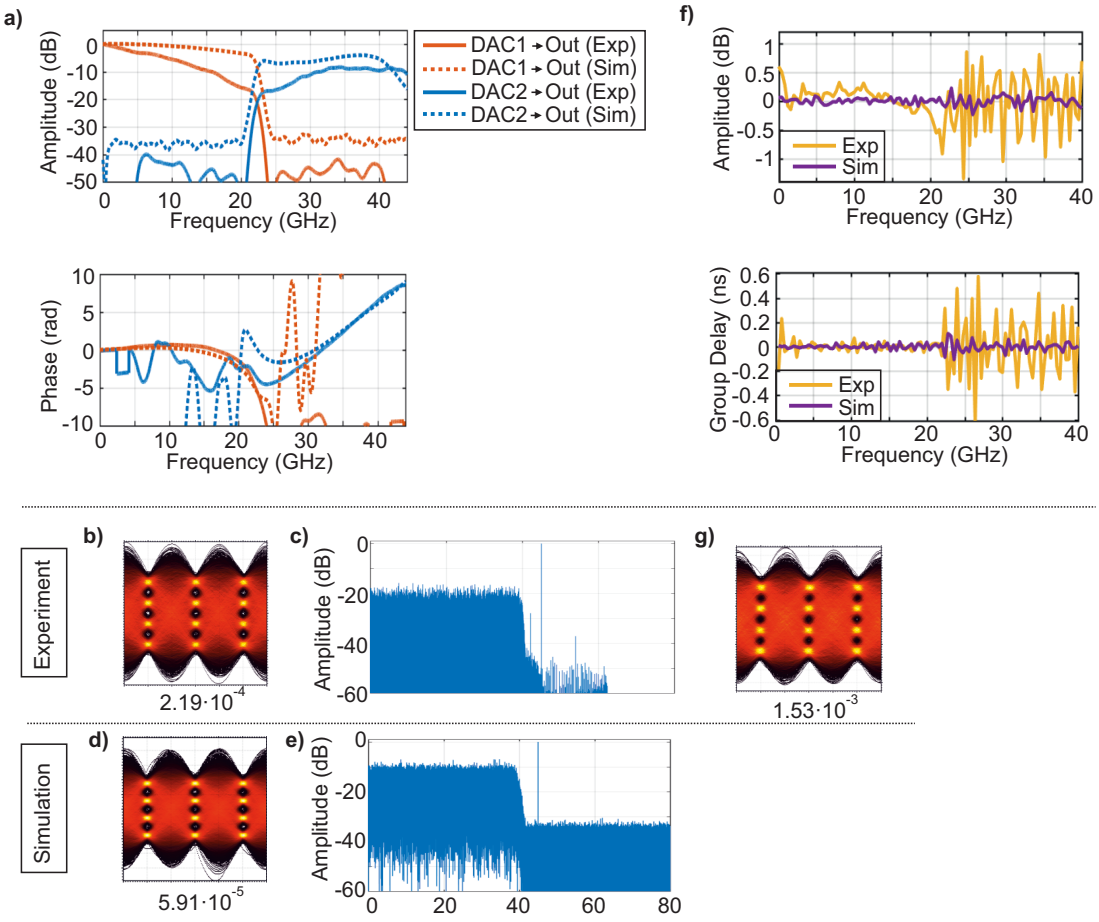

FIGURE 3.46: Measurement results: (a) frequency response of the uncompensated FI-DAC; (b) experimental electrical btb eye diagram with a BER of $2.2 \cdot 10^{-4}$ and (c) corresponding spectrum; (d) simulated electrical btb eye diagram with BER of $5.9 \cdot 10^{-5}$ and (e) corresponding spectrum; (f) magnitude and phase of the compensated channel frequency response; (g) experimental optical eye diagram for 2 km IM/DD-based transmission with additional post-equalizer with a BER of $1.5 \cdot 10^{-3}$.

sheet. The phase is fairly linear in frequency ranges, where substantial amplitude is present.

By using the DSP as described in the previous section, the frequency responses are corrected by means of zero forcing pre-equalization, enabling an open 4-PAM electrical btb eye diagram at the output of the FI-DAC system with a BER of $2.2 \cdot 10^{-4}$ as shown in Fig. 3.46 (b). The corresponding flat spectrum with the raised-cosine roll-off is shown in Fig. 3.46 (c). Spurious components between 40 and 45 GHz can be observed, which are presumably caused by mixer nonlinearities. The corresponding simulation results are shown in Fig. 3.46 (d) and Fig. 3.46 (e). The eye diagram is related to a BER of $5.9 \cdot 10^{-5}$. The noise floor (from noise loading) is clearly visible in the corresponding spectrum for frequencies beyond 41 GHz. The difference in BER results from the fact, that with the noise loading the SNR values are not matched perfectly between simulation and experiment, as shown later in Section 3.7.4.4. By using a half-symbol spaced post-equalizer, the BER could be improved for both experiment and simulation to $5.1 \cdot 10^{-5}$ and $1.3 \cdot 10^{-6}$, respectively. Note, that the LO signal has

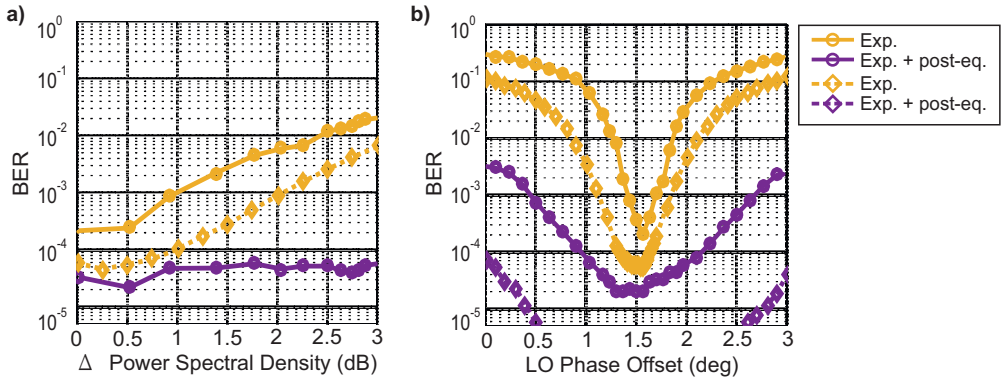

FIGURE 3.47: Results for experiment and simulation for power and phase mismatch between sub-bands: (a) BER vs. power spectral density difference between the bands; (b) BER versus LO phase offset.

been digitally removed prior to plotting the eye diagram for the experimental results, due to the lack of a LPF with a smaller cut-off frequency than 43 GHz.

Since the post-equalizer is able to improve the BER for the electrical btb case, residual distortions are present. In Fig. 3.46 (f) the channel estimation of the pre-compensated FI-DAC frequency response is shown. The experimental results show a fairly flat magnitude for the first sub-signal spectrum. It has distortions of up to 0.9 dB for frequencies up to the cross-over frequency of 22.5 GHz. For the second sub-signal's spectrum, there are stronger distortions of up to 1.5 dB. For the phase (i.e. group delay), the findings are similar. The first sub-signal spectrum is fairly flat and the second sub-signal spectrum exhibits several distortions. The corresponding simulations show a significantly better behavior, although the frequency response in the upper band is distorted stronger as well. These effects can be attributed to the non-linear transfer function of the mixer in the second path, and the phase-locked-loop integrated in the DAC (experiment only), which reduces the phase stability between the first and the second sub-signal. In Fig. 3.46 (g), the eye diagram is shown after the optical transmission over 2 km of SSMF using the IM/DD-based link shown in the experimental setup. Due to the distortions of the optical transmission channel, an additional post-equalizer is required (half-symbol-spaced MMSE). The achieved BER is $1.5 \cdot 10^{-3}$ and hence below the 7% HD-FEC limit.

3.7.4.2 Power and phase mismatches

In order to study the required precision for power and phase matching between the two frequency bands, both the spectral power difference and the phase of the LO are swept and the corresponding results are shown in Fig. 3.47. In Fig. 3.47 (a), the BER is shown with respect to the mean power spectral density between both bands. The mean power spectral density difference is controlled by increasing the power of the first sub-signal with the gain control of the external amplifier. The raw BER without post-correction is rising almost by two orders, if the power difference raises to 3 dB. If using an additional post-equalizer, the error could be almost fully corrected and the BER is constant. In the simulation, the post-equalizer is able to obtain a roughly constant BER of $2 \cdot 10^{-6}$. In Fig. 3.47 (b) the phase of the mixer LO is varied in the

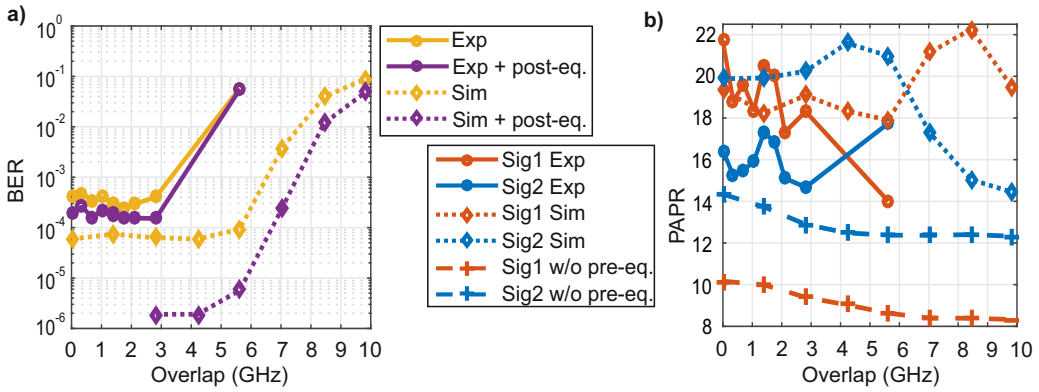

FIGURE 3.48: Results from experiment and simulation for spectral overlap between sub-band: (a) BER versus spectral overlap; (b) PAPR versus spectral overlap.

interval $\pm 150°$[110]. In the experiment, a manual phase shifter is used before the LO driver amplifier in order to control the LO phase. The resulting phase shift for the LO frequency is obtained by the number of turns of the phase-shifter adjusting screw and the phase-shift-per-turn value given in the data sheet. For the experiment, the phase offset has to be below 15° in order to ensure, that the BER stays below 10^{-3}. By using an additional post-equalizer, there is a wider margin, i.e. $\pm 45°$ and $\pm 90°$ can be tolerated to keep the BER below 10^{-4} and 10^{-3}, respectively.

There is a good match between the experimental and the simulation based results regarding the trend of the curves, however, the simulation results are offset as in Section 3.7.4.1. The results regarding the power mismatch indicate that slight deviations are tolerable, even if no further post-equalization is applied. On the other hand, phase mismatches are critical and additional post-equalization is recommended[111] for system robustness.

3.7.4.3 Spectral overlap

In contrast to the resulting 4-PAM signal, the PAPR of both sub-signals is much higher due to their nearly rectangular spectrum, which originates from the digital splitting as described in Section 3.7.3. Typical values are beyond 13 dB which is critical for the D/A conversion due to the limited resolution of the used high-speed DACs. The common solution to reduce these high PAPR values is digital clipping prior to the D/A conversion as is done in the experiment[112]. A second solution is a spectral overlap between both sub-signals as is illustrated in Fig. 3.45 (g,h). In theory, the overlap changes the original rectangular spectrum of both sub-signals, with commonly high PAPR values, into a softer form with lower PAPRs. This is tested in both the experiment and the simulation by applying a raised-cosine filter function for the overlap. In Fig. 3.48 (a) the achieved BER and in Fig. 3.48 (b) the PAPR of both sub-signal with respect to the overlap are shown. Regarding the experimental results in Fig. 3.48 (a), an overlap of up to 3 GHz is tolerable without performance degradation. After that, the effort for

[110] In contrast to a signal delay the LO phase offset results in the same constant phase offset at each frequency component. Hence, it is not possible to compensate the offset with a simple few tap equalizer.

[111] However, a post-equalizer is not desirable for such a FI-DAC and amplitude and phase mismatches have to be corrected sufficiently at the Tx, which can be challenging for timing impairments.

[112] Target PAPR 10 dB.

pre-equalization becomes too high, such that the pre-equalization fails by putting too much effort in the equalization of high frequency components. In the simulation, there is a wider margin for an overlap of up to 5.7 GHz without performance degradation. This may be based on the weaker filter roll-off and better phase behavior.

The linear PAPR values of both sub-signals in Fig. 3.48 (b) decrease monotonously with higher overlap (striped curves), if no pre-equalization is used which corresponds to the theory. However, the results for both simulation and experiment with pre-equalization do not show a monotonic behavior. In the experiment, the PAPR values decrease for a small overlap of up to 1 GHz, but then rise again for an overlap of up to 1.5 GHz. Then, they decrease again for an overlap of 2 GHz to 17.3 and 15.1 for sub-signal one and two, respectively. Note, that these changes are relatively small, since the linear PAPR of both sub-signals is plotted. The simulation results show slightly decreasing values for the first sub-signal, but increasing values for the second sub-signal, whereby the loss of one seems to cancel the benefit of the other. The PAPR values do not decrease, because the values highly depend on the sub-signal characteristics and the frequency response of the pre-equalizer. For more overlap, more pre-equalization is necessary, hence the sub-signals PAPR is worse.

Concluding, for filters (diplexer) with steep roll-offs as used in both experiment and simulation, a small overlap is tolerable. However, a significant reduction in PAPR is not observed due to the increasing pre-equalization effort required. At larger overlaps severe signal degradations occur, since too much effort has to be spent for the pre-equalization of the frequency responses, which significantly reduces the signal power after the diplexer. A small overlap may be useful for algorithms performing phase matching of the frequency bands.

3.7.4.4 SNR progress FI-DAC concept

To give a better understanding of the signal SNR degradation for the FI-DAC concept, a transmission experiment using DMT is performed[113]. The relatively simple SNR estimation at each subcarrier enables a conclusion about the frequency dependent degradation of the transmission system. The used DMT signal consists of 229 modulated subcarriers (512 point FFT/IFFT) with a total bandwidth of 41 GHz. The cyclic prefix is 16 samples and a standard single-tap equalizer for each subcarrier is applied at the Rx. Additionally, to maximize the data rate, an optimized bit loading for a target BER below the 7% HD-FEC limit is used. Prior to transmission, the same pre-equalization scheme used for the PAM transmission is applied to cancel phase and amplitude mismatches between both sub-signals.

In Fig. 3.49, the measured SNR values of the DMT subcarriers are shown at three points in the transmission system: directly after the DAC, after the diplexer in an electrical btb scenario and after the optical transmission, as shown in Fig. 3.44. At first, the behavior for the lower DMT sub-signal, ranging from 0 to 22.5 GHz is discussed (red curve). Directly after the first DAC, SNR values of ~24 dB can be observed. At this point, only DAC properties like resolution, nonlinearities and frequency response are limiting the SNR[114]. The slight increase in SNR up to higher frequencies can be attributed to the pre-equalization, which compensates for the DAC and the diplexer

[113] Similar to the SNR consideration in Section 3.5.3.8

[114] The digital clipping which limits the PAPR (10 dB) has only a minor influence on the SNR.

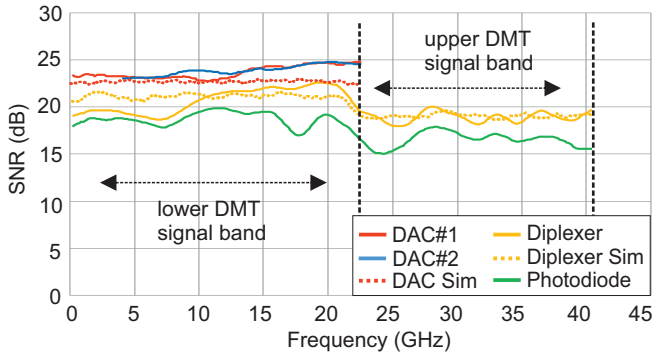

FIGURE 3.49: Experimental and simulative subcarrier SNRs of a DMT signal at different points in the transmission system: after the DAC #1+2, after the diplexer and after the photodiode.

in the lower band[115]. The SNR values at the second point in the transmission system, after the diplexer, show a clear drop of up to 4 dB (yellow curve). While the SNR degradation at frequencies between close to 22.5 GHz is mainly influenced by the diplexer[116], it is not clear where the strong drop at lower frequencies originates from. With the additional optical transmission, a further drop in the SNR can be observed, mostly due to the limitations of the optical modulator.

For the upper DMT signal band between 22.5 and 41 GHz, a similar behavior can be observed. Directly after the second DAC, nearly the same SNR values compared to the sub-signal for the lower band exist (blue curve), even if a different pre-equalization is applied. Note that the gap at frequencies near DC is necessary to limit the total signal bandwidth to 41 GHz since the LO, located at 45 GHz, has to be removed. After up-conversion to the target frequency range and after the diplexer, significantly lower SNR values can be observed. This is largely caused by the mixer's properties, like nonlinearities and bandwidth limitations, in addition to the small degradations due to the amplifier and the diplexer. After the optical transmission, a further SNR drop of 3 dB occurs, similar to the lower band.

In the simulation, the noise loading has been adapted, in order to match the measured SNR values in the upper band for a mixer input power of 2 dBm. As a result, the SNR values in the first band do not match the simulation perfectly, since noise loading is performed on the combined signal.

The average drop in SNR for the lower and the upper band are 3 and 6 dB for the electrical transmission case and 5 and 8 dB for the optical case, respectively. Hence, the overall degradation of the upper band due to the electrical up-conversion, is the primary limitation for these systems, even with a significant application of DSP. The measured DMT transmission rates are 205 Gb/s and 174 Gb/s for the electrical and the optical scenario[117], respectively. The reduction in data rate can be attributed to the optical modulator, especially due to its bandwidth limitations and the ASE noise of the

[115]Due to the pre-equalization of the signal, i.e. the compensation of the system frequency response up to the point after the diplexer, a nearly constant SNR can be observed after the DAC. This stands in contrast to the SNR curves from the bandwidth extension approach without pre-equalization and with independent sub-bands as shown in Section 3.5.3.8. For these experiments, a decrease in SNR up to higher frequencies has been observed. Note that the used oscilloscope is superior compared to the one used in Section 3.5, which additionally improves the SNR compared to the measurements in Section 3.5.3.8.

[116]cross-over frequency 22.5 GHz

[117]Both scenarios with an optimized bit loading at a target BER below the 7% HD-FEC limit.

optical amplifier. Compared to the PAM transmission, a slightly better performance is observed, due to the easier adaptation of the DMT signal to the channel properties. Note that DMT did not requires the pre-equalization of both sub-bands and the phase lock of both signals, since its subcarriers are independent and can be demodulated individually.

3.7.5 Conclusions about the FI-DAC concept

The demonstrated FI-DAC system consisting of two DACs enables the generation of spectrally continuous signals with bandwidths up to 40 GHz at sampling rates of 180 GS/s[118]. The system characterized in this chapter enabled the generation of a 80 GBd 4-PAM signal with open eyes without using post-equalization in an electrical btb scenario. After the optical IM/DD-based transmission over 2 km of SSMF, a BER below the 7% HD-FEC limit was measured, using an additional post-equalizer to compensate for the optical part of the transmission. Power and phase mismatches between both sub-signals result in distortions, which can be compensated partly with a post-equalizer. However, for a real system a continuous adaptation of the pre-equalizer coefficients is desirable to avoid these kind of mismatches. If a digital PAM signal is split into two sub-signals in the frequency domain, these sub-signals have a Gaussian amplitude distribution with high PAPR values. This is an issue due to the already limited resolution of high-speed DACs and can be avoided partly by applying a digital clipping. Furthermore, a spectral overlap can reduce high PAPR values theoretically. However in combination with pre-equalization such effect could not be observed. The SNR is decreased about 3-4 dB due to both the amplifiers and the diplexer and another 3 dB due to the mixer, i.e. the mixer is the limiting component in terms of SNR for the system.

3.8 Conclusions and outlook on bandwidth extension approach

The bandwidth extension concept based on analog mixing and passive signal combining enables the generation of wideband signals beyond the capabilities of today's ADCs and DACs and makes possible the full utilization of current optical components. For simple IM/DD-based systems this allows a significant increase in signal bandwidth and data rate without using optical multiplex techniques. Furthermore, no new components are required and current off-the-shelf components are suitable to significantly increase the capacity. Mature products have usually improved general properties[119] compared to the newest laboratory prototypes, which makes the further development of system with higher technology readiness levels a lot easier.

The application of enhanced DSP to compensate for the existing limitations in the used components is also an important aspect of these systems. With the further development and deployment of cost-efficient high-speed ASICs, advanced DSP becomes more viable, even for simple IM/DD systems.

The investigated bandwidth extension concept offers data rates of nearly 200 Gb/s over a single wavelength with current off-the-shelf components. This is especially relevant for 400G Ethernet, if combined with a simple optical multiplex approach like PolMUX.

[118] This is the available theoretical sampling rate with this approach, see Section 3.7.2.

[119] For example in case of DACs, a higher resolution and a better frequency behavior.

In this thesis, different aspects of this system were investigated with the focus on transmission experiments. A detailed model of the key component, i.e. the I/Q mixer, was developed and implemented in a simulative environment to compare its influence on the transmission system with the experimental work. Transmission experiments at longer distances have shown a strong influence of the chromatic dispersion, due to the large signal bandwidth and the transmission at 1550 nm. Both single and multi-carrier modulation formats are feasible for the bandwidth extension approach, with benefits for multi-carrier formats in the upper sub-band. Different hardware realization of the Tx side signal combiner have shown similar performance. The inherent I/Q imbalance of the I/Q mixers can be digitally compensated. The SNR degradations due to the I/Q mixers and the combiner/splitter has a significant impact on the overall system performance.

Furthermore, an FI-DAC concept based on the proposed analog mixing and combining of sub-bands was experimentally investigated. As a result, the critical aspects of the concept were highlighted and its limitations were shown in terms of SNR degradation. The application of such a bandwidth extension scheme offers a significant boost to the available signal bandwidth at the cost of SNR.

The key aspects for a successful realization of the bandwidth extension concept are high-resolution analog/digital converters with sufficient bandwidth, optical intensity modulators with modulation bandwidths clearly beyond their electrical counterparts, custom designed mixers and combiner/splitter and high-speed DSP. High-resolution DACs and ADCs are required to enable SNR values suitable for optical IM/DD transmission systems and advanced modulation formats. The bandwidth of these devices determines directly the number of required sub-bands, which should not be too high to avoid integration issues. Optical intensity modulators with high modulation bandwidths are a fundamental requirement for the bandwidth extension approach and the same applies for the detector. The availability of mixers with acceptable parameters, such as bandwidth, insertion loss and imbalance, is another requirement for the concept. Currently available devices in the market are not very suitable for the targeted signal bandwidths and it can be expected that custom designed devices will show an improved performance. The same is valid for the combiner and splitter. High-speed DSP is mandatory for spectral efficiency modulation formats and to overcome the inherent impairments of all components.

For the future work four aspects are interesting. The first consists of the adaption and integration of the components. The second on the scalability of the concept. The third aspects looks into the development towards a real-time system utilizing FPGAs or ASICs and the fourth consists of the application for longer transmission distances.

The system demonstrated in this work consisted of individual laboratory components, often with non-ideal characteristics. For the realization of the experiments, critical aspects are the frequency range and the required driving power of the different components. It can be assumed that with better adapted components, an improvement in performance can be achieved. A further integration would also ease the issues with reflections in the systems at the combiner and the splitter.

The scalability of the bandwidth extension concept, i.e. the use of more and smaller sub-bands or the transition to higher total signals bandwidths, offers potentially a further improvement of the transmission capacity by utilizing more mature components with generally better properties. A more detailed investigation of the available real-world components, including usability and limitations, would be required.

Real-time implementations of the bandwidth extension concept will be an important step towards a higher technology readiness level. This would require the efficient

implementations of the DSP algorithms into FPGAs or ASICs. The challenges here are the optimization and simplification of the algorithms, e.g. the I/Q imbalance compensation and the further investigation of timing aspects.

The use of high bandwidth IM/DD systems for longer transmission distances is mainly limited by the influence of chromatic dispersion. Concepts to avoid the chromatic dispersion induced fading in IM/DD systems consists of single sideband transmission, the use of DCFs, the transmission in the O-Band or the signal pre-equalization at the Tx using complex modulation. All these methods have benefits and challenges and it has to be investigated if they are suitable for the transmission over longer distances utilizing the bandwidth extension approach.

Chapter 4

Performance improvement of VCSEL-based high-speed short-range transmission systems with advanced digital signal processing

In the first part of the thesis it was shown that the actual bandwidths of the electrical components are an important limitation for high-speed short-range IM/DD-based communications systems. The investigated bandwidth extension approach offers a solution for this problem, by utilizing analog mixing and several independent sub-bands with a total bandwidth beyond the capabilities of today's DACs and ADCs.

A further important limitation for high-speed short-range systems are the non-ideal characteristics of the components. Especially the optical modulator, which is commonly a VCSEL, limits the transmission capacity due to its non-ideal linear and nonlinear behavior. However, these VCSEL-based impairments can be minimized with the help of advanced DSP. The second part of this thesis investigates these techniques with the focus on linear and nonlinear pre-equalization.

The chapter is structured as follows: First, the state-of-the-art for VCSEL-based high-speed short-range links is given, followed by an overview over the relevant VCSEL properties. Second, the VCSEL transmission system is presented, the influence of all components is briefly discussed and the pre-equalization scheme presented. Third, the influence of linear pre-equalization for a DMT modulation based high-speed short-range system is experimentally investigated. Furthermore, the gain of nonlinear pre-equalization is discussed by means of simulations and additional experiments. Finally, a conclusion over the application of linear and nonlinear pre-equalization of VCSEL-based high-speed systems is given.

4.1 Applications of VCSEL-based high-speed short-range transmission links

The further growing amount of transmitted data in the different network types further increases the transmission rates in short-range applications, like in data center environments. These short-range links encompass distances from in-rack connections (<m) up to intra data center connects (a few km). For these links key parameters are high throughput, small footprint, low power consumption and low cost [123], [124]. These requirements are met by systems based on VCSELs in combination with MMFs

for short distances (<500 m) and SMFs for longer distances. VCSELs generally have low manufacturing costs, especially due to the easy on-wafer testing, a low power consumption and wide bandwidths in the optical as well as in the electrical domain. MMF-based systems enable an easy coupling, due to the relatively large core diameter of the fiber, but suffer at longer distances and higher data rates compared to SMF-based systems. This is primarily caused by the modal and chromatic dispersion in MMFs for systems when using standard multi-mode VCSELs (MM-VCSEL) [125]. Further challenges in these short-range systems are on the one hand the linear and nonlinear behavior of the VCSELs and on the other hand the limits of modern DACs and ADCs, if advanced modulation formats and DSP are used.

The increasing demand of high-speed short-range links, mainly driven by the application in data centers and the 100/400G Ethernet standardization [3]–[5], has led to many activities in the research community, with the goal to overcome those challenges and further improve the capacity of VCSEL-based links. Different approaches were investigated, like technology improvements, the use of more complex modulation formats and the application of advanced DSP. Especially the last two steps enabled a significant improvement in transmission rate, however at the cost of more complex systems.

4.2 State-of-the-art VCSEL-based high-speed links

VCSEL-based links utilizing OOK as modulation format are the current standard for commercial high-speed short-range solutions [126]. The simple link design, e.g. signal generation at the Tx and application of limiting amplifiers at the Rx, results in low cost and easy fabrication. In the research community several OOK-based VCSEL links were demonstrated in the last years, showing the feasibility for data rates of 50 Gb/s per lane.

In 2013 Westbergh showed an error free (BER $<10^{-12}$) OOK transmission at a data rate of 56 Gb/s back-to-back and 47 Gb/s over 100 m of OM4 type MMF without any digital or analog compensation using an MM-VCSEL [127]. One year later, the same group showed 64 Gb/s over 57 m of MMF with an additional analog equalizer circuit [128]. Larger distances were obtained with OOK by Stepniak, who demonstrated 54 Gb/s over 2.2 km MMF using a single-mode VCSEL (SM-VCSEL) and a digital equalizer at the Rx [77].

Higher data rates can be achieved with higher order modulation formats like 4- and 8-PAM, due to the limited bandwidth of VCSELs and the spectrally inefficient OOK modulation. This led to many research activities in this field, especially after the announcement of 4-PAM as a solution for 100/400 G Ethernet [3], [4]. In 2013 Szczerba showed an error free 60 Gb/s 4-PAM transmission over 100 m of MMF without any equalization [129]. The 4-PAM signal was generated by combining two individual PRBS sequences of different amplitudes. After transmission, the total BER was determined from the independent BER estimations of each 4-PAM sub-eye. Slightly higher transmission rates of 70 Gb/s were also shown by Szczerba in 2015 using an additional equalizer at the Rx [130].

To enable data rates beyond 100 Gb/s with 4-PAM, which would for example be necessary for short range 4x100G single lane Ethernet links, more complex equalizers in combination with FEC are required. Stepniak showed in [79] various 4-PAM transmission experiments utilizing MM/SM-VCSELs, trellis coding and different equalizer structures. Data rates greater than 100 Gb/s were presented over 100 m of MMF. In [80] a group around Karinou investigated the use of maximum likelihood sequence

estimation (MLSE) together with standard finite impulse response (FIR) filters for VCSEL and MMF-based systems. It was shown that 112 Gb/s 4-PAM transmissions over 100 m of MMF are feasible at BERs below the 7% overhead HD-FEC limit and with using MM-VCSELs. Furthermore, it was shown that the bandwidth limitations of the used DACs had a significant influence on the overall DSP performance.

An unconventional 4-PAM format, i.e. 13-level duobinary 4-PAM, enabled in [131] transmission rates of 150 Gb/s over 100 m of OM4 MMF using an MM-VCSEL. It was shown that the spectrum of the 13-level duo-binary format fits ideally to the system frequency response, thus resulting in these ultra high data rates in combination with a FIR/MLSE-based equalizer at Rx and a linear pre-equalizer at the Tx. The VCSEL used in these experiments had a side-mode suppression ratio (SMSR) of only 6 dB, resulting in strong performance degradations at larger distances.

Similar to 4-PAM, 8-PAM is of interest for high-speed short-range VCSEL-based links. It offers a narrower signal bandwidth at the expense of higher SNR requirements and increased sensitivity to ISI. In [130] Szczerba presented a 56 Gb/s transmission over 50 m of MMF below the 7% HD-FEC BER limit without equalizer. The main limitation for these experiments is the ISI and it was shown that for 8-PAM, at least a system bandwidth equal to the symbol rate is required. Experiments with 8-PAM and MM/SM-VCSELs in [79] showed lower transmission rates than 4-PAM for the same setup, especially with severe limitations for MM-VCSEL and 8-PAM scenarios. Data rates beyond 100 Gb/s using 8-PAM, were recently shown by Gebrewold [132] with an MM-VCSEL. The 25 m MMF transmission was realized with linear pre-equalization of the system transfer function and an FFE approach in combination with a maximum-a-posteriori detector.

Multi-carrier modulation formats like multi-band carrier-less amplitude phase modulation[1] (Multi-CAP) and DMT are also of increasing interest for VCSEL-based high-speed short-range links. Multi-carrier approaches offer a better adaptation of the signal to the channel, thus simplifying the equalization effort. However, high-speed and high resolution A/D and D/A converters are required for the generation and detection of these signals. Lu investigated in [134] several MM/SM-VCSELs, in combination with MMFs and a DMT-based transmission. The MM-types showed a better performance for shorter distances (up to 60 Gb/s for 200 m), whereas SM-types performed better at longer distances (up to 50 Gb/s for 2000 m). Similar experiments were presented by Wu in [135], with data rates of up to 68 Gb/s and 82 Gb/s for MM and SM-VCSEL scenarios, respectively. In [136] the same group improved their results and achieved 112 Gb/s over 300 m of OM4 MMF. Own transmission experiments with DMT[2] showed 135 Gb/s over 10 m and 112 Gb/s over 550 m of MMF. Another experiment beyond 100 Gb/s was presented in [133], using Multi-CAP as modulation format. This unconventional modulation format uses several Nyquist-shaped QAM-modulated subcarriers to generate a wideband signal. In theory Multi-CAP has a better PAPR than DMT[3], which makes it more suitable for IM/DD systems but also offers an easy adaptation to the channel and thus relaxes the equalization effort. In detail, a transmission rate of 107.5 Gb/s over 10/100 m of MMF using a MM/SM-VCSELs was presented, respectively.

The use of MMFs for high-speed systems at larger distances (>500 m) is primarily

[1] Multi-CAP modulation consists of several CAP modulated sub-bands (e.g in [133] 16 CAP modulated sub-bands are used), each with its own frequency allocation and modulation order.

[2] Which are presented in this thesis

[3] only a few subcarriers are added, compared to many for DMT

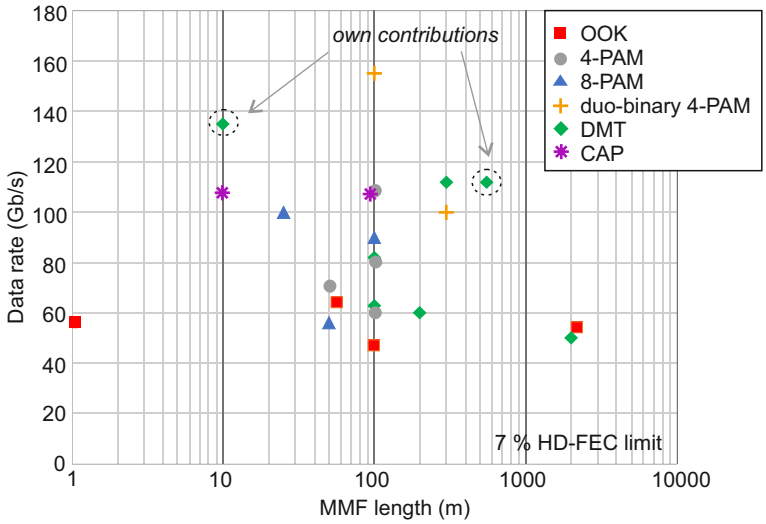

FIGURE 4.1: Overview of state-the-art VCSEL transmissions.

limited due to the chromatic/modal dispersion and high attenuation. Instead, SMF-based systems combined with C-band SM-VCSELs can be used for these links. With simple OOK in combination with a low dispersion SMF, Kuchta showed in [137] an error free transmission of 50 Gb/s over 2 km without DSP. For 4-PAM similar data rates were shown by Karinou over 2 km of SMF using a hybrid FFE/MLSE equalizer at the Rx [138]. In [139] a 1550 nm SM-VCSEL-based link was demonstrated, using DMT as modulation format. The achieved gross rate was beyond 100 Gb/s at distances of few km with BERs below the HD-FEC limit. Distances up to 12 km were reached by Dochhan in [140] with the help of vestigial sideband filtering at the Tx to reduce the influence of the chromatic dispersion. Fig. 4.1 shows an overview of the listed publications.

In the field of nonlinear equalization of VCSEL-based links, there are some interesting publications using different approaches to improve the transmission performance. In [141] static linearisation of measured VCSEL characteristics showed a slight gain for over 300 m of MMF using DMT. Another static approach was shown in [142], also using DMT at 15 Gb/s, resulting in a gain in sensitivity of 1 dB for different MMF lengths. The linear and nonlinear post-equalization of the system transfer function was used in [143], resulting in a 4-PAM transmission of 64 Gb/s over 2 km of MMF. The nonlinear part of the compensation consisted of a pure static approach. The pre-compensation of higher order nonlinear terms with additional memory effects were investigated in [144] using a standard Volterra filter. This resulted in data rates of 50 Gb/s over 200 m of MMF. A further improvement of the performance was realized with an additional post-equalizer.

The publications listed above investigated many aspects of VCSEL-based systems. The focus is on different VCSEL types and technologies, advanced modulation formats and complex equalizer schemes with the common goal to further improve the transmission performance. Nevertheless, there are still many open questions like the compensation of VCSEL nonlinearities and the application of Tx-based equalization. For example in [131], [132], linear Tx pre-equalization was applied to improve the performance. However, further detailed information such as the optimal amount pre-equalization were not given. Also the actual gain of nonlinear compensation is an

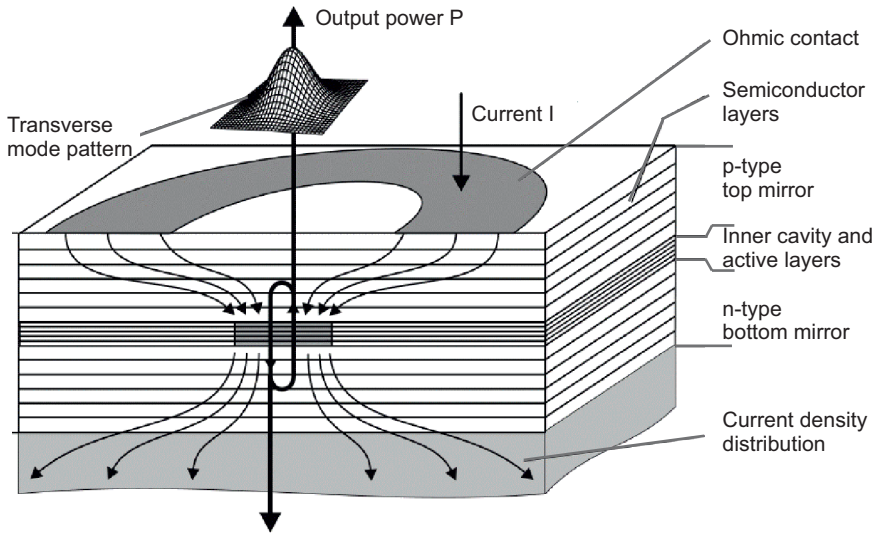

FIGURE 4.2: Schematic layer structure of a VCSEL [40].

open question for these high-speed VCSEL-based links, especially if memory effects are included (i.e. non-static nonlinear compensation). Only few transmission experiments applying nonlinear compensation have been demonstrated at high data rates so far [143], [144] and most of them do not differentiate between linear and nonlinear equalization. The following sections try to answer these questions, give a more detailed insight from the experimental point of view and demonstrate what transmission rates are possible with state-of-the art VCSELs and advanced DSP.

4.3 Vertical cavity surface emitting lasers

This section gives an overview about VCSELs. This includes the structure, the relevant characteristics and their impact on communications systems.

4.3.1 VCSEL structure

Laser is an acronym which stands for "Light Amplification by Stimulated Emission of Radiation" and is used for devices that produce light based on the laser principle. The first laser was demonstrated by Theodore Maiman 58 years ago in 1960 in the form of an optically pumped ruby crystal [145] and led to a wide variety of lasers. The basic operating principle however remains the same, independent of size and results in the unique properties of being highly coherent and monochromatic. Each laser has two basic components, a resonance cavity and an optical gain medium. The stimulated emission takes place in the gain medium, i.e. by stimulating the recombination of an electron-hole pair which results in a new photon with the same wavelength and phase as the stimulating photon. Two mirrors form the resonance cavity and provide a confinement for the photons. This leads to a repeated stimulation process, thus amplifying the light. To enable a positive resonance in the laser, the round-trip distance of the photons has to be an integer number of the photon wavelength.

The gain medium in an electrically pumped semiconductor (in communication applications), usually consists of an intrinsic (undoped) layer of semiconductor material placed between *p*- and *n*-doped layers, which forms a semiconductor diode. If

forward biased, electrons in the conduction band can transit to lower energy states, either spontaneously or stimulated, and emit the surplus energy as light. The specific wavelength of the light is defined by the band gap, i.e. the material used for the gain medium. If the bias current is increased, the amount of stimulated emission exceeds the loss due to absorption and radiation, resulting in the lasing state.

VCSELs were introduced 30 years ago by Kenichi Iga [146] and have gained significant popularity in the last decade [147]. The common structure of most VCSELs is shown in Fig. 4.2. The cavity is located between two parallel distributed Bragg reflectors, which consists of multiple pairs of layers of high and low refractive indices. Each layer has a thickness of one quarter of the material wavelength. The reflectivity of the Bragg reflectors is usually very high to compensate for the small cavity length. Additionally, at least one of the reflectors must be partially transmissive to enable the output of light. The resonance cavity is located between the reflectors and is very short and wide. This geometry supports the emission of a single longitudinal and multiple transverse optical modes. Light is emitted from the VCSEL vertically, along the direction of the cavity. The current is injected from ohmic contacts on the top epitaxial side. Methods such as ion implantation or mesa etching are used to confine the current to a predefined active area [40].

The popularity of VCSELs can be attributed to some of their unique properties, like longitudinal single mode operation, large modulation bandwidth and high-quality circular beams. Further benefits are the convenient 2D array integration and the simple on-wafer testing, which result in overall low-cost fabrication and low power consumption.

4.3.2 VCSEL characteristics

In the following sections relevant VCSEL parameters for optical communications systems are described. These are the static and thermal behavior, the (non)linearity, the frequency behavior, the spectral characteristics and the noise.

4.3.2.1 Static characteristic and thermal behavior

The static characteristics of VCSELs are defined by the relation of input current to the input voltage and output power. Fig. 4.3 shows two examples, (a) from the VCSEL used in the high-speed experiment in Section 4.5 and (b) for the VCSEL simulation model from Section 4.6.2. The figure shows the output power and the voltage across the device as a function of the input current (L-I-V curve). For very small currents below the threshold current, there is nearly no output power. At currents beyond the threshold a strong increase in output power can be observed. In the example this threshold is at 0.3 mA. Above the threshold, the output power grows almost linearly with the input current up to a certain level. Afterwards, saturation occurs and for even higher currents a decrease in output power can be observed. This is known as thermal roll-over and is originated from the heating of the VCSEL.

Thermal mechanisms in VCSELs have a significant influence on their operation and have to be considered. The most important effects are thermal lensing, absorption, optical gain, carrier leakage and carrier recombination [148], [149]. Thermal lensing is a guiding effect induced by refractive index increase at increasing temperature. Free carrier absorption depends on the inverse of the carrier mobility, which scales approximately inversely, nearly quadratic with the temperature [40], [150]. The optical gain decreases with higher temperatures, resulting in higher threshold currents. Carrier leakage describes the phenomenon of escaping carriers from the active region.

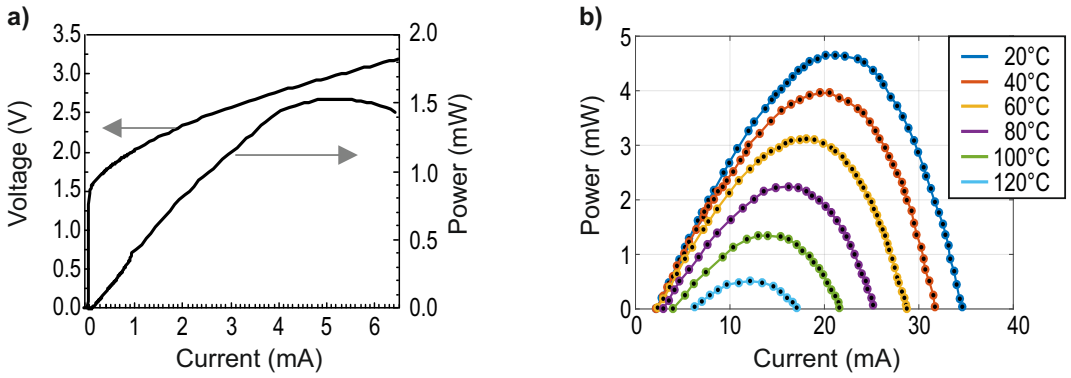

FIGURE 4.3: Examples of optical output power and voltage as a function of bias current for a VCSEL, (a) for the VCSEL used in the high-speed experiments in Section 4.5 and (b) for the used VCSEL simulation model from Section 4.6.2.

It can be explained by the rise of the Fermi levels relative to the potential barrier edges at higher temperatures, thus increasing the escaping probability. Also carrier recombination increases with temperature, reducing the number of carriers available for stimulated emission. The thermal roll-over observed in the VCSEL L-I-V curve can mainly be attributed to carrier leakage and reduced optical gain [148]. Fig. 4.3 (b) shows an example of the SM-VCSEL model used in the simulation [151]. It illustrates the decrease of the output power and the increase of the threshold current with higher temperatures.

Despite the strong influence of thermal mechanisms, today's communication VCSEL are commonly capable to operate at wide temperatures ranges, of up to 80 °C [40]. This simplifies the cooling and enables the application of VCSELs in different environments.

4.3.2.2 VCSEL linearity

Linear behavior is important for communications systems and requires that all devices operate in their linear range. However, since VCSELs are real world devices, their linear dynamic range is limited. The static characteristic from above, commonly gives only insufficient insight into the nonlinear behavior. The static curve originates from the much slower thermal response of the VCSEL compared to the modulation speed. However, with a constant bias and some limited modulation around the bias, the dynamic nonlinearity is typically weaker compared to the static one, which leads to a much better performance for data transmission, as the static characteristic would suggest [152]. This aspect is illustrated in Fig. 4.4. On the left side, in Fig. 4.4 (a), the static behavior of the VCSEL used for the simulations in Section 4.6.2 is shown[4]. As can be observed, the curve indicates a strong nonlinear behavior at bias currents beyond 20 mA. In Fig. 4.4 (b) the same VCSEL is modulated with a single tone of different frequencies at a bias current of 20 mA. After optical-electrical conversion, the power of the tone is measured for different driving VCSEL driving amplitudes, i.e Tx tone powers and compared to the electrical power of the tone in front of the VCSEL. Three observations can be made. First, the maximum power of the tones drops with higher

[4]For a temperature of 20° as already shown in Fig. 4.3

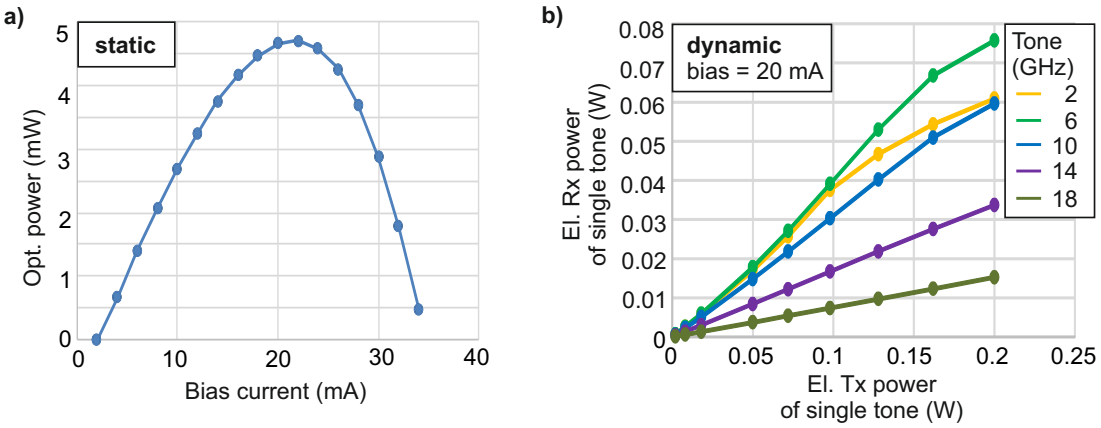

FIGURE 4.4: (a) Static L-I curve of a VCSEL with strong static nonlinearities at bias currents beyond 20 mA.(b) Electrical power of a single tone before the VCSEL (Tx) and after the photodiode (Rx) at different frequencies and a bias current of 20 mA.

frequencies due to the low-pass behavior of the VCSEL. Second, a linear relation of Tx and Rx tone power can be observed up to a certain input power. The exact input power depends on the frequency. In conclusion, even at bias currents which indicates a strong nonlinear behavior of the VCSEL, a linear operation of the VCSEL is possible. Furthermore, higher signal frequency terms are less affected by the nonlinear VCSEL behavior.

For IM/DD-based transmission systems, sufficient optical power in the data signal compared to the optical carrier is required. This results in a trade-off for the modulation amplitude in these systems. For too small amplitudes, the SNR requirements are not met and for too high amplitudes nonlinear distortions dominate. This is more critical for more advanced modulation formats like DMT or pulse-shaped PAM, which have higher PAPRs and thus require higher linearity. The description of the dynamic nonlinearities can be done with the classic spurious-free dynamic range (SFDR) measurement, which takes the distance[5] between the wanted tone and the worst harmonics into account [153]. The so gained values allows a description of the device with the help of polynomials and filters, as shown in Section 3.4.1. However, SFDR measurements do not include nonlinear memory effects[6]. These can be characterized with a Volterra series approach as used in this thesis.

Additional to the static nonlinear characteristic of the L-I curve, there are several modulation effects which have a negative impact on the linearity of the VCSEL, especially if OOK is applied. These are e.g. turn-on delays, relaxations oscillations or off-state bounces. Turn-on delays are only relevant, if the pulse zero level is below the threshold current, due to the required time to build up a sufficient carrier density. Relaxation oscillations are critical at very low modulation and bias currents [154]. Note that at symbol rates close to the relaxation frequency, impairments due to the drop in the frequency response occur. Off-state bounce is a small increase in optical power after the falling edge of a pulse and is related to carrier gradient between the lasing region and the surrounded material [154]. A further interesting effect is the skew of each sub-eye for multilevel modulation formats like 4- and 8-PAM. In Fig. 4.5 an example

[5] relative power

[6] For example the dependency of the delay and the VCSEL bias cannot be described with SFDR measurements

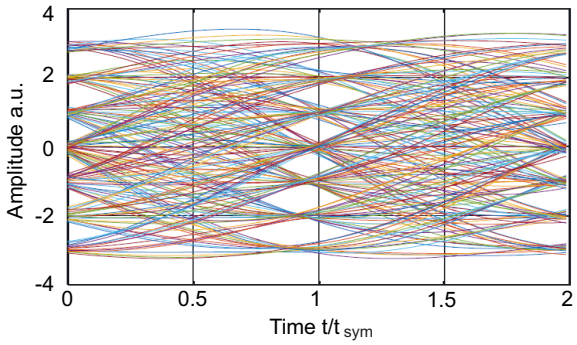

FIGURE 4.5: Averaged eye diagram for VCSEL-based btb transmission using duo-binary 4-PAM [155].

for an electrical duobinary 4-PAM signal with 7 amplitude levels after the transmission over a VCSEL-based link is shown[7]. The eye diagram was published in [155], where a DSP approach for the skew compensation is demonstrated. At the decider this skew would results in a large amount of errors and has to be avoided, either by lowering the VCSEL driving amplitude or with compensation approaches. The compensation approach presented in [155], is based on interpolation plus calculation of the standard deviation of each sub-eye to determinate the skew value. A further approach, utilized in this thesis, is a nonlinear Volterra-based pre-equalization described in Section 4.4.2.4.

4.3.2.3 VCSEL frequency response

The frequency response of a VCSEL is an important parameter for a communication system and defines the maximum useful modulation bandwidth. An analytical description can be deduced from the well known laser rate equations [40] in the form of

$$\frac{\mathrm{d}N_{\mathrm{cr}}}{\mathrm{d}t} = \frac{\eta_{\mathrm{I}} j_{\mathrm{IN}}}{q d_{\mathrm{a}}} - \frac{N_{\mathrm{cr}}}{\tau_{\mathrm{sp}}(N_{\mathrm{cr}})} - \Gamma_{\mathrm{r}} g(N_{\mathrm{cr}}) S_{\mathrm{ph}} \nu_{\mathrm{gr}} + F_1(t) \tag{4.1}$$

$$\frac{\mathrm{d}S_{\mathrm{ph}}}{\mathrm{d}t} = \Gamma \beta_{\mathrm{sp}} \frac{N_{\mathrm{cr}}}{\tau_{\mathrm{sp,r}}(N_{\mathrm{cr}})} + \Gamma \Gamma_{\mathrm{r}} g(N_{\mathrm{cr}}) S_{\mathrm{ph}} \nu_{\mathrm{gr}} - \frac{S_{\mathrm{ph}}}{\tau_{\mathrm{p}}} + F_2(t), \tag{4.2}$$

where Equation 4.1 is the change in carrier N_{cr} (electron or hole) density and Equation 4.2 in photon density S_{ph} for a single transverse mode emission. The first term in Equation 4.1 relates to the gain in carriers, generated by the injected current density j_{IN} which is additionally scaled by the injection efficiency η_{I} (takes into account loss due to lateral leakage and carrier overflow over confining barriers, commonly $\eta_{\mathrm{I}} >$ 95% [40]). The values q and d_{a} are the elementary charge and the total thickness of the active layer, respectively. The second term in Equation 4.2 relates to the loss in carriers due to the spontaneous emission. It is defined by carrier density dependent spontaneous recombination lifetime[8] $\tau_{\mathrm{sp}}(N_{\mathrm{cr}})$, which takes the non-radiative surface

[7] Interestingly, the delay is stronger at higher amplitudes. This is counter intuitive, since it can be expected that the VCSEL response improves with higher amplitudes, which is confirmed by own eye diagrams from measurements and simulations in Section 4.6

[8] Note that the spontaneous recombination lifetime, as described in [40], depends on the carrier density as $\frac{1}{\tau_{\mathrm{sp}}(N_{\mathrm{cr}})} = \frac{1}{\tau_{\mathrm{sp,r}}(N_{\mathrm{cr}})} + \frac{1}{\tau_{\mathrm{sp,n}}(N_{\mathrm{cr}})} = A + BN_{\mathrm{cr}} + CN_{\mathrm{cr}}^2$ with the A-, B- and C-terms characterizing non-radiative surface, radiative bimolecular recombination and Auger recombination, respectively. The radiative recombination is denoted as $\tau_{\mathrm{sp,r}}$ and the radiative as $\tau_{\mathrm{sp,n}}$.

or interface recombination[9] , radiative bimolecular recombination[10] and the Auger recombination[11] into account [40]. The third term is the loss due to the stimulated emission. It is given by the gain enhancement factor Γ_r, which represented the average longitudinal intensity in the active layer normalized to that of the inner cavity and is typically between 1 and 2 [40]. The next terms are the carrier-dependent material gain $g(N_{cr})$, the photon density S_{ph} and the group velocity of the laser mode ν_{gr}. The last term stands for the Langevin forces $F(t)$, which describe the statistical nature of the spontaneous emission events that are responsible for the laser noise.

Equation 4.2 defines the change in the photon density S_{ph} similar to Equation 4.1. The first term relates to the gain in photons due to the spontaneous recombination with the spontaneous recombination rate $\beta_{sp} N_{cr} / \tau_{sp,r}(N_{cr})$ and the total confinements factor Γ (total gain enhancement factor), which considers the transverse and longitudinal overlap of the intensity profile. The factor β_{sp} is the spontaneous emission factor and $\tau_{sp,r}$ the radiative part of the spontaneous recombination lifetime. The second term in Equation 4.2 relates to the gain in photons due to the stimulated emission. The third term is the photon loss due to optical loss and out-coupling, defined by the photon lifetime τ_p. Note that these equations neglect the carrier transport effects into the quantum wells surrounding barrier layers, spatial hole burning[12] effects and the associated lateral carrier diffusion as well as temperature dependencies.

To infer the transfer function of the VCSEL, the rate equations are developed around an operation point, linearized and Fourier transformed [40]. Neglecting the spontaneous emission and the Langevin forces, the transfer function, i.e. the relation between the photon density fluctuation to those of the modulation current is given as

$$H_{laser}(\nu) = \frac{\Delta S_{ph}(\nu)}{\Delta I(\nu)/q} = \frac{A}{4\pi^2(\nu_r^2 - \nu^2) + i2\pi\gamma\nu} \tag{4.3}$$

with the amplitude factor A

$$A = \frac{\eta_I \nu_{gr} \Gamma_r \bar{a} S_{ph,0}}{V_p(1 + \epsilon S_{ph,0})}. \tag{4.4}$$

Here $S_{ph,0}$ is the operating point photon density, $\bar{a}$ the differential gain coefficient[13] , ϵ a gain compression factor considering spectral hole burning and V_p the effective volume occupied by the lasing mode. The factors γ and ν_r are the damping coefficient (damping of the relaxation oscillation) and the relaxation resonance frequency, respectively. The relaxation resonance frequency is related to the damping factor by the so called K-factor [40]

$$K = \frac{\gamma - \frac{1}{\tau_{sp}}}{\nu_r^2}\ , \tag{4.5}$$

which defines the maximum 3 dB modulation frequency of the VCSEL.

$$\nu_{max} = \sqrt{2}\frac{2\pi}{K}. \tag{4.6}$$

[9] Atoms at the surface of a semiconductor can have electronic states that can be located in the forbidden gap of the semiconductor where they act as recombination center.

[10] The recombination that involves two free carriers simultaneously

[11] In Auger recombination the energy is given to a third carrier, which is excited to a higher energy level without moving to another energy band. After the interaction, the third carrier normally loses its excess energy to thermal vibrations

[12] Spatial hole burning is a distortion of the gain shape in a laser medium, caused by saturation effects of a standing wave.

[13] The linearized part of the carrier dependent gain coefficient $g(N_{cr})$

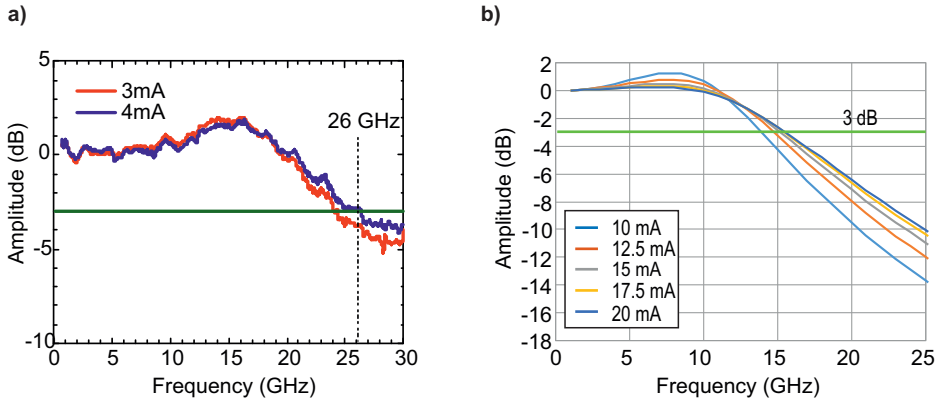

FIGURE 4.6: (a) Frequency response of the high-speed VCSEL type used in the experiments in Section 4.5 for different bias currents. (b) Frequency response of the lower-speed VCSEL simulation model from Section 4.6 at different bias currents.

Note that this relation only takes into account the intrinsic modulation limit of the VCSEL and no additional parasitic effects. The values of ν_r and γ can be obtained from measurements and they result, if used in Fig. 4.3, in the typical VCSEL frequency response.

Fig. 4.6 shows two different examples for a VCSEL frequency response, (a) for the VCSEL type used in the experiments in Section 4.5 and (b) for the VCSEL simulation model used in Section 4.6. Both show the typical shift in resonance frequency[14] and an increased 3 dB bandwidth at higher bias currents. This reveals an interesting trade-off for high-speed systems. On the one hand a high modulation bandwidth is necessary to maximize the data rate, which requires higher bias currents, on the other hand, high bias currents result in a smaller modulation index and more nonlinearities. In Section 4.6.5 this trade-off is further discussed in detail. Today's VCSELs have 3 dB bandwidths >25 GHz, which enables their application for 100/400G Ethernet. For example in [156] a 28 GHz bandwidth SM-VCSEL was demonstrated, enabling an error-free 47 Gb/s OOK transmission. The VCSELs used in this thesis have 3 dB bandwidths of up to 25 GHz and have been modulated up to 30 GHz [157].

4.3.2.4 Spectral characteristics

Today's VCSELs in communication applications have a single longitudinal mode and multiple transverse modes. Since each transverse mode has a slightly different wavelength, a relatively broad spectrum exists[15]. This is originated in the different effective refractive indices for each transverse mode, due to their different field distributions in the VCSEL [158]. Further, there is a dependence on the laser bias current, resulting in a broader spectrum at higher currents. The total laser bandwidth is therefore much larger than the typical signal modulation bandwidth, thus the spectral efficiency in the optical domain is very small. However, due the broad spectrum, effects related to the chromatic dispersion are critical. The different group velocities of the VCSEL modes result in the typical RF fading effect after transmission over a dispersive medium and direct detection at a photodiode. Approaches to overcome these issues are the use of

[14] the relaxation oscillation is temperature dependent [40]

[15] At 1000 nm emission wavelength, a wavelength difference of $\Delta\lambda \approx 1$ nm is possible [158]

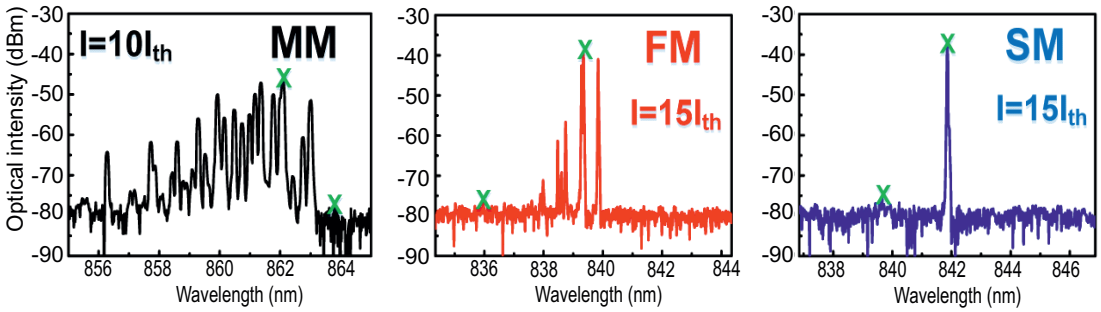

FIGURE 4.7: Optical spectra of multi, few and single mode VCSEL shown in [125].

VCSELs with only a few or a single transverse mode (FM and SM-VCSEL). These devices have a stronger transverse confinement around the active layer, e.g. realized with oxidation [40] and thus permit only the generation of a single or only a few transverse mode(s). Examples of an MM, FM and SM-VCSEL emission spectra are shown in Fig. 4.7. The challenge of the stronger transverse confinement is typically a reduced output power and a more complicated realization. Transmission experiments over 100 m of MMF with these devices showed a significantly better performance for the FM and SM-VCSEL [125]. However, for very short distances (a few m) MM-VCSEL are more advantageous due to their easier realization and generally higher output power.

4.3.2.5 VCSEL noise

The most important noise parameter in VCSELs is the relative intensity noise, which captures all noise sources related to fluctuations in the laser intensity. This includes fundamental aspects like spontaneous emission, shot noise and the mixing of spontaneous emission with the lasing field. Further aspects are electrical noise, back reflections and vibrations. The RIN generally varies with the bias current and the frequency. The amount of RIN is commonly given in dB/Hz and can be measured [159]. High RIN values impose power penalties at the receiver, which results in a BER error floor [160]. For high-speed systems RIN values <-140 dB/Hz are recommended [161], which is satisfied by the high-speed VCSELs used in this thesis[16]. The spectrum of the RIN is not white and peaks at the laser resonance frequency and for MM-VCSEL also at low frequencies due to mode competition [162]. Another noise source is related to the different transverse modes of a VCSEL and is called mode partition noise (MPN). The total power of an MM-VCSEL is partitioned between several transverse lasing modes, which fluctuate over time. In total these fluctuation are compensating each other, resulting in a relatively small total noise. However, if there is mode dispersion or discrimination of certain modes, as it is the case during the fiber transmission, the compensation fails and a significant increase in noise can be observed [163].

4.4 VCSEL-based high-speed transmission link

This section describes the VCSEL-based high-speed transmission system, as used in the experiments and simulations. This includes all components, the occurring distortion effects and the DSP approaches to improve the transmission performance. Since

[16] data sheet RIN values

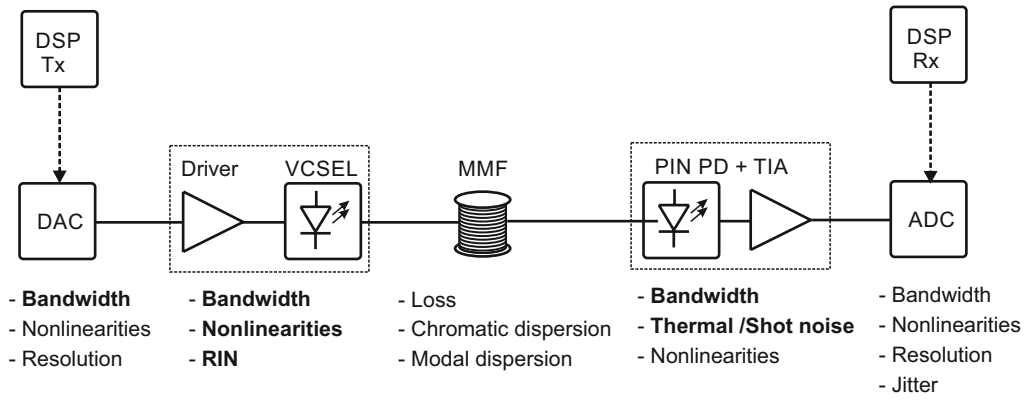

FIGURE 4.8: System model for high-speed short-range VCSEL-based transmission with impairments of each component. Relevant impairments for this work are highlighted.

most of the components are the same as in the more general description of high-speed short-range systems in Chapter 2, only the differences are discussed. Further, remarks about the used modulation formats are given.

4.4.1 System model for VCSEL-based high-speed link

The system model for the high-speed VCSEL-based links used in this work is shown in Fig. 4.8. Below each component, the most important impairments and noise sources are shown. For the DAC, ADC and the photoreceiver these were already discussed in Chapter 2. The VCSEL driver consists of an amplifier with an additional bias-tee, to set the VCSEL bias current and the necessary driving amplitude. The bandwidth of the driver is commonly not a critical aspect, e.g. in the experiment a 40 GHz device is used and the additional noise from the amplifier is minor compared to other noise sources in the system. Note that the amplifier nonlinearities are small compared to the VCSEL nonlinearities, due to the low signal power required to drive the VCSEL. Therefore the influence of the driver is neglected.

The important VCSEL parameters are the modulation bandwidth, the linearity and the RIN. The bandwidth of the VCSEL is commonly higher than of the DAC and the photoreceiver for today's high-end systems but the linearity is worse [157], [164], especially at higher bias currents which are required to minimize the RIN and to improve the VCSEL frequency response.

The main impairments for MMF-based transmissions are the modal and chromatic dispersion. For the transmission experiments, both are relevant at longer distances due to the very high signal bandwidth and the limited side-mode suppression ratio of the VCSELs. The dispersion induced RF power fading results in a strong low-pass characteristic for the MMF, which degrades the transmission performance at longer distances. The higher fiber loss of the MMF compared to the SMF is typically only relevant for longer distances but can limit the transmission performance[17].

At the receiver side, there is an additional bandwidth limitation due to the integrated photoreceiver. Currently, commercially available MMF receivers have bandwidths up to 22 GHz. This is less compare to the VCSELs used in the experiments

[17]The used MMF in the experiments (OM4 type) has an attenuation of ~3 dB/km. The relatively small output power of the used high-speed VCSELs [164] can be critical if a sufficient optical power at the photodiode is targeted, especially if additional losses are considered, e.g. from connectors.

[164]. The used ADC has a significantly higher bandwidth (32 GHz) and a better bit resolution compared to the DAC (19 GHz), but the additional noise from the integrated ADC amplifiers decreases the signal SNR further.

The transmission system shown in Fig. 4.8 can be improved, i.e. increasing the transmission rate, by utilizing DSP in terms of linear and nonlinear pre-equalization[18]. The main noise sources in the system from Fig. 4.8 are located at the VCSEL and the receiver, whereas the main bandwidth limitation is located at the DAC prior to the VCSEL. This should result in a gain in transmission performance, if a linear pre-equalization is applied, since the negative implications of pre-equalization like noise enhancement[19] are minor due to the relatively low noise level at the output of the DAC. The nonlinear pre-equalization should compensate for the nonlinear VCSEL characteristic, enabling the transmission of a less distorted signal.

4.4.2 Volterra-based system model

To give an accurate description of the transmission system a Volterra series approach is used. This Volterra model includes all linear and nonlinear memory effects, like low-pass behavior and VCSEL nonlinearity. With the known system model it is possible to compensate the non-ideal transfer characteristic. This section is divided into three parts. First, a brief introduction to the Volterra series is given, followed by the definition of the Volterra filter. Afterwards, the calculation of the pre-equalized signal is explained.

4.4.2.1 Volterra filter

The Italian mathematician Vito Volterra first introduced the notion of Volterra series in his "Theory of Functionals and of Integrals and Integro-Differential Equations" [165]. The first major application of Volterra's work to nonlinear circuit analysis was done by Wiener in a classified wartime report in 1943 [166]. Since then, Volterra series have found a great deal of use in calculating small but nevertheless troublesome distortion terms in various nonlinear systems.

A linear, causal system with memory can be described by the convolution representation

$$y_1(t) = \int_{t_1=0}^{t} x(t-t_1)h(t_1)dt_1, \tag{4.7}$$

where $x(t)$ is the causal driving function, $y_1(t)$ is the output and $h_1(t)$ is the linear causal impulse response of the system. For a nonlinear system of second order, the following can be written

$$y_2(t) = \int_{t_1=0}^{t}\int_{t_2=0}^{t} x(t-t_1)x(t-t_2)h(t_1,t_2)dt_1dt_2, \tag{4.8}$$

where $h_2(t_1,t_2)$ represents the second order impulse response. For p orders this results in

$$\begin{aligned} y(t) &= \sum_{i=1}^{p} y_p(t) = \int_{t_1=0}^{t} x(t-t_1)h(t_1)dt_1 + ... \\ &+ \int_{t_1=0}^{t} ... \int_{t_p=0}^{t} x(t-t_1)\cdot ...x(t-t_p)h_p(t_1,...,t_p)dt_1...dt_p. \end{aligned} \tag{4.9}$$

[18]Note that equalizers at the Rx are mandatory for high-speed application as shown in Section 4.2

[19]The SNR after the DAC is reduced by pre-equalization, e.g. by compensating the low-pass characteristics of the DAC.

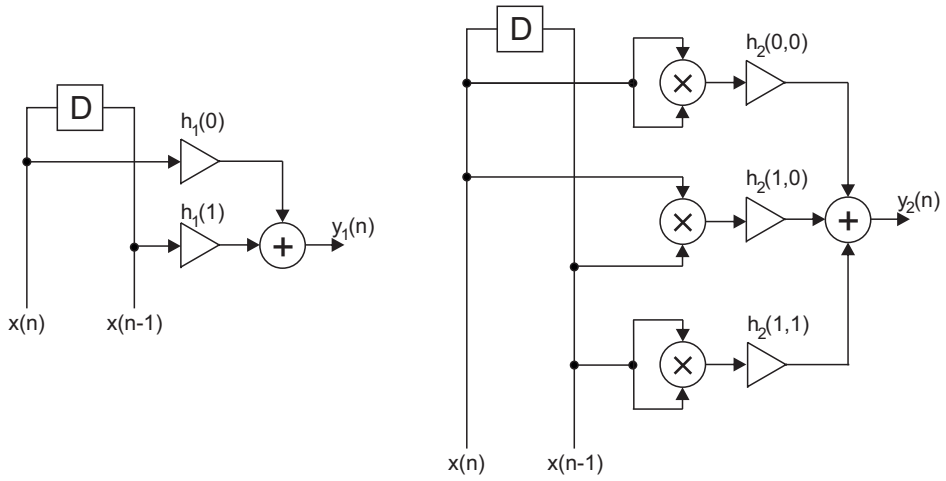

FIGURE 4.9: Realization of a Volterra filter consisting of linear and nonlinear terms with a memory length of two. The DC part is neglected.

where $h_{1...p}$ are the impulse responses of order p known as the Volterra kernels. The discrete (digital) form is

$$y(n) = h_0 + \sum_{k_1=0}^{N_1-1} h_1(k_1)x(n-k_1) + \sum_{k_1=0}^{N_1-1} + ... + \sum_{k_p=0}^{N_p-1} h_p(k_1,...,k_p)x(n-k_1)\cdot ...x(n-k_p), \tag{4.10}$$

where $N_{1...p}$ denotes the memory length of the Volterra kernels of the different orders and h_0 an additional DC part[20]. One important property of the Volterra series is the kernel symmetry. This means that for any p permutations of indices in $h_p(k_1,...,k_p)$, h_p does not change. For example, the second order Volterra kernels with memory length 2 are $h_2(0,0)$, $h_2(1,0)$, $h_2(0,1)$ and $h_2(1,1)$. Due to the symmetry, $h_2(1,0)$ and $h_2(0,1)$ are identical. This results in a significant reduction of kernel elements, which reduces the calculation complexity. The output of a system, consisting of linear and 2nd order nonlinear terms with channel lengths of N_1 and N_2 respectively[21], can therefore be written as

$$y(n) = \sum_{k_1=0}^{N_1-1} h_1(k_1)x(n-k_1) + \sum_{k_1=0}^{N_2-1}\sum_{k_2=k_1}^{N_2-1} h_2(k_1,k_2)x(n-k_1)x(n-k_2). \tag{4.11}$$

Note that the factor 2 originating from the kernel symmetry can be included into $h_2(k_1,k_2)$. If we represent the first order term as y_1 and second order term as y_2, we can write

$$y(n) = y_1(n) + y_2(n). \tag{4.12}$$

A Volterra filter with linear and nonlinear (2nd order) channel lengths of $N_1 = N_2 = 2$, can be realized as shown in Fig. 4.9. In the analog domain, the linear term can be realized with the help of a delay represented by D in Fig. 4.9, amplifiers with a gain corresponding to the Volterra coefficients and an adder [167]. The realization of the second order term requires additional multipliers, adders and amplifiers. As can be observed, higher order terms and longer channel memories require significantly more

[20]The DC part originates from the integration.
[21]without DC

kernel elements. For example, a filter length of 10 taps requires 10, 100 and 1000 kernel elements for the 1st, 2nd and 3th order Volterra kernel, respectively. This limits its usability in communication systems due to computational effort and delay.

4.4.2.2 Linearity of Volterra filter

One of the properties of a Volterra filter is the linearity with respect to the filter coefficients [168], i.e. it can be applied with a simple matrix multiplication. The property is evident from the realization of the individual terms of the series in Equation 4.11. The Volterra kernels are being multiplied by bias terms, first order input samples, second order input samples constructed with the help of multipliers and so on and then is summed. This enables the application of tools that are used for linear system analysis such as least squares (LS) and can be visualized with the help of matrix notations. For the previous example of a second order Volterra filter with the uniform filter length $N_1 = N_2 = 2$, the expanded Volterra series for the specific example is obtained as

$$\begin{aligned} y(n) = h_1(n)x(n) + h_1(1)x(n-1) + h_2(0,0)x^2(n) \\ +h_2(0,1)x(n)x(n-1) + h_2(1,1)x^2(n-1). \end{aligned} \tag{4.13}$$

In form of a matrix vector product this is

$$[\boldsymbol{y}] = [\boldsymbol{x}][\boldsymbol{h}], \tag{4.14}$$

with

$$\begin{aligned} [\boldsymbol{y}] &= \begin{bmatrix} y(0) & y(1) & \dots & y(j-1) \end{bmatrix}_j^T \\ [\boldsymbol{x}] &= \begin{bmatrix} x(0) & x(-1) & x^2(0) & x(0)x(-1) & x^2(-1) \\ x(1) & x(0) & x^2(1) & x(1)x(0) & x^2(0) \\ \vdots & \ddots & \vdots & & \\ x(j-1) & x(j-1) & x^2(j-1) & x(j-1)x(j-2) & x^2(j-1) \end{bmatrix}_{jxq} \\ [\boldsymbol{h}] &= \begin{bmatrix} h_1(0) & h_1(1) & h_2(0,0) & h_2(0,1) & h_2(1,1) \end{bmatrix}_q^T, \end{aligned} \tag{4.15}$$

where j is the number of samples in the input sequence and q is the total number of Volterra kernel elements and ^{T} denotes the transposed matrix. The matrix $[\boldsymbol{x}]$ consists of the linear and higher order terms of the input signal $x(n)$ extended to a Toeplitz structure[22] , $[\boldsymbol{y}]$ is the output signal vector and $[\boldsymbol{h}]$ a vector consisting of all Volterra kernels. This representation simplifies the channel convolution into a simple matrix multiplication and enables the estimation of all kernel elements with e.g. an LS approach.

4.4.2.3 Channel estimation using Volterra filter

Prior to the pre-equalization of the Tx signal, a sufficient estimation of the system transfer function is required. In case of the Volterra filter approach all kernel elements or coefficients must be estimated. This is done with the help of a known test sequence as shown in Fig. 4.10.

[22] A Toeplitz matrix is a matrix in which each descending diagonal from left to right is constant. A equation system in the form of $Ax = b$, with A a Toeplitz matrix, can be solved more efficiently due to the reduced numbers of degrees of freedom.

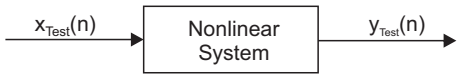

FIGURE 4.10: Schematic for channel estimation using a test sequence.

The known test sequence $x_{\text{Test}}(n)$ is transmitted over the channel and enables the calculation of all filter elements at the receiver. A possible solution is the use of the LS algorithm for the calculation [117]. Using the matrix vector form of Equation 4.14, the received test sequence vector is:

$$[\boldsymbol{y}_{\text{Test}}] = [\boldsymbol{x}_{\text{Test}}][\boldsymbol{h}] \tag{4.16}$$

where $[\boldsymbol{x}_{\text{Test}}]$ consists of the linear and higher order terms of the input signal $x_{\text{Test}}(n)$ extended to a Toeplitz structure, $[\boldsymbol{y}_{\text{Test}}]$ is the output signal vector and $[\boldsymbol{h}]$ a vector consisting of all Volterra kernels. The filter coefficients can now be calculated by

$$[\boldsymbol{h}] = [\boldsymbol{x}^{+}_{\text{Test}}][\boldsymbol{y}_{\text{Test}}] = \left([\boldsymbol{x}_{\text{Test}}]^{T}[\boldsymbol{x}_{\text{Test}}]\right)^{-1}[\boldsymbol{x}_{\text{Test}}]^{T}[\boldsymbol{y}_{\text{Test}}]. \tag{4.17}$$

with $[\boldsymbol{x}^{+}_{\text{Test}}]$ the pseudo-inverse[23] input matrix and $^{-1}$ denoting the matrix inverse. Note that the used test sequence $x_{\text{Test}}(n)$ is commonly significantly longer than the channel memory, which results in an over determined system[24]. For a valid approximation of the channel, it is required that the influence of the nonlinearities do not dominate the linearities. Otherwise, the matrix will be ill conditioned and the optimization and calculation of the pseudo inverse can result in large numerical errors. This condition is satisfied in case of the VCSEL-based communication system, since bandwidth limitations are the dominating restrictions.

There are two additional properties for the successful estimation and pre-equalization of the system characteristic. The first one is related to the properties of the test sequence, which should have no gaps in the targeted channel bandwidth. For example, a simple solution is the use of a test signal with a white Gaussian noise structure. The second property is related to the bandwidth of the actual data signal relative to the estimated channel bandwidth and is especially important for the correct estimation of the nonlinear Volterra kernels. The bandwidth of the actual test sequence has to be as close as possible the used signal bandwidth, with a slight overhead[25]. In the experiments and simulations, the test sequence consisted of uniformly distributed random numbers, with the signal bandwidth adapted to the expected data signal.

4.4.2.4 Signal pre-equalization using Volterra filter

With the information of the channel in form of a Volterra filter, it is possible to apply post or pre-equalization schemes to the signal to compensate for the channel transfer characteristic. In Section 4.2 it was shown that many different post-equalization

[23] a generalized inverse of a non quadratic matrix

[24] j » q in Equation 4.15

[25] A test signal with a smaller bandwidth than the data signal results in a lack of information at frequencies beyond the test sequence. A test signal with a bandwidth beyond the data signal results in less nonlinear impairments due to the low-pass characteristic of the system, thus the estimation of the nonlinear Volterra kernels is not sufficient.

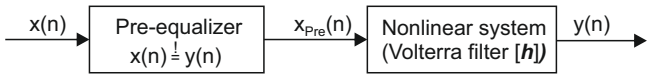

FIGURE 4.11: Schematic for signal pre-equalization at the Tx.

schemes can successfully be applied for these high-speed links, resulting in a significant improvement of the transmission performance. However, only minor investigations of linear and nonlinear pre-equalization schemes were demonstrated for high-speed short-range links.

In contrast to post-equalization schemes, which are performed at the receiver after channel transmission, pre-equalization schemes are applied at the transmitter prior to transmission. One benefit of this approach is the mitigation of noise enhancement, which is the increase of the total amount of signal noise at the receiver after necessary post-equalization. The nonlinear pre-compensation offers the transmission of a less disturbed signal over the fiber, which can ease the post-equalization effort. However, there are a few challenges as well. First, pre-equalization requires the exact channel information at the transmitter site, which can be difficult to obtain due to the channel noise and may be delayed as it has to be transmitted over the reverse link direction. To overcome this, it is common to apply an additional simplified post-equalizer[26], especially regarding the exact phase relation of the signal before decision. A second problem is the loss in SNR for strong linear pre-equalization, since the pre-equalization may shift power from the lower frequencies of the signal to the higher ones[27], which are still strongly attenuated by the channel.

The pre-equalization approach used in this thesis, shown in Fig. 4.11, is based on the calculation of the pre-equalized signal [169] and not on an inverse Volterra filter. The input signal $x(n)$ is pre-equalized, resulting in $x_{\mathrm{Pre}}(n)$ and filtered with the previously gained Volterra filter[28] resulting in $y(n)$. A successful pre-equalization is achieved, if $x(n) = y(n)$. Therefore, the desired pre-equalized signal $x_{\mathrm{Pre}}(n)$ and the input signal $x(n)$ are related as

$$[\mathbf{y}] = [\boldsymbol{x}] = [\boldsymbol{x}_{\mathrm{Pre}}][\boldsymbol{h}] \tag{4.18}$$

where $[\boldsymbol{x}_{\mathrm{Pre}}]$ consists of the linear and higher order terms of the desired input signal $x_{\mathrm{Pre}}(n)$ extended to a Toeplitz structure, $[\boldsymbol{x}]$ is the input signal vector, $[\boldsymbol{y}]$ is the output signal vector and $[\boldsymbol{h}]$ a vector consisting of all Volterra kernels, describing the previously estimated channel. After splitting $[\boldsymbol{h}]$ and $[\boldsymbol{x}_{\mathrm{Pre}}]$ in the linear ($[\boldsymbol{x}_{\mathrm{Pre},1}]$, $[\boldsymbol{h}_1]$) and higher order terms[29] ($[\boldsymbol{x}_{\mathrm{Pre},m}]$, $[\boldsymbol{h}_m]$) and neglecting the DC part

$$[\boldsymbol{x}] = [\boldsymbol{x_1}] + \sum_{m=2}^{p} [\boldsymbol{x_m}] = [\boldsymbol{x}_{\mathrm{Pre},1}][\boldsymbol{h}_1] + \sum_{m=2}^{p} [\boldsymbol{x}_{\mathrm{Pre},m}][\boldsymbol{h}_m]. \tag{4.19}$$

The variable p is the highest order of the filter. For the example shown in Equation 4.15 with a second order Volterra filter ($\boldsymbol{h}_{1,2}$]) and a uniform filter length of $N = 2$, this results in

$$[\boldsymbol{x}_{\mathrm{Pre},\mathbf{1}}] = [\boldsymbol{x_1}] + [\boldsymbol{x_2}] = [\boldsymbol{x}_{\mathrm{Pre},1}][\boldsymbol{h}_1] + [\boldsymbol{x}_{\mathrm{Pre},2}][\boldsymbol{h}_2] \tag{4.20}$$

[26] e.g. a linear equalizer consisting only of a few taps
[27] in case of a low-pass characteristic
[28] From Equation 4.17
[29] second order and beyond

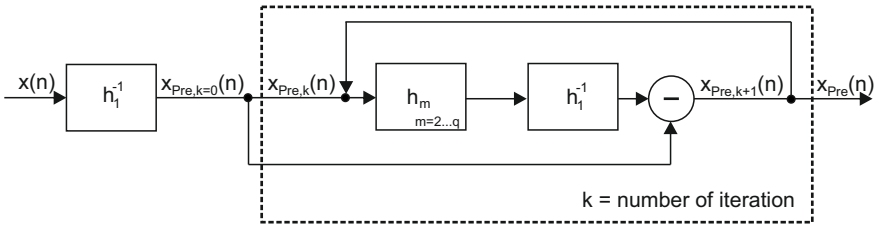

FIGURE 4.12: Estimation of the pre-equalized signal with an iterative approach.

with

$$
\begin{aligned}
[\boldsymbol{x}_{\mathrm{Pre},1}] &= \begin{bmatrix} x(0) & x(-1) \\ x(1) & x(0) \\ \vdots & \vdots \\ x(j-1) & x(j-1) \end{bmatrix} & [\boldsymbol{h}_1] &= \begin{bmatrix} h_1(0) \\ h_1(1) \end{bmatrix} \\
[\boldsymbol{x}_{\mathrm{Pre},2}] &= \begin{bmatrix} x^2(0) & x(0)x(-1) & x^2(-1) \\ x^2(1) & x(1)x(0) & x^2(0) \\ \vdots & \ddots & \vdots \\ x^2(j-1) & x(j-1)x(j-2) & x^2(j-1) \end{bmatrix} & [\boldsymbol{h}_2] &= \begin{bmatrix} h_2(0,0) \\ h_2(0,1) \\ h_2(1,1) \end{bmatrix}
\end{aligned}
\tag{4.21}
$$

In the next step Equation 4.19 is multiplied with the inverse linear Volterra coefficients $[\boldsymbol{h}_1]^{-1}$,

$$
[\boldsymbol{h}_1]^{-1}[\boldsymbol{x}] = [\boldsymbol{x}_{\mathrm{Pre},1}] + \sum_{m=2}^{p} [\boldsymbol{x}_{\mathrm{Pre},m}][\boldsymbol{h}_m][\boldsymbol{h}_1]^{-1} \tag{4.22}
$$

and rearranged into

$$
[\boldsymbol{x}_{\mathrm{Pre},1}] = [\boldsymbol{x}][\boldsymbol{h}_1]^{-1} - \sum_{m=2}^{p} [\boldsymbol{x}_{\mathrm{Pre},m}][\boldsymbol{h}_m][\boldsymbol{h}_1]^{-1}. \tag{4.23}
$$

This equation is a so called fixed point problem [169] with the structure of $x = g(x)$ and can be numerically solved with an iterative approach and a guessed start value for x[30]. Note that $[\boldsymbol{x}_{\mathrm{Pre},m}]$ can be directly calculated from $[\boldsymbol{x}_{\mathrm{Pre},1}]$ as shown in Equation 4.21. In Fig. 4.12 the process is shown. At first, the inverse of the linear channel h_1^{-1} is convolved with the input signal $x(n)$. The resulting signal is called $x_{\mathrm{Pre},k=0}$,with k the actual number of the iteration. Then $x_{\mathrm{Pre},k}$ is convolved only with the higher order terms h_m of the Volterra filter and further convolved with the inverse of the linear channel. The resulting signal is subtracted from the linear inverted input signal $x_{\mathrm{Pre},k=0}$ resulting in $x_{\mathrm{Pre},k+1}$. This process is repeated up to the point where the difference between $x_{\mathrm{Pre},k+1}$ and $x_{\mathrm{Pre},k}$ is minimal or below a threshold.

This approach commonly converges successfully, when only minor nonlinearities are present. However, in the experiments and simulations it was observed that strict limitations regarding the signal amplitudes are necessary, otherwise no convergence can be achieved. This is especially important for OFDM due to its high PAPR. There are also several other solutions to calculate the nonlinear pre-equalized signal, like the estimation of an inverse Volterra filter with an iterative learning algorithm as described in [170].

[30] In the actual case the linear inverted signal is used as a start value for the fixed point problem.

4.4.3 Modulation formats for VCSEL-based high-speed links

Current transmission experiments for high-speed short-range links commonly use PAM and DMT as modulation formats. Both formats have their advantages and disadvantages with their performance strongly depending on the transmission scenario. In general, PAM realizations are more beneficial for a relatively flat channel, since no complex equalization is required. The generally smaller PAPR of PAM compared to DMT offers an improved relation of the optical carrier compared to the data signal in a IM/DD system, thus improving the sensitivity at the receiver. Furthermore, the signal generation is easier, since no high-resolution DACs and ADCs are required. However, simple PAM schemes[31] require more bandwidth compared to advanced PAM formats[32] or DMT, which results in a bandwidth bottleneck. Since today's VCSELs have the smallest bandwidth of all standard modulator types, simple PAM schemes are not very suitable if high symbol rates are targeted. Advanced PAM formats, like Nyquist-shaped or duo-binary schemes offer smaller signal bandwidths with only slightly higher PAPRs. This enables better performance in bandwidth-limited systems as show in Section 4.2. The challenges are a greater signal generation effort in terms of high-resolution DACs and ADCs and more complex DSP.

DMT is the optimal modulation format for frequency-selective channels, as in the case of multipath propagation in mobile environments, due to its ideal adaptation to the channel. For the fixed point-to-point links of high-speed short-range connects, the channel is commonly simpler, showing the typical low-pass behavior. However, even in these scenarios DMT offers benefits due to its easy adaptation[33]. One of the challenges of DMT is the high PAPR. First, a high PAPR requires a sufficient DAC and ADC resolution to minimize quantization noise. Second, high PAPRs reduce the optical carrier-to-signal ratio in IM/DD systems, which results in a lower sensitivity at the Rx. For the investigated high-speed VCSEL-based systems, DMT offers an easy adaptation to the channel in terms of bandwidth and modulation depth. The bandwidth can be modified by turning subcarriers on and off and the modulation order of each subcarrier is adapted to the channel SNR.

The impairments of the VCSEL nonlinearities are also different for PAM and DMT. Issues for PAM are different vertical sub-eye openings, e.g. the outer eyes are more compressed than the center ones and different sub-eye skews due to the amplitude-dependent delays [155]. As expected, these effects are more critical for higher modulation orders. Both effects can be addressed with a nonlinear equalization scheme as will be demonstrated in Section 4.6.3. The high PAPR of DMT leads to a significantly smaller effective modulation of the VCSEL L-I curve, if the same peak-to-peak driving amplitude is chosen as for PAM (refer to Appendix A.2). This results in overall smaller nonlinear effects, since most of the signal modulates only in the linear region of the VCSEL curve. However, this is not desirable in IM/DD systems due to the drop in receiver sensitivity. To overcome the high PAPR of DMT, a digital clipping is commonly applied and a higher peak-to-peak driving amplitude is chosen compared to PAM[34], which can result in an additional analog clipping. Both effects introduce additional nonlinear distortions into the signal and have to be considered for the optimal VCSEL driving amplitude.

[31] e.g. without pulse-shaping
[32] Nyquist-shaped or duo-binary, see Section 2.2.5
[33] In terms of numbers of subcarrier, cyclic prefix length and modulation order
[34] as done in the experiments

4.5 High-speed VCSEL-based transmission experiments

This section presents high-speed transmission experiments based on prototype VCSELs to investigate linear and nonlinear pre-equalization. Similar devices were already used in a few publications showing their superior performance [79], [131], [133], [135]. The authors tested different modulation techniques and equalizer schemes and investigated the performance over MMF-based links[35]. The use of DMT modulation was also shown, but only standard equalizer schemes[36] were utilized.

The high-speed VCSEL experiments in this thesis demonstrates what transmission rates are possible today and how they can be improved by advanced DSP in terms of linear and nonlinear pre-equalization in combination with DMT and PAM modulation. The results are published in [164], [171].

The section is structured as follows: First, the VCSELs are characterized, followed by the experimental setup and the DSP chain. This includes the detailed implementation of the pre-equalization approach and the determination of the VCSEL operation point regarding driving amplitude and bias current. The next part consists of the results and is divided into the achieved transmission rates for DMT, the optimization of the linear pre-equalization and the discussion of the nonlinear pre-equalization.

4.5.1 VCSEL characterization

For the high-speed experiments three different VCSELs of the same type are available. These VCSEL are provided by VI-Systems [172] and are designed to stimulate single-mode lasing. The latter is achieved by leakage of the optical modes from the all-semiconductor core region to the selectively oxidized periphery. The leakage losses are stronger for high-order transverse modes, which have a higher field intensity close to the oxidized region. Single mode lasing in the fundamental mode can thus proceed up to large aperture diameters. A more detailed description of this concept and the practical realization can be found in [157]. The L-I-V curves[37] provided by VI-Systems of the three devices are presented in Fig. 4.13 (a-c). The threshold current is found below 0.5 mA while thermal roll-over is reached between 4 and 5 mA. The maximum optical power is between 1 and 1.5 mW, with VCSEL#1 the highest and VCSEL#2 the lowest. Fig. 4.13 (d-f) shows the optical spectrum at different bias currents for the three devices. The SMSR at 3 mA bias current is between 10 and 22 dB. For VCSEL#1 it's improving for higher currents, whereas a decrease in SMSR is seen for VCSEL#2 and VCSEL#3. In the experiments a bias current of 4 mA is used for all devices, resulting in an SMSR of at least 13 dB.

These VCSEL types have 3 dB bandwidths generally greater than 25 GHz, as shown by the exemplary curve in Fig. 4.13 (g). The RIN is generally lower than -150 dB/Hz [157], which enables high-order modulation formats with data rates beyond 100 Gb/s. The devices are completely encapsulated and have a V-type RF connector and an MMF connector.

In Fig. 4.14 the measured spectra for VCSEL#2 for CW (blue curve) and when modulated (orange curve) are shown for two different resolutions of the spectrum analyzer. In Fig. 4.14 (a), measured with a resolution of 5 nm, a second VCSEL mode can be observed with a suppression of 20 dB relative to the main mode. This fits well into the given values from the data sheet and confirms the quasi single-mode operation of the VCSEL. The modulated spectrum (25 GHz DMT signal) shows a slightly different

[35] with the focus on the VCSEL
[36] single tap for each DMT subcarrier
[37] Confirmed by own measurements

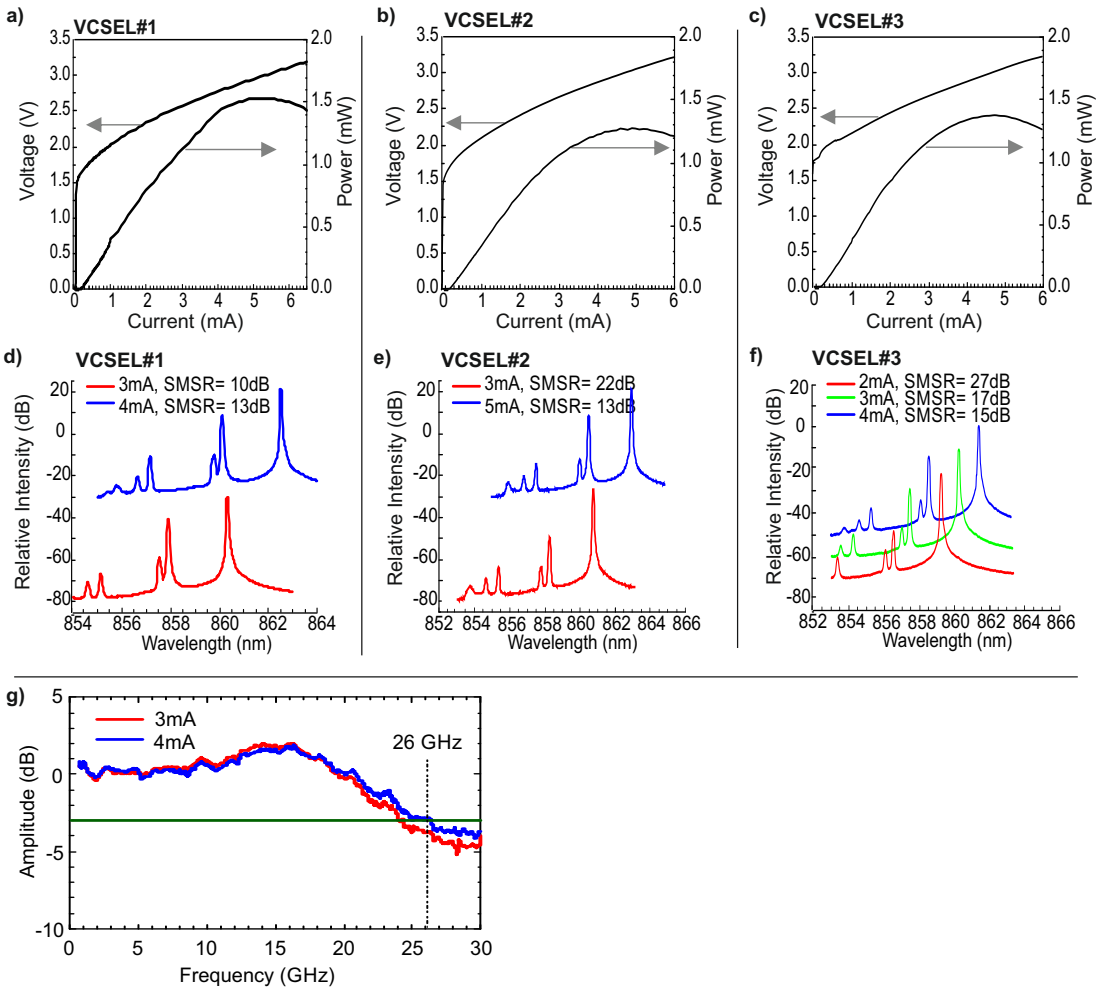

FIGURE 4.13: Data sheet values of the used high-seed SM-VCSEL: (a-c) L-I-V curves of the three VCSELs; (d-f) emission spectra at different bias currents; (g) exemplary frequency response of the SM-VCSEL type.

behavior. First the peak power is lower, which can be attributed to the broader spectrum in combination with the windowing filter effect of the spectrum analyzer. Second, a shift to higher wavelengths occurs. Higher VCSEL currents lead to a shift up to higher wavelengths as can be seen in Fig. 4.13 (d-f). This is caused by the strong determination of VCSEL emission wavelength from the cavity resonance, which in turn depends on the temperature sensitive average refractive index. With turned on modulation of the VCSEL, there are different amounts of currents and a change in the temperature of the device, which results in the small wavelength shift[38]. In Fig. 4.14 (b), with a resolution of 0.5 nm, this behavior is shown in more detail.

4.5.2 Experimental setup and system characteristic

The experimental setup is shown in Fig. 4.15. The electrical DMT signals are generated by a high-speed DAC with a sampling rate of 80 GS/s and a 3 dB bandwidth of 19 GHz. A set of passive attenuators and a tunable microwave amplifier (EA, SHF

[38]Not to be mixed up with laser chirp, which originates from the dependencies of the refractive index to the carrier density.

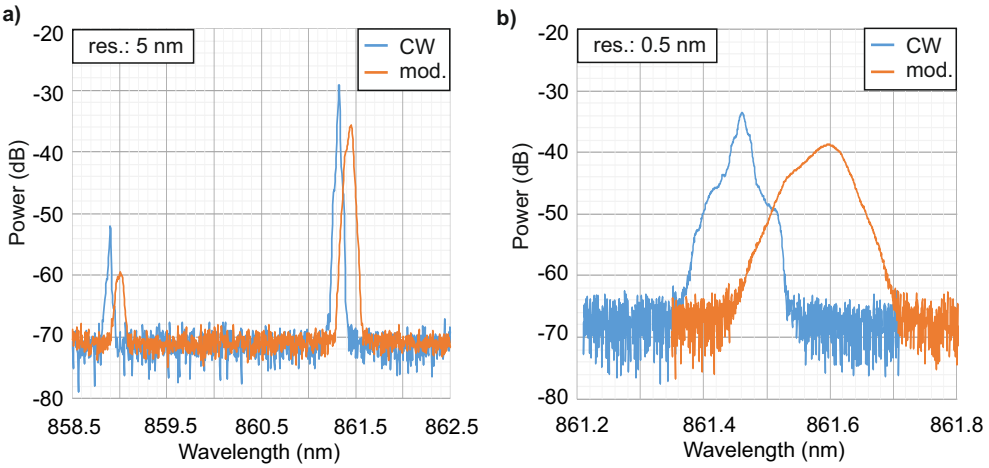

FIGURE 4.14: Measured spectra of the VCSEL#2 for CW and modulated operation with (a) 5 nm resolution and (b) 0.5 nm resolution.

804TL) with a 3 dB bandwidth of 55 GHz are used in order to provide the necessary driving signal amplitude. The VCSELs are all biased at 4 mA, using a bias-tee (Anritsu K250) with a 3 dB bandwidth of 40 GHz and a current source (Keithley 2400-LV SourceMeter). After the VCSEL module, OM4 MMFs of 10 m (i.e. optical btb) or 550 m are applied. To adjust the optical power, a variable optical attenuator (Agilent N7766A) is put in front of the receiver.

The photoreceiver (PD+TIA) is a New Focus 1484-A-50 with a 3 dB bandwidth of 22 GHz and 103 V/W conversion gain. The resulting signal is captured with a real-time sampling oscilloscope (80 GS/s) of 30 GHz bandwidth (LeCroy SDA80000). Both the DAC and the oscilloscope are synchronized with a 10 MHz reference clock, so that no additional clock recovery is necessary. For all measurements an optical power of 0 dBm is set a the photoreceiver, if not otherwise stated.

Prior to the transmission measurements, the optimal bias current and the optimal driving amplitude are determined and fixed for all experiments[39]. This is done by transmitting a DMT signal[40] of 20 GHz bandwidth and a fixed bit loading over the

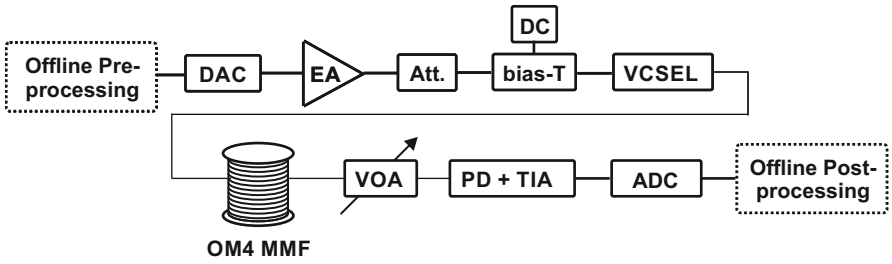

FIGURE 4.15: Experimental setup. DAC (digital-analog-converter, 80 GS/s), EA (electrical amplifier), Att. (electrical attenuator), VOA (variable optical attenuator), PD+TIA (photodiode and transimpedance amplifier), ADC (analog-digital converter, 80 GS/s).

[39] if not otherwise stated

[40] using the DMT DSP shown in Fig. 4.18 without pre-equalization

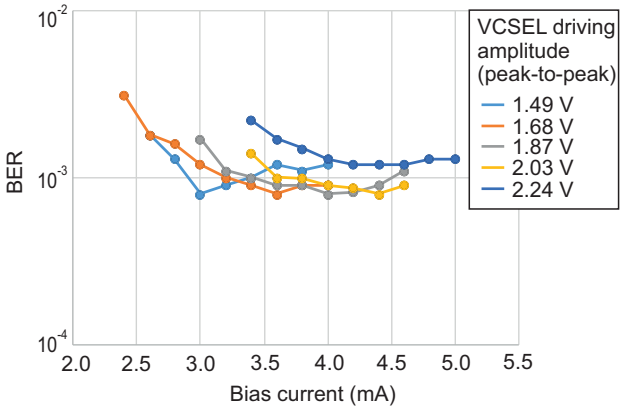

FIGURE 4.16: Bias current and driving amplitude determination for the high-speed VCSEL experiment.

optical btb link and optimizing the BER by adjusting the bias and the driving amplitude. In Fig. 4.16 the result is shown. The x-axis shows the bias current of the VCSEL and the y-axis the measured BER. The different colors indicate different peak-to-peak driving amplitudes. The amplitudes are set by the tunable amplifier. For each peak-to-peak driving amplitude, the bias current is swept and the BER estimated. As can be observed, one optimum is at 4 mA bias current and a peak-to-peak driving amplitude of 1.87 V at the input of the VCSEL. The low variation of the BER around these parameters indicates a robust behavior of the VCSEL. This is very beneficial for the experiments, since variations in the signal bandwidth and different amounts of pre-equalization often result in small variations in the signal amplitude.

Fig. 4.17 (a) shows the measured system frequency response of six transmission scenarios, i.e. the three VCSELs and 10/550 m of MMF. Fig. 4.17 (b) shows a detailed view, with the 3 dB limit indicated by the orange line. The frequency responses show the typical characteristics of low-pass limited systems, which can mainly be attributed to the DAC, the VCSELs, the MMF and the receiver behavior. The influence of the electrical Tx amplifier and the bias-tee are negligible, due to their significantly higher bandwidth. For 550 m of MMF, a further drop can be observed compared to 10 m caused by the chromatic and modal dispersion induced RF fading effect in combination with the finite SMSR of the VCSELs [125]. For comparison, the electrical frequency response is also shown, i.e. without the VCSEL, MMF and the photoreceiver. The 3 dB frequency of the optical btb system is <10 GHz as indicated by the orange line in Fig. 4.17 (b). However, the relatively slow drop of the frequency response allows modulation bandwidths up to 30 GHz. Fig. 4.17 (c) shows the impulse responses for electrical back-to-back (btb) and for VCSEL#1 with 10 m MMF. As can be observed, at least 50 taps[41] are required to describe the full response. This can be presumably be attributed to small reflections in the transmission system, which are most likely located between the DAC and the VCSEL.

4.5.3 DSP and pre-equalization scheme

In Fig. 4.18 the digital signal processing for the DMT transmission is shown. It is very similar to DMT transmission in the bandwidth extension experiments (Section 3.5.2.1),

[41] time interval of each tap = 1/80E9 s

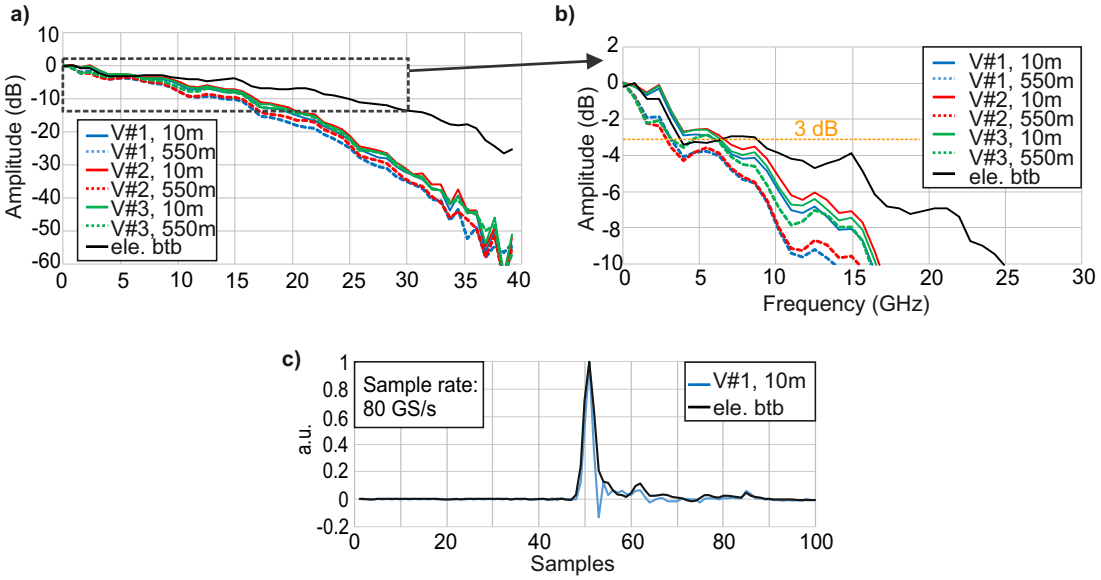

FIGURE 4.17: (a) Measured system frequency response for VCSEL#1-3, 10 and 550 m of MMF and the electrical btb case; (b) Detailed view; (c) Impulse response for electrical and optical btb (for VCSEL#1) at 80GS/s.

except for the pre-equalization scheme. The transmitter side includes the bit-stream generation, serial-to-parallel conversion, bit mapping, addition of training symbols for the channel estimation, IFFT (256 subcarrier, IFFT length 512 with Hermitian symmetry), cyclic prefix insertion (16 samples), and parallel-to-serial conversion followed by up-sampling to the DAC sampling rate. Then samples for synchronization are added and the pre-equalization scheme is applied. Finally, the signal is clipped to limit the PAPR and to enable a nearly constant signal power after the DAC. The clipping ratio is set to achieve a PAPR of 10 dB. The bit loading for each QAM modulated DMT subcarrier (maximum of 256 subcarrier) is determined by SNR measurements, based on a training sequence consisting of 4-QAM modulated subcarriers. The bit loading optimum for each transmission case is determined by the SNR values and the BER of each subcarrier. This is done by generating a lookup-table, using the analytical relation between the SNR, the BER and the modulation order of a white Gaussian noise limited system (please refer to Appendix A.8 for details). Power loading is not applied[42]. The receiver side DSP includes low-pass filtering, down-sampling to the DMT processing rate, synchronization, serial-to-parallel conversion, cyclic prefix removal, the FFT, a single-tap equalizer for each subcarrier, demapping, parallel-to-serial conversion, the BER and EVM estimation and the bit loading algorithm.

The pre-equalization scheme is based on the Volterra series approach as described in Section 4.4.2. The Volterra filter with it's kernel elements describes the complete system, including all components as shown in Fig. 4.19. With this information the system behavior, i.e. the channel is linear and nonlinear pre-equalized. Note that during the VCSEL-based experiments for [164], [171], [173] and in previous work, it was observed that the nonlinear pre-equalization had only minor influence compared to the linear part, especially for DMT modulation. Therefore, the focus of the experiments

[42]Test with power loading schemes like Krongold, showed no measurable improvement, which can presumably be attributed to the nonlinear system behavior.

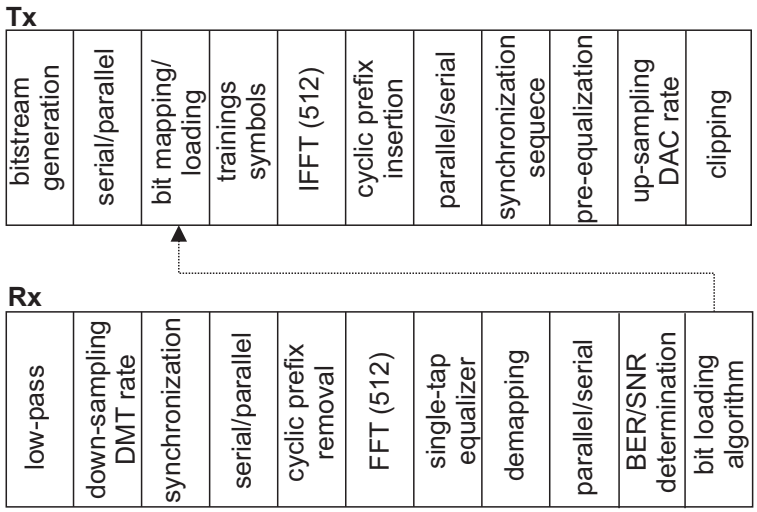

FIGURE 4.18: DMT digital signal processing including pre-equalization block and bit loading algorithm.

presented in this section is on the linear pre-equalization[43]. The amount of linear pre-equalization can be controlled by scaling the linear transfer function, i.e. the 1st order Volterra kernel $[\boldsymbol{h}_1]$. Fig. 4.20 (a) shows the realization. At first, the Volterra filter transfer function h is determined for each transmission scenario, i.e. 10/550 m of MMF and the three different VCSELs, as explained in Section 4.4.2.3. For this experiment, a Volterra filter of up to the 3rd order with memory lengths of $N_1 = 100$, $N_2 = 7$ and $N_3 = 2$ is used. The exact numbers of kernel elements, i.e. memory of each order, are chosen to optimize the transmission performance without considering the computational effort[44]. The high number of taps for the 1st order kernel is required to compensate for the minor reflections in the electrical part of the experimental setup.

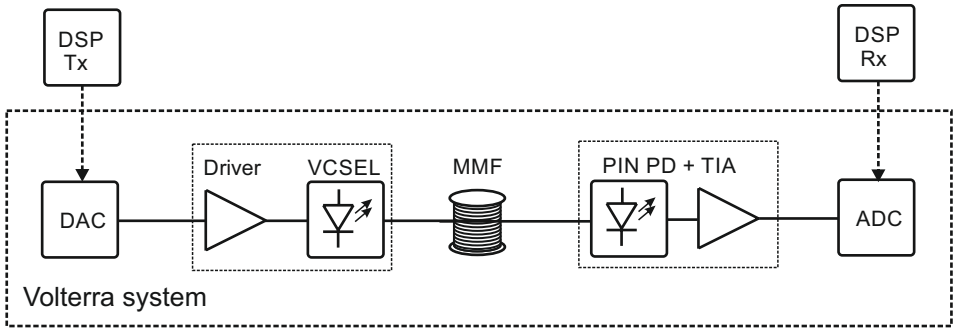

FIGURE 4.19: Model of the VCSEL transmission system used in the experiment. The Volterra filter used describes the complete system, with all components.

[43]The results for the nonlinear pre-equalization are nevertheless presented.

[44]In Section 4.6.4 the influence of different memory lengths is shown for the PAM transmission case. In this experiment[45] only the first order kernel length had a significant influence on the transmission performance. The higher order memory lengths are nonetheless generously chosen.

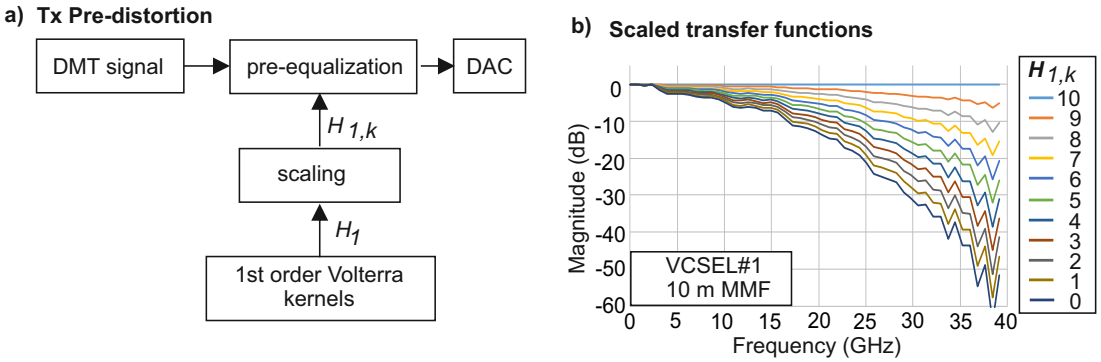

FIGURE 4.20: Pre-equalization approach. (a) The linear part h_1 of the determined Volterra filter is scaled to generate a new set of transfer functions for the pre-distortion of the Tx DMT signal. (b) Examples of new transfer functions after scaling (obtained with VCSEL#1 and 10m MMF).

This can be observed from the measured impulse response in Fig. 4.17. The 1st order kernel ($[\boldsymbol{h}_1]$) is converted into the frequency domain ($[\boldsymbol{H}_1]$) and represents with its absolute values ($|[\boldsymbol{H}_1]|$) the magnitudes of the linear frequency response. To enable different amounts of linear pre-equalization, $|[\boldsymbol{H}_1]|$ is transformed in dB and scaled to generate a new set of k different transfer characteristics $|[\boldsymbol{H}_{1,k}]|$.

$$|[\boldsymbol{H}_{1,k}]|_{\mathrm{dB}} = |[\boldsymbol{H}_1]|_{\mathrm{dB}} - k\frac{|[\boldsymbol{H}_1]|_{\mathrm{dB}}}{10}. \tag{4.24}$$

Here $k = 0...10$ is also the scaling factor. For $k = 0$ no change in the magnitudes of the 1st order Volterra kernels occurs, thus the full linear pre-equalization is applied and for $k = 10$ a flat characteristic is set, resulting in no linear pre-equalization. The scaled amplitudes of the 1st order kernel have equal distances to their neighboring ones, as exemplary shown for VCSEL#1 and 10 m MMF in Fig. 4.20 (b). This results in a set of 1st order Volterra kernels, ranging from a completely flat frequency behavior up to the original transfer function. Ten new transfer functions[46] are generated for each scenario, indicated by $H_{1,k}$ in Fig. 4.20 (b). Note that the phase behavior of the 1st order kernels is not changed by the scaling process, only their magnitude. After converting back into the time domain and combining with the unchanged nonlinear kernels, the Volterra coefficients are used to feed the pre-equalization block as shown in Section 4.4.2.4.

In Fig. 4.21 three examples of a pre-equalized DMT signal are shown before and after transmission[47]. The case in Fig. 4.21 (a) represents no scaling of the linear transfer function with $k = 0$, thus the full linear pre-equalization is applied. This results in rising amplitudes at higher frequencies before the channel and a flat spectrum after the channel. The second case with $k = 4$ is shown in Fig. 4.21 (b). As can be observed, the amount of pre-equalization is smaller with slightly rising amplitudes at higher frequencies before and slightly falling amplitudes after the channel. Full channel scaling is applied for the last case shown in Fig. 4.21 (c) with $k = 10$. This results in no pre-equalization, with a flat spectrum at the Tx and falling amplitudes at higher frequencies after the channel. A further interesting point is related to the signal power,

[46] the original one and ten scaled versions
[47] before D/A conversion and after A/D conversion

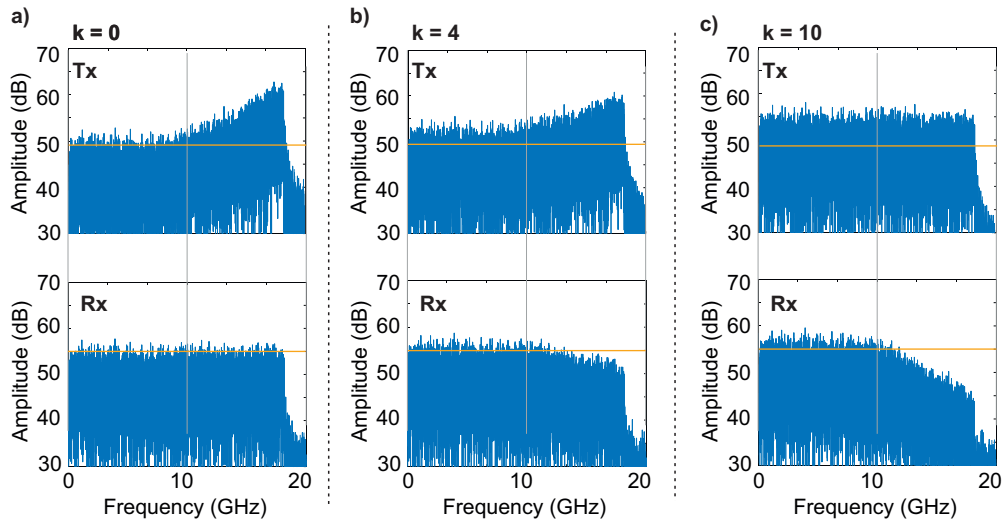

FIGURE 4.21: Spectrum of DMT signal before D/A conversion and after A/D conversion with different amounts of linear pre-equalization. For $k = 0$ full linear pre-equalization is applied at the Tx and for $k = 10$ no pre-equalization.

which is the same for all Tx signals. Due to the high amount of pre-equalization for the case $k = 0$ a drop in amplitude at the lower frequencies can be observed (indicated by the orange line at 50 dB). For example the average amplitude at 2 GHz is 50 dB for $k = 0$ and 55 dB for $k = 10$. This results in a significant loss in SNR at lower frequencies, if white noise is considered in the system.

Next to the different amounts of linear pre-distortion, a maximum bandwidth of the DMT signal has to be defined. This can be explained by the following consideration. A DMT signal with a bandwidth far beyond the 3 dB bandwidth of the transmission system suffers significantly due to the high attenuation at higher frequencies. In general, the SNR at high frequency subcarriers will be too low for a modulation and the useful signal bandwidth is limited. If a linear pre-equalization is applied, to fully compensate the system frequency response at the Tx, the modulation of even the highest frequency subcarriers is possible. However, as seen in Fig. 4.21 (a) at the cost of signal power at the lower subcarriers, since the total signal power is constant. In theory, the signal bandwidth could now be further increased, up to the point where no modulation at lower subcarriers is possible any more. Since this is not desirable, different maximum signals bandwidths of 22.5, 25, 27.5 and 30 GHz are defined for the measurements[48]. This is realized by turning on only a part of the subcarriers, i.e. 180/256 for 22.5 GHz, 200/256 for 25 GHz, 220/256 for 27.5 GHz and 240/256 for 30 GHz. Note that these are only the maximum limits and there can be lower signal bandwidths for cases with too low SNR values at subcarriers and no modulation possible.

4.5.4 Results high-speed VCSEL transmission experiments

The results section is divided into three parts. The first part studies the transmission performance for the different scenarios and compares the three VCSELs. The second part presents the performance for the different amounts of linear pre-equalization and

[48]Theses values were determined after initial transmission experiments.

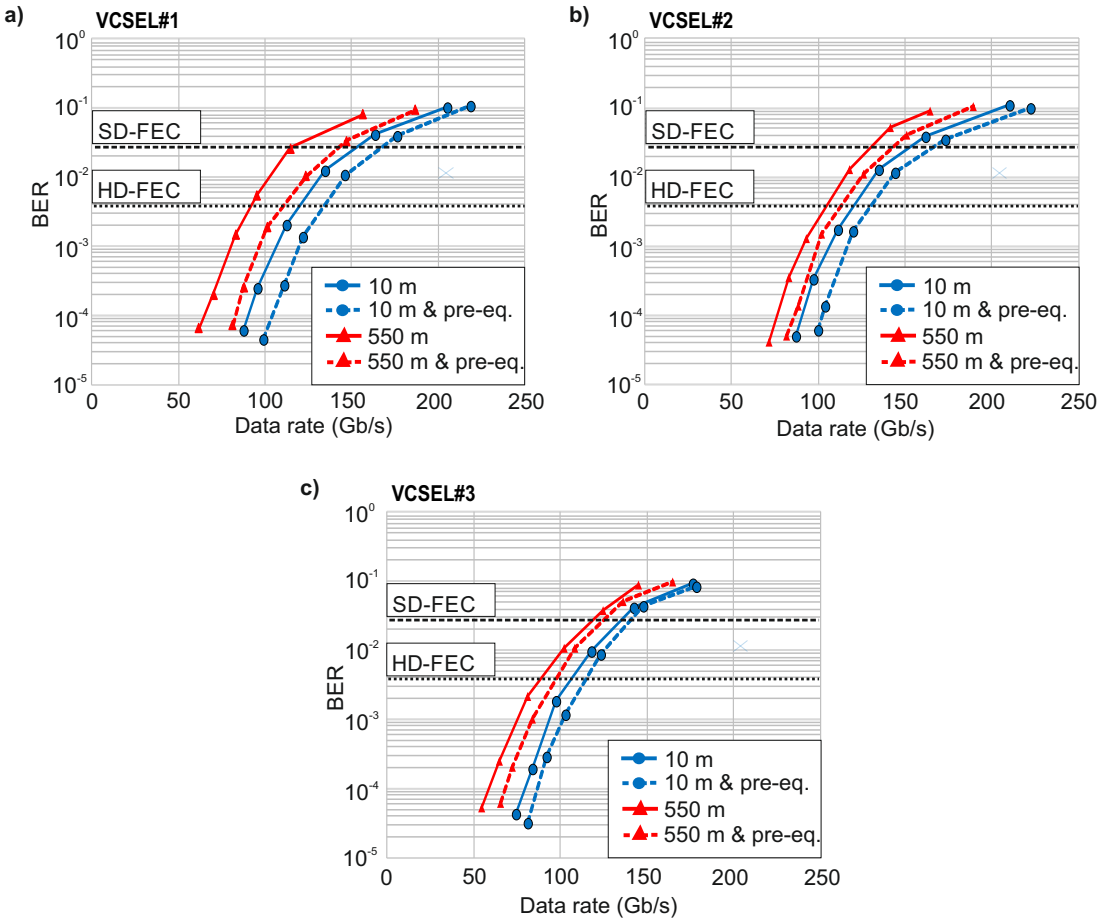

FIGURE 4.22: Measured gross data rates for the three VCSEL, 10/550 m MMF and w & wo optimized pre-equalization are shown. Additionally the 7% HD-FEC BER limit ($3.8 \cdot 10^{-3}$) and the 20% SD-FEC BER limit ($2.7 \cdot 10^{-2}$) are marked.

discusses the results. In the last part the nonlinear pre-equalization performance is investigated.

4.5.4.1 Transmission performance

To evaluate the performance of the link, the maximum achievable gross data rate for different target BERs, MMF lengths and the three VCSELs is measured. Additionally, the performance with and without the optimized pre-equalization is determined. Note that the optimum k factor is discussed in the next section.

Fig. 4.22 shows the achieved gross data rates for the different scenarios and Table 4.1 summarizes the results. The exact data rates at the 7% HD-FEC and 20% SD-FEC limit are interpolated from the measurement curves. As can be observed, transmission rates beyond 100 Gb/s are feasible with all three VCSELs at 10 m of MMF and below the 7% HD-FEC limit. For 550 m only VCSEL#1+2 reach 100 Gb/s and for the case without pre-equalization, only VCSEL#2 is feasible. For the higher 20% SD-FEC BER limit, similar trends can be observed. The general drop in the performance for the 550 m MMF cases compared to 10 m can be attributed to the modal and chromatic dispersion induced RF fading effect in combination with the finite SMSR of the VCSELs.

TABLE 4.1: Measured gross data rates for high-speed VCSEL experiments

Performance of high-speed VCSEL transmission using DMT at transmission distances of 10 and 550 m (MMF) with and without optimized pre-equalization at the 7% and 20% FEC BER limit, i.e. $3.8 \cdot 10^{-3}$ and $2.7 \cdot 10^{-2}$ respectively.

7% HD-FEC limit	VCSEL#1	VCSEL#2	VCSEL#3
10 m	122	120	105
10 m & pre-eq.	135	130	115
550 m	91	105	88
550 m & pre-eq.	113	114	97
20% SD-FEC limit	VCSEL#1	VCSEL#2	VCSEL#3
10 m	148	149	135
10 m & pre-eq.	161	160	142
550 m	111	130	118
550 m & pre-eq.	135	144	126

The measured data rates of VCSEL#1 and VCSEL#2 are very similar compared to VCSEL#3, with slightly less performance. Fig. 4.23 (a) shows the performance difference with and without pre-equalization for the 7% HD-FEC BER limit and the calculated gain. A clear improvement of 10% in data rate for the scenarios with pre-equalization can be observed for all VCSEL and transmission distances. An interesting exception is

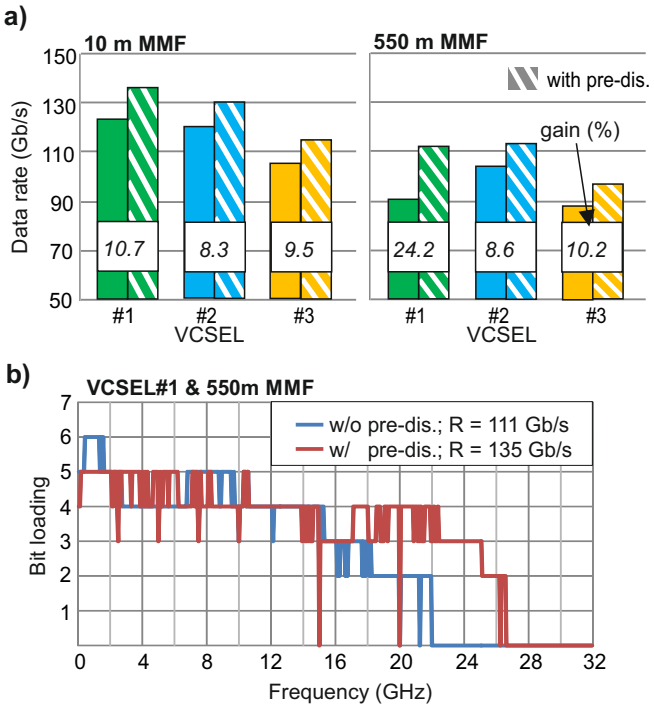

FIGURE 4.23: (a) Performance and gain difference for the different transmission scenarios (VCSEL#1-3, 10/550 m MMF, with and without pre-equalization). (b) Bit loading for VCSEL#1 and 550 m MMF case with and without pre-equalization.

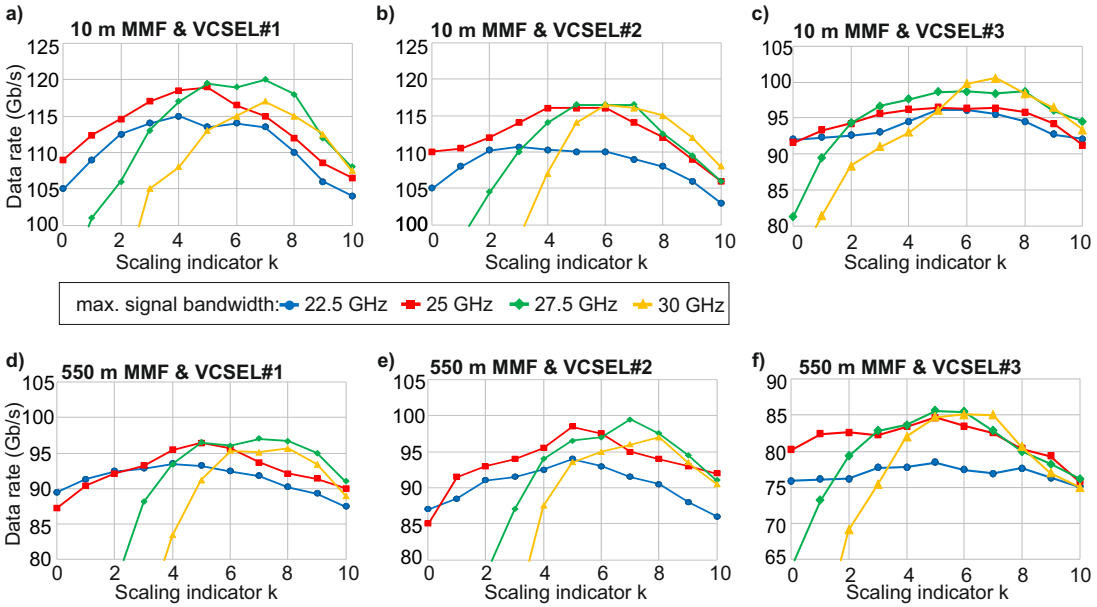

FIGURE 4.24: Performance for different amounts of pre-equalization at a BER of 10^{-3}, fiber lengths of 10/550 m and VCSEL#1-3. The x-axis shows the pre-equalization scaling indicator k: For k=10 no linear pre-distortion is applied, whereas for k=0 the full linear system frequency response is compensated at the Tx.

the 550 m case for VCSEL#1, with a gain of 24% compared to 8.6% and 10.2% for VCSEL#2 and VCSEL#3, respectively. The bit loading in this case is shown in Fig. 4.23 (b). It can be observed that the highest modulated subcarrier is located at 22 GHz for the case without pre-equalization and at 26.5 GHz with pre-equalization. This results in a significantly higher signal bandwidth and data rate, however at the cost of a slightly decreased maximum bit loading at lower frequencies. The measured improvements in bandwidth with VCSEL#2 and VCSEL#3 are only 2.4 and 3.1 GHz respectively, compared to VCSEL#1 with 4.5 GHz in the same scenario. It can be assumed this is the main reason for the significantly higher gain in data rate.

4.5.4.2 Linear pre-equalization optimization results

As described above, different amounts of pre-equalization are applied and the performance is measured. Fig. 4.24 shows the achievable data rates at a BER of 10^{-3} for VCSEL#1-3 at 10/550 m of MMF and for different maximum signal bandwidths. The x-axis shows the scaling indicator k. Here, $k = 10$ relates to no linear pre-equalization, whereas for $k = 0$ the full compensation of the system frequency function is applied. In Fig. 4.24 (a) the scenario with VCSEL#1 and 10 m of MMF is shown. The blue curve relates to a maximum DMT signal bandwidth of 22.5 GHz for this transmission case. Starting at $k = 10$ at the right side, it can be observed that with an increasing power of the linear pre-equalization (k gets smaller), the achievable data rates increase up to a maximum at $k = 4$. At lower amounts of k, the data rate decreases again, down to the point without linear pre-equalization ($k = 10$). For the other maximum signal bandwidth cases, a similar behavior can be observed. However, there are two important differences. First, the achievable data rate differs for each bandwidth case, as it can be expected due to the artificial limitation of the signal bandwidth. Second, the optimal

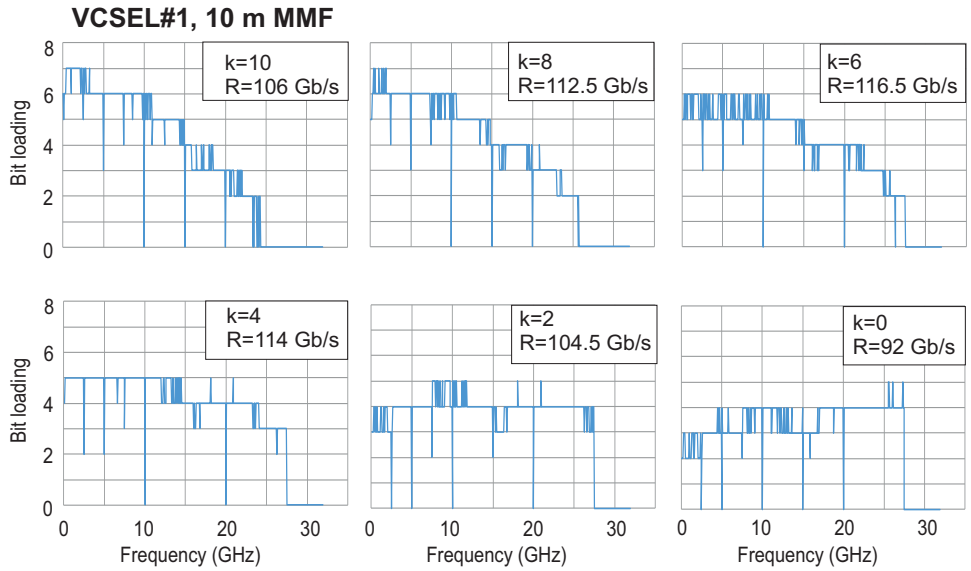

FIGURE 4.25: Bit loading and data rate for different amounts of linear pre-distortion (indicated by k) in case of VCSEL#1 and 10 m MMF.

amount of linear pre-equalization, which maximizes the data rate, also differs. In detail: for 22.5 GHz $k = 4$, for 25 GHz $k = 5$, for 27.5 GHz $k = 7$ and for 30 GHz $k = 8$. This implies that the amount of optimal pre-equalization decreases, when signals with higher bandwidth are transmitted. Additionally, it can be observed that with the full pre-equalization of the electrical frequency response, which relates roughly to $k = 5$ (please refer to Fig. 4.17 and Fig. 4.20), only the optimum for one bandwidth case is met. Note that the measured Volterra kernels h, which are used to calculate the set of new transfer functions, are the same for all bandwidth and pre-equalization cases in Fig. 4.24 (a).

For VCSEL#2 and 10 m MMF, as shown in Fig. 4.24 (b), a similar behavior can be observed. In case of VCSEL#3 and 10 m of MMF shown in Fig. 4.24 (c), the best performance is achieved with the 27.5 GHz bandwidth limitation. Furthermore, it is more difficult to recognize the optimal pre-equalization/bandwidth relation as could be observed in Fig. 4.24 (a+b). Fig. 4.24 (d-f) shows the scenarios for 550 m transmission distance. The behavior of the curves is similar compared to the 10 m case, apart from the overall drop in data rate.

For the higher bandwidth cases it can also be observed, that the data rate for the full linear pre-equalization ($k = 0$) is significantly worse compared to no linear pre-equalization ($k = 10$). This can be explained by the high loss in signal power at the lower subcarriers, as could be observed in Fig. 4.21.

To have a better understanding of this behavior, the used QAM bit loading of each DMT subcarrier[49] is shown in Fig. 4.25 for different amounts of linear pre-equalization, for the VCSEL#2, 10 m MMF and 27.5 GHz maximum bandwidth[50]. For $k = 10$ no linear pre-equalization is applied, which results in the typical DMT bit loading in low-pass limited transmission systems. There are higher modulation orders at the lower frequencies and lower at the higher frequencies, going from 128-QAM to 4-QAM. If

[49] indicated by the frequency
[50] at an average BER of = 10^{-3}

the amount of linear pre-equalization is increased, e.g. $k = 8, 6, 4$, several observations can be made. First, the total data rate increases, as it could already be observed in Fig. 4.24 (b). Second, the QAM modulation order decreases at lower frequencies (subcarriers) and increases at higher frequencies. Third, the useful signal bandwidth increases. For the cases of $k = 2$ and $k = 0$, where (nearly) the total system frequency response is compensated at the Tx, the data rate decreases again. Furthermore, the QAM modulation order at lower frequencies is smaller compared to that at higher frequencies. It can be assumed that the latter can be attributed to a non-white noise distribution in the system.

The gain in data rate due to the application of linear pre-equalization can attributed to following reasons. First, SNR degradations through the DAC and the electrical Tx amplifier are small compared to that of the VCSEL and the photoreceiver. However, their influence onto the system frequency response is significant[51]. This offers the possibility to have a decent SNR improvement at higher frequencies, when a partial pre-equalization is applied at the cost of minor overall SNR degradations. As a rule of thumb, it can be assumed that with the pre-equalization of the electrical components in such systems, a gain in data rate can be expected. Nevertheless, this is not the optimum as could be observed in Fig. 4.24, since the actual signal bandwidth is significant as well. The second reason for the gain in data rate is the availability of an increased system bandwidth as shown in Fig. 4.23. The bandwidth goes linear into the capacity formula, whereas the SNR is considered in the logarithm. If the loss in capacity, due to the overall SNR degradation when applying a pre-equalization, is smaller than the gain, due to the increased bandwidth, a net gain can be expected. However, this strongly depends on the exact behavior of the system frequency response and the noise sources.

4.5.4.3 Nonlinear pre-equalization results

In the previous experiments, the linear and the nonlinear systems characteristics are compensated at the Tx DSP. However, nearly no gain for the nonlinear compensation can be observed for DMT. In Fig. 4.26 this is shown for the optical btb transmission case[52]. In Fig. 4.26 (a) the achievable data rate at a BER of 10^{-3} is shown for the transmission of two DMT signals with 20 and 25 GHz bandwidth, with the optimal linear pre-equalization and with the additional nonlinear pre-equalization[53]. The exact data rates at a BER of 10^{-3} are estimated by interpolating measured BER/data rate curves[54].

To change the amount of nonlinearities, the VCSEL peak-to-peak driving amplitude (DA) is swept as shown in Fig. 4.26 (a). Then, for each driving amplitude the optimal bit loading is determined at the target BER. Starting at a peak-to-peak amplitude of 1.87 V[55], a very small gain in data rate can be observed, if the amplitude is increased. However, even higher amplitudes result in a decrease in data rate, which can be attributed to the increasing analog clipping of the DMT signal at the VCSEL. This is the case for all scenarios, i.e. linear and nonlinear pre-equalization and 20/25 GHz signal bandwidth. The performance with and without the additional nonlinear pre-equalization is more or less equal, with a very small gain for the 20 GHz signal case.

[51] Refer to the electrical system frequency response in Fig. 4.17.

[52] VCSEL#1 and 10 m of MMF

[53] The optimal scaling factor for the linear channel is $k = 3$ for the 20 GHz and $k = 5$ for the 25 GHz DMT signal.

[54] Similar as in Fig. 4.22 in Section 4.5.4.1

[55] corresponds to the amplitude used for the previous experiments

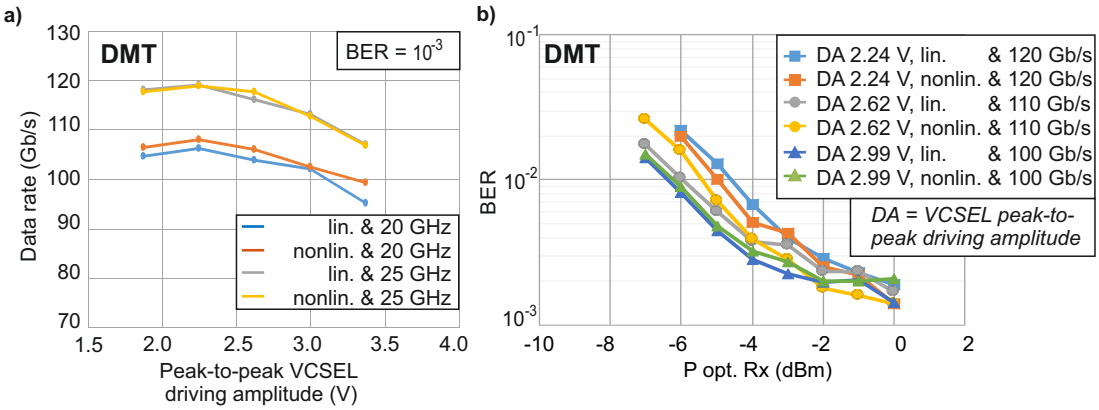

FIGURE 4.26: (a) Performance of DMT with linear and nonlinear pre-equalization for different VCSEL peak-to-peak driving amplitudes (DA) and for 20 and 25 GHz signal bandwidth at a BER of 10^{-3}. (b) Performance of DMT with linear and nonlinear pre-equalization for different Rx powers and VCSEL peak-to-peak driving amplitudes with three different bit loading masks.

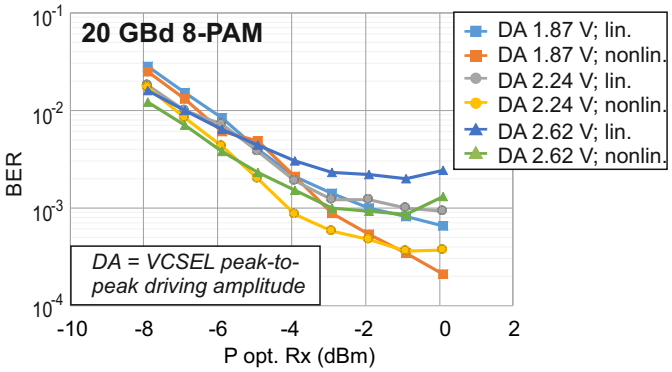

FIGURE 4.27: 8-PAM performance with linear and nonlinear pre-equalization for different Rx powers and for 20 and 25 GHz signal bandwidth.

Another representation of the nonlinear pre-equalization gain for DMT in the system is shown in Fig. 4.26 (b). The figure shows the average BER at different optical power levels at the photoreceiver. Three different data rates, i.e. bit loading masks, are used in combination with linear and nonlinear pre-equalization and different VCSEL driving amplitudes. Again, nearly no gain[56] for the additional nonlinear pre-equalization can be observed. Additionally, as indicated by the error floor at higher Rx power levels, the non ideal transmitter properties are critical for the system, e.g. mainly DAC bandwidth, effective DAC bit resolution and VCSEL RIN. Note, the saturation power of the receiver is 9 dBm, thus the receiver operated in the linear regime for all measurements.

For comparison, the same transmission experiment is performed with a 20 GBd

[56]There is a very small improvement for the case with a driving amplitude of 2.62 V. However, no clear trend can be observed.

8-PAM signal[57]. In Fig. 4.27 the measured BER is shown for different optical power levels at the receiver, in combination with different driving amplitudes and for linear and nonlinear pre-equalization. The behavior is similar compared to DMT with decreasing BER values and an error floor at power levels beyond -2 dBm. However, in contrast to the DMT experiment, a gain for the nonlinear pre-equalization is clearly visible, e.g. for a driving amplitude of 2.62 V shown by the green and blue curves. The optimal driving amplitude is also smaller compared to the DMT transmission, which can be explained by the different PAPR of the 8-PAM signal. The issues and challenges with nonlinear pre-equalization are discussed in more detail in Section 4.6.

4.5.5 Conclusions on experiments for VCSEL-based high-speed links

These experiments demonstrate that low-cost directly-modulated VCSEL-based transmitters can be used for data transmission significantly beyond 100 Gb/s. Successful transmissions of 135 and 114 Gb/s are shown over 10 and 550 m of MMF respectively, below the 7% HD-FEC limit. For higher 20% SD-FEC BER thresholds, data rates of up to 161 Gb/s are achieved.

Furthermore, linear and nonlinear pre-equalization schemes are investigated experimentally. The use of linear pre-equalization enabled a significant gain in transmission rate when using DMT. The optimal amount, i.e. the k factor, depends on the actual signal bandwidth and the transmission scenario. The pre-compensation of the electrical system transfer function already offers an improved data rate, however it is not the optimum. The nonlinear pre-compensation of DMT showed nearly no gain for these high-speed systems, while for PAM a small gain could be observed.

4.6 Nonlinear pre-equalization for VCSEL-based high-speed links

With the knowledge from the high-speed VCSEL-based experiments, there are two interesting questions. First, what is the exact gain for a PAM-based transmission using nonlinear pre-equalization compared to only linear pre-equalization? Second, why there is a lack of gain for DMT? To investigate these question in more detail, additional simulations and measurements are performed. The simulations utilize a simplified transmission system, with the focus on the VCSEL, to investigate the various degrees of freedom without the measurement related limitations. These are primarily located in the interactions of the component properties, like bandwidth limitations and impede experimental approaches. To validate the simulation results, additional selected measurements are performed at a lower speed system. The results for the nonlinear pre-equalization of PAM modulated VCSEL-based systems are published in [173].

This section is organized as follows. At first, the simulation environment is presented, followed by a brief introduction into the VCSEL model. Secondly, the DSP, the pre-equalization approach and the procedure of the simulation are described. Thirdly, the performance for PAM under different driving condition is shown and analyzed. Finally selected measurements are performed to validate the simulation results.

[57]MMSE-based linear equalizer at the Rx, pre-equalization with $k = 6$, pulse-shaping roll-off factor = 1

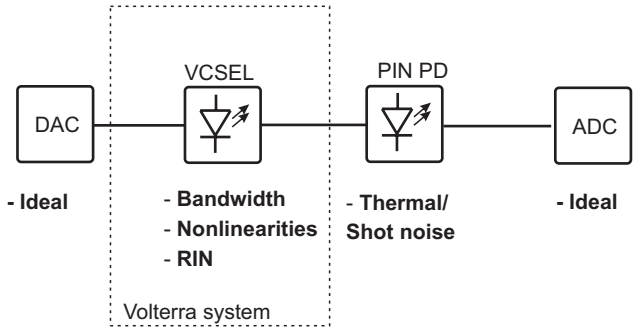

FIGURE 4.28: System model for VCSEL-based simulation.

The investigations for the nonlinear pre-equalization of PAM signals were partly done in cooperation with the main author of [173]. A detailed descriptions of the own contributions can be found in Appendix B.

4.6.1 Simulation model of the transmission system

The transmission system used in the simulations is a simplified version of the system used for the experiments. It is shown in Fig. 4.28. The ADC and the DAC are ideal and do not contribute to the system impairments. The influence of the MMF is also omitted like in the optical btb scenario, thus neglecting any modal and chromatic dispersion. The VCSEL model is based on a thermal approach and is explained in more detail in the next section. The receiver is modeled with a simple PIN photodiode, with shot and thermal noise. After the photodiode, the signal is directly A/D converted without any further amplification.

The simulation environment consists of a co-simulation approach between MATLAB and VPItransmissionMaker. The analog/digital conversion is done in MATLAB and the optical/electrical conversion in VPItransmission Maker. The important simulation parameters can be found in Appendix A.7.

4.6.2 VCSEL simulation model

The SM-VCSEL model used in the simulations (VPItransmissionMaker) is based on semi-empirical thermal rate equations [174], [175]. It enables the modeling of L-I curves at different temperatures and takes advantage of many of the desirable properties of the rate equations, in particular the ability to model non-dc behavior such as signal modulation. Static and dynamic effects like RIN, thermal impedance, thermal rollover, parasitic effects etc. are provided by the model [176]. This section provides a brief overview about the model, focused on the the thermal aspect.

The static L-I curves of a VCSEL under thermal dependency and above the threshold current can be described as [174]:

$$P_0 = \eta_{\mathrm{sl}}(T)(I - I_{\mathrm{th}}(N_{\mathrm{cr}}, T)), \tag{4.25}$$

with the optical output power P_0, the temperature dependent differential slope efficiency $\eta_{\mathrm{sl}}(T)$, the injection current I and the threshold current $I_{\mathrm{th}}(N_{\mathrm{cr}}, T)$. The latter depends on the temperature T and the carrier density N_{cr} [177]. This expression can be simplified under the assumption of a non temperature dependent slope efficiency [178] and a non carrier density dependent threshold current [179]. After partition of

the threshold current into a constant value I_{tho} and thermal offset current $I_{\text{off}}(T)$, the equation can be written as [178]

$$P_0 = \eta_{\text{sl}}(I - I_{\text{tho}} - I_{\text{off}}(T)). \tag{4.26}$$

This equation takes into account all static thermal effects, without the need to modify the intrinsic laser parameter, like the thermal dependent laser gain.

The thermal offset current $I_{\text{off}}(T)$ can be described with a polynomial function of the temperature as [178]

$$I_{\text{off}}(T) = a_0 + a_1 T + a_2 T^2 + a_3 T^3 ..., \tag{4.27}$$

with the coefficients determined by parameter extraction from measured L-I curves at different temperatures. Note there is a redundancy between a_0 and I_{tho}, which was introduced for practical reasons to allow more realistic values for I_{tho} [174].

The L-I curve in Equation 4.25 can be described by the laser rate equations [180]. This enables the introduction of the thermal offset current $I_{\text{off}}(T)$ in the these equation, thus L-I curves as well as the non-dc behavior can be modeled at different temperatures. Taking the laser rate equations 4.1, 4.2 from Section 4.3.2.3 and modifying them by neglecting the Langevin forces, removing the carrier density dependency of the carrier recombination time, introducing of a gain compression factor ϵ and including the confinement factor Γ into the gain G_0 leads to [178]

$$\frac{\mathrm{d}N_{\text{cr}}}{\mathrm{d}t} = \frac{\eta_{\text{I}}(I - I_{\text{off}}(T))}{q} - \frac{N_{\text{cr}}}{\tau_{\text{sp}}} - \frac{G_0(N_{\text{cr}} - N_{\text{cr,0}})S}{1 + \epsilon S} \tag{4.28}$$

$$\frac{\mathrm{d}S}{\mathrm{d}t} = \beta_{\text{sp}} \frac{N_{\text{cr}}}{\tau_{\text{sp,r}}} + \frac{G_0(N_{\text{cr}} - N_{\text{cr,0}})S}{1 + \epsilon S} - \frac{S}{\tau_{\text{p}}}. \tag{4.29}$$

Here G_0 is the gain coefficient, $N_{cr,0}$ the carrier transparency number[58] and ϵ the gain compression factor[59]. Using these rate equations, the optical output power can be described as $P_0 = k_{cpl} S$, with k_{cpl} a scaling factor related to the VCSEL coupling efficiency.

The prior equations are the basis for the VPItransmissionMaker VCSEL model. Additionally, an expression for the VCSEL current-voltage and temperature characteristics can be introduced. The latter can be described with the help of a thermal rate equation [178] in the form of

$$T = T_0 + (IV - P_0)R_{\text{th}} - \tau_{\text{th}} \frac{\mathrm{d}T}{\mathrm{d}t}. \tag{4.30}$$

The parameter R_{th} is the thermal impedance, which relates to the change in the device temperature due to the power dissipated as heat, τ_{th} the thermal time constant taking into account the relatively slow thermal response time, T_0 the ambient temperature and V the laser voltage.

The current-voltage relation of the VCSEL can be represented with a polynomial approach similar to the thermal offset current $I_{\text{off}}(T)$ [178] with

$$V = f(I, T) = (b_0 + b_1 T + b_2 T^2 + ...)(c_0 + c_1 I + c_2 I^2 + ...). \tag{4.31}$$

[58] the carrier density at which the gain is zero

[59] gain saturation at high photon densities [158]

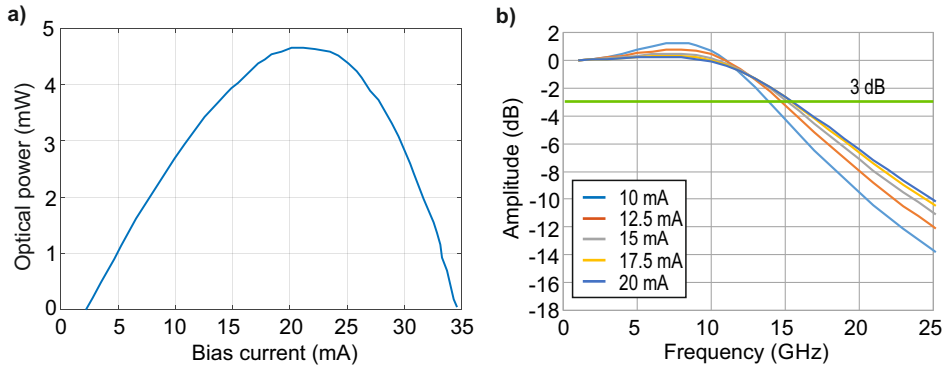

FIGURE 4.29: (a) L-I curve and system frequency response for different bias currents of the VCSEL simulation model (VPItransmissionMaker default model).

The coefficients can also be extracted from measured V-I curves at different temperatures. Equation 4.31 is a generic expression for the current and temperature relation of the VCSEL voltage. Other forms are possible like a relationship which accounts for a resistance in series with a diode [178].

The VPItransmissionMaker VCSEL model [176] takes into account several other parameters, e.g. geometrical data, which are of no further interests in this evaluation. The key idea is the use of measured L-I and V-I curves to feed the SM-VCSEL laser model, which in turn adapts the parameters of the laser rate equations and creates the numerical laser model. The L-I and V-I curves used for the simulative investigations originate from [181] and are provided with the VPItransmissionMaker default model. Note that the use of own measured curves would also be possible. However, there are some aspects to be considered. First, the VPI VCSEL model consists of several parameters, like the geometrical data of the VCSEL, which are not known for the used high-speed VCSELs. Second, the focus in this part of the thesis is on the gain for nonlinear pre-equalization and not on the VCSEL model, thus a dynamic nonlinear system, as provided by the standard VPI VCSEL model, is already adequate.

The L-I curve of the VCSEL model is shown in Fig. 4.29 (a). The static thermal roll-over is at 20 mA, with a corresponding output power of 5 mW. The threshold current is at 2.2 mA. From a static point of view, a useful operation point would be at a bias current of 10 mA with a driving amplitude[60] of 10 mA[61]. However, due to the difference in the static and dynamic VCSEL behavior, higher bias and driving amplitudes are possible. Fig. 4.29 (b) shows the frequency response for different bias currents. As can be observed, a 3 dB bandwidth of 16 GHz is available at a bias current of 20 mA. This is sufficient for symbol rates beyond 10 GBd. Note that the slope efficiency of the VCSEL model is similar compared to the used high-speed VCSELs with ~0.2 W/A but with overall higher output powers (4 vs. 1.5 mW). The 3 dB bandwidth of the VCSEL model is smaller compared to the used high-speed VCSELs with 16 GHz vs. 26 GHz.

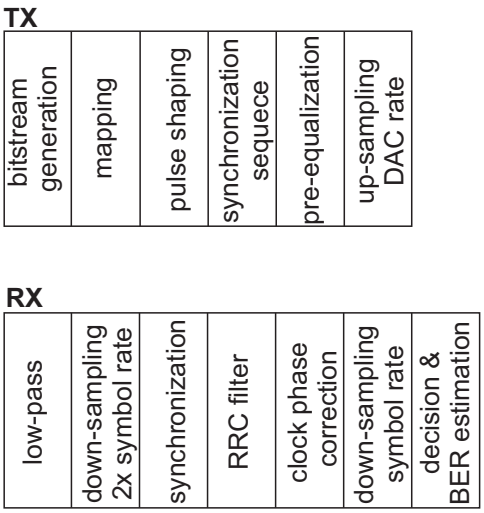

FIGURE 4.30: DSP for PAM transmission with pre-equalization block.

4.6.3 DSP for simulation of VCSEL system

In Fig. 4.30 the DSP for PAM transmission is shown. The transmitter side includes the bit-stream generation, symbol mapping and root-raised cosine pulse shaping[62]. Then samples for synchronization are added and pre-equalization is applied. Finally, the signal is up-sampled to the DAC sampling rate, i.e. 4x symbol rate. The receiver side consists of an LPF (FIR type), down-sampling to the processing rate (2x symbol rate), synchronization, RRC filter, clock phase correction[63] , down-sampling to the symbol rate and BER estimation after the decision. Note, there is no further equalizer at the Rx, since it can be assumed that the channel estimation is nearly perfect in the simulation and thus the Tx pre-equalization is sufficient[64].

The estimation of system behavior, i.e. the channel, is equal to the experiment and based on a test sequence. Note that the Volterra kernels are only determined by the VCSEL behavior, since there are no other relevant components (refer to Fig. 4.28). The pre-equalization scheme used in this simulation differs from the high-speed VCSEL experiment. There is no scaling of the linear pre-equalization[65], thus the full system response is always pre-equalized. Two cases for the pre-equalization are investigated, only linear and linear plus nonlinear. Both are applied and their influence is determined.

4.6.4 Volterra kernels of simulation system

The Volterra kernels greatly depend on the VCSEL operation point and must be determined for every new set of VCSEL bias and driving amplitude. In Fig. 4.31 (a) an

[60]The term driving amplitude relates to the difference between bias current and maximum current for the VCSEL modulation. Refer to Appendix A.10 for details.

[61]i.e. 20 mA peak-to-peak

[62]roll-off factor = 1

[63]The clock phase correction is required since the synchronization (simple cross correlation) commonly doesn't find the optimal phase relation

[64]verified in the simulations with an additional Rx equalizer

[65]this relates to $k = 0$

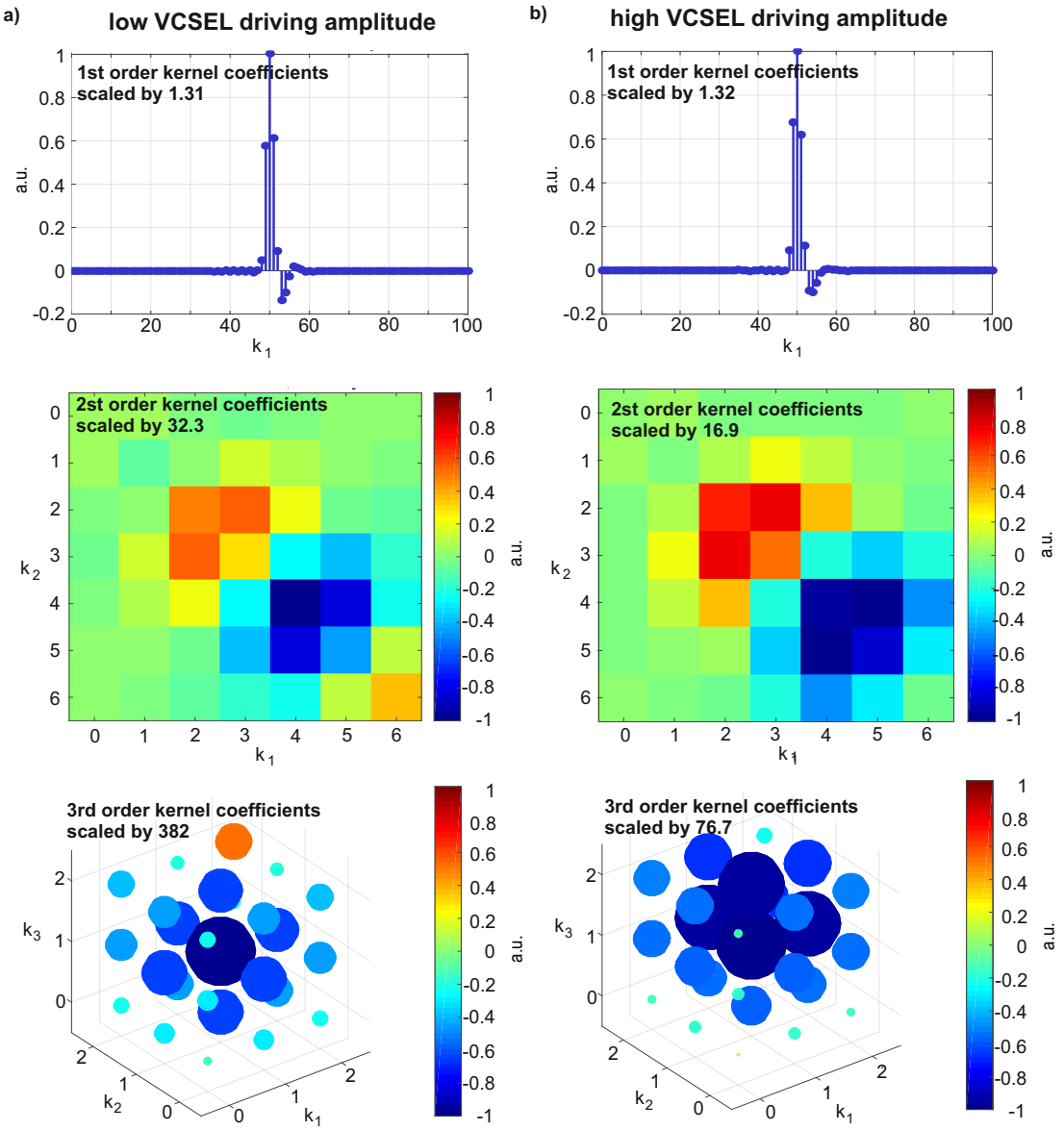

FIGURE 4.31: Examples of 1st, 2nd and 3rd order Volterra kernels for two different VCSEL driving amplitudes in the simulation.

example for a 3rd order approach is shown[66]. The first order is the impulse response of the system and the second and third orders represent the nonlinear behavior (refer to Equation 4.10). The first order kernel $h_1(k_1)$ with a memory length of $N_1 = 100$ shows the typical low-pass behavior, if transformed into the frequency domain. The second order kernel $h_2(k_1, k_2)$ with memory length of $N_2 = 7$ consists of N_2^2 elements and can be illustrated in a 2D-plot. The colors indicate the power of each element. There is a strong peak in the center, representing the static nonlinearity and additional side-peaks, representing the nonlinear memory effects. The third order kernel $h_3(k_1, k_2, k_3)$ with memory length $N_3 = 3$ consists of N_3^3 elements and can be illustrated as in a 3D-plot. The power of each element is indicated by the circle area and the color. Fig. 4.31 (b) shows the same illustration but with a higher VCSEL driving

[66]Similar to the experiments, only kernel orders up to three are used. Tests with higher orders showed no further improvement.

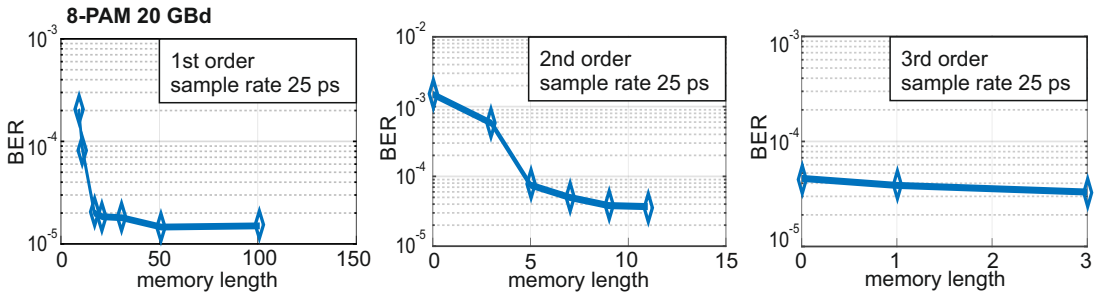

FIGURE 4.32: Performance of 20 GBd 8-PAM for different Volterra filter memory lengths.

amplitude. The linear part differs slightly compared to Fig. 4.31 (a), which can be attributed to the estimation of the linear transfer function, which is not based on a small signal assumption. The second and third order terms are significantly stronger, as indicated by the scaling factor at the top left of each figure. This behavior is expected, since higher driving amplitudes increase the nonlinearities.

The optimal length of each Volterra kernel can be estimated for the simulations. In Fig. 4.32 its influence on the BER is shown in case of a 20 GBd 8-PAM transmission. The length of each kernel is separately swept and the resulting BER calculated. Note that the time spacing between each tap is two times the symbol rate (i.e. 25 ps for 20 GBd). The linear part shows no further improvement at lengths beyond 20 taps. The second order kernel shows no improvement beyond 7 taps and the third order nearly no improvement at all. Nonetheless, for the simulations with 20 GBd 8-PAM kernel lengths of 100, 7, and 3 are chosen for practical reasons. At higher symbol rates these values are accordingly adapted.

To get an idea about the relevant nonlinear distortion effects of the PAM transmission, two eye diagrams with linear and nonlinear pre-equalization are shown in Fig. 4.33. To generate both eye diagrams, an 20 GBd 8-PAM signal is pre-equalized with the previously estimated Volterra kernels and used to drive the VCSEL. After optical-electrical conversion, the signals are recorded. Note that the photodiode noise is turned off and the same VCSEL driving amplitude is applied for both cases. In Fig. 4.33 (a) two nonlinear distortions can be observed. First, the lower eyes are slightly compressed, as indicated by the equidistant horizontal green marker lines. This results in a higher sensitivity regarding the common noise sources[67] in the system and errors, if equivalent decision levels are used. Second, an amplitude dependent skew of each sub-eye can be observed, with a stronger delay for lower amplitudes (sub-eyes). For a fixed decision time, indicated by the vertical green marker lines, a significant number of errors can be expected in the lower sub-eyes. This is especially critical, if additional timing inaccuracies like jitter are considered. To get an idea about the relevant nonlinear distortion effects of the PAM transmission, two eye diagrams with linear and nonlinear pre-equalization are shown in Fig. 4.33. To generate both eye diagrams, an 20 GBd 8-PAM signal is pre-equalized with the previously estimated Volterra kernels and used to drive the VCSEL. After optical-electrical conversion, the signals are recorded. Note that the photodiode noise is turned off and the same VCSEL driving amplitude is applied for both cases. In Fig. 4.33 (a) two nonlinear distortions can be observed. First, the lower eyes are slightly compressed, as indicated by the

[67] i.e. RIN and PD+TIA thermal noise

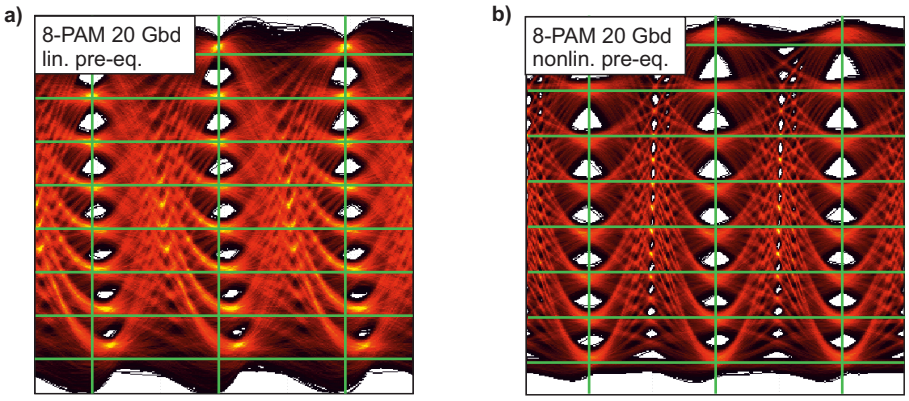

FIGURE 4.33: Electrical eye diagram of 8-PAM with (a) linear pre-equalization and (b) nonlinear pre-equalization.

equidistant horizontal green marker lines. This results in a higher sensitivity regarding the common noise sources[68] in the system and errors, if equivalent decision levels are used. Second, an amplitude dependent skew of each sub-eye can be observed, with a stronger delay for lower amplitudes (sub-eyes). For a fixed decision time, indicated by the vertical green marker lines, a significant number of errors can be expected in the lower sub-eyes. This is especially critical, if additional timing inaccuracies like jitter are considered. In Fig. 4.33 (b) the same eye diagram with an additional nonlinear pre-equalization is shown. Both distortion effects are reduced, with a remarkable reduction of the sub-eye skew.

4.6.5 Simulation results

Before comparing the performance of the linear and the nonlinear pre-equalization, various simulation parameters have to be set. These are the VCSEL operation point, the optical power at the receiver and signal parameters. The VCSEL operation point is defined by the bias and the driving amplitude and determines the linear and nonlinear behavior of the system. In Appendix A.10 this aspect is illustrated and the relation to the extinction ratio is shown. The next parameter is the optical power at the receiver. On the one hand, it has to be low enough to allow the BER estimation by simple error counting for reasonably long signal sequences, but on the other hand high enough to prevent the domination of the system by the photodiode noise.

The signal parameters include the symbol rate, the PAM modulation order and the pulse shaping roll-off factor. The used modulation format is 8-PAM. Simulations with 4-PAM showed no gain, if an additional nonlinear pre-equalization is applied. This can be attributed to the higher robustness of 4-PAM compared to 8-PAM. Simulations with 16-PAM are only possible for very small symbol rates, which contradicts the usefulness on such systems. Symbol rates >20 GBd in combination with a roll-off factor of 1 are used, which allow the full utilization of the VCSEL bandwidth[69], while ensuring relatively small PAPR values[70].

[68] i.e. RIN and PD+TIA thermal noise

[69] Current transmission experiments utilize VCSELs far beyond their 3 dB bandwidth, like in the demonstrated measurements in Section 4.5. Thus, signal bandwidths beyond the VCSEL 3 dB bandwidth (16 GHz) are used, i.e. 20 GHz for 20 GBd 8-PAM with roll-off = 1

[70] see Appendix A.2

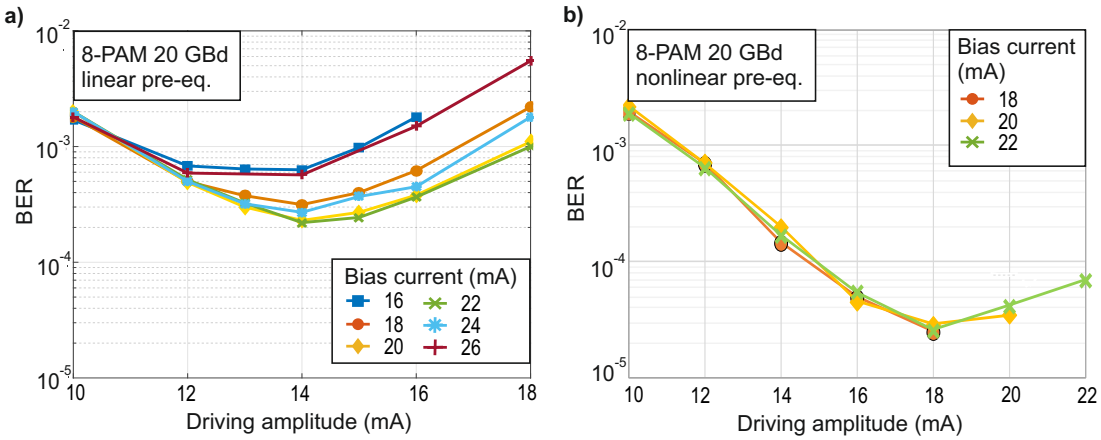

FIGURE 4.34: Bias current and driving amplitude determination for the VCSEL simulation with linear (a) and nonlinear (b) pre-equalization transmitting 20 GBd 8-PAM.

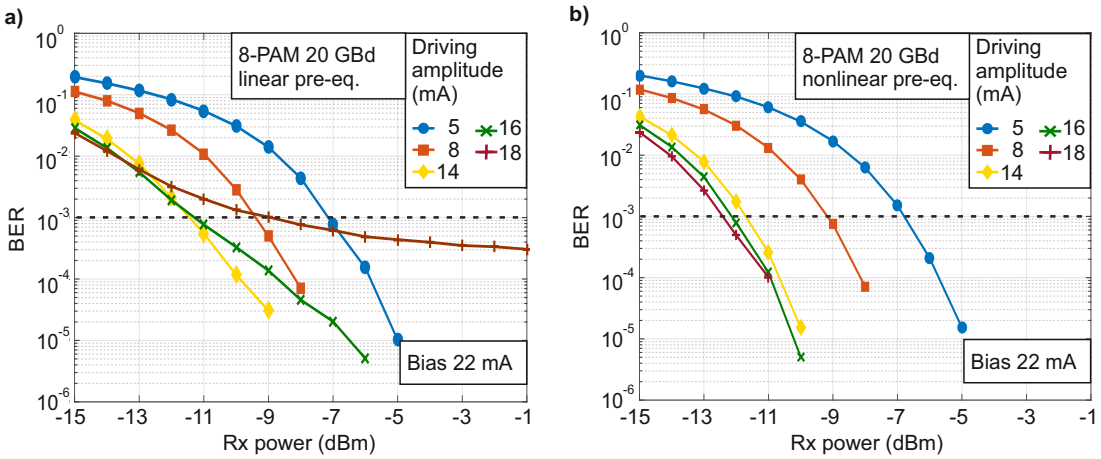

FIGURE 4.35: Performance of 20 GBd 8-PAM for different bias currents and driving amplitudes and for (a) linear and (b) nonlinear pre-equalization.

At first the optimum driving amplitude[71] and bias current for 20 GBd 8-PAM is determined. This is done by estimating the BER of the linear pre-equalized 8-PAM signal for various bias currents and driving amplitudes and the same Rx power (-9 dBm). Note that the transmission of 8-PAM is only possible with linear pre-equalization and no pre-equalization would result in BERs in the order of 0.1 due to ISI. The results of the optimization are shown in Fig. 4.34 (a). Starting with a bias current of 16 mA (blue square curve) the following aspects can be observed. At low driving amplitudes the system is limited by the receiver noise, resulting in high BER values. Increasing the driving amplitude improves the performance with an optimum at 14 mA. Even higher values decrease the performance again, since more and more nonlinear distortions occur.

With higher bias currents the same behavior can be observed, with a BER optimum

[71] Driving amplitude relates to the peak amplitude of a sine and not to the peak-to-peak amplitude, see Appendix A.10.

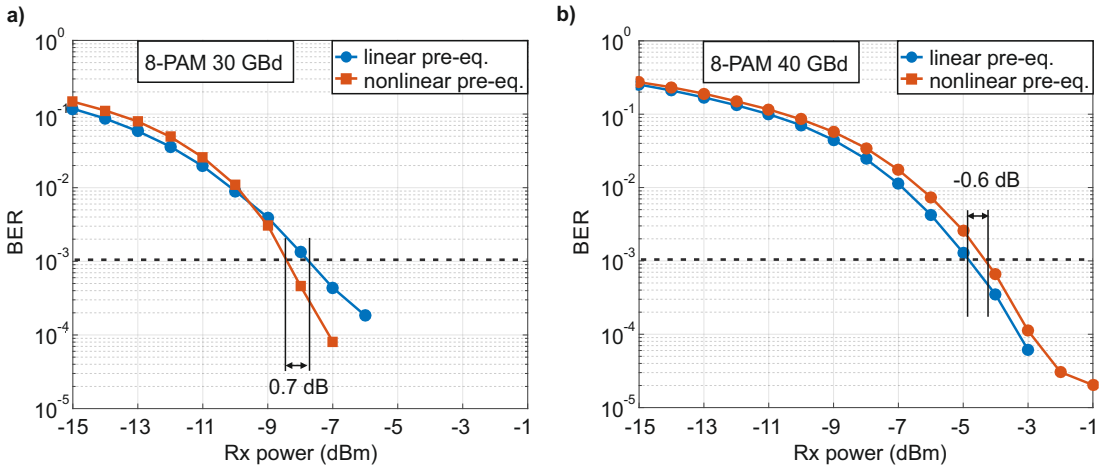

FIGURE 4.36: Performance of 30 and 40 GBd 8-PAM for linear and nonlinear pre-equalization.

at 22 mA bias current. The increased bias current has two effects. First, the 3 dB bandwidth improves as could already be observed in Fig. 4.29. This simplifies the linear pre-equalization and improves the SNR after the photodiode. Second, the amount of nonlinearities increases as well, since the operating point is shifted towards the nonlinear region. This degrades the performance and contradicts the first effect. The optimum operation point for the 20 GBd 8-PAM transmission with linear pre-equalization is therefore at 22 mA bias and 14 mA driving amplitude.

Now the additional nonlinear pre-equalization is turned on and the same optimization process is repeated. The results are shown in Fig. 4.34 (b). First, the BER has improved by an order of magnitude (i.e. $2.2 \cdot 10^{-4}$ vs. $2 \cdot 10^{-5}$) and second, the optimal driving amplitude has increased to 18 mA. This can be expected, since the additional nonlinearities are compensated by the nonlinear pre-equalization. In contrast to the linear approach, no impact for different bias currents can be observed. It can be assumed that the additional nonlinearities at slightly higher bias currents can be compensated, thus minimizing the impact[72]. With the optimal operation points for both pre-equalization approaches, the gain in performance regarding the optical Rx power at the photodiode can be determined. In Fig. 4.35 (a) the achieved BER vs. the optical power at the photodiode is shown for linear pre-equalization at different driving amplitudes. At a target BER of 10^{-3}, which can be corrected with a standard HD-FEC algorithm, the optimum driving amplitude is 14 mA as already shown in Fig. 4.34. At smaller driving amplitudes, the performance is limited by the photodiode noise and at higher driving amplitudes limitations due to nonlinear VCSEL behavior occur, which results in an error floor. The required Rx power at the target BER is -11.4 dBm.

For the nonlinear pre-equalization case, shown in Fig. 4.35 (b), the optimal driving amplitude is 18 mA at the target BER. The required Rx power is -12.5 dBm, which results in a gain in sensitivity of 1.1 dB compared to the linear case. The gain can be explained by the higher VCSEL driving amplitude, which enables a better utilization of the optical carrier in an IM/DD-based system.

The next question regarding the nonlinear pre-equalization gain is the behavior at higher symbol rates, like 30 and 40 GBd 8-PAM. In these cases the VCSEL is modulated

[72] stronger variation of the bias currents as shown in the figure have an impact

TABLE 4.2: 8-PAM performance gain with nonlinear pre-equalization

Required optical power at the receiver for 20, 30 and 40 GBd 8-PAM at a BER of 10^{-3} with and without nonlinear pre-equalization. Difference in required optical power of linear pre-equalization compared to additional nonlinear pre-equalization at the target BER.

	20 GBd 8-PAM	30 GBd 8-PAM	40 GBd 8-PAM
linear	-12.5 dBm	-8.4 dBm	-4.1 dBm
linear & nonlinear	-11.4 dBm	-7.7 dBm	-4.8 dBm
power difference	1.1 dB	0.7 dB	-0.6 dB

far beyond its cut-off frequency[73]. To evaluate the performance, the same process as for 20 GBd is repeated. At first the optimal bias current and the optimal driving amplitude are determined for liner and nonlinear pre-equalization[74]. Then the performance at different Rx powers for the optimal operation point is determined. In Fig. 4.36 the results are shown for (a) 30 GBd 8-PAM and (b) 40 GBd 8-PAM. For the 30 GBd case, a gain in sensitivity of 0.7 dB for the nonlinear pre-equalization can be observed at the target BER. For the 40 GBd the gain becomes a loss and is -0.6 dB.

In Table 4.2 the results for all data rates are summarized. As can be observed, the sensitivity drops with higher data rates, as it is expected. Furthermore, a decrease in nonlinear pre-equalization gain occurs. Before a more detailed explanation of these findings is given, a transmission experiment is shortly presented in the next section, to verify the simulative findings.

4.6.6 Experimental verification of simulation results

To verify the simulation results additional measurements are performed. The experimental setup corresponds to the one for high-speed VCSEL experiments in btb configuration (shown in Fig. 4.15), except for the VCSEL and the DAC. The VCSEL is a multi-mode type with a 3 dB bandwidth of 11 GHz and the DAC has 6 bit nominal resolution and a 3 dB bandwidth of 9 GHz[75]. The Tx and Rx DSP is the same as in the simulations (see Fig. 4.30) except for an additional T/2-spaced MMSE-based equalizer at the Rx side, due to imperfections in the linear pre-equalization[76]. Similar to the simulations, the optimum bias currents and driving amplitudes are determined for each symbol rate and pre-equalization scenario.

The BER vs. the Rx power curves for 10, 13.6, 17 and 20 GBd 8-PAM are shown in Fig. 4.37. The blue curves represent the linear and the orange curves the additional nonlinear pre-equalization. First, for 10 and 13 GBd a slight gain for the additional nonlinear pre-equalization can be observed at the target BER of 10^{-3}. Higher symbol rates show no gain, as predicted in the simulations. However, there is a strong error floor even at low symbol rates, which impedes a detailed conclusion. The error

[73] 16 GHz

[74] For 30 GBd 8-PAM: linear pre-eq. bias current (BC) = 21 mA, driving amplitude (DA) = 18 mA; nonlinear-preeq. BC = 23 mA, DA = 22 mA. For 40 GBd 8-PAM: linear pre-eq. BC = 24 mA, DA = 24 mA; nonlinear-preeq. BC = 23 mA, DA = 23 mA.

[75] Note, due to limited frequency characteristics of the devices, only lower symbol rates are possible in these experiments compared to the simulations

[76] During the measurements it was observed that a small improvement in BER is possible with an additional linear post-equalizer.

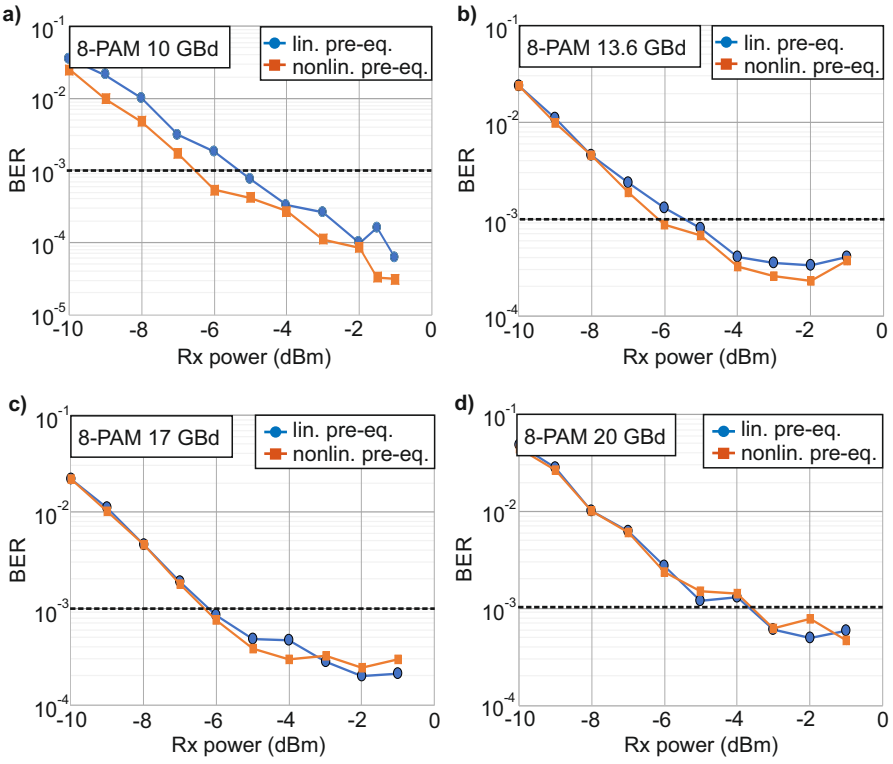

FIGURE 4.37: Experimental results for 20 GBd 8-PAM, BER vs. Rx power at 10, 13.6, 17 and 20 GBd 8-PAM with linear (orange curve) and nonlinear pre-equalization (blue curve).

floor increases with higher symbol rates and originates mainly from the limited resolution of the DAC[77], the VCSEL RIN[78] and the thermal noise of the receiver. Additional measurements with 4-PAM showed a significantly better performance, however nearly no nonlinear distortions[79] could be observed and thus no gain for the nonlinear pre-equalization can be expected even at the maximum acceptable VCSEL driving amplitudes. Altogether the experimental findings support the simulative investigation.

4.6.7 Conclusions on nonlinear pre-equalization for VCSEL-based high-speed links

Two questions remain after the findings in the previous sections. First, why the gain of the nonlinear pre-equalization is decreasing at higher PAM symbol rates and second, why there is nearly no gain for DMT at all (refer to Section 4.5.4.3). Starting with the first question, the following can be taken in consideration: nonlinearities arise due different static and dynamics effects (thermal heating mechanism of the VCSEL, modulation effects) and are represented by the nonlinear characteristic. Higher signal power levels, i.e. driving amplitudes, result in stronger nonlinearities. These can be compensated by applying a nonlinear pre-equalization as shown, thus a gain in sensitivity occurs with the nonlinear pre-equalization. However, there are also linear

[77] The ENOB of the DAC at higher frequencies is only 3.5 bit.

[78] Note that the quantitative estimation of the noise sources for the VCSEL system in Section 2.2.3 used the high-speed system from Section 4.5.1 as a reference and not this system.

[79] e.g. amplitude depended skew

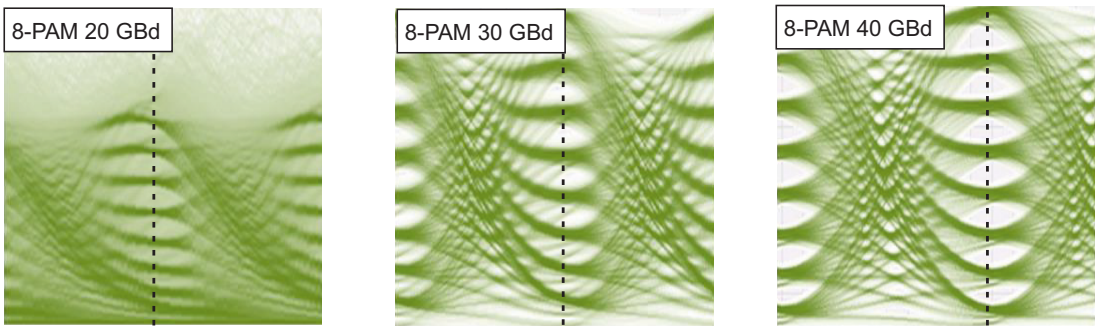

FIGURE 4.38: Simulated eye diagram of 20,30 and 40 GBd 8-PAM with linear pre-equalization directly after the VCSEL.

effects such as the bandwidth limitation of the VCSEL. If the VCSEL is considered as the combination of a linear system followed by a nonlinear dynamic system, higher signal bandwidths result in less signal power going into the nonlinear system, which in turn decreases the amount of nonlinear distortion and the gain from the nonlinear pre-equalization.

This can be tested easily as shown in Fig. 4.38. Here, eye diagrams[80] for 20, 30 and 40 GBd 8-PAM signals are illustrated directly after the VCSEL with only linear pre-equalization turned on. The bias current and the driving amplitude are equal for all three symbol rates. The 20 GBd eye diagram clearly indicates several nonlinear effects, like compression of the outer eyes and an amplitude dependent skew of the sub-eyes. These effects become smaller as the symbol rate increases, thus the amount of nonlinear distortion decreases.

Another effect is the raise of the signal PAPR with higher symbol rates and with additional nonlinear pre-equalization[81]. In Table 4.3 this behavior is shown. The shown PAPR values are mean values of several data blocks and calculated in front of the VCSEL. Since the VCSEL driving amplitude is fixed, higher PAPR values degrade the relation between the optical carrier and the sidebands (data signal) in IM/DD systems. This in turn decreases the receiver sensitivity for signals with higher PAPR.

Taking both effects in conclusion, the smaller amounts of nonlinear distortions with higher symbol rates and the increase in PAPR with nonlinear pre-equalization, the first question can be answered. As the symbol rate increases from 20 GBd to 40 GBd, the impact of nonlinearities decreases. This results in a smaller gain from the nonlinear pre-equalization. On the other hand, the PAPR increases with the application of linear and nonlinear pre-equalization, resulting in a loss in receiver sensitivity. Both points combined explain the different behavior in terms of sensitivity gain from the nonlinear pre-equalization for different symbol rates.

The second question, regarding the negligible nonlinear pre-equalization gain for DMT compared to PAM, can also be answered taking the signal PAPR into account. DMT has typically very high PAPRs and requires a digital clipping to limit the PAPR. If a fixed VCSEL driving amplitude is set, signals with high PAPRs experience much less nonlinear distortions due to the lower probability of higher amplitudes. This results in less gain from the nonlinear pre-equalization for signals with high PAPR such as

[80] An averaging is applied to the simulated signal after the VCSEL, thus most of the VCSEL noise is neglected

[81] The signal form deviates from its ideal pulse shaped-form due to the linear and nonlinear pre-equalization. This effect is stronger at higher symbol rates.

TABLE 4.3: Signal PAPR in front of the VCSEL

PAPR values for 20, 30 and 40 GBd 8-PAM in front of the VCSEL with and without nonlinear pre-equalization.

	20 GBd 8-PAM	30 GBd 8-PAM	40 GBd 8-PAM
linear	8 dB	8.7 dB	9.7 dB
linear & nonlinear	9.1 dB	9.5 dB	10.3 dB

DMT. Furthermore, the PAPR degradation due to the nonlinear pre-equalization is an important problem for DMT since it directly contradicts the digital clipping of the DMT signal prior to the transmission. That means that a nonlinear pre-equalization of a DMT signal is partly hindered by the digital clipping prior to D/A conversion.

Another important aspect is also the kind of nonlinear distortion. For PAM the amplitude dependent skew is especially critical as could be observed in Fig. 4.38. If a fixed decision time is set, indicated by the vertical line, many errors occur in the outer sub-eyes. The same problem exists for the horizontal decision levels, due to the horizontal compression of the outer sub-eyes. Since DMT symbols are decided in the frequency domain, this effect does not occur in this form. In conclusion, both effects make DMT much more resilient to nonlinear distortions in these IM/DD-based systems.

4.7 Conclusion and outlook on the performance improvement of VCSEL-based high-speed links

Today's high-speed short-range transmission systems based on VCSELs enable capacities beyond 100 Gb/s for simple IM/DD-based operation. Approaches to further improve the performance consist of enhancing the used VCSELs and the application of advanced DSP. In this thesis, the DSP approach is investigated by utilizing linear and nonlinear pre-equalization.

The demonstrated high-speed VCSEL experiments achieved transmission rates beyond the state-of-the-art at the time of publication. This was realized with the pre-equalization of only a part of the total linear system transfer function, with the optimum still depending on the actual transmission scenario. The use of nonlinear pre-equalization showed a further improvement of the transmission performance compared to sole linear pre-equalization, but only under certain conditions. At high signal bandwidths, far beyond the 3 dB system bandwidth, the improvement is small or even a loss occurs. The differences in nonlinear pre-equalization gains for PAM and DMT can be attributed to the differences in PAPR and the actual kind of nonlinear distortion, with PAM profiting significantly more. Therefore, the application of nonlinear pre-equalization offers only a limited improvement for such high-speed systems, even without considering the additional computational effect.

Further work may look into a more analytical description of the optimized linear pre-equalization, based on bandwidth and SNR measurements of the transmission system. This would allow a calculation of the optimum linear pre-equalization prior to the transmission. Difficulties arise from the interaction between the different components bandwidths and the dependencies on the actual VCSEL operation point. Another open aspect is the computation effort for the pre-equalization in relation to the gain in transmission performance, which is a trade-off for such high-speed systems.

Chapter 5

Summary

In this thesis two different approaches to improve the transmission capacity of high-speed short-range links were investigated. The first approach is a bandwidth extension scheme based on analog mixing and passive signal combining. The second scheme utilizes linear and nonlinear pre-equalization to compensate for the channel impairments.

The bandwidth extension approach was demonstrated on a IM/DD-based optical link and enables transmission rates close to 200 Gb/s at a single wavelength and single polarization. For IM/DD-based systems, this enables a significant increase in signal bandwidth and data rate compared to the state-of-the-art, without utilizing optical multiplex techniques or coherent transmission. Furthermore, no new components are required and current off-the-shelf components are suitable to significantly increase the capacity.

The investigation was focused on the experimental verification of the approach, with simulations being performed mainly to support the experiments. The limitations of such systems were discussed and the inherent impairments analyzed. Equalization schemes to overcome theses impairments were developed, implemented and verified. Also different hardware realizations were discussed and the influence of the modulation formats shown. Furthermore, the realization of a wideband DAC based on this concept was demonstrated, enabling the generation of true spectrally continuous waveforms. The successful experimental realization of the bandwidth extension approach proved the feasibility but indicated also the limitations of the concept. Main challenges are the SNR degradation due to the non-ideal mixer, combiner and splitter properties and the limitation of today's DACs.

The second approach to improve the transmission capacity of high-speed short-range links is based on linear and nonlinear pre-equalization of a VCSEL-based system. Today's VCSELs are the primary optical modulator for short-range applications but suffer from stronger nonlinear behavior, higher bandwidth limitations and increased RIN compared to other modulator types. DSP concepts to improve or compensate these impairments enable a significant boost to the transmission performance. The use of linear pre-equalization was demonstrated in a high-speed transmission system and enabled a significantly increased data rate. This was achieved by carefully optimizing the amount of linear pre-equalization in different transmission scenarios and using DMT as a modulation format. The gain in transmission performance for the linear pre-equalization strongly depends on the actual transmission scenario and the interaction between the components properties, primary the DAC and the VCSEL.

The investigation of nonlinear pre-equalization for VCSEL-based high-speed short-range systems consisted of the analysis of the relevant nonlinear impairments and the implementation of a Volterra-based filter to describe the system characteristic and to

calculate the pre-equalized signal. A detailed simulative study was presented, including the dependencies on the VCSEL operation point and the verification by experimental means. Furthermore, the performance gain for different modulation formats was investigated. Nonlinear pre-equalization of VCSEL-based links offers primary an improvement in performance for PAM formats and symbol rates well below the bandwidth limit of the VCSEL. In contrast, DMT and PAM showed no gain from nonlinear pre-equalization at higher symbol rates. This implies that when the symbol rate is increased in the near future, simpler DSP can be used without noticeable performance degradation.

The feasibility to achieve the increased transmission capacity demands of the two concepts presented in this thesis has been demonstrated. Both approaches meet the requirements of low-cost and simple optical components demanded by short-range optical link applications. These approaches are therefore suitable candidates for the future implementation of optical short-range interconnects.

Appendix A

Further remarks

A.1 Raised cosine filter

The raised-cosine filter is a filter used for pulse-shaping that fulfills the first Nyquist criterion, i.e. minimizing the ISI. The filter response in the frequency domain is:

$$H(f) = \begin{cases} = 1, & |f| \leq \frac{1-\beta}{2T} \\ = \cos^2\left(\frac{\pi T}{2\beta}\left(|f| - \frac{1-\beta}{2T}\right)\right), & \frac{1-\beta}{2T} < |f| \leq \frac{1+\beta}{2T} \\ = 0 & \text{otherwise} \end{cases}, \tag{A.1}$$

with β the roll-off factor between 0 and 1 and T the symbol time. Fig. A.1 shows the filter response for different β factors. For transmission systems commonly a matched pair of $\sqrt{H(f)}$ is used at the Tx and the Rx side. The Tx side filter limits the signal bandwidth prior to the transmission and the Rx side filter suppresses the channel noise outside the signal bandwidth after the transmission and before the decider. Smaller β factors decreases the signal bandwidth down to $\frac{1}{2T}$, which is beneficial for bandwidth limited systems, however at the cost of increased jitter sensitivity and higher PAPR values.

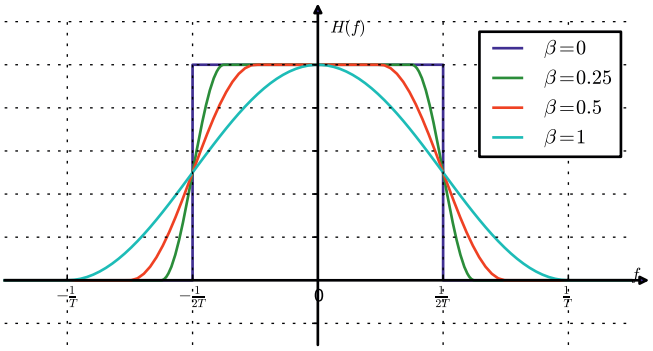

FIGURE A.1: Frequency domain representation of the raised cosine filter for different β factors.

A.2 PAPR and signal clipping

PAPR is the relation of the squared peak amplitude (i.e. peak power) to the squared root mean square (RMS) value of a signal. It can be written as:

$$PAPR = \frac{|x_{\text{peak}}|^2}{x_{\text{RMS}}^2}, \tag{A.2}$$

with x_{peak} the peak amplitude and x_{RMS} the RMS value of a signal. In Fig. A.2 (a) amplitude distributions[1] of different modulation formats used in this thesis are shown with their average PAPR in dB. As can be observed, PAM offers the lowest PAPR followed by slightly higher values for QAM. As can be expected, the PAPR of OFDM is the highest. However, the application of smaller β factors for the Tx-side raised-cosine pulse shaping of PAM and QAM results also in significantly higher PAPRs.

A low PAPR allows an efficient modulation of the optical carrier in IM/DD system. This aspect is illustrated in Fig. A.2 (b) for two signals with different PAPRs (i.e. OFDM and 8-PAM with roll-off factor $\beta = 1$) modulating a laser. The parameter I_{th} is the laser threshold current, I_{b} the DC bias current and I_{pp} the peak-to-peak driving amplitude. For the same driving amplitude of the optical intensity modulator, only a small part of the optical power is modulated by the OFDM signal compared to the 8-PAM signal. This results in higher sensitivity requirements at the receiver for OFDM or generally for modulation formats with high PAPRs.

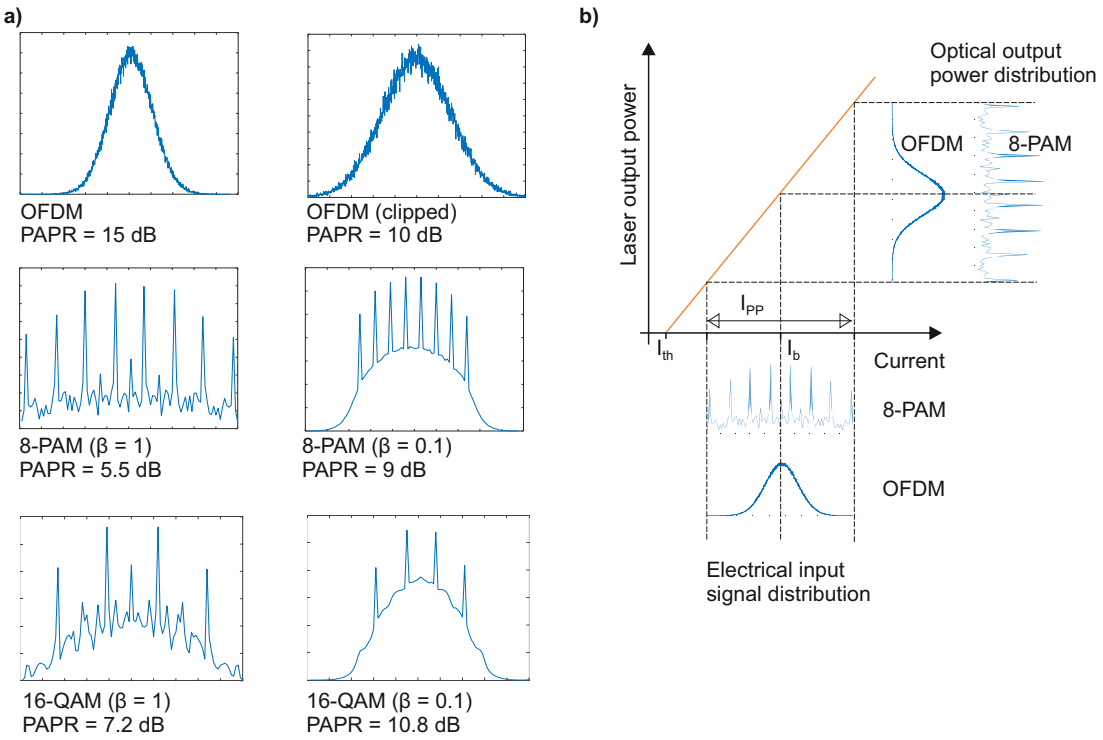

FIGURE A.2: (a) Amplitude distribution of modulation formats used in this thesis with different PAPRs and (b) influence of PAPR on optical intensity modulation.

[1] of the up-sampled signal

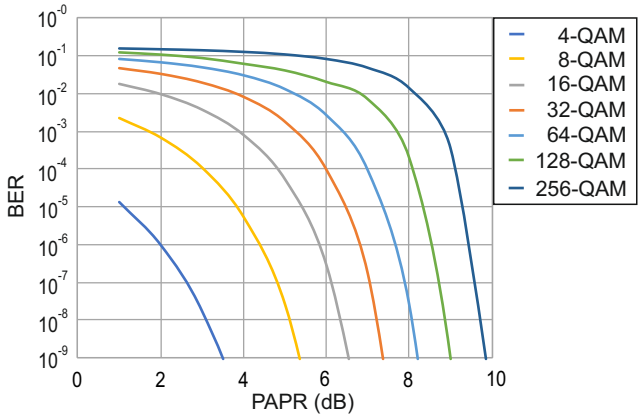

FIGURE A.3: Influence of digital clipping for OFDM for different subcarrier modulation orders.

The high PAPR of OFDM can be reduced by introducing a digital amplitude clipping before D/A conversion. The optimal clipping amplitude depends on the transmission scenario and the subcarrier modulation order. In Fig. A.3 the BER of an OFDM transmission at different clipping levels and modulation orders is shown[2]. As can be observed, BERs below 10^{-9} are possible even for 256-QAM with a PAPR of 10 dB. Therefore, for all transmissions experiments and simulation in this thesis a maximum PAPR of 10 dB is set by digital clipping at the Tx.

Additionally to the digital clipping, an analog clipping is commonly present in the experiments. Analog clipping refers to the clipping of the signal due to the characteristics of the optical modulator. The amount of analog clipping is controlled by adapting the driving amplitude of the optical modulators (MZM, VCSEL) with respect to the BER, which generally resulted in an additional analog clipping of the signal. This procedure is for example illustrated in Fig 4.16. Small driving amplitudes result in no analog clipping and a linear behavior but a poor extinction ratio and thus a poor sensitivity. High driving amplitudes result in a strong analog clipping and nonlinear distortions.

[2]no other noise contribution

A.3 QAM constellation diagrams used in this thesis

Fig. A.4 shows the used QAM constellations diagrams. Each state in the constellation diagrams is gray coded, i.e. neighboring points differ only by one bit.

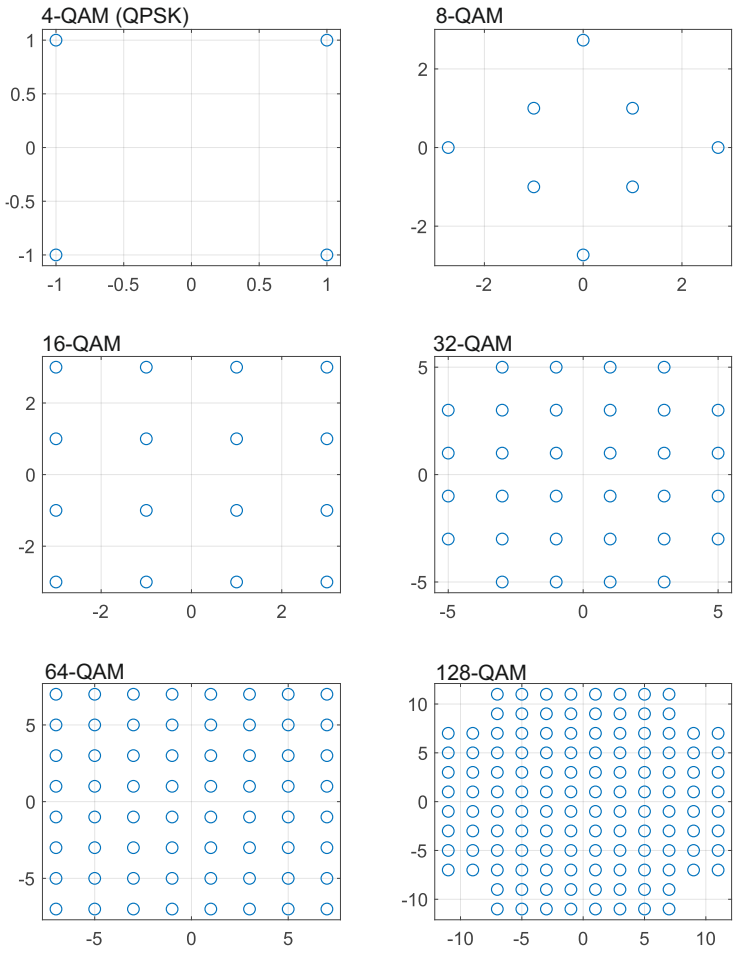

FIGURE A.4: QAM constellation diagrams used in this thesis.

A.4 Small signal approximation of the diode current.

Fig. A.5 shows a typical V-I characteristic of a Schottky diode [105], which is commonly used for microwave mixers. The V-I relation can be expressed by

$$I(V) = I_S(\exp^{\alpha V} - 1)\,, \tag{A.3}$$

with $\alpha = q/n_D kT$, q the elementary charge, k the Boltzman constant, n_D the idealty factor which is between 1 and 2 and depends on the diode structure, T the temperature and I_S the reverse bias saturation current.

The diode voltage V at its bias point can be expressed by

$$V = V_0 + v, \tag{A.4}$$

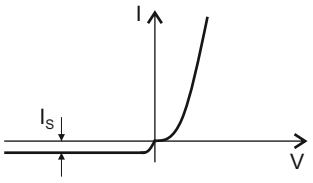

FIGURE A.5: V-I characteristic of a Schottky diode.

with V_0 the bias voltage and v the small signal voltage. Expanding Equation A.3 with a Taylor series leads to

$$I(V) = I_0 + v\frac{\mathrm{d}I}{\mathrm{d}V}\bigg|_{V_0} + \frac{v^2}{2}\frac{\mathrm{d}^2I}{\mathrm{d}V^2}\bigg|_{V_0} + \dots , \tag{A.5}$$

with $I_0 = I(V_0)$ the bias current. The derivatives can be calculated from Equation A.3 and may be written as

$$\begin{aligned} \frac{\mathrm{d}I}{\mathrm{d}V}\bigg|_{V_0} &= \alpha I_S \exp^{\alpha V_0} = \alpha(I_0 + I_S) = G_D = \frac{1}{R_j} , \\ \frac{\mathrm{d}^2I}{\mathrm{d}V^2}\bigg|_{V_0} &= \alpha^2 I_S \exp^{\alpha V_0} = \alpha^2(I_0 + I_S) = G'_D , \end{aligned} \tag{A.6}$$

with R_j the junction resistance and G_D the dynamic conductance of the diode. Equation A.5 can now be written as

$$I(V) = I_0 + i = I_0 + vG_D + \frac{v^2}{2}G'_D + \dots . \tag{A.7}$$

This three term approximation for the diode current is called small-signal approximation and is adequate for most calculations.

A.5 Scattering parameter of electrical hybrids

The scattering parameters of an electrical 3 dB 90° hybrid coupler are [105]:

$$[S] = \frac{-1}{\sqrt{2}}\begin{bmatrix} 0 & j & 1 & 0 \\ j & 0 & 0 & 1 \\ 1 & 0 & 0 & j \\ 0 & 1 & j & 0 \end{bmatrix} . \tag{A.8}$$

The scattering parameters of an electrical 3 dB 180° hybrid coupler are [105]:

$$[S] = \frac{-j}{\sqrt{2}}\begin{bmatrix} 0 & 1 & 1 & 0 \\ 1 & 0 & 0 & -1 \\ 1 & 0 & 0 & j \\ 0 & -1 & 1 & 0 \end{bmatrix} . \tag{A.9}$$

A.6 Calculations of the mixer model

In the following the detailed calculation of the polynomial coefficients for the nonlinear mixer model is given. Starting with the polynomial description of the n LO order output signal of the mixer (Equation 3.30 in Section 3.4.1) for intermodulation orders m up to 5:

$$\begin{aligned} s_{\mathrm{OUT},n} &= \sum_{m=0}^{5} a_{m,n} s_{\mathrm{IN}}^{m} \\ &= a_{0,n} + a_{1,n} s_{\mathrm{IN}} + a_{2,n} s_{\mathrm{IN}}^{2} + a_{3,n} s_{\mathrm{IN}}^{3} + a_{4,n} s_{\mathrm{IN}}^{4} + a_{5,n} s_{\mathrm{IN}}^{5} \, . \end{aligned} \tag{A.10}$$

For a single tone input signal $s_{\mathrm{IN}} = A\cos(\omega_{\mathrm{IN}} t)$ this is

$$\begin{aligned} s_{\mathrm{OUT},n} = \; & a_{0,n} + a_{1,n} A\cos(\omega_{\mathrm{IN}} t) + a_{2,n}(A\cos(\omega_{\mathrm{IN}} t))^2 + a_{3,n}(A\cos(\omega_{\mathrm{IN}} t))^3 \\ & + a_{4,n}(A\cos(\omega_{\mathrm{IN}} t))^4 + a_{5,n}(A\cos(\omega_{\mathrm{IN}} t))^5 \, . \end{aligned} \tag{A.11}$$

Calculating the brackets and separation of the different frequency terms results in

$$\begin{aligned} s_{\mathrm{OUT},n} = \; & a_{0,n} + \frac{1}{2}A^2 a_{2,n} + \frac{2}{3}A^4 a_{4,n} \\ & + A a_{1,n}\cos(\omega_{\mathrm{IN}} t) + \frac{3}{4}A^3 a_{3,n}\cos(\omega_{\mathrm{IN}} t) + \frac{5}{8}A^5 a_{5,n}\cos(\omega_{\mathrm{IN}} t) \\ & + \frac{1}{2}A^2 a_{2,n}\cos(2\omega_{\mathrm{IN}} t) + \frac{1}{2}A^4 a_{4,n}\cos(2\omega_{\mathrm{IN}} t) \\ & + \frac{1}{4}A^3 a_{3,n}\cos(3\omega_{\mathrm{IN}} t) + \frac{5}{16}A^5 a_{5,n}\cos(3\omega_{\mathrm{IN}} t) \\ & + \frac{1}{8}A^4 a_{4,n}\cos(4\omega_{\mathrm{IN}} t) \\ & + \frac{1}{16}A^5 a_{5,n}\cos(5\omega_{\mathrm{IN}} t) \, . \end{aligned} \tag{A.12}$$

The first line in Equation A.12 represented the DC terms and the second line the desired signal terms of the first order $m = 1$. The subsequent lines are the undesired harmonics up to intermodulation order $m = 5$.

The total power of each frequency component in Equation A.12 can be compared to the IMP relation given is the mixer SST table (Table. 3.1 in Chapter 3.4.1). The power of each IMP ($P_{m,n}$) at a certain input power can be calculated as

$$P_{m,n}\Big|_{\mathrm{dBm}} = P_{\mathrm{IN}}\Big|_{\mathrm{dBm}} - C_{\mathrm{cl}}\Big|_{\mathrm{dB}} - IMP_{m,n}\Big|_{\mathrm{dBc}} \, , \tag{A.13}$$

where P_{IN} is the new input power in dBm, C_{cl} the conversion loss in dB and $IMP_{m,n}$ the new relation of the desired signal to the IMP in dBc. This relation can be calculated directly from the SST

$$IMP_{m,n}\Big|_{\mathrm{dBc}} = (m-1)(P_{\mathrm{IN,ref}} - P_{\mathrm{IN}})\Big|_{\mathrm{dBm}} + IMP_{m,n,\mathrm{ref}}\Big|_{\mathrm{dBc}} \, , \tag{A.14}$$

with $P_{\mathrm{IN,ref}}$ the reference input power and $IMP_{m,n,\mathrm{ref}}$ the reference IMP in dBc form the SST. Combining Equations A.12, A.13 and A.14 leads to the following equation

system:

$$
\begin{aligned}
10^{\frac{P_{0,n}}{10}} &= \frac{1}{T_{\text{sig}}}\int_0^{T_{\text{sig}}}\left(a_{0,n}+\frac{1}{2}A^2a_{2,n}+\frac{2}{3}A^4a_{4,n}\right)^2dt\\
10^{\frac{P_{1,n}}{10}} &= \frac{1}{T_{\text{sig}}}\int_0^{T_{\text{sig}}}\left(Aa_{1,n}\cos(\omega_{\text{IN}}t)+\frac{3}{4}A^3a_{3,n}\cos(\omega_{\text{IN}}t)+\frac{10}{16}A^5a_{5,n}\cos(\omega_{\text{IN}}t)\right)^2dt\\
10^{\frac{P_{2,n}}{10}} &= \frac{1}{T_{\text{sig}}}\int_0^{T_{\text{sig}}}\left(\frac{1}{2}A^2a_{2,n}\cos(2\omega_{\text{IN}}t)+\frac{1}{2}A^4a_{4,n}\cos(2\omega_{\text{IN}}t)\right)^2dt\\
10^{\frac{P_{3,n}}{10}} &= \frac{1}{T_{\text{sig}}}\int_0^{T_{\text{sig}}}\left(\frac{1}{4}A^3a_{3,n}\cos(3\omega_{\text{IN}}t)+\frac{5}{16}A^5a_{5,n}\cos(3\omega_{\text{IN}}t)\right)^2dt\\
10^{\frac{P_{4,n}}{10}} &= \frac{1}{T_{\text{sig}}}\int_0^{T_{\text{sig}}}\left(\frac{1}{8}A^4a_{4,n}\cos(4\omega_{\text{IN}}t)\right)^2dt\\
10^{\frac{P_{5,n}}{10}} &= \frac{1}{T_{\text{sig}}}\int_0^{T_{\text{sig}}}\left(\frac{1}{16}A^5a_{5,n}\cos(5\omega_{\text{IN}}t)\right)^2dt\ ,
\end{aligned}
\tag{A.15}
$$

with T_{sig} the period time of the relevant signal, $P_{0..5,n}$ in dBW and using an impedance of 1 Ω. Calculation of the integrals result in

$$
\begin{aligned}
10^{\frac{P_{0,n}}{10}} &= \frac{9A^8a_{4,n}^2+(24A^6a_{2,n}+48A^4a_{0,n})a_{4,n}+16A^4a_{2,n}^2+64A^2a_{0,n}a_{2,n}+64a_{0,n}}{64}\\
10^{\frac{P_{1,n}}{10}} &= \frac{25A^{10}a_{5,n}^2+(60A^8a_{3,n}+80A^6a_{1,n})a_{5,n}+36A^6a_{3,n}^2+96A^4a_{1,n}a_{3,n}+64A^2a_{1,n}^2}{128}\\
10^{\frac{P_{2,n}}{10}} &= \frac{A^8a_{4,n}^2+2A^6a_{2,n}a_{4,n}+A^4a_{2,n}^2}{8}\\
10^{\frac{P_{3,n}}{10}} &= \frac{25A^{10}a_{5,n}^2+40A^8a_{3,n}a_{5,n}+16A^6a_{3,n}}{512}\\
10^{\frac{P_{4,n}}{10}} &= \frac{A^8a_{4,n}^2}{128}\\
10^{\frac{P_{5,n}}{10}} &= \frac{A^{10}a_{5,n}^2}{512}\ .
\end{aligned}
\tag{A.16}
$$

Now the coefficients can be calculated, starting with $a_{5,n}$

$$
\begin{aligned}
a_{5,n} &= \frac{2^{\frac{9}{2}}10^{\frac{P_{5,n}}{20}}}{A^5}\\
a_{4,n} &= \frac{2^{\frac{7}{2}}10^{\frac{P_{4,n}}{20}}}{A^4}\\
a_{3,n} &= \frac{5A^5a5,n-2^{\frac{9}{2}}10^{\frac{P_{3,n}}{20}}}{4A^3}\\
a_{2,n} &= \frac{A^4a4,n-2^{\frac{3}{2}}10^{\frac{P_{2,n}}{20}}}{A^2}\\
a_{1,n} &= \frac{-2^{\frac{7}{2}}10^{\frac{P_{1,n}}{20}}+5A^5a5,n+6A^3a_{3,n}}{8A}\\
a_{0,n} &= \frac{-8\cdot10^{\frac{P_{0,n}}{20}}+3A^4a4,n+4A^2a_{2,n}}{8}\ .
\end{aligned}
\tag{A.17}
$$

The resulting polynomial is then used in the mixer simulation model as shown in Fig. 3.20 in Chapter 3.4.1. For the LO order $n = 1$, Equation A.12 describes all IMPs at $\omega_{\mathrm{IN}}, 2\omega_{\mathrm{IN}}, ...5\omega_{\mathrm{IN}}$ including the desired signal. The DC part in Equation A.12 is the mixer offset and describes the LO-IF and LO-RF isolation, when multiplying $s_{\mathrm{OUT},n}$ with the ideal LO signal. Equation A.12 also describes the IF-RF and RF-IF isolation with the LO order $n = 0$ case. The resulting signal $s_{\mathrm{OUT},0}$ after applying the polynomial at the IF or RF signal, is then added to the signal of LO order $n = 1$. Signals with LO orders $n > 1$ are not considered in the simulation model due to the bandpass behavior of the mixer.

Fig. A.6 shows the block diagram of the mixer in case of up-conversion operation.

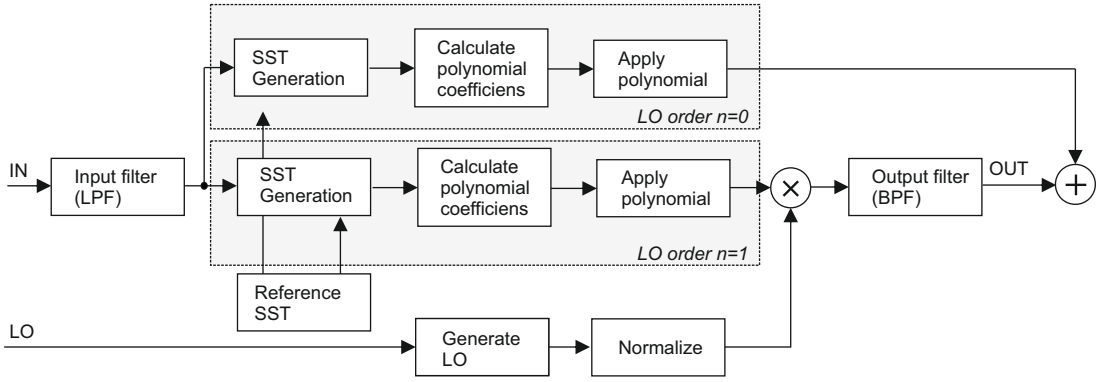

FIGURE A.6: Mixer up-conversion operation simulation model for LO orders $n = 0, 1$

A.7 Simulation Parameters VPItransmissionMaker

Two simulation environments for the optical transmissions have been used in this thesis, both realized in VPItransmission Maker. The first one for the investigation of the bandwidth extension approach shown in Fig. 3.4 and the second for the investigation of the nonlinear VCSEL pre-equalization shown in Fig. 4.28. The used component models are specified in the tables below with their relevant parameters. Deviations from the VPItransmission Maker default values are highlighted by italic script.

TABLE A.1: Simulation parameters VPItransmissionMaker

Bandwidth extension approach		
Optical amplitude modulator	*Ideal - with modulation index = 1*	
CW laser source	Emission frequency Linewidth	$193.1 \cdot 10^{12}$ Hz $100 \cdot 10^{5}$ Hz
Optical amplifier	*Ideal - noise turned off*	
Standard single mode fiber	Attenuation Dispersion	0.2 dB/m $16 \cdot 10^{6}$ s/m^2
Photodiode	Responsivity Thermal noise Shot noise	0.75 A/W $10 \cdot 10^{-12}$ A/$\sqrt{\text{Hz}}$ ON
VCSEL simulation		
VCSEL	*VPI single-mode VCSEL model, with thermal behavior using a polynomial gained from measurements in [181]. Otherwise default values are used.* Reference power Thermal time constant Thermal frequency shift Emission Frequency	 1 mW 10^{-6} -10^{-12} $350 \cdot 10^{12}$
Photodiode	Responsivity Thermal noise Shot noise	0.75 A/W $10 \cdot 10^{-12}$ A/$\sqrt{\text{Hz}}$ ON

A.8 Relation of EVM, SNR and BER

The average EVM of a received signal can be calculated from [64], [116] as:

$$EVM = \sqrt{\frac{\sum_{n=1}^{N} |S_n - S_{0,n}|^2}{\sum_{n=1}^{N} |S_{0,n}|^2}} \,, \tag{A.18}$$

where S_n is the normalized nth symbol in the received signal, $S_{0,n}$ is the ideal normalized symbol of the Tx signal and N is the number of symbols of the signal. Form here the SNR can be calculated as:

$$SNR = \frac{1}{\left(\frac{EVM}{100}\right)^2} \,. \tag{A.19}$$

Assuming a white Gaussian noise distribution, the BER can be calculated in case of QAM as:

$$BER = \frac{1}{\log_2(M)} \cdot \frac{4}{1 - \frac{1}{\sqrt{M}}} \cdot \operatorname{erfc}\left[\left(\frac{4}{\sqrt{M}} - 1\right)\sqrt{\frac{3SNR}{M-1}}\frac{1}{\sqrt{2}}\right] \tag{A.20}$$

with M the modulation order and *erfc* the complementary error function defined as:

$$\operatorname{erfc}(x) = \frac{2}{\sqrt{\pi}} \int_x^{\infty} \exp -t^2 dt \,. \tag{A.21}$$

In case of PAM the BER is:

$$\begin{aligned} BER = \frac{1}{\log_2(M)} \cdot \frac{1}{M} \Bigg\{ & \exp\left(\frac{1}{2}(B \cdot \sqrt{2}SNR)\right) \\ & + (2M-3) \cdot \frac{1}{2} \cdot \operatorname{erfc}\left(\sqrt{\frac{\log_2(M) \cdot B \cdot \sqrt{2}SNR}{2}}\right)\Bigg\} \,, \end{aligned} \tag{A.22}$$

with B:

$$B = \frac{3}{2M^2 - 3M + 1} \,. \tag{A.23}$$

Note that the theoretical BER calculation from the EVM and SNR is unreliable, if nonlinear distortions are present due to the different noise characteristics compared to white Gaussian noise. In this thesis the theoretical BER estimation is only used for BER values below $5 \cdot 10^{-5}$ for the simulations and experiments due to the limited numbers of transmitted symbols.

A.9 Channel estimation for single-carrier QAM and PAM

The linear channel estimation for QAM and PAM is based on a test sequence and an MMSE estimation algorithm. Let $[\boldsymbol{x}_{\text{Test}}]$ be a matrix which contains all send samples of a know test sequence extended to a Toeplitz structure and $[\boldsymbol{y}_{\text{Test}}]$ a vector of all received samples of the same test sequence. Using an LS approach [117], the linear channel is described by

$$[\boldsymbol{h}] = [\boldsymbol{x}^{+}_{\text{Test}}][\boldsymbol{y}_{\text{Test}}] = \Big([\boldsymbol{x}_{\text{Test}}]^{T}[\boldsymbol{x}_{\text{Test}}]\Big)^{-1}[\boldsymbol{x}_{\text{Test}}]^{T}[\boldsymbol{y}_{\text{Test}}], \tag{A.24}$$

with $[\boldsymbol{x}^{+}_{\text{Test}}]$ the pseudo-inverse input matrix and $^{-1}$ denoting the matrix inverse. In case of a noisy channel, $[\boldsymbol{h}]$ can sometimes consist of huge coefficients, which is not beneficial for the equalization of the signal. This issue can be solved with a MMSE approach by introducing a weighting factor into the calculation. The MMSE solution for the channel estimation is based on minimizing the power of the difference between the input and output test signal [117]. The channel can now be estimated by

$$[\boldsymbol{h}] = [\boldsymbol{x}^{+}_{\text{Test}}][\boldsymbol{y}_{\text{Test}}] = \Big([\boldsymbol{x}_{\text{Test}}]^{T}[\boldsymbol{x}_{\text{Test}}] + \gamma[\boldsymbol{I}]\Big)^{-1}[\boldsymbol{x}_{\text{Test}}]^{T}[\boldsymbol{y}_{\text{Test}}], \tag{A.25}$$

with $[\boldsymbol{I}]$ the Identity matrix and γ a non-negative weighting factor. The optimal amount of γ depends on the scenario.

A.10 VCSEL modulation and extinction ratio

The VCSEL modulation parameters for the simulations in Section 4.6 consist of the bias current and the driving amplitude. Both are illustrated in Fig. A.7 for the used L-I characteristic of the VCSEL model. Depending on the amount of both, there are different values for the minimum P_0 and maximum P_1 optical power after the laser, i.e. P_0 and P_1. These are related in the extinction ratio in the form

$$r_{\text{e}} = \frac{P_1}{P_0}\,. \tag{A.26}$$

For example, for OOK it is the optical power of a *one* relative to a *zero*.

Note that the extinction ratios can be calculated for each simulation in Section 4.6 with the help of given driving amplitudes, bias currents and the static L-I characteristics[3]. For example with a bias current of 12 mA and a driving amplitude of 8 mA, an extinction ratio of 8 dB is possible. However, these calculation are based on the static behavior of the system, which differs from the dynamic behavior as could already be observed in Section 4.3.2.2. To give an accurate estimation of the VCSEL extinction ratio for each modulation scenario, i.e. driving amplitude and bias current, the measurement of the minimum and maximum optical power after the VCSEL would be required.

Note that due to the high PAPR of the used modulation formats in combination with the analog clipping, its difficult and not very useful to define the extinction ratios for the experiments. It was observed that in case of the VCSEL experiments, always an analog clipping of the negative and positive peaks was present at the optimal driving amplitude, i.e. the minimum BER. This relates to zero optical power for the negative

[3] default values from VPItransmission maker VCSEL model

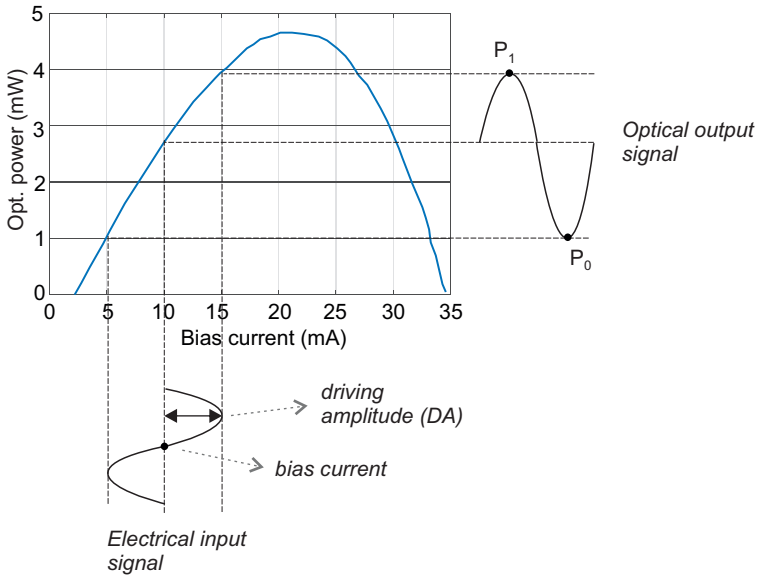

FIGURE A.7: Modulation of a VCSEL.

peaks, thus an infinite extinction ratio. However, for the MZM the data sheet extinction ratio can be assumed.

Appendix B

Own contributions used for this thesis

[A] C. Kottke , K. Habel, C. Schmidt, V. Jungnickel, "154.9 Gb/s OFDM Transmission Using IM-DD, Electrical IQ-Mixing and Signal Combining ", in *Opt. Fiber Commun. Conf. (OFC)*, 2016.
Abstract: We demonstrate a wideband OFDM transmission, using electrical IQ-mixing and signal combining. Transmission rates of 154.9 Gb/s over 2 km of SSMF were achieved with an IM/DD system on a single wavelength and a single polarization.
My contributions: I did the theoretical and simulative work, set up and performed the experiments and wrote the paper.

[B] C. Kottke, C. Schmidt, K. Habel, and V. Jungnickel, "178 Gb/s Short-Range Optical Transmission Based on OFDM, Electrical Up-Conversion and Signal Combining" ", in *Eur. Conf. Opt. Commun. (ECOC)*, 2016.
Abstract: We demonstrate our improved wideband OFDM transmission system, using electrical up-conversion and signal combining. Transmission rates of 178 Gb/s over 2 km of SSMF were achieved with an IM/DD system on a single wavelength and single polarization.
My contributions: I did the theoretical and simulative work, set up and performed the experiments and wrote the paper.

[C] C. Kottke, C. Schmidt, K. Habel, V. Jungnickel, and R. Freund, "Performance of Single- and Multi-Carrier Modulation with Additional Spectral Up-conversion forWideband IM/DD Transmission", in *Photonic Networks, 17. ITG-Symposium*, 2017.
Abstract: The demand for high capacity transmission links in future optical networks is further increasing and requires the application of advanced modulation formats in combination with digital signal processing (DSP). For the necessary analog/digital conversion of these signals, high-speed and high-resolution DACs and ADCs are mandatory, which are not always commercially available. Furthermore, especially for short-range communication links with lengths of up to 20 km approximately, the use of low-cost optical components is a key requirement. In general, this results in the application of intensity modulation (IM) and direct detection (DD) schemes. This paper compares the performance of single- and multicarrier modulation formats with spectral up-conversion for wideband IM/DD transmission for data rates beyond 100 Gb/s. The generation of wideband signals is thereby not realized with a high-speed DAC, but instead with multiple lower speed DACs in combination with electrical up-conversion.

The resulting signal sub-bands are passively combined, thus enable a total signal bandwidth of up to 39 GHz. The achievable bandwidth corresponds to that of today's high-end DACs. The optical link to experimentally validate the concept utilized of IM at the transmitter (Tx), DD at the receiver (Rx) and fiber lengths of up to 20 km. Different modulation formats like PAM, QAM, DMT and OFDM, together with standard digital signal processing were applied. We experimentally verify, that by utilizing different electrical sub-bands data rates of up to 180 Gb/s are achievable, with simple IM/DD schemes and without using the latest high-end DACs. Furthermore, the suitability of various modulation formats for different sub-bands is shown and the occurring penalties are investigated.
My contributions: I did the theoretical and simulative work, set up and performed the experiments and wrote the paper.

[D] C. Kottke, C. Schmidt, R. Freund, and V. Jungnickel, "Bandwidth Extension Techniques for High-Speed Access Networks", in *Opt. Fiber Commun. Conf. (OFC)*, 2018.
Abstract: Recent advances in bandwidth extension techniques for high-speed access environments are presented together with own transmission experiments. Current issues and critical aspects are highlighted.
My contributions: I did the theoretical and simulative work and set up and performed the experiments, but only partially for the FI-DAC concept. The theoretical and simulative work for the FI-DAC approach was mostly done by my colleague Christian Schmidt. I wrote the paper

[E] C. Kottke, C. Schmidt, V. Jungnickel and R. Freund, "Performance of Bandwidth Extension Techniques for High-Speed Access Networks ", *J. Light. Technol.*, vol. 37, no. 2, pp. 665-672, 2018.
Abstract: The demand for high capacity short-range transmission links is further increasing and requires the use of advanced modulation formats in combination with digital signal processing (DSP). For the necessary analog/digital conversion, high-speed and high-resolution digital-to-analog DACs and analog-to-digital ADCs are required, which often have bandwidths lower than nowadays electro-optical components. This bottleneck can be overcome with bandwidth extension techniques, which enable signal bandwidths beyond the capabilities of today's commercial DACs and ADCs. In this paper, two high-speed systems are presented and experimentally analyzed for an optical link based on intensity modulation (IM) and direct detection (DD), utilizing a bandwidth extension technique based on electrical up/down-conversion and passive signal combining. The experiment for the first system uses two independent sub-signals, with a total bandwidth beyond 40 GHz and enables transmission rates up to 180 Gb/s. Different aspects of the system are highlighted including general performance, transmission distance, use of different modulation formats and the influence of important components. For the second system, the experiment consists of the generation of a spectrally continuous pulse amplitude modulation (PAM) signal with the help of two sub-signals and its transmission over optical IM/DD link. The challenges and requirements for hardware and software are discussed and the impact of power and phase mismatches between both sub-signals are investigated as well.

My contributions: I did the theoretical and simulative work and set up and performed the experiments, but only partially for the FI-DAC concept. The theoretical and simulative work for the FI-DAC approach was mostly done by my colleague Christian Schmidt. I wrote the paper.

[F] C. Schmidt, C. Kottke, R. Freund, F. Gerfers, and V. Jungnickel, "Digital-to-Analog Converters for High-Speed Optical Communications using Frequency Interleaving: Impairments & Characteristics", *Opt. Express*, vol. 25, no. 14, pp. 6758-6770, 2018.

Abstract: Digital-to-analog converters (DACs) for high-speed optical communication systems based on CMOS technology have bandwidths lower than nowadays electro-optic components. A promising concept to circumvent this bottleneck is the frequency-interleaved DAC (FI-DAC) concept. In this paper, experimental results for the application of a 180 GS/s FI-DAC with 40 GHz analog bandwidth based on two DACs in a high-speed optical link are discussed and compared with simulation results. Thereby, phase and power mismatches, spectral overlap, clipping and the required DAC resolution are investigated. Signal-to-noise ratio (SNR) estimations based on a discrete multi-tone (DMT) signal show the influence of the individual analog components on the signal quality.

My contributions: I took part in the set up and performing of the experiments and in theoretical discussions and wrote sections of the paper.

[G] C. Schmidt, C. Kottke, R. Freund, and V. Jungnickel, "Bandwidth Enhancement for an Optical Access Link by using a Frequency Interleaved DAC", in *Opt. Fiber Commun. Conf. (OFC)*, 2018.

Abstract: We present the experimental realization of the frequency interleaved DAC concept for an IM/DD based access link. The first open 80 GBd PAM-4 electrical eye diagram of the frequency-interleaved DAC without using post-equalization is presented.

My contributions: I took part in the set up and performing of the experiments and in theoretical discussions.

[H] V. Shivashankar, C. Kottke, V. Jungnickel, and R. Freund, "Investigation of Linear and Nonlinear Pre-Equalization of VCSEL", in *Broadband Coverage in Germany, 11. ITG-Symposium*, 2017.

Abstract: Current trends for short-reach data interconnects are determined by the necessity of higher bitrates as well as the need of reducing the power consumption. Attention is focused on optical solutions to face these challenges. In particular, the use of directly modulated 850 nm vertical cavity surface emitting lasers (VCSEL) as an inexpensive reliable light source with wide bandwidth and low-energy consumption, together with the use of advanced modulation techniques, like pulse amplitude modulation (PAM) or discrete multi-tone (DMT) to increase the spectral efficiency are considered as keys to achieve low-cost fast optical interconnects. However, these advanced modulation techniques require additional signal processing to compensate the inherent linear and nonlinear VCSEL properties. In this paper, a simulative and experimental investigation of linear and nonlinear compensation of the VCSEL characteristic is presented.

We show that nonlinear pre-equalization of VCSEL-based transmitters can be used to improve the sensitivity of IM/DD based links, however with limitations when high-bandwidth signals are considered. Investigations of the performance of equalizers designed using Volterra series for compensating linear and nonlinear distortions that arise in VCSELs are carried out. The simulation environment is built using the simulation tools Matlab for the signal processing and VPItransmissionMaker for the optical link. The designed system is using 8-PAM modulation with multiple symbol rates. A detailed VCSEL model, based on semi-empirical rate equation, is utilized in the simulations. The model takes into account effects like relaxation oscillations, thermal impedance or thermal rollover. To verify the simulative results, the experimental realization of a pre-compensated high-speed optical transmission, based on PAM is also shown.
My contributions: My colleague Veena Shivashankar and I did the theoretical and simulative work together, I set up and performed the experiments and wrote most sections of the paper.

[I] C. Kottke, C. Caspar, V. Jungnickel, R. Freund, M. Agustin, J. Kropp, and N. N. Ledentsov, "High Speed 160 Gb/s DMT VCSEL Transmission Using Pre-equalization", in *Opt. Fiber Commun. Conf. (OFC)*, 2017.
Abstract: High speed single channel DMT operation of a directly modulated 850nm VCSEL with 26 GHz bandwidth is presented. Successful transmission of 161, 152, 135 Gb/s over 10, 300, 550 m of OM4 MMF is demonstrated at the SD-FEC limit.
My contributions: I did the theoretical and simulative work, set up and performed the experiments and wrote the paper.

[J] C. Kottke, C. Caspar, V. Jungnickel, R. Freund, M. Agustin, J. Kropp, and N. N. Ledentsov, "High Speed DMT and VCSEL Based MMF Transmission Using Pre-distortion", *J. Light. Technol.*, vol. 36, no. 2, 2018.
Abstract: We present high-speed single channel discrete multitone (DMT) operations of directly modulated 850 nm vertical cavity surface emitting lasers (VCSEL). Successful transmission of 135 Gb/s over 10 m of OM4 multimode fiber (MMF) and 114 Gb/s over 550 m is demonstrated below the 7% overhead hard-decision forward error correction (7% HD-FEC) bit error rate (BER) limit. At higher BER limits, i.e. 20% overhead soft decision FEC, which are of arising interest for these high-speed short-range links, data rates of up to 161 Gb/s are presented. This is enabled by high bandwidth, low noise VCSELs, which operate in quasi single-mode to overcome the mode dispersion limitations of the MMF. The applied modulation format is discrete multitone in combination with a Volterra filter based pre-distortion approach, which pre-compensates the linear and nonlinear behavior of the transmission system, primarily the digital-analog converter, the VCSEL, the MMF and the photoreceiver. Furthermore, a detailed investigation of the pre-distortion is given by experimental means, showing that the optimum amount of pre-distortion depends on the applied components and the signal bandwidth. This makes it challenging to predict the optimum, however a pure electrical pre-distortion offers already a fair gain in performance.
My contributions: I did the theoretical and simulative work, set up and performed the experiments and wrote the paper.

Bibliography

[1] I. T. Union, *Measuring the Information Society Report*. [Online]. Available: https://www.itu.int/en/ITU-D/Statistics/Pages/default.aspx.

[2] Finisar, *Press Release: Finisar Introduces Industry's First 400G QSFP-DD Active Optical Cable and Transceivers for Switching and Routing Applications at OFC 2018*, 2018. [Online]. Available: http://investor.finisar.com/news-releases/news-release-details/finisar-introduces-industrys-first-400g-qsfp-dd-active-optical.

[3] *Ethernet roadmap*. [Online]. Available: http://ethernetalliance.org/roadmap/.

[4] *IEEE802.3bs 400 Gb/s Ethernet task force*. [Online]. Available: http://www.ieee802.org/3/bs/.

[5] J. Wei, Q. Cheng, R. V. Pentry, I. H. White, and D. G. Cunningham, "400 Gigabit Ethernet Using Advanced Modulation formats: Performance, Complexity, and Power Dissipation", *IEEE Commun. Mag.*, vol. 53, no. 2, pp. 182–189, 2015.

[6] W. Hartmann, M. Lauermann, S. Wolf, H. Zwickel, Y. Kutuvantavida, J. Luo, A. K.-Y. Jen, R. Freude, and C. Koos, "100 Gbit/s OOK Using a Silicon-Organic Hybrid (SOH) Modulator", in *Eur. Conf. Opt. Commun. (ECOC)*, 2015.

[7] O. Ozolins, M. I. Olmedo, X. Pang, S. Gaiarin, A. Kakkar, A. Udalcovs, K. M. Engenhardt, T. Asyngier, R. Schatz, J. Li, F. Nordwall, U. Westergren, D. Zibar, S. Popov, and G. Jacobsen, "100 GHz EML for High Speed Optical Interconnect Applications", in *Eur. Conf. Opt. Commun. (ECOC)*, 2016.

[8] M. Verplaetse, R. Lin, J. V. Kerrebrouck, O. Ozolins, T. D. Keulenaer, X. Pang, R. Pierco, R. Vaernewyck, A. Vyncke, R. Schatz, U. Westergren, G. Jacobsen, S. Popov, J. Chen, G. Torfs, J. Bauwelinck, and X. Yin, "Real-Time 100 Gb/s Transmission Using Three-Level Electrical Duobinary Modulation for Short-Reach Optical Interconnects", *J. Light. Technol.*, vol. 35, no. 7, 2017.

[9] J. Lee, N. Kaneda, T. Pfau, A. Konczykowska, F. Jorge, J.-Y. Dupuy, and Y.-K. Chen, "Serial 103.125-Gb/s Transmission over 1 km SSMF for Low-Cost, Short-Reach Optical Interconnects", in *Opt. Fiber Commun. Conf. (OFC)*, 2014.

[10] M. Chagnon, M. Morsy-Osman, M. Poulin, C. Paquet, S. Lessard, and D. V. Plant, "Experimental Parametric Study of a Silicon Photonic Modulator Enabled 112-Gb/s PAM Transmission System With a DAC and ADC", in *J. Light. Technol.*, ser. 7, vol. 33, 2015, pp. 1380–1387.

[11] N. Stojanovic, Z. Qiang, C. Prodaniuc, and F. Karinou, "Performance and DSP Complexity Evaluation of a 112-Gbit/s PAM-4 Transceiver Employing a 25-GHz TOSA and ROSA", in *Eur. Conf. Opt. Commun. (ECOC)*, 2015.

[12] Q. Zhang, N. Stojanovic, C. Prodaniuc, C. Xie, M. Koenigsmann, and P. Laskowski, "Single-lane 180 Gbit/s PAM-4 signal transmission over 2 km SSMF for short-reach applications", *Optics Letters*, vol. 41, no. 19, pp. 4449–4452,

[13] S. Lange, S. Wolf, J. Lutz, L. Altenhain, R. Schmid, R. Kaiser, C. Koos, S. Randel, and M. Schell, "100 GBd intensity modulation and direct detection with an InP-based monolithic DFB laser Mach-Zehnder modulator", in *Opt. Fiber Commun. Conf. (OFC)*, 2017.

[14] L. F. Suhr, J. J. V. Olmos, B. Mao, X. Xu, G. N. Liu, and I. T. Monroy, "112-Gbit/s x 4-Lane Duobinary-4-PAM for 400GBa", in *Eur. Conf. Opt. Commun. (ECOC)*, 2014.

[15] M. A. Mestre, H. Mardoyan, A. Konczykowska, R. Rios-Müller, J. Renaudier, F. Jorge, B. Duval, J.-Y. Dupuy, A. Ghazisaeidi, P. Jennevé, and S. Bigo, "Direct Detection Transceiver at 150-Gbit/s Net Data Rate Using PAM 8 for Optical Interconnects", in *Eur. Conf. Opt. Commun. (ECOC)*, 2015.

[16] G. H. Werner, "Bandwidth-efficient digital transmission up to 155 Mb/s over unshielded twisted pair wiring", in *IEEE International Conference on Communications (ICC)*, 1993.

[17] M. I. Olmedo, T. Zuo, J. B. Jensen, Q. Zhong, X. Xu, S. Popov, and I. T. Monroy, "Multiband Carrierless Amplitude Phase Modulation for High Capacity Optical Data Links", *J. Light. Technol.*, vol. 32, no. 14, 2014.

[18] J. L. Wei, Q. Cheng, D. G. Cunningham, R. V. Pentry, I. H. White, and H. Griesser, "High Performance 400 Gigabit Ethernet Links using Hybrid Multiband CAP/QAM Scheme", in *Opt. Fiber Commun. Conf. (OFC)*, 2015.

[19] H. C. Chien, Z. Jia, J. Yu, F. Li, S. Shi, C. Ge, Y. Xia, and Y. Chen, "160-Gbps IMDD optical links based on Nyquist 256QAM", in *Opt. Fiber Commun. Conf. (OFC)*, 2016.

[20] W. Yan, T. Tanaka, B. Liu, M. Nishihara, L. Li, T. Takahara, Z. Tao, J. C. Rasmussen, and T. Drenski, "100 Gb/s Optical IM-DD Transmission with 10G-Class Devices Enabled by 65 GSamples/s CMOS DAC Core", in *Opt. Fiber Commun. Conf. (OFC)*, 2013.

[21] J. Lee, P. Dong, N. Kaneda, and Y.-K. Chen, "Discrete Multi-Tone Transmission for Short-Reach Optical Connections", in *Opt. Fiber Commun. Conf. (OFC)*, 2016.

[22] T. Takahara, T. Tanaka, M. Nishihara, Y. Kai, L. Li, Z. Tao, and J. C. Rasmussen, "Discrete Multi-Tone for 100 Gb/s Optical Access Networks", in *Opt. Fiber Commun. Conf. (OFC)*, 2014.

[23] Y. Kai, M. Nishihara, T. Tanaka, R. Okabe, T. Takahara, J. C. Rasmussen, H. Ishihara, K. Goi, and K. Ogawa, "130-Gbps DMT Transmission using Silicon Mach-Zehnder Modulator with Chirp Control at 1.55-um", in *Opt. Fiber Commun. Conf. (OFC)*, 2015.

[24] K. Zhong, X. Zhou, T. Gui, Y. Gao, W. Chen, J. Man, L. Zeng, A. P. L. Lau, and C. Lu, "Experimental study of PAM-4, CAP-16, and DMT for 100 Gb/s Short Reach Optical Transmission Systems", *Opt. Express*, vol. 23, no. 2, 2015.

[25] Y. Kai, M. Nishihara, T. Tanaka, T. Takahara, L. Li, Z. Tao, B. Liu, J. C. Rasmussen, and T. Drenski, "Experimental Comparison of Pulse Amplitude Modulation (PAM) and Discrete Multi-tone (DMT) for Short-Reach 400-Gbps Data Communication", in *Opt. Fiber Commun. Conf. (OFC)*, 2013.

[26] C. Peucheret, *Direct and External Modulation of Light*, 2009. [Online]. Available: `http://web-files.ait.dtu.dk/cpeu/download/34129_E2009_CPEU_DML_EML.pdf`.

[27] T. Yamamoto, "High-Speed Directly Modulated Lasers", presented at the Optical Fiber Communication Conference and Exposition (OFC/NFOEC), 2010, [Online]. Available: `http://ieeexplore.ieee.org/abstract/document/6476546/`.

[28] Y. Matsui, R. Schatz, G. Carey, T. Sudo, and C. Roxlo, "Direct modulation laser technology toward 50-GHz bandwidth", in *Semiconductor Laser Conference (ISLC)*, 2016.

[29] Y. Matsui, T. Pham, W. A. Ling, R. Schatz, G. Carey, H. Daghighian, T. Sudo, and C. Roxlo, "55-GHz Bandwidth Short-Cavity Distributed Reflector Laser and its Application to 112-Gb/s PAM-4", in *Opt. Fiber Commun. Conf. (OFC)*, 2016.

[30] C. Haffner, W. Heini, Y. Fedoryshyn, J. Niegemann, A. Melikyan, D. L. Elder, B. Baeuerle, Y. Salamin, A. Josten, U. Koch, C. Hoessbacher, F. Ducry, L. Juchli, A. Emboras, D. Hillerkuss, M. Kohl, and L. R. Dalton, "All-plasmonic mach-zehnder modulator enabling optical high-speed communication at the microscale", *Nature Photonics*, vol. 9(8), pp. 525–528, 2015.

[31] Thorlabs, *Ln05s-fc specifcations*, 2016.

[32] Fujitsu, *Ftm7992hma data sheet*, 2016.

[33] C. Kottke, C. Schmidt, K. Habel, and V. Jungnickel, "178 Gb/s Short-Range Optical Transmission Based on OFDM, Electrical Up-Conversion and Signal Combining", in *Eur. Conf. Opt. Commun. (ECOC)*, 2016.

[34] C. Caillaud, M. A. Mestre, F. Blache, F. Pommereau, J. Decobert, F. Jorge, P. Charbonnier, A. Konczykowska, J.-Y. Dupuy, H. Mardoyan, K. Mekhazni, J. F. Paret, M. Faugeron, F. Mallecot, and M. Achouche, "Low cost 112 Gb/s InP DFB-EAM for PAM-4 2 km Transmission", in *Eur. Conf. Opt. Commun. (ECOC)*, 2015.

[35] S. Kanazawa, H. Yamazaki, Y. Nakanishi, Y. Ueda, W. Kobayashi, Y. Muramoto, H. Ishii, and H. Sanjoh, "214-Gb/s 4-PAM Operation of Flip-Chip Interconnection EADFB Laser Module", *J. Light. Technol.*, vol. 35, no. 3, pp. 418–422, 2017.

[36] S. Bottacchi, *Multi-Gigabit Transmission Voer Multimode Optical Fibre*.

[37] E. Peral and A. Yariv, "Large-Signal Theory of the Effect of Dispersive Propagation on the Intensity Modulation Response of Semiconductor Lasers", *J. Light. Technol.*, vol. 18, no. 1, pp. 84–89, 2000.

[38] V. V. Shcherbakov and A. A. Zadernovsky, "Analysis of Intensity Modulation Response of Analog Fiber-Optic Links", presented at the IEEE 13th International Conference on Laser and Fiber-Optical Networks Modeling (LFNM), 2016.

[39] R. Pimpinella and A. Brunsting, "Modeling and simulation of next generation multimode fiber links", *J. Light. Technol.*, vol. 21, no. 5, pp. 1242–1255, 2003.

[40] R. Michalzik, *Fundamentals, Technology and Applications of Vertical-Cavity Surface-Emitting Lasers*. Springer, 2012.

[41] D. Gloge and E. A. J. Marcatili, "Multimode theory of graded-core fibers", *Bell Syst. Tech. J.*, vol. 52, no. 9, pp. 1563–1578, 1973.

[42] *IS)/IEC 11801:2002/Amd 2:2010*, 2010.

[43] R. S. Quimby, *Photonics and Lasers*. 2006.

[44] Finisar, *XPRV2021(A) data sheet*.

[45] N. Focus, *1484-A-50 data sheet*.

[46] G. P. Agrawal, *Lightwave Technology: Telecommunication Systems*. Wiley-Interscience, 2005.

[47] B. Razavi, *Design of Analog CMOS Integrated Circuits*. McGraw-Hill Education, 2016.

[48] A. Van den Bosch, M. Steyart, and W. Sansen, "SFDR-bandwidth limitations for high speed high resolution current steering CMOS D/A converters", in *IEEE International Conference on Electronics, Circuits, & Systems*, 1999, pp. 1193–1196.

[49] F. Maloberti, *Data Converters*. Springer, 2007, vol. 1.

[50] J. Bergeron, "Analyzing and managing the impact of supply noise clock jitter on high speed dac phase noise", *Analog Dialogue*, vol. 51, no. 3, pp. 1–6, 2017.

[51] K. Schuh, F. Buchali, W. Idler, Q. Hu, W. Templ, A. Bielik, L. Altenhain, H. Langenhagen, J. Rupeter, U. Dümler, T. Ellermeyer, R. Schmid, and M. Möller, "100 GSa/s BiCMOS DAC Supporting 400 Gb/s Dual Channel Transmission", in *Eur. Conf. Opt. Commun. (ECOC)*, 2016.

[52] K. Technologies, *M8196a 92 GS/s arbitrary waveform generator data sheet*, 2016.

[53] Socionext, *100G to 400G ADC and DAC for ultra-high-speed optical networks*, 2016.

[54] Anritsu, *64GBd PAM4 DAC G0374A product introduction*, 2016.

[55] *Shf 614b datasheet, SHF AG*, 2016. [Online]. Available: `www.shf.de`.

[56] H. Huang, J. Heilmeyer, M. Grozing, M. Berroth, J. Leibrich, and W. Rosenkranz, "An 8-bit 100-GS/s distributed DAC in 28-nm CMOS for optical communications", *IEEE Trans. Microw. Theory Techn.*, vol. 63, no. 4, pp. 1211–1218, 2015.

[57] M. Nagatani, H. Wakita, H. Nosaka, K. Kurishima, M. Ida, A. Sano, and Y. Miyamoto, "75 GBd InP-HBT MUX-DAC module for high-symbol-rate optical transmission", *Electron. Lett.*, vol. 51, no. 9, pp. 710–712, 2015.

[58] A. Konczykowska, F. Jorge, J.-Y. Dupuy, M. Riet, V. Nodjiadjim, H. Aubry, and A. Adamiecki, "84 GBd (168 Gbit/s) PAM-4 3.7 Vpp power DAC in InP DHBT for short reach and long haul optical network", *Electron. Lett.*, vol. 51, no. 20, pp. 1591–1593, 2015.

[59] P. Pupalaikis, B. Yamrone, R. Delbue, A. S. Khanna, K. Doshi, B. Bhat, and A. Sureka, "N: Bipolar/BiCMOS Circuits and Technology Meeting (BCTM), 2014 IEEE", in *IEEE Bipolar/BiCMOS Circuits and Technology Meeting*, 2014.

[60] C. Laperle and M. O'Sullivan, "Advances in High-Speed DACs, ADCs, and DSP for Optical Coherent Transceivers", *J. Light. Technol.*, vol. 32, no. 4, 2014.

[61] G. Raybon, B. Guan, A. Adamiecki, P. J. Winzer, N. Fontaine, S. Chen, P. Pupalaikis, R. Delbue, K. Doshi, B. Bhat, A. Blankman, A. Konczykowska, J.-Y. Dupuy, and F. Jorge, "160-Gbaud coherent receiver based on 100-GHz 240-GS/s analog-to-digital coversion", in *Opt. Fiber Commun. Conf. (OFC)*, 2015.

[62] X. Chen, S. Chandrasekhar, S. Randel, G. Raybon, A. Adamiecki, P. Pupalaikis, and P. J. Winzer, "All-Electronic 100-GHz Bandwidth Digital-to-Analog Converter Generating PAM Signals up to 190 GBaud", *J. Light. Technol.*, vol. 35, no. 3, pp. 411–417, 2017.

[63] W. Shieh and I. B. Djordjecic, *OFDM for Optical Communication*. Elsevier, 2010.

[64] F. Xiong, *Digital Modulation Techniques*, 2nd ed. Artech House, 2000.

[65] J. Armstrong and B. J. C. Schmidt, "Comparison of Asymmetrically Clipped Optical OFDM and DC-Biased Optical OFDM in AWGN", *IEEE Commun. Lett.*, vol. 12, no. 5, pp. 343–345, 2008.

[66] K. Szczerba, "Multilevel modulation in short-range optical links", Chalmer University of Technology, 2013.

[67] S. Randel, F. Breyer, and J. Lee, "High-speed transmission over multimode optical fibers", in *Opt. Fiber Commun. Conf. (OFC)*, 2008.

[68] A. V. Oppenheim and R. W. Schafer, *Discrete-Time Signal Processing*, ser. Prenice-Hall Signal Processing Seires. Prenice-Hall Signal Processing Series, 1989.

[69] *WiFi standard IEEE 802.11*.

[70] *3GGP LTE standard*. [Online]. Available: `http://www.3gpp2.org/`.

[71] J. Campello, "Practical Bit Loading for DMT", in *IEEE International Conference on Communications*, 1999.

[72] B. S. Krongold, K. Ramchandran, and D. L. Jones, "Computationally Efficient Optimal Power Allocation Algorithms for Multicarrier Communication Systems", *IEEE Trans. Signal Process.*, vol. 48, no. 1, pp. 23–27,

[73] J. Armstrong, "Peak-to-average power reduction for OFDM by repeated clipping and frequency domain filtering", *Electron. Lett.*, vol. 38, no. 5, pp. 246–247, 2002.

[74] R. W. Bauml, R. F. H. Fischer, and J. B. Huber, "Reducing the peak-to-average power ration of multicarrier modulation by scelective mapping", *IET Electron Lett*, vol. 32, no. 22, pp. 2056–2057, 1996.

[75] Socionext, *Press release: World's lowest-power IC for single-wavelength, 100Gbps transmission over SMF optical links*, 2016.

[76] K. D. Kammeyer, *Nachrichtenübertragung*. Vieweg & Taubner, 2011, vol. 5.

[77] G. Stepniak, A Lewandowski, J. Kropp, N. N. Ledentsov, V. Shchukin, N. Ledentsov Jr., G. Schaefer, M. Agustin, and J. P. Turkiewicz, "54 Gbit/s OOK transmission using singlemode VCSEL up to 2.2 km MMF", *Electron. Lett.*, vol. 52, no. 8, 2016.

[78] M. A. Mestre, F. Jorge, H. Mardoyan, J. Estaran, F. Blache, P. Angelini, A. Konczykowska, M. Riet, V. Nodjiadjim, J.-Y. Dupuy, and S. Bigo, "100-Gbaud PAM-4 Intensity-Modulation Direct-Detection Transceiver for Datacenter Interconnect", in *Eur. Conf. Opt. Commun. (ECOC)*, 2016.

[79] G. Stepniak, L. Chorchos, M. Agustin, J. Kropp, N. N. Ledentsov, V. Shchukin, N. Ledentsov Jr., and J. P. Turkiewicz, "Up to 108 Gb/s PAM 850 nm Multi and Single Mode VCSEL Transmission over 100 m of Multi Mode Fiber", in *Opt. Fiber Commun. Conf. (OFC)*, 2016.

[80] F. Karinou, N. Stojanovic, C. Prodaniuc, M. Agustin, J. Kropp, and N. N. Ledentsov, "Solutions for 100/400-Gb/s Ethernet Systems based on Multimode Photonic Technologies", *J. Light. Technol.*, vol. 35, no. 15, pp. 3214–3222, 2017.

[81] S. Dave, "Soft-decision forward error correction in a 40-nm ASIC for 100-Gbps OTN applicationsNational Fiber Optic Engineers Conf., Los Angeles, CA, USA, Mar. 6–11, 2011, JWA014.", in *National Fiber Optic Engineers Conf.*, 2011.

[82] O. I. Forum, *100 G forward error correction white paper*. [Online]. Available: `www.oiforum.com`.

[83] M. N. Sakib and O. Liboriron-Ladouceur, "Study of Error Correction Codes for PAM Signals in Data Center Applications", *IEEE Photon. Technol. Lett.*, vol. 25, no. 23, pp. 2274–2277, 2013.

[84] *ITU-T Recommendation G.975.1, 2004, Appendix I.9*.

[85] H. Yamazaki, M. Nagatani, F. Hamaoka, S. Kanazawa, H. Nosaka, T. Hashimoto, and Y. Miyamoto, "300-Gbps Discrete Multi-tone Transmission Using Digital Preprocessed Analog Multiplexed DAC with Halved Clock Frequency and Suppressed Image", in *Eur. Conf. Opt. Commun. (ECOC)*, 2016.

[86] D. Chang, F. Yu, Z. Xiao, N. Stojanovic, F. N. Hauske, Y. Cai, C. Xie, L. Li, X. Xu, and Q. Xiong, "LDPC convolutional codes using layered decoding algorithm for high speed coherent optical transmission", in *Opt. Fiber Commun. Conf. (OFC)*, 2012.

[87] W. Zhongfeng, *FEC Considerations for 400Gbps Ethernet*, 2014. [Online]. Available: `www.ieee802.org/3/bs/public/adhoc/logic/jul01_14/wangz_01_0714_logic.pdf`.

[88] N. Bozinovic, Y. Yue, Y. Ren, M. Tur, P. Kristensen, H. Huang, A. E. Willner, and S. Ramachandran, "Terabit-Scale Orbital Angular Momentum Mode Division Multiplexing in Fibers", *Science*, vol. 340, no. 6140, pp. 1545–1548, 2013.

[89] H. Mardoyan, M. A. Mestre, J. Estaran, F. Jorge, F. Blache, P. Angelini, J.-Y. Dupuy, and S. Bigo, "84-, 100-, and 107-GBd PAM-4 Intensity-Modulation Direct-Detection Transceiver for Datacenter Interconnects", *J. Light. Technol.*, vol. 35, no. 5, 2017.

[90] T. Tannert, X. Q. Du, D. Widmann, M. Agustin, M. Berroth, C. Schmidt, C. Caspar, J. H. Choi, V. Jungnickel, and R. Freund, "A SiGe-HBT 2:1 analog multiplexer with more than 67 GHz bandwidth", in *Bipolar / BiCMOS Circuits and Technology Meeting*, 2017.

[91] H. Yamazaki, M. Nagatani, S. Kanazawa, H. Nosaka, T. Hashimoto, A. Sano, and Y. Miyamoto, "160-Gbps Nyquist PAM4 Transmitter Using a Digital Preprocessed Analog Multiplexed DAC", in *Eur. Conf. Opt. Commun. (ECOC)*, 2015.

[92] H. Yamazaki, U. Unkown, and U. Un, "Digital preprocessed analog multiplexed DAC for ultrawideband multilevel transmitter", *J. Light. Technol.*, vol. 34, no. 3, pp. 1570–1584, 2016.

[93] H. Yamazaki, M. Nagatani, S. Kanazawa, H. Nosaka, T. Hashimoto, F. Hamaoka, and Y. Miyamoto, "Discrete Multi-tone Transmitter at Net Data Rate of 200 Gbps Using a Digital Preprocessed Analog Multiplexed DAC", in *Eur. Conf. Opt. Commun. (ECOC)*, 2016.

[94] S. L. Jansen, I. Morita, T. C. W. Schenk, and T. Tanaka, "121.9-Gb/s PDM-OFDM transmission with 2-b/s/Hz spectral efficiency over 1000 km of SSMF", *J. Light. Technol.*, vol. 27, no. 3, pp. 177–188, 2009.

[95] C. Kottke, K. Habel, C. Schmidt, and V. Jungnickel, "154.9 Gb/s OFDM Transmission Using IM-DD, Electrical IQ-Mixing and Signal Combining", in *Opt. Fiber Commun. Conf. (OFC)*, 2016.

[96] C. Kottke, C. Schmidt, K. Habel, V. Jungnickel, and R. Freund, "Performance of Single- and Multi-Carrier Modulation with Additional Spectral Up-conversion for Wideband IM/DD Transmission", in *Photonic Networks, 17. ITG-Symposium*, 2017.

[97] C. Kottke, C. Schmidt, R. Freund, and V. Jungnickel, "Bandwidth Extension Techniques for High-Speed Access Networks", in *Opt. Fiber Commun. Conf. (OFC)*, 2018.

[98] C. Kottke, C. Schmidt, V. Jungnickel, and R. Freund, "Performance of Bandwidth Extension Techniques for High-Speed Access Networks", *J. Light. Technol.*, vol. 37, no. 2, pp. 665–672, 2018.

[99] C. Schmidt, C. Kottke, V. Jungnickel, and R. Freund, "Enhancing the Bandwidth of DACs by Analog Bandwidth Interleaving", in *Broadband Coverage in Germany, 10. ITG-Symposium*, 2016.

[100] C. Schmidt, C. Kottke, R. Freund, and V. Jungnickel, "Bandwidth Enhancement for an Optical Access Link by using a Frequency Interleaved DAC", in *Opt. Fiber Commun. Conf. (OFC)*, 2018.

[101] C. Schmidt, C. Kottke, V. Jungnickel, and R. Freund, "High-Speed Digital-to-Analog Converter Concepts", in *Proc. SPIE*, vol. 10130, 2017, 101300N–1.

[102] C. Schmidt, C. Kottke, R. Freund, F. Gerfers, and V. Jungnickel, "Digital-to-Analog Converters for High-Speed Optical Communications using Frequency Interleaving: Impairments & Characteristics", *Opt. Express*, vol. 26, no. 6, pp. 6758–6770, 2018.

[103] S. Overhoff, *Selecting High-Linearity Mixers for Wireless Base Stations*, 2009. [Online]. Available: `https://www.maximintegrated.com`.

[104] F. Marki and C. Marki, *Mixer basics primer*, 2010. [Online]. Available: `www.markimicrowave.com`.

[105] D. M. Pozar, *Microwave Engineering*, ser. 4. Wiley, 2012.

[106] B. C. Henderson, *Mixers in Microwave Systems*. [Online]. Available: `www.wj.com`.

[107] L. Devlin, "Mixers", in *How to Design RF Circuits, IEE Training Course*, vol. 2000 / 027.

[108] M. Microwave, *Datasheet I/Q mixer MLIQ-1845, Marki Microwave*. [Online]. Available: `www.markimicrowave.com`.

[109] D. N. Held and A. R. Kerr, "Conversion Loss and Noise of Microwave and MillirneterWave Mixers", *IEEE Trans. Microw. Theory Techn.*, vol. 26, no. 2, pp. 49–55, 1978.

[110] D. H. Steinbrecher, "Mixer Fundamentals", in *RF Technology Expo*, 1989.

[111] M. Valkama, M. Renfors, and V. Koivunen, "Advanced Methods for I/Q Imbalance Compensation in Communication Receivers", *IEEE Trans. Signal Process.*, vol. 49, no. 10, pp. 2335–2344, 2001.

[112] T. C. W. Schenk, P. F. M. Smulders, and E. R. Fledderus, "Estimation and Compensation of TX and RX IQ Imbalance in OFDM-based MIMO Systems", in *IEEE Radio and Wireless Symposium*, 2006.

[113] T. C. W. Schenk, P. F. M. Smulders, and E. R. Fledderus, "Estimation and compensation of frequency selective TX/RX IQ imbalance in MIMO OFDM systems", in *IEEE International Conference on Communications*, 2006.

[114] Y. Ma, W. Shieh, and Q. Yang, "Bandwidth-Efficient 21.4 Gb/s Coherent Optical 2×2 MIMO OFDM Transmission", in *Opt. Fiber Commun. Conf. (OFC)*, 2008.

[115] J. Tubbax, B. Come, L. Van der Perre, L. Deneire, S. Donnay, and M. Engels, "Compensation of IQ imbalance in OFDM systems", in *IEEE International Conference on Communications*, 2003.

[116] R. A. Shafik, M. S. Rahman, and R. Islam, "On the Extended Relationships Among EVM, BER and SNR as Performance Metrics", in *IEEE International Conference on Electrical and Computer Engineering*, 2006.

[117] K. D. Kammeyer and V. Kühn, *Matlab in Der Nachrichtentechnik*. J. Schlembach, 2001.

[118] D. Falconer, S. L. Ariyavisitakul, A. Benyamin-Seeyar, and B. Eidson, "Frequency Domain Equalization for Single-Carrier Broadband Wireless Systems", *IEEE Commun. Mag.*, vol. 40, no. 4, pp. 58–66, 2002.

[119] L. R. Rabiner and B. Gold, *Theory and Application of Digital Signal Processing*. Prentice-Hall, 1975.

[120] M. Microwave, *Microwave Power Dividers and Couplers Tutorial*. [Online]. Available: `http://www.markimicrowave.com/assets/appnotes/Microwave_Power_Dividers_and_Couplers_Primer.pdf`..

[121] J. J. Carr, *RF Components and Circuits*. Newnes, 2002.

[122] C. Schmidt, V. H. Tanzil, C. Kottke, R. Freund, and V. Jungnickel, "Digital Signal Splitting Among Multiple DACs for Analog Bandwidth Interleaving (ABI)", in *IEEE International Conference on Electronics, Circuits, & Systems*.

[123] C. Kachris and I. Tomkos, "A roadmap on optical interconnects in data centre networks", in *International Conference on Transparent Optical Networks (ICTON)*, 2015.

[124] L. A. Graham, H. Chen, D. Gazula, T. Gray, J. K. Guenter, B. Hawkins, R. Johnson, C. Kocot, A. N. MacInnes, G. D. Landry, and j. A. Tatum, "The next generation of high speed VCSELs at Finisar", *Proc. SPIE*, vol. 8276, pp. 1–9, 2012.

[125] H. Y. Kao, C. T. Tsai, S. F. Leong, C. Y. Peng, Y. C. Chi, J. J. Huang, H. C. Kuo, T. T. Shih, J. J. Jou, W. H. Cheng, C. H. Wu, and G. R. Lin, "Comparison of single-/few-/multi-mode 850 nm VCSELs for optical OFDM transmission", *Opt. Express*, vol. 25, no. 14, pp. 16 347–16 363, 2017.

[126] E. Alliance, *Finisar 400G products*. [Online]. Available: `http://investor.finisar.com/releasedetail.cfm?releaseid=1018197`.

[127] P. Westbergh, E. P. Haglund, E. Haglund, R. Safaisini, J. Gustavsson, and A. Larsson, "High-speed 850 nm VCSELs operating error free up to 57 Gbit/s", *Electron. Lett.*, vol. 49, no. 16, 2013.

[128] D. Kuchta, A. V. Rylyakov, C. L. Schow, J. E. Proesel, and C. Baks, "64Gb/s Transmission over 57m MMF using an NRZ Modulated 850nm VCSEL", in *Opt. Fiber Commun. Conf. (OFC)*, 2014.

[129] K. Szczerba, P. Westbergh, M Karlsson, P. A. Andrekson, and A. Larsson, "60 Gbits error-free 4-PAM operation with 850 nm VCSEL", *Electron. Lett.*, vol. 49, no. 15, 2013.

[130] K. Szczerba, P. Westbergh, M Karlsson, P. A. Andrekson, and A. Larsson, "70 Gbps 4-PAM and 56 Gbps 8-PAM Using an 850 nm VCSEL", *J. Light. Technol.*, vol. 33, no. 7, 2015.

[131] T. Zuo, L. Zhang, J. Zhou, Q. Zhang, E. Zhou, and G. N. Liu, "Single Lane 150-Gb/s, 100-Gb/s and 70-Gb/s 4-PAM Transmission over 100-m, 300-m and 500-m MMF Using 25-G Class 850nm VCSEL", in *Eur. Conf. Opt. Commun. (ECOC)*, 2016.

[132] S. A. Gebrewold, A. Josten, B. Baeuerle, M. Stubenrauch, S. Eitel, and J. Leuthold, "PAM-8 108 Gbit/s Transmission Using an 850nm Multi-Mode VCSEL", in *Lasers and Electro-Optics Europe & European Quantum Electronics Conference (CLEO /Europe-EQEC)*, 2017.

[133] R. Puerta, M. Agustin, L. Chorchos, J. Tonski, J. Kropp, N. Ledentsov Jr., V. Shchukin, N. N. Ledentsov, R. Henker, I. T. Monroy, J. J. V. Olmos, and J. P. Turkiewicz, "Effective 100 Gb/s IM/DD 850 nm multi- and single-mode VCSEL transmission through OM4 MMF", *J. Light. Technol.*, vol. 35, no. 15, pp. 423–429, 2017.

[134] I. Lu, C. Wei, H. Chen, K. Z. Chen, C. H. Huang, K. Chi, J. Shi, F. I. Lai, D. H. Hsieh, H. C. Kuo, W. Lin, S. W. Chiu, and J. Chen, "Very High Bit-Rate Distance Product Using High-Power Single-Mode 850-nm VCSEL With Discrete Multitone Modulation Formats Through OM4 Multimode Fiber", *IEEE J. Sel. Top. Quantum Electron.*, vol. 21, no. 6, pp. 444–452, 2015.

[135] B. Wu, M. Yanan, L. Jun, Z. Kangping, Q. Shaofeng, F. Zhiyong, L. Yazhi, M. Agustin, N. Ledentsov Jr., J. Kropp, V. Shchukin, N. N. Ledentsov, I. Eddie, and L. Chao, "Close to 100 Gbps Discrete Multitone Transmission over 100m of Multimode Fiber Using a Single Transverse Mode 850nm VCSEL", *Proc. SPIE*, vol. 9766, 97660K–97660K–7, 2016.

[136] B. Wu, Z. Xian, M. Yanan, J. Luo, Q. Shaofeng, Z. Kangping, F. Zhiyong, L. Chao, V. Shchukin, J. Kropp, and N. N. Ledentsov, "Single-Lane 112Gbps Transmission over 300m OM4 Multimode Fiber Based on A Single-Transverse-Mode 850nm VCSEL", in *Eur. Conf. Opt. Commun. (ECOC)*, 2016.

[137] D. Kuchta and et al., "Error-free 56 Gb/s NRZ Modulation of a 1530 nm VCSEL Link", *J. Light. Technol.*, vol. 34, no. 14, pp. 3275–3282, 2016.

[138] F. Karinou, C. Prodaniuc, N. Stojanovic, M. Ortsiefer, A. Daly, R. Hohenleitner, B. Kögel, and C. Neumeyr, "Directly PAM-4 Modulated 1530-nm VCSEL Enabling 56 Gb/s/λ Data-Center Interconnects", *IEEE Photon. Technol. Lett.*, vol. 27, no. 17, pp. 1872–1875, 2015.

[139] C. Xie, P. Dong, S. Randel, D. Pilori, P. Winzer, S. Spiga, B. Kögel, C. Neumeyr, and M. C. Amann, "Single-VCSEL 100-Gb/s Short-Reach System Using Discrete Multi-Tone Modulation and Direct Detection", in *Opt. Fiber Commun. Conf. (OFC)*, 2015.

[140] A. Dochhan, N. Eiselt, R. Hohenleitner, H. Griesser, M. Eiselt, M. Ortsiefer, C. Neumeyr, J. Olmos, I. T. Monroy, and J. P. Elbers, "56 Gb/s DMT Transmission with VCSELs in 1.5 um Wavelength Range over up to 12 km for DWDM Intra-Data Center Connects", in *Eur. Conf. Opt. Commun. (ECOC)*, 2016.

[141] C. Vasconcelos, D. Mello, and F. Simoes, "Signal Predistortion for Nonlinear Transmitters in Direct-Detection OFDM over Multimode Fibers", in *Telecommunications Symposium (ITS)*, Sao Paulo, Brazil, 2014.

[142] I. Lu, C. Wei, H. Chen, P. Chung, P. Huang, J. Jiang, K. Chi, J. Shi, and J. Chen, "Nonlinear Compensation for 980 nm High Power, Single- Mode VCSELs for Energy Efficient OM 4 Fiber Transmission", in *Opt. Fiber Commun. Conf. (OFC)*, 2014.

[143] J. Liu, K. Chi, C. Wei, T. Lin, C. Chuang, X. Chen, J. Shi, and J. Chen, "High Bit-Rate Distance Product of 128 Gbps*km 4-PAM Transmission over 2 km OM4 fiber Using a 850 nm VCSEL and a Volterra Nonlinear Equalizer", in *Opt. Fiber Commun. Conf. (OFC)*, 2017.

[144] J. Castro, R. Pimpinella, B. Kose, Y. Huang, B. Lane, A. Amezuca, M. Bigot, D. Molin, and P. Sillard, "200m 2x50 Gb/s PAM-4 SWDM Transmission Over Wideband Multimode Fiber using VCSELs and Pre-distortion Signaling", in *Opt. Fiber Commun. Conf. (OFC)*, 2016.

[145] T. Maiman, "Stimulated Optical Radiation in Ruby", *Nature*, vol. 187, pp. 493–494, 1960, Nature 187, 493-494 (6 August 1960) | Theodore Maiman.

[146] K. Iga, S. Kinoshita, and F. Koyama, "Microvavity GaAl/GaAs surface-emitting laser with I = 6 mA", *Electron. Lett.*, vol. 23, no. 4, pp. 134–136, 1987.

[147] J. Tatum, "VCSEL Proliferation", *Proc. SPIE*, vol. 6484, pp. 648 403–648403–7,

[148] S. Yu, "Thermal Characteristics of Vertical Cavity Surface Emitting Lasers", in *Analysis and Design of Vertical Cavity Surface Emitting Lasers*, John Wiley & Sons, Inc., 2003.

[149] P. Baveja, P. P. Baveja, B. Kögel, P. Westbergh, J. Gustavsson, A. Haglund, D. N. Maywar, G. P. Agrawal, and A. Larsson, "Assessment of VCSEL thermal rollover mechanisms from measurements and empirical modeling", *Opt. Express*, vol. 19, no. 16, pp. 15 490–15 505, Optics Express Vol. 19, Issue 16, pp. 15490-15505 (2011).

[150] P. Nyakas, G. Varga, Z. Puskas, N. Hashizume, T. Karpati, T. Veszpremi, and G. Zsombok, "Self-consistent real three-dimensional simulation of vertical-cavity surface-emitting lasers", *J. Opt. Soc. Am. B*, vol. 23, no. 9, pp. 1761–1769,

[151] V. Photonics, "Vpi vcsel model",

[152] W. Way, *Broadband Hybrid Fiber Coax Access System Technologies*. Orlando, FL, USA: Academic Press, Inc., 1998.

[153] *Understand SINAD, ENOB, SNR, THD, THD + N, and SFDR so you Don't Get Lost in the Noise Floor, ANALOG DEVICES*, 2008. [Online]. Available: `http://www.analog.com/media/en/training-seminars/tutorials/MT-003.pdf`.

[154] *Finisar APPLICATION NOTE Modulating VCSELs*. [Online]. Available: `https://www.finisar.com/products/application-notes`.

[155] N. Stojanovic, Z. Qiang, C. Prodaniuc, and F. Karinou, "Eye Deskewing Algorithms for PAM Modulation Formats in IM-DD Transmission Systems", in *Opt. Fiber Commun. Conf. (OFC)*, 2017.

[156] E. Westbergh, R. Safaisini, E. Haglund, J. Gustavsson, A. Larsson, and A. Joel, "High-speed 850 nm VCSELs with 28 GHz modulation bandwidth for short reach communication", *Proc. SPIE*, vol. 8639, pp. 86390X1–86390X6,

[157] V. Shchukin, N. Ledentsov, J. Kropp, G. Steinle, N. Ledentsov Jr., S. Burger, and F. Schmidt, "Single-Mode Vertical Cavity Surface Emitting Laser via Oxide-Aperture-Engineering of Leakage of High-Order Transverse Modes", *IEEE J. Quantum Electron.*, vol. 50, no. 12, pp. 990–995, 2014.

[158] E. Voges and K. Petermann, *Optische Kommunikationstechnik*. Springer, 2002.

[159] I. Joindot, "Measurements of relative intensity noise (RIN) in semiconductor lasers", *J. Phys.*, vol. 111, no. 2, 1992.

[160] S. Pavan, J. Lavrencik, and S. E. Ralph, "Experimental demonstration of 51.56 Gbit/s PAM-4 at 905nm and impact of level dependent RIN", in *Eur. Conf. Opt. Commun. (ECOC)*, 2014.

[161] S. Ralph, "Requirements and Results for Practical VCSEL Transmission using PAM-4 over MMF", in *Opt. Fiber Commun. Conf. (OFC)*, 2016.

[162] A. Valle and L. Pesquera, "Relative Intensity Noise of Multitransverse-Mode Vertical-Cavity Surface-Emitting Lasers", *IEEE Photon. Technol. Lett.*, vol. 13, no. 4, pp. 272–274, 2001.

[163] J. Lavrencik, S. K. Pavan, D. K. Haupt, and S. E. Ralph, "Direct Measurement of Transverse Mode Correlation and MPN using 900nm VCSELs", in *Opt. Fiber Commun. Conf. (OFC)*, 2015.

[164] C. Kottke, C. Caspar, V. Jungnickel, R. Freund, M. Agustin, J. Kropp, and N. N. Ledentsov, "High Speed 160 Gb/s DMT VCSEL Transmission Using Preequalization", in *Opt. Fiber Commun. Conf. (OFC)*, 2017.

[165] V. Volterra, *Theory of Functionals and of Integrals and Integro-Differential Equations*. New York: Dover Publications, 1959.

[166] N. Wiener, *Response of a nonlinear device to noise*. [Online]. Available: `http://www.dtic.mil/dtic/tr/fulltext/u2/a800212.pdf`.

[167] M. Schetzen, *The Volterra & Wiener Theories of Nonlinear Systems*. Mlaabar, USA: Krieger Publishing Company, 2006.

[168] T. Ogunfunmi, *Adaptive Nonlinear System Identification, The Volterra and Wiener Model Approaches*. Springer, 2006.

[169] R. Nowak and B. Van Veen, "Volterra Filter Equalization: A Fixed Point Approach", *IEEE Trans. Signal Process.*, vol. 45, no. 2, pp. 377–388, 1997.

[170] C. Eun and J. Powers, "A New Volterra Predistorter Based on the Indirect Learning Architecture", *IEEE Trans. Signal Process.*, vol. 45, no. 1, pp. 223–227, 1997.

[171] C. Kottke, C. Caspar, V. Jungnickel, R. Freund, M. Agustin, J. Kropp, and N. N. Ledentsov, "High Speed DMT and VCSEL Based MMF Transmission Using Pre-distortion", *J. Light. Technol.*, vol. 36, no. 2, pp. 168–174, 2018.

[172] *VI-Systems*. [Online]. Available: `http://v-i-systems.com/`.

[173] V. Shivashankar, C. Kottke, V. Jungnickel, and R. Freund, "Investigation of Linear and Nonlinear Pre-Equalization of VCSEL", in *Broadband Coverage in Germany, 11. ITG-Symposium*, 2017.

[174] P. Mena, J. Morikuni, S.-M. Kang, A. Harton, and K. Wyatt, "A Simple Rate-Equation-Based Thermal VCSEL Model", *J. Light. Technol.*, vol. 17, no. 5, 1999.

[175] K. Petermann, *Laser Diode Modulation and Noise*. Kluwer Academic, 1988, K. Petermann, Laser Diode Modulation and Noise, Dordrecht, the Netherlands, Kluwer Academic, 1988.

[176] *VPI VCSEL Manual*.

[177] J. W. Scott, R. S. Geels, S. W. Corzine, and L. A. Coldren, "Modeling Temperature Effects and Spatial Hole Burning to Optimize Vertical-Cavity Surface-Emitting Laser Performance", *IEEE J. Quantum Electron.*, vol. 29, no. 5, pp. 1295–1308, 1993.

[178] R. Michalzik and K. J. Ebeling, "Modeling and design of protonimplanted ultralow threshold vertical cavity laser diodes", *IEEE J. Quantum Electron.*, vol. 29, pp. 1963–1974,

[179] Y. Su, Y. Chang, and X. Chen, "Y. Su, Y. Chang, and X. Chen,"Circuit model for studying temperature effects on vertical-cavity surface-emitting laser," in Proc. IEEE LEOS Annu. Meeting, 1996, vol. 1, pp. 215–216.", in *IEEE LEOS Annu. Meeting*, vol. 1, 1996, pp. 215–216.

[180] G. P. Agrawal and N. K. Dutta, *Semiconductor Lasers*, 2nd ed. New York: Van Nostrand Reinhold, 1993.

[181] Y. Ohiso, K. Tateno, Y. Kohama, A. Wakatsuki, H. Tsunetsugu, and T. Kurokawa, "Flip-Chip Bonded 0.85 um Bottom-Emitting Vertical-Cavity Laser Array on an AlGaAs Substrate", *IEEE Photon. Technol. Lett.*, vol. 8, no. 9, pp. 1115–1117, 1996.